THEORETICAL STUDIES ON ELECTRON BEAM BASED COMPACT TERAHERTZ SOURCES

By

YASHVIR KALKAL

PHYS03201104013

Raja Ramanna Centre for Advanced Technology, Indore

A thesis submitted to the

Board of Studies in Physical Sciences

In partial fulfillment of requirements

for the Degree of

DOCTOR OF PHILOSOPHY

of

HOMI BHABHA NATIONAL INSTITUTE

September, 2016

Homi Bhabha National Institute[1]

Recommendations of the Viva Voce Committee

As members of the Viva Voce Committee, we certify that we have read the dissertation prepared by **Yashvir Kalkal** entitled **"Theoretical Studies on Electron Beam Based Compact Terahertz Sources"** and recommend that it may be accepted as fulfilling the thesis requirement for the award of Degree of Doctor of Philosophy.

	20/3/17
Chairman – Dr. P. A. Naik	**Date:**
Vinit Kumar	20.3.2017
Guide – Dr. Vinit Kumar	**Date:**
P. Jha	20.3.17
External Examiner – Dr. Pallavi Jha	**Date:**
	20.3.17
External Member – Dr. Ganeshwar Mishra	**Date:**
	20/03/2017
Member1 - Dr. H. S. Rawat	**Date:**
	20-3-17
Member2 - Dr. K. S. Bindra	**Date:**
	20/3/17
Member3 - Dr. S. K. Dixit	**Date:**
	20.3.17
Member4 - Dr. S. M. Gupta	**Date:**
Aparna Chakrabarti	20.3.17
Member5 – Dr. Aparna Chakrabarti	**Date:**

Final approval and acceptance of this thesis is contingent upon the candidate's submission of the final copies of the thesis to HBNI.

I/We hereby certify that I/we have read this thesis prepared under my/our direction and recommend that it may be accepted as fulfilling the thesis requirement.

Date: 20.3.2017

Place: RRCAT, INDORE

Guide: Vinit Kumar

Dr. Vinit Kumar

[1] This page is to be included only for final submission after successful completion of viva voce.

STATEMENT BY AUTHOR

Yashvir Kalkal

DECLARATION

I, hereby declare that the investigation presented in the thesis has been carried out by me. The work is original and has not been submitted earlier as a whole or in part for a degree/diploma at this or any other Institution/University.

Yashvir Kalkal

List of Publications Arising from the Thesis

Journal

1. "Analysis of Čerenkov free-electron lasers" **Yashvir Kalkal** and Vinit Kumar, *Phys. Rev. ST Accel. Beams*, **2015**, *18*, 030707.

2. "Čerenkov free-electron laser with side walls" **Yashvir Kalkal** and Vinit Kumar, *Nucl. Instrum. Methods Phys. Res. A*, **2016**, *827*, 85.

3. "Three-dimensional analysis of the surface mode supported in Čerenkov and Smith-Purcell free-electron lasers" **Yashvir Kalkal** and Vinit Kumar, *Phys. Rev. Accel. Beams*, **2016**, *19*, 060702.

4. "Terahertz radiation source using a high-power industrial electron linear accelerator" **Yashvir Kalkal** and Vinit Kumar, *Pramana – J. Phys.*, **2017**, *88*, 71.

Conferences

1. "Optimization of parameters of a terahertz Čerenkov free-electron laser" **Yashvir Kalkal** and Vinit Kumar, 24th DAE BRNS National Laser Symposium, December 2-5, **2015**, RRCAT, Indore, India.

Yashvir Kalkal

DEDICATION

This thesis is dedicated to my parents

ACKNOWLEDGEMENTS

The completion of the present thesis could not have been possible without the constant support and guidance of many people. First of all, I would like to thank my supervisor Prof. Vinit Kumar for his valuable guidance, support and encouragement throughout the tenure of my PhD. His clear, elegant and simple approach of illustrating scientific ideas has helped me to understand several aspects of *free-electron laser* theory and related research. Apart from physics, I have also learnt from him about presenting scientific work. I acknowledge him humbly for all his support.

I would like to express my gratitude to Dr. Kamal Kumar Pant for his guidance and encouragement. I thank him especially for many useful comments and constructive suggestions which helped me to complete the thesis on time. I am grateful to Prof. S. B. Roy for his constant support and encouragement.

I am grateful to the anonymous referees of my journal publications for their suggestions and comments which helped me to improve the quality of the work presented in this thesis. I sincerely acknowledge the generous help received from Bill Fawley in GINGER simulations. I am thankful to all the members of my doctoral committee for evaluating the progress of my research work during the last five years.

I extend my thanks to Mukesh Kumar Pal, Rinky Dhingra, Rahul Gaur, Arup Ratan Jana, Bhaskar Biswas, Dr. Shankar Lal, Dr. Arvind Kumar and Dr. M. K. Chattopadhyay for their fruitful advices. My gratitude as well to Prof. Arup Banerjee, Prof. Aparna Chakrabarti and Prof. P. D. Gupta for their support. I am obliged to Prof. Jaiveer Suhag and Dr. Milan Agrawal for their contribution in shaping my career.

It is a pleasure to thank Ram Prakash and Sona Chandran P. for creating an intellectually stimulating surrounding. It has been a great fun discussing various aspects of physics, philosophy and mysticism with them. I would like to thank my batchmates Gopal, Paromita, Smriti, DJ, Girish, Uttam, Kuldeep and Newton for their never ending help. Arijit Chakraborty and Sandeep Kumar are acknowledged for their help in preparing the figures presented in this thesis. I am thankful to my friends Mohit, Rajkumar, Manjeet, Pradeep and Raman for making this life a wonderful journey. I am thankful to my friend Kumar Avisek. I do not think I can count what he has done for me.

Finally, I express a deep sense of gratitude to my parents for their love, support and encouragement.

Contents

Synopsis

During recent times, terahertz (THz) sources of radiation are actively being developed for a variety of potential applications in material and biological sciences, information and communication technology, astronomical observation, global environmental monitoring, quality control of food and security etc. [1, 2]. Commercially available conventional laser-enabled THz sources, e.g., parametric oscillators and time domain systems have limited use due to their low average output power (~ tens of nW) [3]. Direct laser based THz sources like quantum cascade lasers and optically or electrically pumped gas lasers give relatively high average power (~ tens or hundreds of mW), but are not continuously tunable [3]. On the other hand, electron beam based THz sources, e.g., traveling wave tubes (TWTs), backward wave oscillators (BWOs), synchrotrons and undulator based conventional free-electron lasers (FELs) are well known for their wide tunability and relatively high average output power [4–7]. The TWTs and the BWOs produce an average output power of the order of few tens of mW, but their operation is limited up to a maximum frequency of about 1 THz [4]. In modern synchrotrons such as BESSY II in Berlin [5] and the recirculating linac at Jefferson Laboratory [6], short electron bunches are used to generate broadband THz radiation with an average power of tens of watts. A dedicated facility having an undulator based FEL can generate high average power (~ tens or hundreds of watt) in the THz regime [7]. Both the synchrotrons and the undulator based FELs are operated with a relativistic electron beam, and consequently require large radiation shielding structures and expensive infrastructure. Recently, efforts have been made to reduce the physical size of undulator based FELs at ENEA-Frascati centre in Italy [8] and at Argonne National Laboratory in the USA [9]; however, their functioning as a viable mobile or a compact tabletop device is yet to be demonstrated [10].

Over the last few decades, a considerable amount of attention has also been paid to make FELs by utilizing the Čerenkov radiation and the Smith-Purcell radiation. Both the Čerenkov free-electron lasers (CFELs) [11–13] and the Smith-Purcell free-electron lasers (SP-FELs) [14–16] use low energy electron beam and therefore require only a nominal radiation shielding. They are very compact, which makes them useful for tabletop THz experiments. In this thesis, we have carried out a detailed analysis of these systems in order to develop an enhanced understanding of the electron beam based compact THz sources. Within the same framework, we have also explored the possibility of generating THz radiation through spontaneous emission by passing an electron beam emerging from a high average power industrial electron linear accelerator (linac) in an irradiation facility through an optimized undulator, before striking the irradiation target. This makes the device compact since it does not require a high-quality electron beam, and enhances the utility of the high average power industrial linac.

The CFELs and the SP-FELs support an electromagnetic wave with phase velocity less than the speed of light, which interacts with the co-propagating electron beam to generate coherent THz radiation. In the CFEL, a thin dielectric material lined on an ideal conductor acts as a slow wave structure and in the SP-FEL, a metallic reflection grating is used as a slow wave structure. The configurations studied so far in these systems are: single or double slab/grating based structures in the planar geometry, and the cylindrical waveguide geometry. Our work in the present thesis remains focused on the planar geometry of these devices, which is helpful in achieving a high frequency of operation [17] and in reducing the space charge effects.

Earlier analyses of the planar geometries of the CFELs have used the Maxwell-Vlasov approach [18–20] and the hydrodynamic approach [21–24] to find the small-signal gain and growth rate. Despite their success in the linear regime, both these approaches are difficult to extend to the non-linear regime to analyze the saturation behavior of the system. We would like to mention that in the conventional undulator based FELs, the approach based on the coupled

Maxwell-Lorentz equations has been extremely successful to study the saturation behavior of the system. It is therefore natural to ask whether this approach can be established for the detailed analysis of CFEL and SP-FEL system. A detailed non-linear analysis based on the coupled Maxwell-Lorentz equations has recently been presented by Kumar and Kim [25] for the planar geometry based SP-FELs, driven by a flat electron beam. In the present thesis, we have established the Maxwell-Lorentz approach for the single slab based CFELs. A computer code based on the leapfrog method has been developed to solve the coupled Maxwell-Lorentz equations. We would like to mention that there have been earlier attempts to establish the Maxwell-Lorentz approach for the single slab based CFELs in Refs. [26–28], however, the evanescent nature of the electromagnetic field was not included in these analyses, which we have included in the present thesis. It is important to mention here that the reported output power in the experimental studies on the CFELs [11–13] and the SP-FELs [14–16] was very low. In order to obtain a copious amount of coherent THz radiation from these devices, an enhanced understanding is required; which includes analyzing the realistic effects due to diffraction and attenuation of the surface mode supported by these systems, and then working out the requirement on electron beam parameters, which is very critical for the performance of the system. Andrew and Brau [22] have included the effect of diffraction in the hydrodynamic approach for the CFELs, and the hydrodynamic approach has also been explored to evaluate the growth rate of the SP-FELs [29] including the effects of diffraction [30] and attenuation [31]. These results [21–24, 29–31] are however not directly useful in obtaining the required electron beam parameters in the vertical direction. This is because the analysis is for the case of an electron beam filling uniformly the entire half space above the dielectric or grating, as opposed to an electron beam with a very small vertical width in the realistic situation. For the case of SP-FEL, Kim and Kumar [32, 33] have extended the Maxwell-Lorentz approach to include the effects of diffraction and attenuation and found the requirements on the electron beam parameters for the successful operation. In the present thesis, we have used a similar approach to include the diffraction and attenuation effects in the analysis of CFELs by setting up the three-dimensional (3D) coupled Maxwell-Lorentz equations. More importantly, the stringent requirements on the electron beam parameters for the successful operation of the CFELs have been worked out to explain the poor performance of past experiments. Inclusion of deleterious effect of attenuation turns out to be very important, like for any high frequency device that uses a metallic conductor. However, all the earlier analyses on single slab based CFELs have neglected the effect of attenuation. In the present thesis, we have included the effect of attenuation and optimized the parameters of a CFEL working in a realistic condition. By following the approach quite similar to the case of the CFELs, we provide a rigorous derivation of the 3D coupled Maxwell-Lorentz equations for the SP-FELs also, and highlighted some important and interesting differences in the behavior of CFELs and SP-FELs. We have then further explored the Maxwell-Lorentz approach for two novel configurations of CFELs, i.e., a side wall configuration and a double slab configuration, which are shown to give enhanced performance. Our results in the present thesis indicate that it should be possible to produce copious amount of THz radiation from the CFELs and the SP-FELs, even after including the attenuation and 3D effects, if the electron beam parameters are chosen properly.

Next, we have also explored the possibility of generating THz radiation through spontaneous emission in an undulator by utilizing an electron beam emerging from a high average power ($\sim$ 100 kW) industrial linac. Typically, a low average power ($\sim$ tens or hundreds of watt) electron beam is used in undulator based conventional FELs to generate few tens or hundreds of mW output power through the process of stimulated emission. This, however, requires a high quality electron beam with low energy spread and high peak current. The infrastructure needed to meet these requirements makes an undulator based FEL bulky and impractical for the table top THz experiments. The quality of the electron beam emerging from a 100 kW industrial linac may not be very good for the operation of an FEL system, but such a high average power electron beam passing through an undulator can emit THz radiation with average power of the order of μW through spontaneous emission. The spent electron beam can be used subsequently for irradiation applications. We have performed a detailed optimization study for such a device in the thesis.

The organization of the thesis is as follows. In **Chapter 1** of the thesis, we provide an overview of existing THz sources and their applications. It is followed by a brief discussion on the importance of Čerenkov and Smith-Purcell FELs, which are electron beam based compact sources of powerful and tunable terahertz radiation. Here, we also mention various approaches used to study beam-wave interaction in the Čerenkov and Smith-Purcell FELs and emphasize the need to set up the non-linear Maxwell-Lorentz equations including realistic effects, i.e., diffraction effects, attenuation effects, and effect due to finite beam emittance in these systems. The possibility of using a high power industrial electron linear accelerator to produce THz radiation is also discussed at the end of this chapter.

The detailed analysis of the surface mode supported by a dielectric slab placed on a conducting surface is presented in **Chapter 2**. These calculations have been performed under the two-dimensional (2D) approximation, where the system is assumed to be uniform along the dielectric surface in the direction perpendicular to the electron beam propagation. Calculations for the electromagnetic fields in this structure have been carried out by evaluating the reflectivity of the dielectric slab for an incident plane evanescent wave. We have shown that the surface mode arises when there is a singularity in the reflectivity for the incident evanescent wave. This condition gives us the dispersion relation of the surface mode. This is followed by calculations for the energy stored and the energy velocity of the surface mode. We have then calculated the attenuation coefficient of the surface mode due to the finite conductivity of the metal and the dielectric. It is observed that the effect of attenuation becomes prominent at higher frequencies, and can be reduced by cooling the system. Finally, we have briefly discussed important properties of the surface mode supported by a metallic grating. The results obtained in this chapter are important ingredients for the detailed analysis of beam-wave interaction in the CFELs and the SP-FELs, which are discussed later in the thesis.

In **Chapter 3** we present a 2D analysis of single dielectric slab based CFEL driven by a flat electron beam. For this purpose, we have carried out a rigorous analysis of reflectivity of the dielectric slab around the singularity, for the growing evanescent waves, and set up the coupled Maxwell-Lorentz equations for the system. We solve these equations analytically to obtain formulas for the small-signal gain and growth rate of the CFEL system. It is observed that the results obtained for the growth rate are in exact agreement with those obtained using the hydrodynamic approach discussed in Refs. [22, 34]. To study the saturation behavior of the system, we have developed a computer code based on the leapfrog scheme and obtained numerical solution of the coupled Maxwell-Lorentz equations in the non-linear regime. As an example case, we have considered parameters used in the Dartmouth experiment [12]. We find that the CFEL is a low gain system for these parameters and needs to be operated in the oscillator configuration to get an appreciable power. The observed power in the Dartmouth experiment was very low compared to the theoretical results.

With an objective to explain the poor performance of the past experiments, we have performed analysis for the realistic situation by setting up the 3D coupled Maxwell-Lorentz equations for the CFELs and SP-FELs in **Chapter 4**. We observe that the size of the optical beam increases due to diffraction. This affects the overlap of the optical beam with the electron beam, resulting in reduction of the gain and saturated power obtained in the system. We perform a detailed 3D surface mode analysis for CFELs and choose electron beam parameters such that the electron beam envelope remains inside the optical beam envelope over the interaction length, which is necessary for maximum beam-wave interaction. We would like to mention that the optical field is confined within a very short distance (evanescent wavelength) from the dielectric surface in the vertical direction. The electron beam therefore needs to maintain a very small vertical size over the entire interaction length, which means that the beam should have a very small vertical emittance. In the horizontal direction, the required electron beam parameters depend on the diffraction effects and the conditions on the beam emittance in this direction is quite relaxed compared to the conditions on beam emittance in the vertical direction. It is observed that a flat electron beam with horizontal to vertical emittance ratio of about 1000 is required for the successful operation of a typical THz CFEL. This value is 10 times higher than the maximum value achieved in recent experiments [35, 36]. To relax the stringent requirements on the vertical beam emittance, we have discussed techniques of external focusing of a flat beam by using wiggler and solenoid magnetic fields, and also proposed several ways to achieve the required beam quality. We then perform a detailed optimization study of a CFEL, including the effects of attenuation of the surface mode. To optimize the system for minimum losses, we suggest that the metallic base should be kept at cryogenic temperature, i.e., 77 K. We find that a CFEL utilizing 5 cm long GaAs dielectric slab can deliver average output power of about ten watt at 0.1 THz frequency by using a 40 keV, 35 mA electron beam. Next, we have established 3D coupled Maxwell-Lorentz equations for the SP-FELs by following an approach similar to our analysis of the CFELs, and observed that the diffraction effects are more prominent in the SP-FELs as compared to the CFELs. Based on these analyses, we have made some interesting comparisons between the CFELs and the SP-FELs at the end of this chapter. Results presented on this work would be helpful in the detailed optimization of the CFELs and SP-FELs operating in realistic conditions.

In **Chapter 5** we propose two novel configurations of the CFELs in the planar geometry to enhance the performance of these devices. First, we discuss a single slab based CFEL system with metallic side walls, which are used to confine the diffracting electromagnetic surface mode. We set up the coupled Maxwell-Lorentz equations for the system, and obtain expressions for the small-signal gain and growth rate in the case of narrow electron beam limit. By choosing the sidewall separation as two third the value of the minimum optical mode width that can be achieved in the absence of waveguiding, we find that the gain of a sidewall CFEL can be enhanced up to a factor of three as compared to a CFEL without any side wall. We have considered the effects due to finite beam size and finite beam energy spread in the numerical simulations. A sidewall CFEL has higher efficiency and saturates quickly as compared to a CFEL without any sidewall. The stringent requirements on the vertical beam emittance also get relaxed in the case of sidewall CFEL. We then studied the second novel configuration, i.e., a double slab based rectangular waveguide CFEL by setting up the coupled Maxwell-Lorentz equations, and observed that this device has improved single pass gain as compared to a single slab based sidewall CFEL. In the oscillator configuration, however, the presence of severe losses in a double slab based rectangular CFEL offset the marginal improvement in gain that was achieved during a single pass, and this configuration becomes less efficient than the single slab based sidewall CFEL.

In **Chapter 6** we have discussed a proposal in which a high power electron beam emerging from an industrial electron linac is first passed through an undulator to generate powerful THz radiation through spontaneous emission, and the spent electron beam coming out of the undulator can still be used for industrial applications. This enhances the utility of the industrial linac. By taking an example case with typical parameters of a high average power industrial linac, we have optimized the undulator parameters, and shown that an average output power of the order of μW can be obtained from this device. The output radiation can be tuned from 1.6 to 4.3 THz by changing the undulator K parameter from 0.6 to 2.1, and electron beam energy from 7.5 MeV to 10 MeV. Results presented in this work would be helpful in the detailed optimization of a high average power electron linac based source of THz radiation.

We summarize the thesis and provide a brief discussion on the possible future work in **Chapter 7**.

References for synopsis

[1] P. H. Siegel, IEEE Trans. Microwave Theory Tech. **50**, 910 (2002).

[2] M. Tonouchi, Nature Photonics **1**, 97 (2007).

[3] E. R. Muller, The industrial Physicist (American Institute of Physics) **9**, 27 (2003).

[4] K. J. Button and J. C. Wiltse, *Infrared and millimeter waves* (Academic Press, University of Michigan, USA, 1979).

[5] M. Abo-Bakr, J. Feikes, K. Holldack, G. Wüstefeld, and H.-W. Hübers, Phys. Rev. Lett. **88**, 254801 (2002).

[6] G. P. Williams, Rev. Sci. Instrum. **73**, 1461 (2002).

[7] S. Krishnagopal, V. Kumar, S. Maiti, S. Prabhu, and S. K. Sarkar, Curr. Sci. **87**, 1066 (2004).

[8] A. Doria, V. Asgekar, D. Esposito, G. Gallerano, E. Giovenale, G. Messina, and C. Ronsivalle, Nucl. Instrum. Methods Phys. Res. A **475**, 296 (2001).

[9] S. G. Biedron, J. W. Lewellen, S. V. Milton, N. Gopalsami, J. F. Schneider, L. Skubal, Y. Li, M. Virgo, G. P. Gallerano, A. Doria, et al., in *Proceedings of the IEEE* (IEEE, 2007), vol. 95, pp. 1666–1678.

[10] A. V. Smirnov, R. Agustsson, W. J. Berg, S. Boucher, J. Dooling, T. Campese, Y. Chen, L. Erwin, B. Jacobson, J. Hartzell, et al., Phys. Rev. ST Accel. Beams **18**, 090703 (2015).

[11] F. Ciocci, A. Doria, G. P. Gallerano, I. Giabbai, M. F. Kimmitt, G. Messina, A. Renieri, and J. E. Walsh, Phys. Rev. Lett. **66**, 699 (1991).

[12] I. J. Owens and J. H. Brownell, J. Appl. Phys. **97**, 104915 (2005).

[13] M. R. Asakawa, K. Nakao, M. Kusaba, and Y. Tsunawaki, in *Proceedings of the FEL Conference* (JACoW, Berlin, 2006), pp. 364–367.

[14] J. Urata, M. Goldstein, M. F. Kimmitt, A. Naumov, C. Platt, and J. E. Walsh, Phys. Rev. Lett. **80**, 516 (1998).

[15] J. Gardelle, L. Courtois, P. Modin, and J. T. Donohue, Phys. Rev. ST Accel. Beams **12**, 110701 (2009).

[16] H. L. Andrews, C. A. Brau, J. D. Jarvis, C. F. Guertin, A. O'Donnell, B. Durant, T. H. Lowell, and M. R. Mross, Phys. Rev. ST Accel. Beams **12**, 080703 (2009).

[17] F. Ciocci, G. Dattoli, A. Doria, G. Schettini, A. Torre, and J. E. Walsh, Nuovo Cimento **10D**, 1 (1988).

[18] J. Walsh, B. Johnson, G. Dattoli, and A. Renieri, Phys. Rev. Lett. **53**, 779 (1984).

[19] H. Fares and M. Yamada, Phys. Plasmas **18**, 093106 (2011).

[20] H. Fares, Phys. Plasmas **19**, 053109 (2012).

[21] I. J. Owens and J. H. Brownell, Phys. Rev. E **67**, 036611 (2003).

[22] H. L. Andrews and C. A. Brau, J. Appl. Phys. **101**, 104904 (2007).

[23] D. Li, G. Huo, K. Imasaki, and M.Asakawa, Nucl. Instrum. Methods Phys. Res. A **606**, 689 (2009).

[24] G. Sharma and G. Mishra, Nucl. Instrum. Methods Phys. Res. A **685**, 35 (2012).

[25] V. Kumar and K.-J. Kim, Phys. Rev. E **73**, 026501 (2006).

[26] B. W. Gore, V. B. Asgekar, and A. Sen, Phys. Scripta. **53**, 62 (1996).

[27] V. B. Asgekar and G. Dattoli, Opt. Commun. **206**, 373 (2002).

[28] V. B. Asgekar and G. Dattoli, Opt. Commun. **255**, 309 (2005).

[29] H. L. Andrews and C. A. Brau, Phys. Rev. ST Accel. Beams **7**, 070701 (2004).

[30] J. D. Jarvis, H. L. Andrews, and C. A. Brau, Phys. Rev. ST Accel. Beams **13**, 020701 (2010).

[31] H. L. Andrews, C. H. Boulware, C. A. Brau, and J. D. Jarvis, Phys. Rev. ST Accel. Beams **8**, 050703 (2005).

[32] K.-J. Kim and V. Kumar, Phys. Rev. ST Accel. Beams **10**, 080702 (2007).

[33] V. Kumar and K.-J. Kim, Phys. Rev. ST Accel. Beams **12**, 070703 (2009).

[34] D. Li, Y. Wang, M. Hangyo, Y. Wei, Z. Yang, and S. Miyamoto, Appl. Phys. Lett. **104**, 194102 (2014).

[35] P. Piot, Y.-E. Sun, and K.-J. Kim, Phys. Rev. ST Accel. Beams **9**, 031001 (2006).

[36] J. Zhu, P. Piot, D. Mihalcea, and C. R. Prokop, Phys. Rev. ST Accel. Beams **17**, 084401 (2014).

List of Figures

List of Tables

Chapter 1

Introduction

1.1 Why terahertz sources?

About a hundred years ago, the electromagnetic spectrum that exists at the boundary between microwave and infrared radiation started attracting significant interest [1]. This region covers the frequency range from 10^{11} to 10^{13} Hz and is now commonly known as the terahertz (THz) spectral regime. For a long time, the THz spectral regime remained poorly explored due to a paucity of sources in this regime. This situation has however changed in the past three decades because of rapid development of coherent THz sources [2, 3], which in turn has stimulated many key applications in science and industry [4]. The specific appeal of THz radiation in these applications is due to its several attractive and unique properties [5].

One of the most important properties of the THz radiation (below 3 THz) is that it can penetrate through most of the dry, non-metallic and non-polar materials, which block visible radiation [4, 6]. These include plastics, ceramics, cardboards and paper based envelopes. Due to this penetrative ability, THz radiation is used for the non-destructive inspection of materials that show unique spectral features in the THz range, without actually making a physical contact with the envelop containing these materials. Due to this non-intercepting measurement process, THz imaging is sometime advantageous as compared to ultrasound imaging for fragile

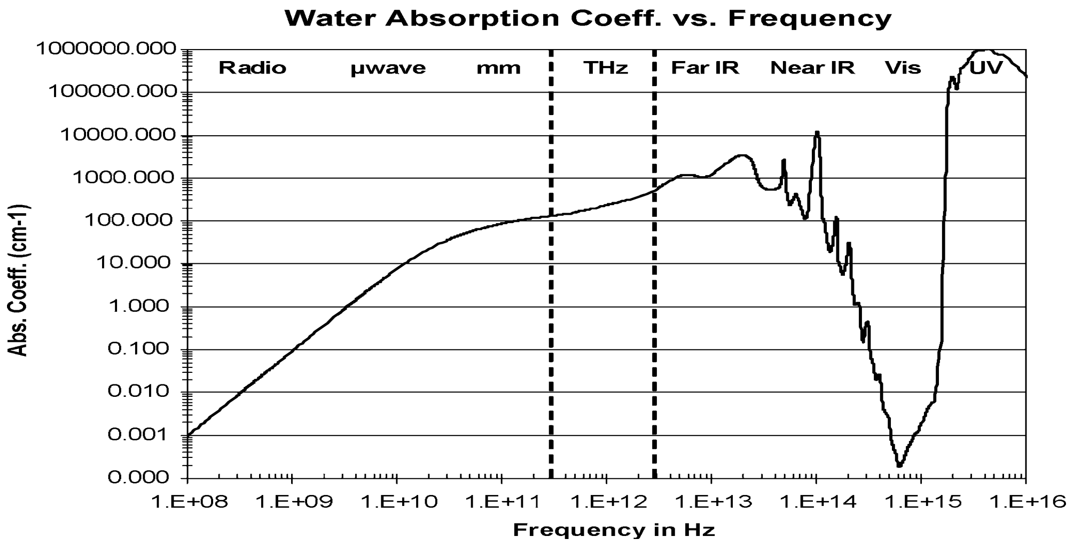

FIGURE 1.1: Absorption coefficient of triply deionized water at 292 K between 100 MHz and the ultraviolet (UV). Reprinted from "Terahertz technology in biology and medicine" by P. H. Siegel, 2004, IEEE Transactions on Microwave Theory and Techniques, **52**, pp. 2438-2447. Copyright © 2004 IEEE.

samples [7]. Another important feature of the THz radiation is that it has a low photon energy (~meV) compared to X-ray photon energy (~keV), which is also lower than the bond energy of several organic molecules and chemicals [6]. Hence, THz radiation does not cause harmful ionizing reaction. The recent studies however indicate that it can damage DNA at higher intensities, but is still safer than X-rays [8, 9]. Due to these features, THz imaging is capable of replacing X-ray imaging for security related applications, and can also be utilized in quality control of food via non-destructive testing [4]. It has important implications for airport security and related areas. The THz radiation band contains enormous spectral information about several organic compounds, polar molecules, explosives, drugs and narcotic materials [4]. These materials have distinct signatures in the THz regime, which allow their identification through THz imaging and spectroscopy. Water, which is main content in various organic and biological compounds absorbs THz radiation [10], as shown in Fig. 1.1. Hence, we can identify substances on the basis of their hydration level. In biological sciences, cancer tissues are detected through THz imaging because of their different hydration level compared to the normal tissues [10]. Research in THz science is also going on to study the structures of DNA molecules, proteins and bacteria [11, 12]. A non-destructive evaluation of biological samples requires low average power (few tens of nW) [10–12]. In the upper part of earth's atmosphere, i.e., in the

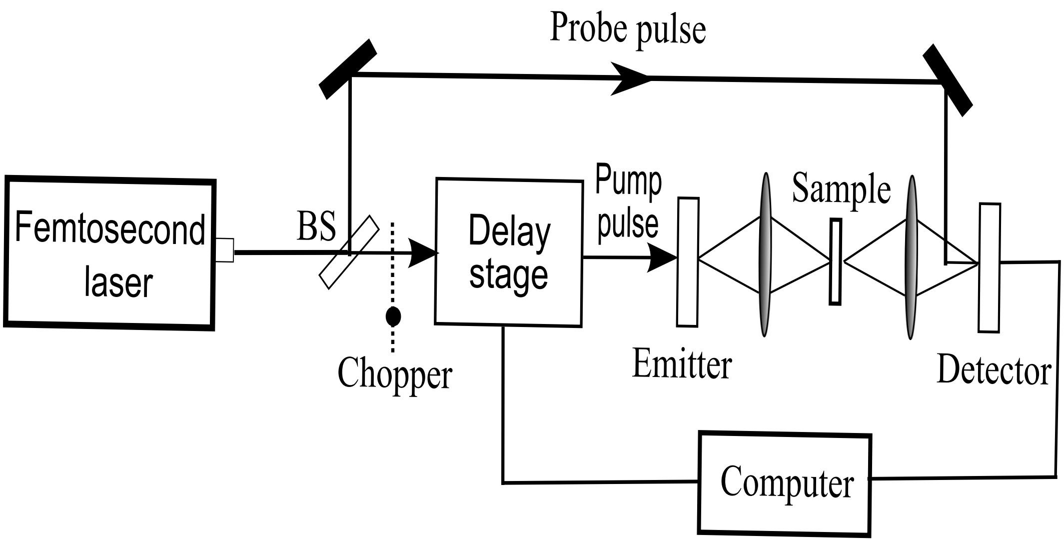

FIGURE 1.2: Schematic illustration of an experimental setup for THz time domain spectroscopy technique.

stratosphere, compounds contain water, chlorine, oxygen and nitrogen, which have vibrational or thermal emission line peaks in the THz spectral range [2]. By performing THz spectroscopy and imaging measurements of these compounds, we can monitor environmental conditions like global warming, ozone destruction, atmospheric pollution and weather forecast [13]. All the above mentioned applications are widely carried out through the THz time-domain imaging and spectroscopy techniques [4, 14–16].

A schematic illustration of the experimental setup for THz time-domain imaging and spectroscopy techniques is shown in Fig. 1.2. In this technique, one starts with a femtosecond laser, which produces an optical-pulse train. Each optical-pulse train is separated into two parts, i.e., pump pulse and probe pulse, by using a beam splitter (BS). The pump pulse is used to generate a broadband pulsed THz radiation with about one picosecond duration from an emitter after passing through a time delay stage. The THz emitter here can be a photoconductive antenna or a non-linear crystal. In photoconductive antenna, the incoming optical-pulse illuminates the gap between the closely spaced electrodes to generate charge carriers, which are then accelerated by an applied voltage to generate THz radiation. In second case, the optical laser pulse passes through a crystal that emits THz radiation through a non-linear optical process known as optical rectification. The THz pulses are usually focused onto a sample and then allowed to reach the THz detector. Now, the probe pulse is combined with the THz beam at the detector. The pump and probe beam are perfectly synchronized since they originate from the same laser pulse. Because the probe beam is much shorter than the THz pulse, it can repeatedly sample the THz waveform at various time delays to perform the THz time domain imaging and spectroscopy measurements. By measuring the decrease in amplitude and delay in THz waveform as compared to the case without any sample in the passage of the THz pulse, one can find the absorption coefficient and refractive index of materials. This gives us the complex value of permittivity without carrying out a detailed Kramers-Kroning analysis. THz radiation can be collimated and focused by using lenses or mirrors and images are obtained by scanning the beam. The imaging resolution depends upon radiation beam diameter, and increases with the radiation frequency. Hence, THz waves provide better imaging resolution than microwaves, but are not good enough for nanoscale applications [17, 18].

A majority of the THz applications are covered with the above mentioned time-domain spectroscopy technique, which describes the equilibrium properties of materials [19]. The dynamical properties are studied by using the time-resolved spectroscopy technique [20]. This technique is now widely used to investigate the dynamics of electrons and phonons in high-T_c superconductors [21], which have energy gap in the THz regime. In this scheme, one employs a near-infrared laser pump pulse and a THz-probe pulse, which are intrinsically synchronized. The laser pump pulse is used to excite an electron above the superconducting gap, and subsequently the THz probe pulse, reflected from the sample, is analyzed to determine the superconducting gap. The superconducting gap closes and opens as time progresses, which is reflected in the THz reflectivity. Research is now focussed on using this technique to understand the energy dynamics and coupling of excitations in recently discovered iron-based superconductors [22].

Clearly, the field of THz science has evolved significantly in last couple of decades and its advancement is critically dependent on the progress in the development of the THz sources. In the next section, we give an overview of existing THz sources that serve ongoing THz applications.

1.2 Overview of the existing terahertz sources

At present, available THz sources are broadly categorized into three types: optically or electrically pumped gas lasers, solid state devices, and electron-beam driven sources. Optically pumped THz lasers (OPTLs), which date back to the 1960's [23], use a grating tuned CO_2 laser to pump the molecules of methanol gas, which undergo molecular rotational transitions to generate THz radiation. These devices are commercially available at selected THz frequencies between 0.5 to 5 THz with output power ranging from 10 μW to 1 W in continuous wave mode [24]. In the pulsed operation mode, a megawatt order of power can be reached in these devices [24]. OPTLs are inherently not tunable and are therefore suitable only for some specific applications [3]. Due to a rapid progress of the semiconductor industry, solid state devices also have been investigated for compact THz sources. These include quantum cascade lasers (QCLs) [25–27], *p*-type Ge lasers [28] and laser driven THz emitters [29]. QCLs [25] are recently developed THz sources in which electrons are injected into a periodic super lattice structure under electrical bias. The electrons cascading down the structure undergo inter subband transition with the emission of a THz photon, which is excited by resonant tunnelling through multiple wells. The frequency of the emitted light is controlled by the width of the quantum well. These devices are now available with hundreds of mW average power. Relatively high output power of these devices is very useful in several spectroscopic applications such as remote sensing of environmental gases and pollutants in the atmosphere, and homeland security [27]. QCLs are not continuously tunable and are operated only in the cryogenic temperature range [26]. A tunable THz radiation in the range 1-4 THz can be obtained from a *p*-type Ge laser, which, however is operated at low temperatures (20 K) and using large external magnetic field (1 T) [28]. Another solid state device, a photoconductive antenna [29], is commonly used to produce broadband pulsed THz radiation with an average power of the order of μW. These are laser driven THz sources where sub-picosecond optical laser pulses are used to illuminate the gap between closely spaced electrodes on a photoconductor (e.g., silicon-on-sapphire or GaAs) to generate carriers, which are then accelerated by an applied bias voltage

(100 V) to generate pulsed THz radiation [30]. Similar type of THz radiation can also be generated in parametric oscillators [31] where a sub-picosecond laser is applied to a non linear crystal like ZnTe, which produce THz radiation through frequency down conversion due to non-linear response of the crystal. Both the above mentioned laser driven THz emitters cover a typical frequency range from 0.2 to 2.0 THz. These sources provide broadband THz pulses with low frequency resolution. Another important laser driven THz emitter is a photomixer [32], which operates with a principle similar to a parametric oscillator except that it uses a continuous wave optical laser to generate a narrow band continuous THz wave with average power of the order of few nW. These sources are very useful in spectroscopy of biological samples, where a low average power THz wave is required [10–12].

Despite the widespread use of the conventional laser based THz sources, many of the THz applications are still limited due to the unavailability of high power pulsed/cw-THz sources that can be continuously tunable. To overcome these limitations, electron beam based sources were proposed [33–44], which include travelling wave tubes (TWTs), backward wave oscillators (BWOs), synchrotrons and free-electron lasers (FELs) utilizing undulator radiation, Čerenkov radiation and Smith-Purcell radiation. These sources provide a *continuously tunable, high power* THz radiation. Both TWTs and BWOs support waveguided transverse electric (TE) or transverse magnetic (TM) modes, which have phase velocity less than the velocity of light. These waves, known as slow waves, interact with a co-propagating electron beam and produce THz radiation with average output power of the order of few tens of mW and output frequency in range from 100 GHz to 1.2 THz [33]. Both TWTs and BWOs cannot be used at higher frequencies because the physical size of the system decreases with the operational frequency [33]. The limitation of reduction of physical size of the source components as the frequency is increased is overcome in coherent synchrotron radiation (CSR) sources and conventional undulator based FEL devices, which convert the kinetic energy of a relativistic electron beam into freely propagating transverse electromagnetic (TEM) modes. The CSR based sources utilize a pre-bunched electron beam, where the bunching is done at the scale of or shorter than the

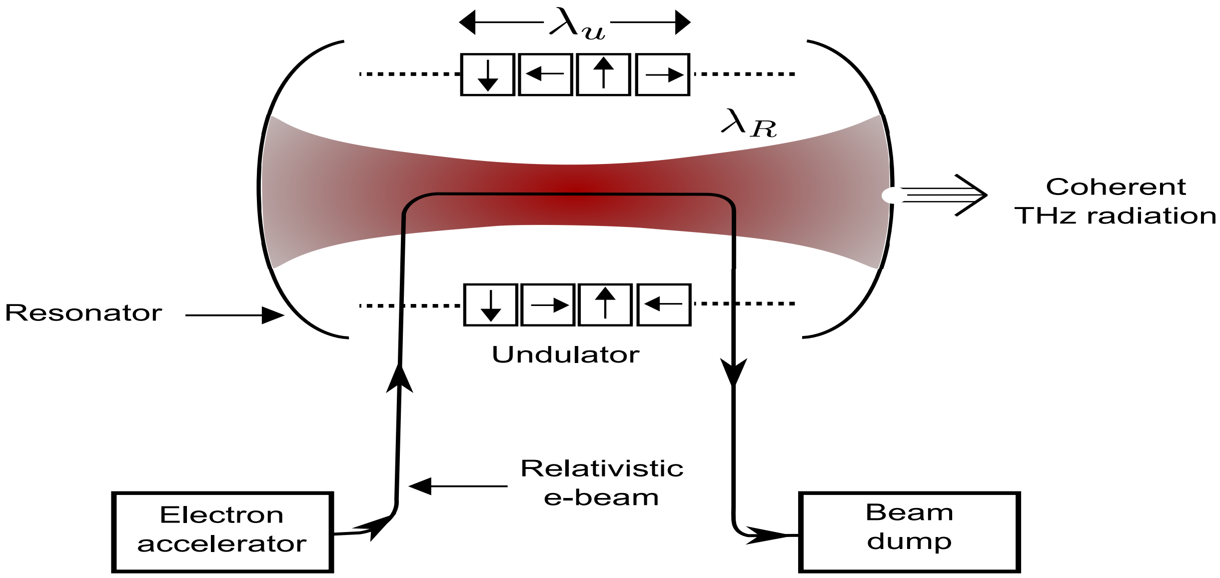

FIGURE 1.3: Schematic of an undulator based FEL using a relativistic electron beam to generate coherent THz radiation .

desired THz wavelength and the electrons in a bunch are transversely accelerated by the magnetic field to generate broadband THz radiation. In a bunch, the fields emitted from different electrons are in phase and add coherently. The total radiated power in this case will have a quadratic dependence on the number of electrons in the bunch. The modern CSR sources such as BESSY II in Berlin [34] and the recirculating linac at Jefferson Laboratory [35] utilize this principle to generate high average power (~ tens of watt) THz radiation. However, an additional radio frequency (RF) accelerator facility is needed here to bunch the electron beam [36, 37]. The performance of these systems is also critically dependent on the shape of the electron bunch; an issue which has been addressed both theoretically and experimentally over the years to improve the system performance [38–40]. As compared to the CSR sources, conventional undulator based FELs can generate orders of magnitude higher peak as well as average radiation power [41]. As shown in Fig. 1.3, coherent THz radiation is produced in an undulator based FEL due to the interaction of a relativistic electron beam with an on-axis, static transverse magnetic field varying sinusoidally along the undulator axis, in the presence of a freely propagating TEM mode building up in the resonator cavity [42, 43]. The radiated power in an undulator based FEL is confined within a narrow spectral width ($\Delta\nu/\nu \simeq 10^{-8} - 10^{-3}$) and has a typical enhancement of 10^6 in average brightness as compared to the synchrotron sources [41].

Apart from the continuous tunability over the entire THz regime, these devices offer control of the spectral and temporal pulse width, which make them very useful in probing materials with higher temporal and spectral resolution. Historically, the first undulator based THz FEL was started at UCSB in 1984 [45]. At the present time, UCSB-FEL provides tunable THz radiation ranging from 0.12 THz to 4.80 THz with peak power in the range from 500 W to 5 kW and a pulse duration of 1-20 μs at 1 Hz repetition rate. Besides the UCSB FEL, there are several undulator based THz FELs in operation, e.g., Novosibirsk THz-FEL (1.6 - 2.5 THz), Stanford FEL (3.75 - 20 THz), Nijmegen FELIX (1.2 - 100 THz) and THz FEL (0.1 THz) in Israel [46]. To meet the requirements of various table top THz applications, efforts are now being made to reduce the physical size of these sources. FEL-CATS at ENEA-Frascati centre in Italy [47] and THz radiator source at Argonne National Laboratory in USA [48, 49] are examples of such compactness. The availability of compact laser wake-field accelerators and an improved understanding of the design of X-ray shielding structures of the accelerator will be helpful to realize these sources as a viable mobile or a compact tabletop device in the near future [48].

Although synchrotron and undulator based FELs are used to generate radiation over the entire electromagnetic spectrum, the successful operation of these devices requires a relativistic electron beam. The necessity of a relativistic electron beam in an undulator based FEL can be easily understand by looking at the formula for the resonant wavelength λ_R, which is given by [42]

$$\lambda_R = \frac{\lambda_u}{2\gamma^2}\left(1 + \frac{K^2}{2}\right). \tag{1.1}$$

Here, λ_u is undulator period, γ is the energy of the electron beam in units of its rest mass energy, $K = eB_0/k_u mc$ is the peak value of the undulator parameter, e is the electronic charge, B_0 represents the on-axis peak undulator magnetic field, $k_u = 2\pi/\lambda_u$, m is rest mass of the electron, and c is the speed of light. It is clear from Eq. (1.1) that if we use a low energy electron beam (small γ) to generate THz radiation, the value of λ_u has to be kept very small. This, however, decreases the value of K parameter or equivalently decreases the effective magnetic field strength, which results in feeble output radiation. Therefore, one has to work with relativistic

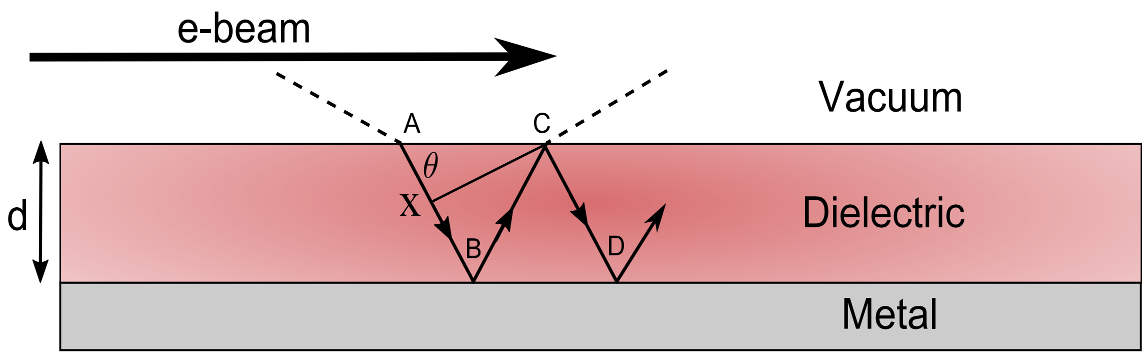

FIGURE 1.4: Schematic of a Čerenkov FEL. This system supports a surface mode which has standing wave pattern (solid lines) inside the dielectric slab, and is evanescent (dashed lines) in the perpendicular direction above the dielectric surface. An electron beam propagating very close to the dielectric surface interacts with this surface mode and generates coherent electromagnetic radiation under suitable conditions.

electron beams to generate THz or higher frequency radiation in these devices. This requires large radiation shielding structures and an expensive infrastructure. Another approach is to use slow wave free-electron lasers, i.e., Čerenkov free-electron lasers (CFELs) [50–68] and Smith-Purcell free-electron lasers (SP-FELs) [53, 69–73], which utilize low energy electron beam for THz generation.

In CFELs, Čerenkov radiation is emitted when an electron moves with a velocity v equal to or greater than the velocity of light in the dielectric medium in close proximity to a dielectric material lining a metallic structure. In the absence of metallic structure, the dielectric emits Čerenkov radiation at a range of wavelengths, but at a fixed angle θ given by the following expression [74]:

$$\cos\theta = \frac{1}{\beta\sqrt{\epsilon\mu^{II}}}. \tag{1.2}$$

Here, $\beta = v/c$ and ϵ and μ^{II} are relative permittivity and relative permeability respectively of the dielectric medium. If there is a metal beneath the dielectric, this radiation gets reflected by the metal, and undergoes reflection at the dielectric-vacuum boundary, and so on to form a standing wave pattern inside the dielectric slab as shown in Fig. 1.4. The path difference between the rays AB and CD will be AB+BC-AX=$2d\sin\theta$, which will give a phase difference $2d\sin\theta \times 2\pi\sqrt{\epsilon}/\lambda$. There will be an extra phase difference of 2δ, where $\delta = -\tan^{-1}(\epsilon/\gamma\tan\theta)$ due to a total internal reflection of ray BC. In this scenario, there is one particular wavelength for which the sum of these two phase differences is zero, resulting into constructive interference, due to which the Čerenkov radiation builds up. This wavelength is the resonant wavelength:

$$\lambda = \frac{2\pi d \sqrt{\epsilon\beta^2 - 1}}{\beta \tan^{-1}\left(\epsilon/\gamma \sqrt{\epsilon\beta^2 - 1}\right)}, \tag{1.3}$$

where d is dielectric slab thickness. For the above mentioned conditions, the system supports an evanescent wave above the dielectric surface and standing wave inside the dielectric slab. Due to the evanescent nature of electromagnetic field, the electromagnetic energy is confined in the close vicinity of the dielectric surface, we call it a surface mode. This system can support TE and TM surface mode having phase velocity less than the speed of light. This is in contrast to the conventional undulator based FELs, where the electromagnetic energy is in the form of freely propagating (TEM) modes having phase velocity equal to the velocity of light, and a relativistic electron beam is required for generating radiation. Due to the presence of a slow wave in a CFEL, a low energy or non-relativistic electron beam propagating very close to the dielectric surface can be used for the beam-wave interaction. This scheme was first proposed by Ginzburg [50] in 1947, and since then many experimental studies have been performed for the generation of electromagnetic radiation from the CFEL devices [55–68, 75]. The configurations studied so far in these systems are: (1) single or double slab based open configuration, (2) rectangular waveguide configuration in a planar geometry, and (3) cylindrical waveguide geometry. The single slab based configurations consist of a rectangular dielectric slab placed on a conducting surface as shown in Fig. 1.4. In a double slab configuration, we have two such slabs with a gap in between them as shown in Fig. 1.5(a). The rectangular waveguide configuration is a closed configuration as shown in Fig. 1.5(b), where a rectangular metallic waveguide supports a dielectric slab on the bottom surface. In the cylindrical waveguide geometry, a dielectric material lines on the inner surface of a cylindrical metallic waveguide as shown in Fig.1.5(c).

The first successful experiment with a CFEL was performed by Walsh *et al.* [55] in a cylindrical waveguide geometry in 1977. They used an intense relativistic electron beam with 0.5 MeV energy and 10 kA beam current. After that, several experimental efforts have been made

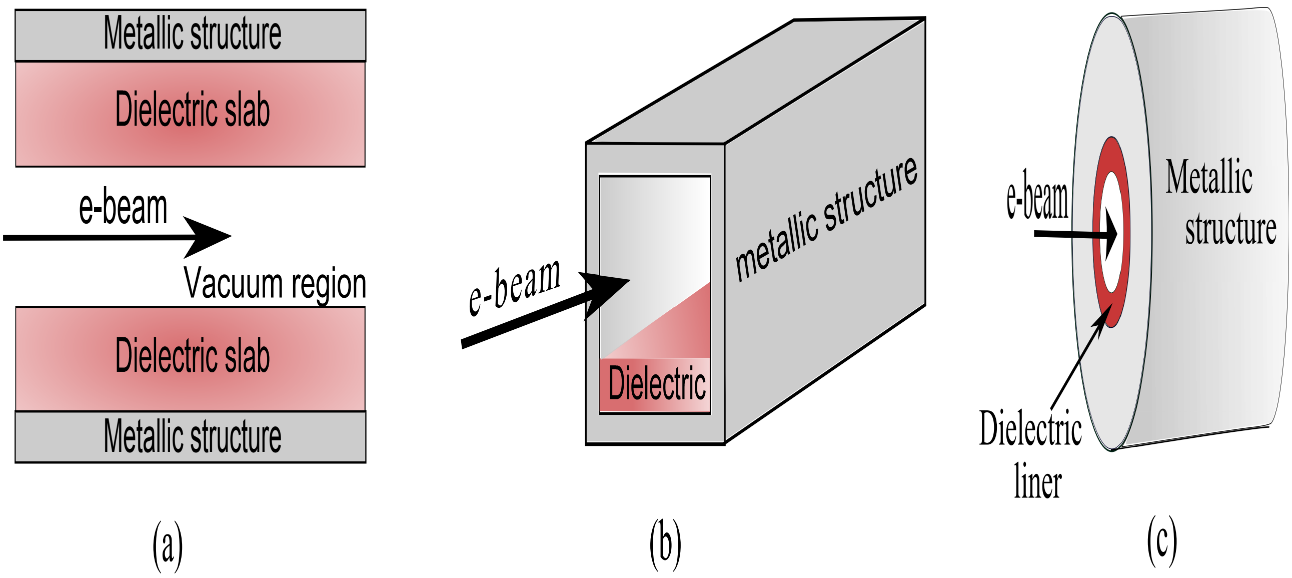

FIGURE 1.5: Schematic showing different configurations of Čerenkov FELs: (a) double slab based open configuration, (b) single slab based rectangular waveguide, and (c) cylindrical waveguide configuration.

to reach higher microwave frequencies by utilising moderate electron beam energies in this geometry [56–58]. Fuente *et al.* have recently demonstrated operation of a cylindrical geometry based CFEL and obtained an average output power of few watts at 24 GHz by using a 250 mA current and 80 keV electron beam [59]. A rectangular waveguide geometry based CFEL was first demonstrated by Garate *et al.* [60] at a frequency 0.3 to 0.8 THz by using a relativistic electron beam with a beam energy of 1 MeV and beam current of 100 A. This system, however, suffers from power handling related instabilities at high power operation. To overcome these problems, a multi-electron-beam multi-dielectric waveguide CFEL was demonstrated at 33.4 GHz by Wang *et al.* [61, 62] by utilizing four sheet beams of total current 280 A at 500 kV. The use of sheet electron beams enables us to achieve high power operation because a sheet beam allows to propagate more current without increasing the space-charge effect due to its larger size in the direction along the dielectric surface compared to the direction perpendicular to the dielectric surface. Open configuration based single slab CFELs are also investigated due to the ease in high frequency operation in these devices [63, 64, 66]. The experimental efforts on the single slab based CFELs began at ENEA Frascati Centre [63, 64], where peak power up to 50 W in pulses of 4 μs duration has been observed at the wavelengths of 1.6 and 0.9 mm. Subsequently, Fisch and Walsh [65] used a low energy electron beam (~30-200 keV) to drive a

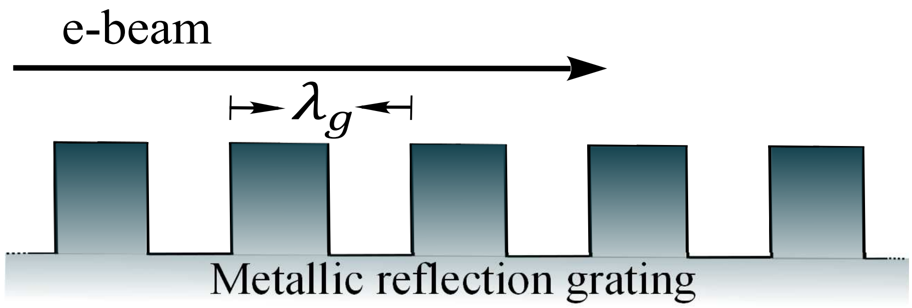

FIGURE 1.6: Schematic of a planar configuration of Smith-Purcell FEL utilizing a rectangular metallic grating.

sapphire based single slab CFEL which was designed to produce 1 mW average power in the frequency range from 0.3 to 1.5 THz. An efficient and compact version of the device described in Ref. [65], which uses a very low energy (~ 30 keV) electron beam has been tested recently at the Dartmouth college [66] for the generation of THz radiation. However, the observed output power in the Dartmouth experiment [66] was very low (~ picowatt). Experimental studies are also in progress on a double slab based THz CFELs in the planar geometry under the joint research of Osaka Sangyo University and Kansai University in Japan [67, 68].

Another electron beam based compact THz source is the SP-FEL, which is similar to a CFEL, except that the “dielectric lining on a conducting surface” is replaced with a “metallic reflection grating” as shown in Fig. 1.6. In this system, an electron beam travelling near and parallel to the metallic reflection grating, with grating ruling perpendicular to the electron beam direction, gives off polarized electromagnetic radiation having a wavelength given by [76]

$$\lambda = \frac{\lambda_g}{|m|\beta}(1 - \boldsymbol{n}.\boldsymbol{\beta}). \tag{1.4}$$

Here, λ_g is period of the metallic grating, m is the spectral order, $\boldsymbol{\beta} = \boldsymbol{v}/c$ is the electron velocity in the unit of speed of light c, and $\boldsymbol{n}$ is the unit vector along the emission direction. Due to the periodicity of the metallic grating, the system supports several harmonics labelled by the spectral order m. Unlike CFELs, the propagation vectors for some of the spectral orders can be real in SP-FELs and these waves, known as propagating waves, can propagate the electromagnetic energy away from the grating. For a given phase velocity, there exists a particular wavelength for which all the outgoing wave are evanescent and they together satisfy the Maxwell equation in the absence of incident evanescent wave. This constitutes a surface mode. The expression for the resonant wavelength of the surface mode supported by a metallic reflection grating will be discussed in Chapter 2. Similar to the case of CFELs, the surface mode supported by a metallic grating interacts with a low energy co-propagating electron beam to generate THz radiation. In the past few years, several efforts have been made to generate electromagnetic radiation using this scheme [69–73]. The most notable experimental work on compact and tunable single grating based THz SP-FEL in the planar geometry was performed by Walsh and co-workers at the Dartmouth College, USA in 1998 [69]. This device was designed to generate THz radiation with frequency ranging from 0.3 to 1 THz and average power of the order of μW by using a low energy (20-40 keV) and low current ($\leq$ 1mA) electron beam emerging from a scanning electron microscope (SEM). A widely tunable (0.3 - 3 THz) and efficient version of the device used at the Dartmouth College, which can operate in the pulsed as well as in the cw mode to give tens of μW average power, was proposed at Vermont, USA in 2003 [70]. However, subsequent experiment performed at the Enrico Fermi Institute (EFI) in the University of Chicago to reproduce the results of Dartmouth experiment has not been successful [77]. This result has motivated several groups to further investigate the conditions under which a THz SP-FEL can lase by utilizing a low-energy electron beam [78]. Recent experiments at Vanderbilt University [71] in USA and at CEA/Cesta [72] in France to generate THz radiation in a planar grating based SP-FEL are example of such efforts. In the cylindrical geometry, the SP-FEL has been demonstrated at 30 GHz frequency in 2015 under the joint research of Advanced Energy Systems, Princeton, USA and Cesta, France [73], and proposals have also been made to utilize the double grating based SP-FEL for the generation of THz radiation [79].

In summary, both the CFELs and the SP-FELs utilize a low energy electron beam, and hence can be realized as a table top compact source. Both these devices can be operated in pulsed as well as continuous wave mode to generate widely tunable and high power THz radiation, which make them very useful for cutting edge THz applications.

1.3 Motivation for the present work

By looking at the overall scenario of existing THz sources, it is clear that FELs may be very helpful in fulfilling the requirements of cutting edge THz applications by providing tunable and high peak/average power THz radiation with controllable spectral and temporal pulse width. Conventional undulator based FELs, however, are *fast-wave* devices, which utilize good quality relativistic electron beam for the THz generation. This requires an expensive and bulky infrastructure with very elaborate radiation shielding, which makes these devices impractical to use like a viable source for the table top THz experiments. On the other hand, CFELs and SP-FELs are *slow-wave* devices, which can be operated with a low-energy electron beam for the THz generation. A low-energy electron beam does not require very elaborate radiation shielding. Hence, such devices can be made compact to fulfil the requirements of novel tabletop THz applications. The experimental studies till date, however, report a very low output power in these devices [65, 66, 69]. One of the important reasons for the performance limitation is the loss due to diffraction and attenuation of the surface mode supported by the CFELs and the SP-FELs. To obtain a copious amount of THz radiation from both these devices, an enhanced understanding of their operation under the realistic effects of diffraction and attenuation is required. In this thesis, we have carried out such a detailed analysis in order to develop an enhanced understanding of electron beam based compact THz sources.

As discussed in Sec. 1.2, CFELs and SP-FELs have been investigated in the planar geometry as well as in the cylindrical geometry. In the planar geometry, CFELs have been investigated in single and double slab based open configurations as well as in the rectangular waveguide configurations. Similarly, SP-FELs have been investigated in single or double grating based open configurations. In the circular geometry, these devices are investigated in a cylindrical waveguide configuration. In this thesis, we have performed detailed investigation of these devices in the planar geometry. This is because the planar geometry has several advantages over the circular geometry, which can be understood as follows. In the circular geometry, the supported electromagnetic surface mode decays when we move away from the dielectric or the grating surface and approach the axis of the waveguide. The decay rate will be very small for an electromagnetic wave having phase velocity nearly equal to the speed of light, which however requires a relativistic electron beam that can co-propagate with the electromagnetic wave to drive these systems. A more practical case of interest is when the phase velocity of the electromagnetic wave is reasonably lower than the speed of light such that a low energy electron beam can exchange energy with the co-propagating electromagnetic wave to drive the system. However, the field decays faster in this case while moving away from the dielectric or the grating surface in the vacuum region. In such a situation, it becomes advantageous to use an annular electron beam having a radius nearly equal to the radius of the waveguide to have an effective beam-wave interaction. For operation at higher frequencies, the transverse dimension of cylindrical waveguide is required to be small [80], and we therefore need to use an annular electron beam of very small radius. This reduces the cross sectional area of the beam, thereby increasing the space charge effects, which may inhibit high power operation of these devices. Also, in order to ensure that the beam remains close to the dielectric or grating surface as it propagates, the hollow cylindrical beam is required to have very stringent transverse emittance in the radial direction, which may be difficult to achieve. These problems can be avoided in the planar geometry, where the supported surface mode is evanescent only in the vertical direction, i.e., perpendicular to the dielectric or the grating surface. To have an effective beam-wave interaction in such case, the electron beam has to maintain a very small beam-size and small beam-emittance only in the vertical direction and can have larger beam-size and beam-emittance in the horizontal direction. This type of electron beam is known as a flat electron beam. By increasing the horizontal size of the flat beam, the cross sectional area can be large such that the space charge effect is reduced compared to the hollow beam used in the circular geometry. In the planar geometry based open configuration, the double slab or the double grating structure has an extra dielectric or metallic surface on the top as compared to the single slab structure. Although the surface mode is already confined close to the dielectric or the grating surface, the top dielectric or grating surface helps in further confining the electromagnetic surface mode if the vertical dimension of the double slab/grating structure is small. This however results in attenuation of the wave due to heat dissipation on the top surface. Similarly, the rectangular waveguide configuration may exhibit limitations on the power-handling capacity at high-power high-frequency operation due to its closed structure. Hence, single dielectric and single grating based open configurations are comparatively more efficient configurations to generate THz radiation in the CFELs and in the SP-FELs respectively.

Over the years, many theoretical studies have been performed to understand the mechanism of generation of electromagnetic radiation in the single slab based CFELs. Walsh *et al.* [81] made one of the earlier theoretical analysis based on the Maxwell-Vlasov equation to evaluate small-signal gain in a single slab based CFEL [82]. In this approach, the linearized Vlasov equation was solved for the distribution of the electrons, treating them like a plasma fluid. This analysis was presented only in the small-signal small-gain regime and by neglecting the space-charge effects [81, 82]. In the small-signal, high-gain regime, this approach has been recently used by Fares [83] to find the growth rate of a CFEL. The growth rate of a single slab based CFEL has also been evaluated by Owens and Brownell by using the hydrodynamic approach [84]. In this approach, one treats the electron beam as a plasma dielectric and solves the Maxwell equations to find the dispersion relation of the system. The dispersion relation can be expanded in a Taylor series about the roots of no-beam dispersion to find the growth rate of the electromagnetic field. Despite their success in the linear regime, both the Maxwell-Vlasov and the hydrodynamic approach are very difficult to extend to the non-linear regime, and to analyze the saturation behavior of the system.

For the conventional undulator based FELs, another approach known as the Maxwell-Lorentz approach [85–87] has been extremely successful to understand both the linear as well as non-linear regime. This is a single-particle approach, where the evolution of the electromagnetic field is described by a self consistent dynamical Maxwell-field equation, and the evolution of electron trajectories is calculated by using the single particle Lorentz equation of motion. This approach turned out to be quite useful in writing computer codes for detailed simulations, and also to include the realistic effects in the simulations [42]. It is therefore natural to ask whether this approach can be established for the detailed analysis of CFEL and SP-FEL systems.

A detailed non-linear analysis based on the coupled Maxwell-Lorentz equations has been presented recently by Kumar and Kim [78, 88–90] for a single grating based SP-FEL driven by a flat-electron beam. In this approach, the electromagnetic field due to a flat beam is presented as a superposition of plane waves having different frequencies but phase velocity equal to the velocity of the electron beam [53]. These waves are evanescent in nature and decay away from the electron beam. When the electron beam propagates close enough to the metallic grating, these evanescent waves are incident on the grating surface and give rise to reflected evanescent waves. Owing to the periodicity of the grating, the waves are reflected at various spectral orders. For some of the spectral orders, the component of the propagation vector normal to the grating is imaginary, and hence they cannot propagate the electromagnetic energy away from the grating surface. An interesting observation in this analysis [88] is that the reflectivity amplitude of the outgoing evanescent waves becomes singular for a particular combination of frequency and wavenumber, satisfying the dispersion relation. This means that the system supports a particular combination of outgoing evanescent waves self consistently, without any incident evanescent wave. This particular combination of outgoing evanescent waves forms the surface mode supported by the structure. Due to the beam-wave interaction, the surface mode starts growing. The reflectivity is then analysed around the singularity for the growing evanescent waves, and Maxwell-Lorentz equations are set up to study the dynamics of the surface mode and the co-propagating electron beam. This approach is used to study the small-signal regime as well as the saturation behaviour of the SP-FELs. The results obtained using this approach [88] were useful to remove the inconsistencies among the earlier analyses of SP-FELs [91–93]. In the present thesis, we have established a similar approach based on the Maxwell-Lorentz equations for the single slab based CFELs in the linear as well in the non-linear regime. A computer code based on the leapfrog method has been developed to explore the non-linear solution of the coupled Maxwell-Lorentz equations. Although attempts have been made earlier to establish Maxwell-Lorentz approach for the single slab based CFELs in Refs. [94–96], the evanescent nature of the electromagnetic field has not been included in these analyses, which we have included in the present thesis.

In order to explain the poor performances of past experiments on the CFELs [63–66] and SP-FELs [69–72], an enhanced understanding is required. This includes analyzing the realistic effects due to diffraction and attenuation of the surface mode supported by these systems, and then working out the requirement on electron beam parameters, which is very critical for the performance of the system. The importance of diffraction effects on the system performance has also been reported in literature for the conventional undulator based FELs [97]. Andrew and Brau [98] have included the effect of diffraction in the hydrodynamic approach for the CFELs, and the hydrodynamic approach has also been explored to evaluate the growth rate of the SP-FELs [93] including the effects of attenuation [99] and diffraction [100]. The results of the hydrodynamic approach [84, 93, 98–102] are however not directly useful in obtaining the required electron beam parameters since the analysis is for the case of an electron beam filling uniformly the entire half space above the dielectric or grating. Recently, Kim and Kumar have included the effects of diffraction and attenuation in their analysis based on the coupled Maxwell-Lorentz equations and found the requirements on the electron beam parameters for the successful operation of a SP-FEL [78, 89]. In the present thesis, we have extended this approach to CFELs by setting up the 3D coupled Maxwell-Lorentz equations, including the diffraction effects. More importantly, the requirements on the electron beam parameters for the successful operation of the CFELs have been worked out to explain the poor performance of past experiments on CFELs. Inclusion of deleterious effect of attenuation turns out to be very important for the THz SP-FELs, like for any high frequency device that uses a metallic conductor. However, all the earlier analyses on single slab based CFELs have neglected the effect of attenuation. In the present thesis, we have included the effect of attenuation and optimized the parameters of a CFEL for minimum losses. By following an approach quite similar to the case of the CFELs, a rigorous derivation has been provided for the 3D coupled Maxwell-Lorentz equations for the SP-FELs. Based on these findings, we have highlighted some important and interesting differences in the behaviour of CFELs and SP-FELs.

The diffraction effects are observed to deteriorate the performance of the CFELs and the

SP-FELs, particularly at longer wavelengths. In order to avoid the diffraction losses, waveguiding can be used with the help of metallic sidewalls, as is done in conventional undulator based waveguided FELs [103] and in waveguided SP-FELs [104–106]. Due to the waveguiding, the diffraction of optical beam reduces, which in turn increases the coupling between the optical mode and the co-propagating electron beam, resulting in the enhancement of system performance. To investigate the enhancement in the performance of a CFEL in the presence of metallic sidewalls, we have set up coupled Maxwell-Lorentz equations for a sidewall CFEL system. These equations have been solved analytically in the linear regime to find the small-signal gain, and solved numerically in the non-linear regime to find the saturation power of the system. The effect of finite-beam size, finite beam-emittance and finite energy-spread on the performance of a sidewall CFEL has also been investigated. In addition, we have extended the Maxwell-Lorentz approach for the rectangular configuration of a double slab based CFEL and compared the results with the case of single slab based CFEL. Our results in the present thesis indicate that it is possible to produce copious THz radiation from both the CFELs and the SP-FELs, even after including the attenuation and 3D effects, if the electron beam parameters are chosen properly.

Within the framework of this thesis, we have also explored the possibility of generating THz radiation through spontaneous emission in an undulator by utilizing an electron beam emerging from a high average power ($\sim$ 100 kW) industrial electron linear accelerator (linac). High average power (up to 100 kW) linacs [107–109] are built nowadays for various industrial applications such as polymer reforming, materials irradiation and sterilization of medical products. The quality of the electron beam emerging from an industrial linac may not be very good for the operation of the undulator based FEL system, where stimulated emission of radiation requires an electron beam with very short pulse duration ($\sim$ picoseconds) and with low energy spread and low emittance. In our proposal, such a high average power electron beam is allowed to pass through an undulator, so that it emits THz radiation with an average power of the order of μW through spontaneous emission. After emitting the THz radiation, the spent electron beam can still be used for the irradiation applications, which gives us a two-fold advantage.

Note that the radiation spectrum of the undulator radiation is broad in the laboratory frame and contains several harmonics of the fundamental mode. The expression for the on axis central wavelength of the fundamental mode is given by Eq. (1.1) [110, 111]. For practical purposes, a narrow bandwidth, quasi-monochromatic and high-brightness radiation inside the central radiation cone having semi-angle $\theta = 1/\gamma\sqrt{N_u}$ around the beam axis [111] can be selected by using a narrow bandpass filter [111]. By taking an example case of electron beam parameters of a typical industrial linac, we have performed detailed calculations for the power of emitted spontaneous radiation in the central radiation cone, and optimized the operational parameters. The proposed device is compact as it does not require a high quality electron beam, and also helps in enhancing the utility of the high power industrial linac.

Chapter 2

Two-dimensional analysis of the surface mode supported in planar geometry of Čerenkov and Smith-Purcell free-electron lasers

Starting from the later half of the 20th century, several efforts [50–55, 81–84, 98] have been made to understand the generation of electromagnetic radiation in Čerenkov free-electron lasers (CFELs). As can be inferred from the literature study presented in the previous chapter, the most basic and convenient configuration of CFEL that can be used to generate THz radiation is the single slab configuration, which consists of a rectangular dielectric slab placed on a conducting surface. This structure supports an evanescent electromagnetic field having decaying amplitude in the perpendicular direction above dielectric surface. The electromagnetic energy for such a field distribution is confined in the close vicinity of the dielectric surface. An electron beam passing very close to the dielectric surface interacts with the co-propagating field supported by the system, gets bunched, and subsequently generates coherent electromagnetic radiation. To understand the mechanism of interaction of electron beam with the electromagnetic field, it is necessary to know the electromagnetic properties, i.e, power flow, energy velocity and attenuation coefficient etc. of the field distribution supported by the system. The electromagnetic field distribution here can be obtained by solving the Helmholtz wave equation, and applying the appropriate boundary conditions at different interfaces in the system [51, 81, 94, 112]. Murphy and Walsh [81] used this approach to find the dispersion relation, i.e., the relation between wavenumber and frequency, and the energy stored in the electromagnetic fields supported by a dielectric slab placed on a conducting surface. The analysis for the dispersion relation of the higher order modes in this system has been presented by Owens and Brwonell in Ref. [84]. Though the results obtained in the above mentioned studies [81, 84] have been successfully used to find the resonant wavelength and also to evaluate the growth rate of the instability of the system; to the best of our knowledge, a systematic study for the power, energy velocity and attenuation of the fields due to the losses present in the system has never been presented for this case. In this chapter, we present such a study.

In order to find the dispersion relation and the electromagnetic field distribution for the surface mode, we have followed a different approach in which one calculates the reflectivity of the *plane evanescent wave* incident on the dielectric slab placed on the conducting surface. Note that the calculation of reflectivity for the *plane propagating waves* is a standard textbook calculation [113, 114], which we have extended here for the case of *plane evanescent waves*. One very interesting thing that happens if the incident wave is evanescent is that the reflectivity becomes infinity for certain combinations of frequency and wavenumber, which means that the reflected evanescent wave along with the standing wave inside the dielectric slab is supported self-consistently without any incident evanescent wave. This is identified as the surface mode and the particular combination of the frequency and wavenumber at which this occurs gives us the dispersion relation. This analysis also gives us the expressions of the electromagnetic fields in different regions. We would like to mention that this approach is similar to the one followed by Kumar and Kim [88, 115] for a detailed analysis of the electromagnetic fields supported by a rectangular metallic grating, where it was shown that extension of this analysis for growing evanescent waves (resulting due to interaction with the co-propagating electron beam) is useful in setting up the coupled Maxwell-Lorentz equations for the system.

After having performed the detailed analysis of the surface mode, we have calculated power, energy, and energy velocity of the electromagnetic fields. These results are then used to study the effect of dielectric and Ohmic losses on the propagation of electromagnetic fields in the system. We would like to mention here that although the effect of attenuation is expected to be significant at THz frequencies, all the previous analyses had ignored it. Finally, we also describe the surface mode analysis of a metallic reflection grating given in Refs. [88, 93, 115], and bring out some interesting comparisons between the metallic grating and dielectric slab structures.

In the next section, we perform calculations for the reflectivity and resonant frequency of a dielectric slab placed on a conducting surface for the incident evanescent wave. We find the expressions for power flow, energy stored, and energy velocity of the electromagnetic fields in Sec. 2.2. In Sec. 2.3, we present calculations for the field attenuation coefficient due to dielectric losses and Ohmic losses due to finite conductivity of metal. The important properties of the electromagnetic field supported by a rectangular metallic grating have been presented in Sec. 2.4. In Sec. 2.5 we conclude the results by comparing some of the interesting properties of the surface mode in dielectric based system and the metallic grating.

2.1 Reflectivity analysis and resonant frequency calculations

In this section, we calculate the reflectivity and the resonant frequency of a dielectric slab placed on a conducting surface for the incident evanescent wave. A schematic of the system is shown in Fig 2.1, where we assign region I to vacuum, region II to the dielectric medium and region III to the metallic structure. The dielectric slab has a thickness d and a relative permittivity ϵ. The length of the system in z-direction is taken as L. The system is assumed to

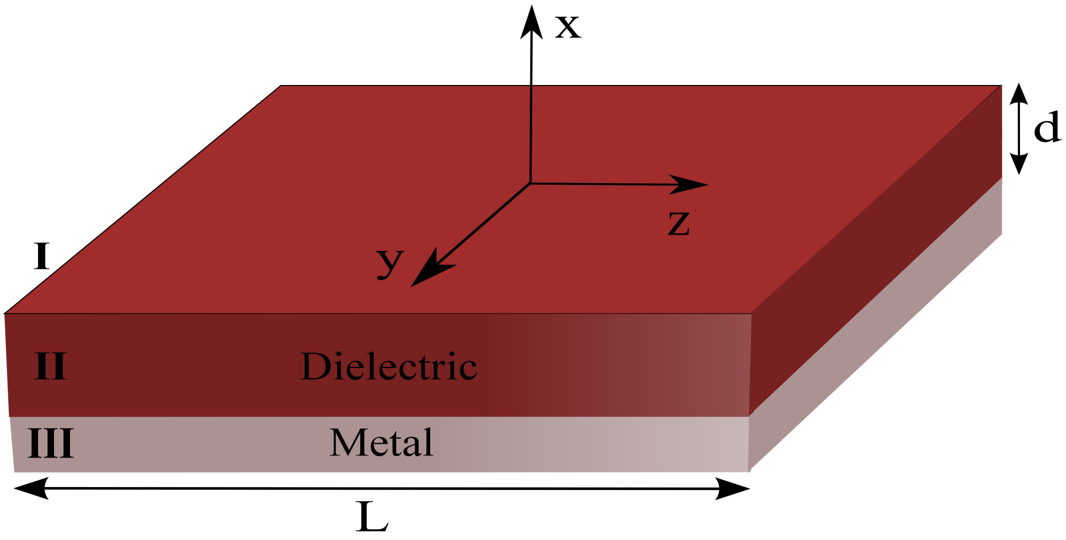

FIGURE 2.1: Schematic of a rectangular dielectric slab placed on a conducting surface.

have translational invariance in the y-direction such that the electromagnetic fields supported by this structure do not have any variation along the y-axis. The appropriate electromagnetic field supported by the system can be in the form of a TM or TE mode. Our analysis focuses here on the TM mode, which has longitudinal electric field and can be easily excited by an electron beam moving along the z-direction. We have assumed that the metallic structure consists of an ideal conductor having infinite conductivity. Due to this assumption, the electromagnetic field inside the metallic structure is zero. The dielectric slab is also assumed to be a lossless structure such that the electromagnetic field propagates without any attenuation. Note that the effect of attenuation will be discussed in Sec. 2.3. For the incident evanescent wave in region I, the components of electromagnetic field that satisfy the Maxwell wave equation can be written as follows:

$$H_y^{\mathcal{I}}(x,z,t) = H \exp[i(k_0 z - \omega t) + \Gamma x], \tag{2.1}$$

$$E_x^{\mathcal{I}}(x,z,t) = \frac{k_0 H}{\epsilon_0 \omega} \exp[i(k_0 z - \omega t) + \Gamma x], \tag{2.2}$$

$$E_z^{\mathcal{I}}(x,z,t) = \frac{i\Gamma H}{\epsilon_0 \omega} \exp[i(k_0 z - \omega t) + \Gamma x], \tag{2.3}$$

and $H_x^{\mathcal{I}} = H_z^{\mathcal{I}} = E_y^{\mathcal{I}} = 0$. Here, H is the amplitude of H_y^I at the dielectric surface, i.e., at $x = 0$, $k_0 = \omega/v$ is the longitudinal wavenumber in the z-direction, ω is angular frequency of the electromagnetic field, v is the phase velocity of the field, ϵ_0 is permittivity of free space, $\Gamma = \sqrt{k_0^2 - \omega^2/c^2}$ is wavenumber in the x-direction and c is the speed of light. Due to presence of the dielectric slab, the incident wave gives rise to a reflected wave in region I. The electromagnetic field components of the outgoing evanescent wave are given by

$$H_y^R(x,z,t) = RH\exp[i(k_0z-\omega t)-\Gamma x], \tag{2.4}$$

$$E_x^R(x,z,t) = \frac{k_0RH}{\epsilon_0\omega}\exp[i(k_0z-\omega t)-\Gamma x], \tag{2.5}$$

$$E_z^R(x,z,t) = \frac{-i\Gamma RH}{\epsilon_0\omega}\exp[i(k_0z-\omega t)-\Gamma x], \tag{2.6}$$

where R is the amplitude reflectivity. The transmitted field components inside the dielectric slab, which satisfy the wave equation inside the dielectric, and the boundary conditions at the metallic surface ($x = -d$) are given as follows:

$$H_y^{\mathcal{T}}(x,z,t) = TH\cos[k_1(x+d)]\exp[i(k_0z-\omega t)], \tag{2.7}$$

$$E_x^{\mathcal{T}}(x,z,t) = \frac{k_0TH}{\epsilon_0\epsilon\omega}\cos[k_1(x+d)]\exp[i(k_0z-\omega t)], \tag{2.8}$$

$$E_z^{\mathcal{T}}(x,z,t) = \frac{-ik_1TH}{\epsilon_0\epsilon\omega}\sin[k_1(x+d)]\exp[i(k_0z-\omega t)]. \tag{2.9}$$

Here, TH represents the amplitude of H_y inside the dielectric slab, and $k_1 = \sqrt{\epsilon\omega^2/c^2 - k_0^2}$.

Now, by applying the boundary condition that H_y and E_z are continuous at the dielectric surface, i.e., at $x = 0$, we obtain the following expression for the reflectivity R:

$$R = \frac{1 + (k_1/\Gamma\epsilon)\tan(k_1d)}{1 - (k_1/\Gamma\epsilon)\tan(k_1d)}. \tag{2.10}$$

It can be seen that for a given phase velocity $v = \omega/k_o$, the denominator in the above equation vanishes for a combination of ω and k_0, and R becomes singular. The condition under which this occurs is given by the following expression:

$$k_1\tan(k_1d) = \epsilon\Gamma. \tag{2.11}$$

We would like to digress here a bit and explain this interesting result. If the incident wave is a propagating wave, the reflectivity is always less than one. If the reflectivity is greater than one, it would mean that the reflected power is more than the incident power, which would violate the conservation of energy. In the case of an evanescent wave, the reflectivity can be greater than one, and it can even become infinite as shown here. Since the evanescent waves do not propagate any power in the x-direction here, this does not violate conservation of energy. A singularity in R means that the dielectric slab placed on the conducting surface supports an outgoing evanescent wave and the standing wave inside the dielectric on its own, i.e., in the absence of any incident wave. This represents the surface mode supported by the system and the above equation is the dispersion relation, i.e., a relation between the frequency and phase velocity of the surface mode.

It may be in order here to discuss briefly the different choices of dielectric material for a CFEL system. Many different dielectric materials, e.g., lucite [55], quartz [56], boron-nitride [58], polymethylene or TPX [60], polyethylene [64], sapphire [65] and GaAs [66] have been used for the operation of CFELs. These materials have also been employed in dielectric wakefield accelerating structures in modern electron accelerators [116–118]. In order to find the resonant frequency, we plot the Doppler line for the electron beam and dispersion curve of the surface mode supported by the structure. In Fig. 2.2, we have shown such a plot for an example case of parameters, which are discussed below in detail and are used in a recent experiment performed at the Dartmouth College, USA [66]. The intersection point between the beam line and the dispersion curve in this figure gives us the resonant frequency of the system. At the resonant frequency, the structure supports a surface mode with phase velocity equal to the electron beam velocity, thus capable of exchanging energy with the electron beam. Here, we require the phase velocity at the intersection point should be considerably smaller than c such that the CFEL can be operated with a non-relativistic electron beam. Also, the velocity of electron beam must be greater than the phase velocity of the light inside the dielectric material, i.e., $v_t = c/\sqrt{\epsilon}$, in order to generate the Čerenkov radiation. Hence, by following the above-mentioned conditions, one has to choose a higher value of ϵ to operate a CFEL with a

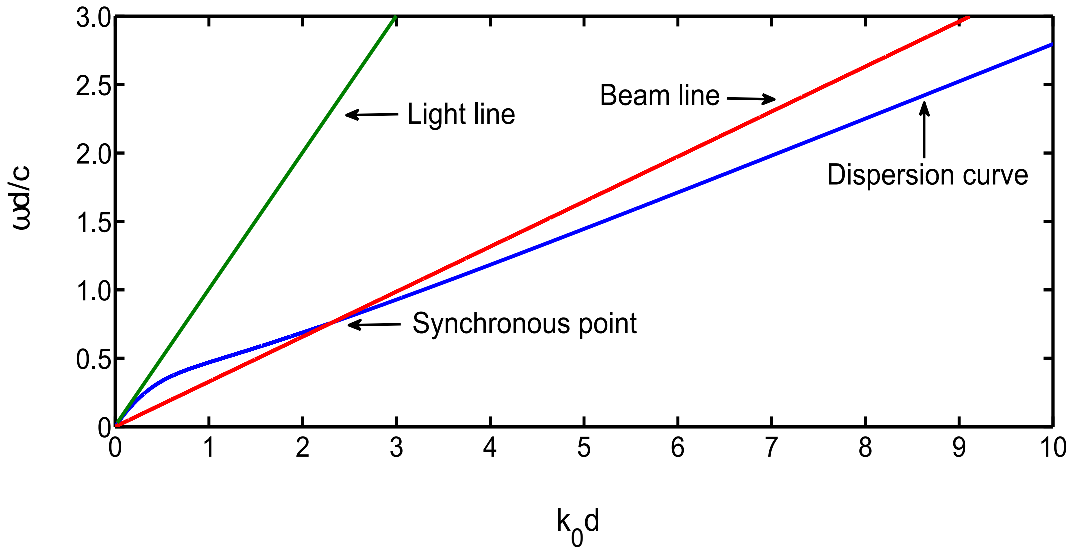

FIGURE 2.2: Plot of dispersion curve of the surface mode, light line, and beam line for a 30 keV electron beam. The dielectric slab consists of GaAs material having dielectric constant $\epsilon = 13.1$, and the slab thickness is taken as 350 μm. At the intersection point of the dispersion curve and the beam line, we find the resonant frequency of the system as 0.1 THz.

non-relativistic electron beam. Typically, a material with $\epsilon \geq 8$ is required to operate a CFEL with a minimum electron beam energy of 35 keV. This condition can be fulfilled by sapphire (dielectric constant ranging from 9.6 to 10) [119] and GaAs (dielectric constant 13.1) [120] among the above mentioned dielectric materials. Both these materials have been used in the Dartmouth experiment [66]. In our example case, we have considered GaAs only because it is an isotropic material. Due to the isotropic nature of the dielectric medium, three-dimensional (3D) effects can be easily incorporated in the analysis of Čerenkov FELs, which will be discussed in detail in Chapters 4 and 5. On the other hand, sapphire, which is single crystal of alumina, is an anisotropic material. The detailed 3D theory of beam-wave interaction for an anisotropic dielectric based CFEL is involved and is not presented in this thesis. The dispersion curve for a GaAs dielectric slab having thickness $d = 350$ μm is plotted in Fig. 2.2 by using Eq. (2.11). The electron beam energy is taken as 30 keV, which gives us the Doppler beam line in Fig. 2.2. The intersection of the dispersion curve and the beam line gives us a resonant frequency of 0.1 THz and phase velocity of the synchronous surface mode as $v = \omega/k_0 = 1 \times 10^8$ m/s for the considered parameters. The group velocity of the surface mode can be evaluated by finding the slope of the dispersion curve at the intersection point.

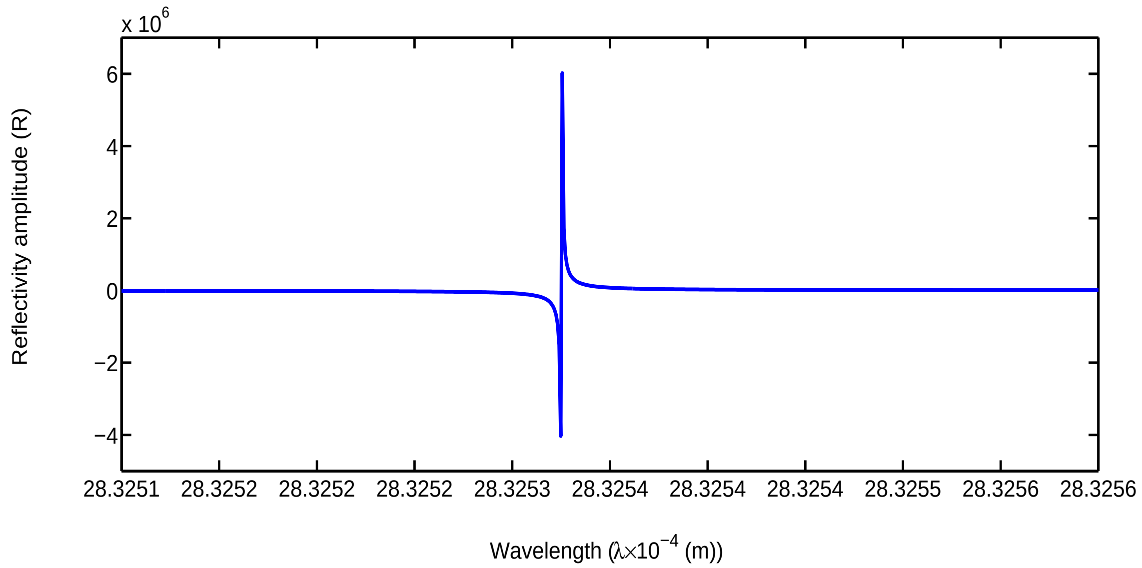

FIGURE 2.3: Plot of reflectivity R as a function of wavelength for the parameters discussed in the text. The singularity in R appears at 0.1 THz, which is the resonant frequency of the system.

In Fig. 2.3, we have plotted R as a function of wavelength for the above mentioned parameters and by keeping the phase velocity constant, i.e., $v = 1 \times 10^8$ m/s corresponding to a 30 keV electron beam. The singularity occurs at 0.1 THz, which is the resonant frequency of the system. Hence, the condition for a system to support surface mode at resonant frequency $\omega = \beta c k_0$ is equivalent to the requirement that the reflectivity is singular at that particular frequency [91]. Equation (2.11) is also solved to obtain an analytical expression for the resonant wavelength of the dielectric slab placed on a conducting surface, which is given by

$$\lambda = \frac{2\pi b}{\beta \tan^{-1}(1/a)}, \tag{2.12}$$

where $\beta = v/c$, $b = d\sqrt{\epsilon\beta^2 - 1}$, $a = (\gamma/\epsilon)\sqrt{\epsilon\beta^2 - 1}$, and $\gamma = 1/\sqrt{1-\beta^2}$. Note that this is similar to Eq. (1.3). From the above equation, it can be inferred that at a fixed phase velocity v of the surface mode, lowering the dielectric constant and decreasing the dielectric thickness tunes the system to higher operating frequency. We find that the resonant frequency increases with decrease in the phase velocity of the surface mode, keeping other system parameters fixed. Hence, to excite a high frequency surface mode in this system, one has to go for a low energy electron beam. This is advantageous since the requirement of radiological shielding is relaxed at a low beam energy.

2.2 Calculations for power, energy and energy velocity

After knowing the dispersion relation of the surface mode, we now set up the electromagnetic fields supported by the configuration shown in Fig. 2.1. These results will be used to calculate the power flow, energy stored and energy velocity of the surface mode. The electromagnetic fields which satisfy Maxwell-wave equation in the region I can be written as follows:

$$H_y^I(x, z, t) = H \exp[i(k_0 z - \omega t) - \Gamma x] + \text{c.c.}, \tag{2.13}$$

$$E_x^I(x, z, t) = (H/\beta\epsilon_0 c) \exp[i(k_0 z - \omega t) - \Gamma(x)] + \text{c.c.}, \tag{2.14}$$

$$E_z^I(x, z, t) = (-iH/\beta\gamma\epsilon_0 c) \exp[i(k_0 z - \omega t) - \Gamma x] + \text{c.c.}. \tag{2.15}$$

Here, H is half amplitude of the peak field at $x = 0$, and c.c. represents complex conjugate of the quantity written on the right hand side. In region II, we obtain the following expressions for the electromagnetic fields:

$$H_y^{II}(x, z, t) = \frac{\epsilon\Gamma}{k_1} \frac{\cos[k_1(x + d)]}{\sin(k_1 d)} H \exp[i(k_0 z - \omega t)] + \text{c.c.}, \tag{2.16}$$

$$E_x^{II}(x, z, t) = \frac{k_0\Gamma}{\omega\epsilon_0 k_1} \frac{\cos[k_1(x + d)]}{\sin(k_1 d)} H \exp[i(k_0 z - \omega t)] + \text{c.c.}, \tag{2.17}$$

$$E_z^{II}(x, z, t) = \frac{-i\Gamma}{\omega\epsilon_0} \frac{\sin[k_1(x + d)]}{\sin(k_1 d)} H \exp[i(k_0 z - \omega t)] + \text{c.c.}. \tag{2.18}$$

These fields are calculated by satisfying the boundary conditions at various interfaces in Fig. 2.1. Power flow in the electromagnetic fields can be calculated by integrating the Poynting vector over an area transverse to the direction of field propagation. Since we have assumed the system to be translational invariant along the y-direction, an arbitrary width Δy is considered in the integration limits along this direction. With this consideration, the region I consists of vacuum having $x \in [0, \infty]$ and $y \in [-\Delta y/2, \Delta y/2]$. The time-averaged power flow due to the fields in region I can be written as $P^I = (1/2) \int_{-\Delta y/2}^{\Delta y/2} \int_0^{\infty} (\boldsymbol{E^I} \times \boldsymbol{H^{I*}}) dxdy$ [113], where the symbols $\boldsymbol{E^I}$ and $\boldsymbol{H^I}$ represents amplitude, i.e., barring the $e^{i(k_0 z - \omega t)}$ dependence, of the electric and magnetic field respectively, and the superscript $*$ is meant for the complex conjugate. Evaluating this integral by explicating the expressions for electromagnetic fields given in Eqs. (2.13-2.15), we obtain the following expression for P^I

$$P^I = \frac{\gamma \Delta y |H|^2}{\epsilon_0 \omega}. \tag{2.19}$$

Inside the dielectric medium, namely the region II, $x \in [-d, 0]$ and $y \in [-\Delta y/2, \Delta y/2]$. The time-averaged power flow in this region is given by $P^{II} = (1/2) \int_{-\Delta y/2}^{\Delta y/2} \int_{-d}^{0} (\boldsymbol{E^{II}} \times \boldsymbol{H^{II*}}) dxdy$. We solve this integral by using the expressions for electromagnetic fields given in Eqs. (2.16-2.18) and obtain

$$P^{II} = \frac{\gamma \Delta y |H|^2}{\epsilon_0 \omega} \left[\frac{1}{\epsilon^2 a^2} + \frac{k_0 d (1 + a^2)}{\epsilon \gamma a^2} \right]. \tag{2.20}$$

Total power P in the surface mode is sum of the power in region I and in region II. By adding Eq. (2.19) and Eq. (2.20), we find the total time-averaged power flow in the surface mode as:

$$P = \frac{\Delta y \gamma |H|^2}{\epsilon_0 \omega} \left[1 + \frac{1}{\epsilon^2 a^2} + \frac{k_0 d (1 + a^2)}{\epsilon \gamma a^2} \right]. \tag{2.21}$$

It is important to note here that the power flow in the x-direction is zero in region I, as well as region II. However, there is a net power flow in the z-direction, which is given by Eq. (2.21).

Next, we derive the expression for the total energy stored in the electromagnetic fields. In region I, the time-averaged energy stored U^I in the fields can be evaluated by integrating the time-averaged energy density $(\epsilon_0 |E^I|^2 + \mu_0 |H^I|^2)/4$ over the volume having $x \in [0, \infty]$, $y \in [-\Delta y/2, \Delta y/2]$, and $z \in [0, L]$. Here, μ_0 is absolute permeability of the free space. Now, by using Eqs. (2.13-2.15) for the components of electric field E^I and magnetic field H^I in the energy density expression, we obtain the following expression for the time-averaged energy stored in fields in the region I

$$U^I = \frac{\gamma \Delta y L |H|^2}{\beta \epsilon_0 c \omega}. \tag{2.22}$$

In region II, the time-averaged energy stored U^{II} in the fields has been evaluated by integrating the time-averaged energy density $(\epsilon_0 \epsilon |E^{II}|^2 + \mu_0 \mu^{II} |H^{II}|^2)/4$ over the volume having $x \in [-d, 0]$, $y \in [-\Delta y/2, \Delta y/2]$, and $z \in [0, L]$. Doing this, we obtain

$$U^{II} = \frac{\gamma \Delta y L |H|^2}{\beta \epsilon_0 c \omega}\Big[\frac{1}{\epsilon^2 a^2} + \frac{k_0 \beta d (1 + a^2)}{\gamma a^2}\Big]. \tag{2.23}$$

Note that we have assumed the dielectric slab to be non-magnetic, i.e., the relative permeability μ^{II} is 1. The total time-averaged energy stored in electromagnetic fields is denoted by U, which is the sum of energy in vacuum and in the dielectric medium, and is obtained by adding Eq. (2.22) and Eq. (2.23). We express this result in terms of energy stored per unit mode width Δy per unit length in the z-direction as:

$$\mathcal{U} = \frac{\gamma |H|^2}{\beta \epsilon_0 c \omega}\Big[1 + \frac{1}{\epsilon^2 a^2} + \frac{k_0 d \beta^2 (1 + a^2)}{\gamma a^2}\Big]. \tag{2.24}$$

By knowing the expression for P and $\mathcal{U}$, one can find the energy velocity as $v_e = P/\Delta y \mathcal{U}$. Substituting for P and $\mathcal{U}$ in this expression, we obtain the following analytical formula for the energy velocity:

$$v_e = \frac{\beta c [\beta^2 \gamma^3 (\epsilon - 1) + k_0 d \epsilon (1 + a^2)]}{[\beta^2 \gamma^3 (\epsilon - 1) + k_0 d \epsilon^2 \beta^2 (1 + a^2)]}. \tag{2.25}$$

We would like to mention that the analytical expression for the group velocity $(\partial\omega/\partial k)$ of the surface mode supported by the dielectric slab placed on the conducting surface has been evaluated in Ref. [121]. We find that the energy velocity given by Eq. (2.25) and the expression of group velocity given in Ref. [121] are identical. The energy velocity of the surface mode here is therefore equal to the group velocity.

2.3 Analysis for the field attenuation coefficient

In the previous sections, we have performed calculations by neglecting the losses occurring due to the lossy dielectric medium and due to the finite conductivity of the metallic structure. Now we consider a more realistic case, where the dielectric slab consists of a lossy dielectric material and the conducting surface consists of a metal having finite conductivity. Due to these losses, there will be an attenuation in the electromagnetic surface mode as it propagates. The importance of attenuation effects due to the lossy dielectric and the Ohmic conductor has been emphasized for the guided surface modes in microwave devices [112, 122], and it is known that these losses typically increase with the frequency of the guided modes. Here, we are discussing the operation of the system at THz frequencies, and therefore, it is important to study the deleterious effect of attenuation. In this section, we will follow a textbook approach [113, 122] to evaluate the field attenuation coefficient due to the dielectric and Ohmic losses present in the system shown in Fig. 2.1. We denote the total field attenuation coefficient by α, which is due to the dielectric and Ohmic losses. As the electromagnetic field propagates down the interaction length L, it will attenuate by a factor of $e^{-\alpha L}$. The power is quadratic in the field amplitude and decays by a factor of $e^{-2\alpha L}$ over the length L. Hence, power P in the surface mode at any arbitrary position z can be written by taking the effect of attenuation as

$$P = P_0 e^{-2\alpha z}, \tag{2.26}$$

where P_0 is initial power at position $z = 0$. By defining the power loss per unit length along the z-direction as $P_l = -dP/dz$, and using Eq. (2.26), we obtain the following expression for the attenuation coefficient of the surface mode:

$$\alpha^{d,c} = \frac{P_l^{d,c}}{2P}, \tag{2.27}$$

where, the superscripts d and c are meant for the dielectric and metallic structure respectively.

In the dielectric medium, namely the region II, we need to take into account the complex nature of relative permittivity in order to evaluate the dielectric losses. The complex relative permittivity is given by $\tilde{\epsilon} = \epsilon - i\epsilon'$, where $\tan\delta = \epsilon'/\epsilon$ is identified as the tangent loss of the dielectric medium [123]. Due to the complex nature of relative permittivity, the wavenumber of the surface mode also becomes complex. The imaginary part of this wavenumeber accounts for the dissipation of the electromagnetic surface mode in a lossy dielectric. The power loss per unit length due to the losses present in the dielectric medium can be written as $P_l^d = \epsilon_0\epsilon\omega\tan\delta\int(|E_x^{II}|^2 + |E_z^{II}|^2)dxdy$ [113], where the integration is carried out from $-d$ to 0 in the x-direction and over length Δy in the y-direction. This integral has been evaluated by using Eqs. (2.17) and (2.18), which gives us the following expression for the power loss in the dielectric medium:

$$\frac{P_l^d}{\Delta y} = \frac{k_0|H|^2\tan\delta}{\epsilon_0\omega\epsilon^2a^2}[\gamma(2-\epsilon\beta^2) + \epsilon^2\beta^2k_0d(1+a^2)]. \tag{2.28}$$

Now, Eqs. (2.21) and (2.28) are used in Eq. (2.27) to obtain the following expression for dielectric attenuation coefficient:

$$\alpha^d = \frac{k_0\tan\delta}{2}\frac{[\gamma(2-\epsilon\beta^2) + \epsilon^2\beta^2k_0d(1+a^2)]}{[\gamma(1+\epsilon^2a^2) + \epsilon k_0d(1+a^2)]}. \tag{2.29}$$

The dielectric attenuation coefficient is directly proportional to the tangent loss ($\tan\delta$) of the dielectric medium. Hence, the dielectric losses increase with tangent loss of the dielectric medium.

In region III, which consists of metal, the power dissipates in the form of Ohmic losses due to the finite conductivity of the metal. In this situation, the electromagnetic field inside the metallic structure is not zero, and for a good but not perfect conductor, the electromagnetic field decays inside the metal within an effective length, known as the skin depth of the metal. Here, we have assumed that the skin depth of metal is very small. Due to this, the volume current flowing within the skin depth acts as a surface current, which produces the resistive heating due to the finite conductivity in a very small region near the metallic surface [113]. The power loss per unit length along the metallic surface is given by $P_l^c = (R_s/2)\int|H_y^{II}|^2dy$ [113, 122], where the integration is carried out over a length Δy in the y-direction. Here, $R_s = \sqrt{\mu_0\omega/2\sigma_{cond}}$ is the surface resistance of the metal and σ_{cond} is conductivity of the metallic structure. The magnitude of electromagnetic field H_y^{II} at the metallic surface, which is given in Eq. (2.16) is now used to evaluate the power loss per unit length along the metallic surface. This gives us the following expression for P_l^c

$$P_l^c = \frac{2R_s(1+a^2)|H|^2}{a^2}. \tag{2.30}$$

Next, by using the above equation together with Eqs. (2.21) and (2.30), we obtain the following expression for Ohmic attenuation coefficient

$$\alpha^c = \frac{R_s}{Z_0}\frac{\beta\epsilon^2 k_0(1+a^2)}{[\gamma(1+\epsilon^2a^2)+\epsilon k_0 d(1+a^2)]}. \tag{2.31}$$

With increase in the operating frequency and decrease in the conductivity of the metallic structure, the surface resistance R_s increases, which implies high Ohmic losses. The sum of dielectric losses and losses due to finite conductivity of the metal gives total losses present in the system, which can be expressed in terms of the total attenuation coefficient α of the surface mode as $\alpha = \alpha^d + \alpha^c$.

2.4 Surface mode analysis for a metallic reflection grating

After discussing the important properties of the surface mode supported by a dielectric slab placed on a conducting surface, we now discuss the properties of the surface mode supported by a metallic reflection grating. The essential features of the surface mode supported by a rectangular grating have been worked out earlier in the literature [88, 93, 115], which we briefly summarize here. In Fig. 2.4, we have shown the schematic of a rectangular reflection grating, which consists of a metallic conductor, having parallel grooves along the y-direction. The grating has period λ_g, groove width w, and groove depth d. For the incident evanescent wave

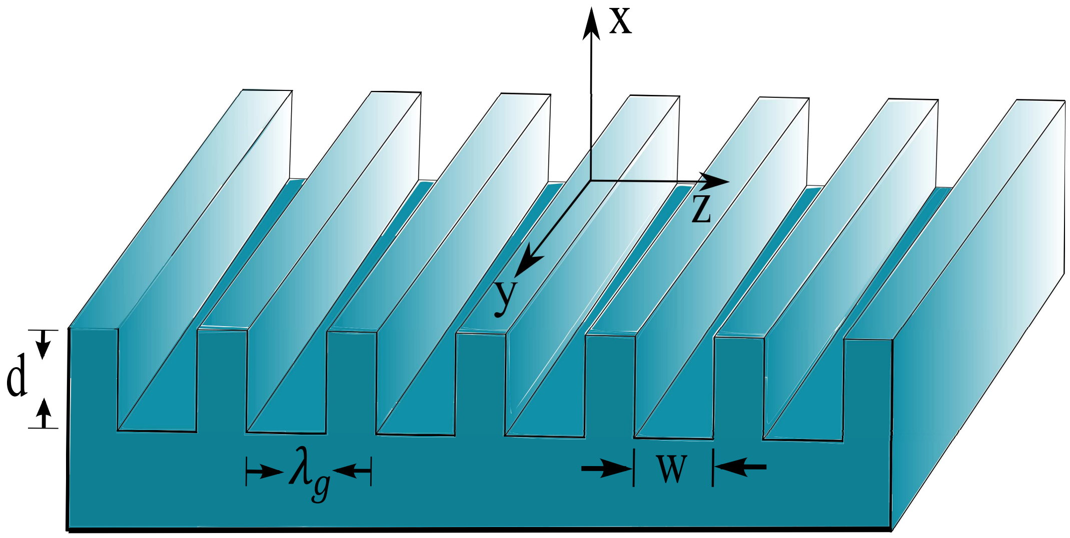

FIGURE 2.4: Schematic of a metallic reflection grating with the co-ordinate system used in our analysis.

in region $x > 0$, the y-component of the electromagnetic (TM) field is given by

$$H_y^I(x,z,t) = A_0^I \exp\left[i(k_0 z - \omega t) + \Gamma_0 x\right]. \tag{2.32}$$

Here, A_0^I is the amplitude of the H_y^I at the grating surface, i.e., at $x = 0$, $k_0 = k/\beta$, $k = \omega/c$, $k_g = 2\pi/\lambda_g$ and $\Gamma_0 = -\sqrt{k_0^2 - k^2}$. In the presence of grating, the incident evanescent field gives rise to the reflected field. Owing to the periodicity of the grating , the reflected electromagnetic field contains several space harmonics satisfying the Floquet-Bloch theorem. The y-component of the electromagnetic field can be written in the following Floquet-Bloch expansion form [115]:

$$H_y^R(x,z,t) = \sum_{m=-\infty}^{+\infty} A_m^R \exp\left[i(k_m z - \omega t) - \Gamma_m x\right], \tag{2.33}$$

where m represents the spectral order, $A_m^R = R_{m0} A_0^I$, R_{m0} is the ratio of amplitude of the mth order reflected wave to the zeroth-order incident evanescent and is identified as the component of the reflection matrix R, $k_m = k/\beta - mk_g$, and $\Gamma_m = -\sqrt{k_m^2 - k^2}$. It is important to mention here that unlike the case of a dielectric slab supported on a conducting surface discussed in Sec. 2.2 where the reflected wave is one evanescent wave, the reflected wave in this case has several spectral orders out of which some could be propagating and others are evanescent. Also, compared to the case of a dielectric slab supported on a conducting surface, the calculation of reflectivity is an extremely involved problem for the case of reflection grating, which has been studied for more than hundred years [124]. The calculation of R requires a detailed numerical computation that was only possible in the later half of the 20th century [125]. The matrix elements of R were first calculated by Van den Berg for the outgoing propagating modes [126, 127]. A more practical case of interest is to study the matrix element R_{00} for the zeroth-order outgoing evanescent wave, which can be easily excited by a co-propagating electron beam [88, 115].

Since the calculation of the reflection matrix of a metallic reflection grating is a fairly involved problem and can be only done numerically, it is not possible to obtain an analytical expression for the dispersion relation of the surface mode here. Andrew and Brau [93] have formulated this problem in terms of the amplitudes of the Floquet space harmonic terms of the electromagnetic fields inside the grooves and shown that the dispersion relation is expressed as $|\mathcal{R}_{mn} - \mathrm{I}_{mn}| = 0$. Here, the scattering matrix $\mathcal{R}_{mn}$ relates mth order wave in the groove to the nth order wave and $|\ |$ indicates the determinant of the matrix. Their computation shows that this dispersion relation is accurately described (within a few percent) even if we take single element $\mathcal{R}_{00}$ in the above dispersion relation. This gives us the following simplified expression for the dispersion relation of the surface mode supported in a metallic reflection grating [93]:

$$\mathcal{R}_{00} = \underbrace{-\frac{2k}{w\lambda_g} \tan(kd)}\sum_{m=-1}^{m=1} \frac{\cos(k_m w) - 1}{\Gamma_m k_m^2} = 1. \tag{2.34}$$

Note that although the full expression for $\mathcal{R}_{00}$ is in terms of an infinite series, we have taken only three terms (that is, $-1 \leq m \leq 1$) in the above equation, which accurately describes the dispersion relation [93]. Kumar and Kim [115] have investigated a solution of Eq. (2.34) for the case of a shallow metallic grating ($kd \ll \pi/2$) and found an analytical expression for the resonant wavelength of the system for that case. They found that for the case of a shallow metallic grating, the underbraced term is very small and the series sum has to be very large in order to satisfy Eq. (2.34). This condition can be satisfied for the $m = 1$ term, which blows up at $\lambda = \lambda_R^0$, where $\lambda_R^0 = \lambda_g(1 + \beta)/\beta$. Using these conditions, Eq. (2.34) has been solved in the vicinity of λ_R^0 by Kumar and Kim [115] to obtain the following expression for the resonant wavelength of the system:

$$\lambda = \lambda_R^0 + \Delta\lambda. \tag{2.35}$$

Here, $k_R^0 = 2\pi/\lambda_R^0$, $\Delta\lambda = (\lambda_g/2)(\delta/K_R^0)^2$, and $\delta = (2\tan(k_R^0 d)/w\lambda_g k_R^0)(1 - \cos(wk_R^0))$. For the applicable cases, this formula has been verified with the results of detailed numerical calculations performed without invoking any approximation discussed in this section [115]. This simple analytical formula for the resonant wavelength was remarkable for the surface mode supported in a metallic grating, where most of the calculations rely on the numerical computation techniques. It is also important to mention here that unlike the case of the dielectric slab placed on a conducting surface, simple analytical expressions for power and attenuation coefficient of the surface mode are difficult to obtain for the reflection metallic grating, since the grating supports several space harmonics. This can be however done numerically as discussed in Ref. [99].

2.5 Discussions and conclusion

In this chapter, we have performed a detailed analysis of the surface mode supported by a dielectric slab placed on a conducting surface. We have assumed the system to be uniform along one direction, i.e., perpendicular to the direction of electron beam propagation and along the dielectric surface. Hence, the calculations presented in this chapter are essentially 2D in nature. These calculations have been performed by evaluating the reflectivity of the system for the incident evanescent wave. It has been observed that at a particular phase velocity of the surface mode, the reflectivity becomes singular for a combination of frequency and wavenumber that satisfy the dispersion relation. This singularity condition gives us the resonant frequency of the surface mode at a particular phase velocity. We have then calculated power flow, energy velocity and group velocity of the surface mode by following a simple textbook approach based on the Poynting vector calculations. These results have been used to evaluate the attenuation coefficient of the surface mode due to the losses present in the dielectric medium and Ohmic loss due to the finite conductivity of the metallic structure. The losses are observed to be prominent at high frequency of the guided surface mode. Finally, we have summarized the essential features of the surface mode supported by a rectangular metallic grating that have been worked out in earlier analyses [88, 93, 115].

Based on these results, it is interesting to compare some of the interesting features of the surface mode supported by a dielectric slab placed on a conducting surface and the surface mode supported by a rectangular grating. The group velocity of the surface mode supported by a dielectric slab placed on a conducting surface is always in the direction of its phase velocity [see Fig. 2.2], while for the case of grating system it can also be opposite to the direction of its phase velocity [93]. Due to the periodicity of metallic structure, a grating is a complex electromagnetic system compared to the dielectric based system. The electromagnetic field supported by the metallic grating, therefore, contains infinite Floquet space harmonics. The presence of several space harmonics increases the attenuation of the surface mode in a metallic grating. A metallic grating is also expected to have more attenuation compared to the dielectric slab placed on the conducting surface because it has more metallic area per unit length. As discussed in Sec. 2.3 for the case of dielectric based system and in Ref. [99] for the metallic grating, the attenuation effect increases with the operating frequency. Hence, grating based system is preferred for *low-frequency* operation and dielectric based system is preferred for *high-frequency* operation. If we ignore the small correction term $\Delta\lambda$ in Eq. (2.35), the radiation wavelength of a rectangular grating can be simply written as $\lambda_g(1+\beta)/\beta$. It can be seen that the resonant wavelength of the grating based system decreases with the phase velocity of the surface mode, while it is opposite for the case of resonant wavelength of the surface mode supported by the dielectric based system. This means that for the dielectric based system, higher frequency can be generated at lower phase velocity or equivalently by using a low-energy electron beam compared to the grating based system. The above results indicate that a dielectric based system can be preferred for high-frequency operation, and this can be achieved by using a relatively low-energy electron beam. However, there is more scope in optimizing and enhancing the system performance for the grating based system compared to the dielectric based system. This is because the grating has more system parameters, i.e., grating period, groove width, and groove depth, which can be optimized for the best performance compared to the dielectric slab based system, where we have only one parameter, i.e., the dielectric slab thickness, to optimize a particular dielectric.

To conclude, we have described a detailed 2D analysis of the surface mode supported by two systems- (i) dielectric slab placed on a conducting surface and (ii) metallic reflection grating. The results obtained in this chapter will be used for the detailed 2D analysis of beam-wave interaction in these two systems in the following chapters.

Chapter 3

Analysis of Čerenkov free-electron lasers

As discussed in the previous chapter, a dielectric slab placed on a metallic conductor supports an electromagnetic surface mode. An electron beam travelling in close proximity and parallel to the dielectric surface may exchange energy with the surface mode, thereby amplifying it and producing a gain in the system. This system is known as a single slab based Čerenkov free-electron laser (CFEL), and can produce copious amount of coherent THz radiation. A theoretical analysis of CFEL involves detailed study of the self consistent evolution of the surface mode and the electron beam. During the last few decades, several theoretical models have been proposed for the analysis of CFELs. One of the earliest analysis was presented by Walsh *et al.* [81, 82], who have presented a model based on the linearized Maxwell-Vlasov equations to calculate the small-signal gain of a single slab based CFEL. In their approach, the evolution of the self-consistent electromagnetic field is described by solving the linearized Vlasov equation treating electrons as a plasma fluid. They have, however, neglected the space charge effect and performed the calculations only in the low-gain regime [81, 82]. The Maxwell-Vlasov approach was extended to the high-gain regime by several authors [83, 128, 129], and the growth rate of the system was calculated. The growth rate of single slab based CFELs was also calculated by using the hydrodynamic approach, as discussed in Refs. [84, 98]. In this approach, one treats the electron beam as a plasma dielectric and solves the Maxwell wave equation to find the dispersion relation of the system. The dispersion relation can be expanded in the Taylor series about the roots of no-beam dispersion to find the growth rate of the electromagnetic field. Both the hydrodynamic approach and the approach based on the coupled Maxwell-Vlasov equations are successful in explaining the behaviour of the CFEL in the linear regime. However, these are very difficult to extend to the non-linear regime.

To study the non-linear regime, an approach based on the Maxwell-Lorentz equations is very well established for the conventional undulator based FELs [42, 85, 130, 131]. This is a single-particle approach, where the evolution of field is given by a self consistent dynamical Maxwell-field equation, and the evolution of electron trajectories is described by single particle Lorentz equation of motion. This approach turned out to be quite useful in writing computer codes for the detailed simulation of the non-linear regime. Several realistic effects, i.e., finite beam emittance, finite energy spread are also included in the simulations [42]. There have been earlier attempts to study the non-linear regime of single slab based CFELs by setting up the Maxwell-Lorentz equations in Refs. [94–96]. However, the evanescent nature of the surface mode has not been included in these analyses in a rigorous way, while setting up the coupled Maxwell-Lorentz equations. Also, their analyses [95, 96] assume an electron beam of infinite vertical size above the dielectric surface, and does not properly describe the case where a CFEL is driven by a flat electron beam with a very small vertical size. As will be discussed later, a flat beam is more appropriate for a single slab based CFEL.

In all the above mentioned analyses of CFELs, the size of the electron beam is taken to be either very large or infinite. Since the surface mode supported in a CFEL is evanescent in the direction perpendicular to the dielectric surface, it is more appropriate to take a flat transverse profile of the electron beam that allows the beam to travel very close to dielectric surface and ensures a significant interaction with the evanescent field. We would like to emphasize that a flat beam has vertical size much smaller than its horizontal size over the entire interaction length. The importance of utilising a flat electron beam to drive the single slab based CFEL has been discussed by several authors [51, 52, 66, 132]. In comparison to a round electron beam, a flat beam with the same current allows more effective interaction with the surface mode, since all the electrons are at a reduced height from the dielectric surface. Also, a flat beam can allow much more current within the required dimension in the vertical direction, and thus will help to enhance the output power of the device [132].

In this chapter, we have performed a detailed non-linear analysis of a single slab based CFEL driven by an infinitesimal thin flat electron beam by setting up the coupled Maxwell-Lorentz equations. Our approach incorporates the evanescent nature of the surface mode and also includes the space charge effect. Unlike the hydrodynamic approach and the approach based on the Maxwell-Vlasov equations, our analysis is easily extended to the non-linear regime. To perform this analysis, we have extended the calculations of amplitude reflectivity given in Chapter 2, for the case of growing evanescent wave. By analyzing the singularity in the reflectivity for this case, we set up a dynamical Maxwell field equation to study the evolution of the amplitude of the surface mode. The dynamics of the electron beam in the presence of this surface mode is described by the Lorentz equations of motion. The coupled-Maxwell Lorentz equations have been solved analytically in the linear regime, and numerically to study the non-linear regime. We would like to mention that our approach based on the coupled Maxwell-Lorentz equations here is similar to the one used by Kumar and Kim to analyze the working of Smith-Purcell free-electron lasers (SP-FELs) [88], except that the group velocity of the surface wave is positive here, which was negative in Ref. [88]. This affects the solution of the coupled Maxwell-Lorentz equations as follows. Due to the positive group velocity in CFELs, the electromagnetic field grows as it travels along the electron beam direction, which is similar to the conventional undulator based FELs [42]. If the single pass gain is not high, a set of external mirrors has to be used, which can reflect back the electromagnetic field to the entrance of the interaction regime so that power can build up to saturation after many round trips. This configuration is known as the oscillator configuration for which we have solved the coupled Maxwell-Lorentz equations in this chapter. When the group velocity is negative, as in SP-FELs discussed in Ref. [88], the electromagnetic field builds up in the direction opposite to the electron beam direction, without the use of the external mirrors. This is because the backward flow of energy modifies the dynamics of electrons at the entrance point, and these electrons, after travelling further, give their energy to the field, which flows backward and again interacts with the incoming electrons. This process continues and the system reaches saturation when the current density exceeds a certain threshold value. This system is known as the backward wave oscillator (BWO) [133], and the coupled Maxwell-Lorentz equations have been solved for a SP-FEL in BWO configuration in Ref. [88], which is different from the case of the CFEL discussed in this chapter.

In the next section, we find the electromagnetic field due to a bunched flat electron beam propagating over the surface of a dielectric slab placed over a conducting surface. In Sec. 3.2, the detailed calculations of the amplitude reflectivity of this system has been presented for the case of a growing evanescent wave. Using these results, the coupled Maxwell-Lorentz equations have been set up to study the beam-wave interaction in CFELs in the same section. Next, we obtain the analytical solutions of the coupled Maxwell-Lorentz equations in linear regime to find the formulas for the small-signal gain in Sec. 3.3.1 and growth rate in Sec. 3.3.2. In Sec. 3.4, we solve the coupled Maxwell-Lorentz equations numerically to study the nonlinear regime of CFELs. Finally, we conclude with a discussion of results in Sec. 3.5.

3.1 Basic electromagnetic field equations

The working mechanism of a CFEL is essentially due to the bunching of the electron beam in the presence of the electromagnetic field supported by the system. The bunched electron beam generates an electromagnetic field, which in turn further bunches the beam and this process continues till saturation. In order to understand the beam-wave interaction phenomena, we start by evaluating the electromagnetic field due to a bunched flat electron beam propagating very close to the dielectric surface in the CFEL system. The schematic of a single slab based CFEL system with the co-ordinate system used in our analysis is shown in Fig. 3.1. The dielectric slab of thickness d, length L and dielectric constant ϵ is supported on an ideal conductor. The system is assumed to be translationally invariant along the y-direction. A flat electron beam with vanishing thickness in the x-direction and width Δy in the y-direction travels with a speed v along the z-direction, at a height h above the dielectric slab. It is clarified here that a flat beam

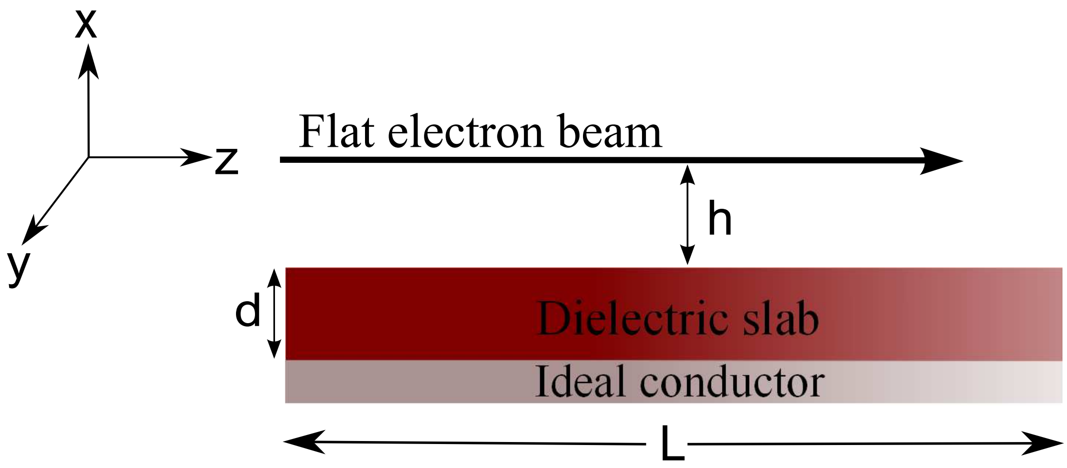

FIGURE 3.1: Schematic of a Čerenkov FEL driven by a flat electron beam.

is actually a simplified way of representing a beam having a thickness $2h$ in the x-direction with its centroid at a height h above the dielectric surface. The thickness as well as the emittance of the beam in the x-direction is much smaller than the corresponding value in the y-direction. The expression for the z-component of the volume current density and surface current density of such a flat electron beam can be written as

$$J_z(x, z, t) = \frac{e}{\Delta y}\delta(x)\sum_i \delta[z - z_i(t)]v, \tag{3.1}$$

$$K_z(z, t) = \frac{e}{\Delta y}\sum_i \delta[z - z_i(t)]v, \tag{3.2}$$

where e is electronic charge, δ is the Dirac delta function, z_i is the position of the ith electron at time t, and the summation is over all the electrons. While propagating along the longitudinal direction, the electron beam interacts with the surface mode supported by the system. As discussed in the previous chapter, the system here supports an evanescent surface mode having a range of frequencies and corresponding k_0 given by the dispersion relation. The electron beam will interact resonantly with the surface mode having a particular frequency $\omega = vk_0$, for which the phase velocity is same as the electron velocity. Due to this interaction, the electron beam develops micro-bunching at the wavelength of the surface mode. This results in a sinusoidal component of electron beam current having frequency ω and wavenumber k_0, same as that of the surface mode. The surface current density can then be expanded in a Fourier series, which will have a component at the fundamental frequency ω, and also higher harmonics. We are interested in the component $K(z,t)e^{i(k_0 z-\omega t)}$ + c.c. of the current density, which contains the fundamental frequency and shows the strongest interaction with the surface mode. Here, c.c. denotes the complex conjugate. The expression for $K(z,t)$ is given by

$$K(z,t) = \frac{ev}{\Delta y}\frac{1}{\lambda_z}\int_{z-\frac{\lambda_z}{2}}^{z+\frac{\lambda_z}{2}} \sum_i \delta[z - z_i(t)]e^{-i(k_0 z-\omega t)}dz, \tag{3.3}$$

where $\lambda_z = 2\pi v/\omega$ is the wavelength of the surface mode. In the above equation, the integration is performed at a particular time t over one wavelength λ_z around the location z. Hence, only the electrons, which are distributed over one wavelength will contribute in the summation term. Following these arguments, we obtain the expression for the surface current density as:

$$K(z,t) = \frac{ev}{\Delta y}\frac{N_{\lambda_z}}{\lambda_z}\langle e^{-i\psi}\rangle, \tag{3.4}$$

where N_{λ_z} is the number of electrons distributed over the wavelength λ_z, $\psi = k_0 z - \omega t$ is the electron phase, $\langle\cdots\rangle$ indicates averaging over the number of particles distributed over λ_z, and term $\langle e^{-i\psi}\rangle$ is the bunching factor, which grows due to interaction between the electron beam and the co-propagating surface mode. The term $evN_{\lambda_z}/\lambda_z$ is identified as the electron beam current I. Following these notations, the total surface current density can be written as $(I/\Delta y)\langle e^{-i\psi}\rangle e^{i(k_0 z-\omega t)}$ + c.c.. Assuming an $\exp(\mu z)$-type dependence of the bunching factor, the total surface current density is given by $K_0 e^{i(\alpha_0 z-\omega t)}$ + c.c.. Here, $\alpha_0 = k_0 - i\mu$, μ is the field growth rate parameter and $K_0 = I/\Delta y$ is independent of z.

Now, we find the electromagnetic field generated by the bunched flat electron beam discussed above. The electromagnetic field due the surface current density $K_0 e^{i(\alpha_0 z-\omega t)}$ should have $e^{i(\alpha_0 z-\omega t)}$-type dependence on z and t in the region above, as well as below the flat beam. In order to satisfy the free-space wave equation in these regions, the field should have $\exp(\pm\Gamma x)$-type dependence in the x-direction, such that $\alpha_0^2 - \Gamma^2 = \omega^2/c^2$. Since the field should not diverge at $x = \pm\infty$, we require that fields should have $\exp(-\theta(x)\Gamma x)$-type dependence on x, where $\theta(x) = 1$ for $x > 0$ and $\theta(x) = -1$ for $x < 0$. We will first calculate the y-component of the magnetic field, which is denoted by H_y. In order to satisfy the boundary conditions, H_y should be discontinuous at $x = 0$ due the presence of the surface current. Due to symmetry arguments, the magnitude of H_y should however be continuous at $x = 0$. These two conditions can be satisfied only if the sign of H_y changes as we cross the plane $x = 0$. Using these arguments and the boundary condition $H_y(x = 0^+) - H_y(x = 0^-) = K_0 e^{i(\alpha_0 z - \omega t)}$, we obtain

$$H_y^{\mathcal{I}}(x, z, t) = \frac{1}{2}\theta(x) K_0 \exp[-\theta(x)\Gamma x] e^{i(\alpha_0 z - \omega t)}. \tag{3.5}$$

Other field components can be easily derived in terms of H_y and are like the field components of a plane evanescent wave. We observe that the electromagnetic field has H polarisation, which means that $H_x = H_z = E_y = 0$. The total y-component of the magnetic field is given by $H_y^{\mathcal{I}}(x, z, t)$+c.c..

The flat electron beam acts as a source of the above described electromagnetic field, which will be incident on the dielectric slab. Due to the presence of the dielectric slab, the incident field is reflected back towards the electron beam. The reflected and incident electromagnetic fields are coupled through the reflectivity R of the dielectric surface. We obtain the following expression for the reflected electromagnetic field:

$$H_y^{\mathcal{R}}(x, z, t) = -\frac{1}{2} K_0 R e^{-\Gamma(2h+x)} e^{i(\alpha_0 z - \omega t)}. \tag{3.6}$$

The sum of incident and reflected electromagnetic field effectively interacts with the electron beam. Using the Maxwell equation, the longitudinal component of the electric field E_z can be written as $E_z = (i/\epsilon_0\omega)(\partial H_y/\partial x - \delta(x)K(z, t))$. We obtain the following expression for the amplitude of the electromagnetic field experienced by the electron beam:

$$E_z(x = 0, z, t) = \frac{iIZ_0}{2\beta\gamma\Delta y}(Re^{-2\Gamma h} - 1)\langle e^{-i\psi}\rangle. \tag{3.7}$$

Here, $Z_0 = 1/(\epsilon_0 c) = 377\ \Omega$ is the characteristic impedance of free space, $\gamma = 1/\sqrt{1-\beta^2}$ is the relativistic Lorentz factor and ϵ_0 is the permittivity of free space. Note that the total longitudinal electric field is given by $E_z e^{i(k_0 z - \omega t)}$ + c.c.. It is clear from the above equation that to calculate the total electromagnetic field experienced by the electron beam, one needs to evaluate the reflectivity of the dielectric slab supported on a conducting surface, for the growing evanescent wave. These calculations are presented in the following section.

3.2 Reflectivity analysis and coupled Maxwell-Lorentz equations

Calculations of reflectivity were presented in Chapter 2 for the case of a plane evanescent wave incident on a dielectric slab placed on a conducting surface. These calculations were performed for the empty structure, i.e., without the electron beam. For this case, the plane evanescent wave does not have any growth as it propagates along the z-direction, hence the wavenumber k_0 along that direction is a real number. In the presence of an electron beam, the evanescent wave supported by the structure grows due to the beam-wave interaction. The longitudinal wavenumber for this wave is a complex quantity, which is given by $\alpha_0 = k_0 - i\mu$, where μ is the growth rate of the electromagnetic field. Hence, we repeat the procedure given in Sec. 2.1 of Chapter 2 by replacing k_0 with α_0, and obtained the following expression for amplitude reflectivity for growing evanescent wave:

$$R = \frac{1 + r\tan\left[d(\epsilon\beta^2 k_0^2 - \alpha_0^2)^{1/2}\right]}{1 - r\tan\left[d(\epsilon\beta^2 k_0^2 - \alpha_0^2)^{1/2}\right]}, \tag{3.8}$$

where $r = (\epsilon\beta^2 k_0^2 - \alpha_0^2)^{1/2}/\epsilon(\alpha_0^2 - \beta^2 k_0^2)^{1/2}$. Note that for $\mu = 0$, i.e., without any beam-wave interaction, the above equation reduce to Eq. (2.10). In this case, R becomes infinity for a combination of ω and k_0 satisfying the dispersion relation of the surface mode as discussed in the previous chapter.

For positive value of μ, the electromagnetic surface mode grows due to interaction with the electron beam and this instability in CFEL can be studied by analyzing the behavior of amplitude reflectivity R given by Eq. (3.8) in the vicinity of $\mu = 0$. Therefore, we perform a Laurent series expansion of R as a function of μ and obtain the following expression of R:

$$R = \frac{m_0 + m_1\mu + m_2\mu^2 + o(\mu^3)....}{n_0 + n_1\mu + n_2\mu^2 + o(\mu^3)....}, \tag{3.9}$$

where the coefficients of expansion are given as:

$$n_1 = \frac{-i}{k_0ab^2}[ad^2 + ab^2\gamma^2 + k_0bd^2(1 + a^2)], \tag{3.10}$$

$$\begin{aligned} n_2 &= \frac{-1}{2k_0^2b^4}[d^4 + b^2d^2(1 - 2\gamma^2) + \gamma^2b^4(1 - 3\gamma^2)]. \\ &+ \frac{(1 + a^2)}{2k_0a^2b^3}[ad^4 + 2k_0bd^4 - ab^2d^2(1 - 2\gamma^2)], \end{aligned} \tag{3.11}$$

$m_0 = 2$, $n_0 = 0$, $m_1 = -n_1$, $m_2 = -n_2$. In Eq. (3.9), we have a division of two infinite series. By keeping the terms of the order of $1/\mu$ and μ^0 in Eq. (3.9) and performing the required algebra, we obtain the following simple expression for the reflectivity:

$$R = \frac{i\chi}{\mu} + \chi_1. \tag{3.12}$$

Here, χ and χ_1 are given by

$$\chi = \frac{-im_0}{n_1}, \tag{3.13}$$

$$\chi_1 = \frac{1}{n_1^2}(m_1n_1 - m_0n_2) . \tag{3.14}$$

This simple parametrization of R in terms of χ and χ_1 is very important to understand the evolution of the surface mode in a CFEL system. As discussed later in this section, the parameter χ is associated with the growth rate of the surface mode and the parameter χ_1 is related to the ac space charge effect in the system. To perform calculations, we now consider an example

TABLE 3.1: Parameters of a CFEL used in the calculation

Electron-beam energy	30 keV
Electron-beam height (h)	35 μm
Electron-beam current (I)	1 mA
Dielectric constant (ϵ)	13.1
Length of slab (L)	0.15 m
Dielectric thickness (d)	350 μm
Operating frequency	0.1 THz

case having the parameters listed in Table 3.1. These parameters are taken from a recent experiment [66, 98] performed at the Dartmouth College, USA, as discussed earlier in Chapter 2. We find $\chi = 1.81$ per cm and $\chi_1 = 0.86$ from Eqs. (3.13) and (3.14) respectively for this case. We also confirmed these values by numerically evaluating the value of μR and plotting it in the vicinity of $\mu = 0$. The value of χ and χ_1 are obtained separately from two graphs in Fig. 3.2, which are in agreement with our analytical calculations.

We now substitute for R in Eq. (3.7) and obtain the following expression for the amplitude of the longitudinal electric field at the position of the electron beam:

$$E_z = \frac{iIZ_0}{2\beta\gamma\Delta y}\left(\frac{i\chi}{\mu}e^{-2\Gamma h} + \chi_1 e^{-2\Gamma h} - 1\right)\langle e^{-i\psi}\rangle. \tag{3.15}$$

The first part of the right hand side of the above expression depends on μ, and is responsible for the growth of the electromagnetic surface mode. The remaining terms are independent of the growth rate parameter and represent the ac space-charge effect in the longitudinal field. This approach of separating the total electromagnetic field into surface mode field and space charge field is similar to the approach described in Ref. [134], where it is stated that "*The total fields from an arbitrary, spatially periodic current are shown to consist of a pole term, which is identified as the structure field, and a remainder, which is identified as the space charge field*". A similar approach was also used by Pierce [135] while studying the travelling wave tubes. The dynamics of the electron beam is governed by the surface mode field as well as the ac space charge field. We write the ac space-charge field as E_{sc} and the amplitude of surface-mode as E

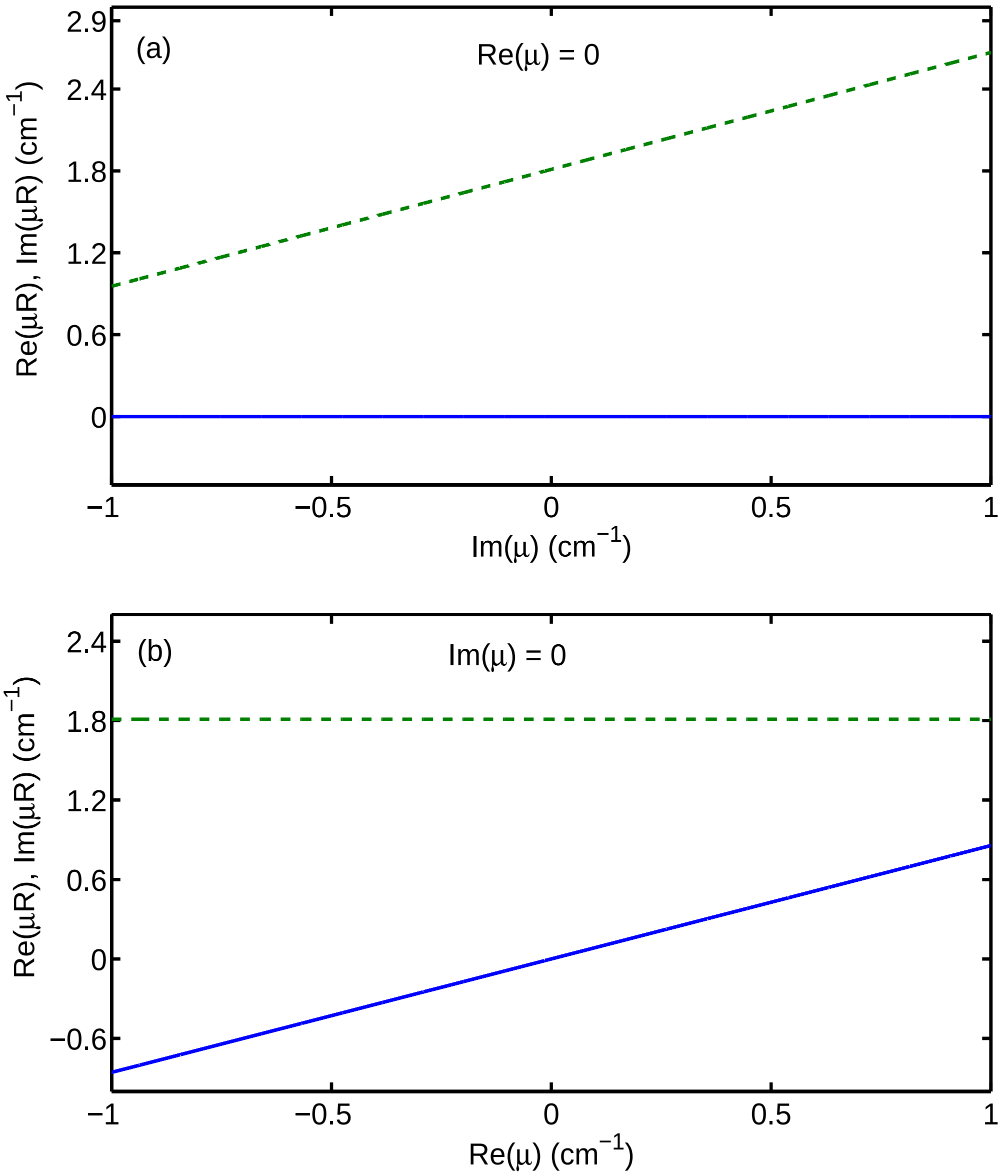

FIGURE 3.2: Plots of imaginary (dashed) and real (solid) parts of μR as a function of the imaginary (a) and real (b) parts of the growth rate parameter μ near the resonance frequency, i.e., 0.1 THz. By parametrising R as $(i\chi/\mu+\chi_1)$ in this graph, we obtain $\chi = 1.81$ per cm and $\chi_1 = 0.86$.

in further calculations. We can replace the growth rate parameter by d/dz in Eq. (3.15), and by including the group velocity v_g, we get the following time-dependent differential equation for E:

$$\frac{\partial E}{\partial z} + \frac{1}{v_g}\frac{\partial E}{\partial t} = \frac{-IZ_0\chi}{2\beta\gamma\Delta y}e^{-2\Gamma h}\langle e^{-i\psi}\rangle. \tag{3.16}$$

The ac space charge field is given by

$$E_{sc} = \frac{-iIZ_0}{2\beta\gamma\Delta y}(1 - \chi_1 e^{-2\Gamma h})\langle e^{-i\psi}\rangle. \tag{3.17}$$

Next, we discuss the longitudinal dynamics of the ith electron in presence of the surface mode field and the ac space charge field. We neglect the transverse motion of the electron beam and obtain the following equations for the evolution of energy and phase of the ith electron:

$$\frac{\partial\gamma_i}{\partial z} + \frac{1}{v}\frac{\partial\gamma_i}{\partial t} = \frac{e}{mc^2}(E + E_{sc})e^{i\psi_i} + \text{c.c.}, \tag{3.18}$$

$$\frac{\partial\psi_i}{\partial z} + \frac{1}{v}\frac{\partial\psi_i}{\partial t} = \frac{\omega}{c\beta_R^3\gamma_R^3}(\gamma_i - \gamma_R). \tag{3.19}$$

Here, the subscript i is meant for the ith particle, the subscript R is meant for the resonant particle, $\beta_R = v_R/c$, $\gamma_R = 1/\sqrt{1-\beta_R^2}$ is the relativistic Lorentz factor, and m is the rest mass of the electron. At resonance, the electron velocity is same as the phase velocity of the co-propagating surface mode. Equations (3.16)-(3.19) are known as the coupled Maxwell-Lorentz equations, which govern the behaviour of a single slab based CFEL driven by a flat electron beam.

3.3 Analytical results

In general, the coupled Maxwell-Lorentz equations described in the previous section have to be solved numerically with the given initial conditions for a detailed analysis of the CFEL system. However, we can find an analytical solution of these equations in two regimes, i.e, the small-signal, small-gain regime and the small-signal, high-gain regime. Before performing these calculations, we first write Eqs. (3.16)-(3.19) in the form of dimensionless variables and present some interesting calculations to obtain an analytical formula for power in the surface mode. The dimensionless variables are introduced as follows:

$$\xi = z/L, \tag{3.20}$$

$$\tau = \left(t - \frac{z}{v_R}\right)\left(\frac{1}{v_g} - \frac{1}{v_R}\right)^{-1}\frac{1}{L}, \tag{3.21}$$

$$\eta_i = \frac{k_0 L}{\beta_R^2 \gamma_R^3}(\gamma_i - \gamma_R), \tag{3.22}$$

$$\mathcal{E} = \frac{4\pi k_0 L^2}{I_A Z_0 \beta_R^2 \gamma_R^3} E_z, \tag{3.23}$$

$$\mathcal{E}_{sc} = \frac{4\pi k_0 L^2}{I_A Z_0 \beta_R^2 \gamma_R^3} E_{sc}, \tag{3.24}$$

$$\mathcal{J} = 2\pi \frac{\chi}{\Delta y} \frac{I}{I_A} \frac{k_0 L^3}{\beta_R^3 \gamma_R^4} e^{-2\Gamma h}. \tag{3.25}$$

Here, ξ is the dimensionless distance, which varies from 0 to 1, and τ is the dimensionless time variable, having an offset of z/v_R from the real time t. The normalised energy detuning of the ith electron is η_i, $\mathcal{E}$ is the dimensionless surface mode field, and $\mathcal{E}_{sc}$ represents dimensionless ac space charge field. The dimensionless beam current is written as $\mathcal{J}$ and $I_A = 4\pi\epsilon_0 mc^3/e = 17.04$ kA is the Alfvén current. These dimensionless variables are helpful in illustrating the importance of various terms in the coupled Maxwell-Lorentz equations, and therefore, in understanding of various physical effects. With these dimensionless variables, the set of Eqs. (3.16)-(3.19) assumes the following elegant form:

$$\frac{\partial \mathcal{E}}{\partial \xi} + \frac{\partial \mathcal{E}}{\partial \tau} = -\mathcal{J}\langle e^{-i\psi}\rangle, \tag{3.26}$$

$$\frac{\partial \eta_i}{\partial \xi} = (\mathcal{E} + \mathcal{E}_{sc})e^{i\psi_i} + \text{c.c.}, \tag{3.27}$$

$$\frac{\partial \psi_i}{\partial \xi} = \eta_i, \tag{3.28}$$

$$\mathcal{E}_{sc} = i\Theta\langle e^{-i\psi}\rangle, \tag{3.29}$$

where $\Theta = (\mathcal{J}/\chi L)(\chi_1 - e^{2\Gamma h})$.

Now, we calculate the power associated to the surface mode by using the principle of energy conservation. For simplicity, we perform the calculations for the steady state regime. In this regime, Eqs. (3.26)-(3.29) are expressed in the following form:

$$\frac{\partial |\mathcal{E}|^2}{\partial \xi} = -2\mathcal{J}\mathrm{Re}[\mathcal{E}\langle e^{i\psi}\rangle], \tag{3.30}$$

$$\frac{\partial \langle \eta \rangle}{\partial \xi} = 2\mathrm{Re}[\mathcal{E}\langle e^{i\psi}\rangle] + 2\mathrm{Re}[\mathcal{E}_s\langle e^{i\psi}\rangle]. \tag{3.31}$$

The second term on the right-hand side of Eq. (3.31) can be shown to be zero by using Eq. (3.29). Using this result and by combining Eqs. (3.30) and (3.31), we obtain

$$\frac{\partial}{\partial \xi}(|\mathcal{E}|^2 + \mathcal{J}\langle \eta \rangle) = 0, \tag{3.32}$$

which is the equation for conservation of energy in the CFEL system. It indicates that the energy lost by the electron beam while travelling down the interaction region, appears in the surface mode. Using Eq. (3.32), we find the energy lost per unit time by the electron beam and by equating it to the power developed in the surface mode, we obtain:

$$\frac{P}{\Delta y} = \frac{2\beta_R \gamma_R}{\chi Z_0}\left(\frac{mc^2\beta_R^2\gamma_R^3}{ek_0 L^2}\right)^2 e^{2\Gamma h}|\mathcal{E}|^2. \tag{3.33}$$

Note that the parameter χ appears in the above expression. We would like to mention that the power in the surface mode supported by the dielectric slab placed on an ideal conductor was also calculated in Chapter 2 by using the Poynting vector, which is given by Eq. (2.21). Here, we have used energy conservation principle to derive the expression for power, and expressed the results in terms of χ parameter. Using the expression for χ given in Eq. (3.13) and the expression for $\mathcal{E}$ given in Eq. (3.23), we find that the expressions for power evaluated using the two approaches, which are given by Eq. (2.21) and (3.33), are exactly identical. This confirms that the formulation of the beam-wave interaction in terms of χ parameter is correct.

3.3.1 Small-signal small-gain regime

We now proceed for the analytical solution of the coupled Maxwell-Lorentz equations in the small-signal, small-gain regime. In this regime, the small-signal gain determines whether the system will reach the threshold to lase. For the small-signal gain analysis, we will proceed with the time-independent form of Eqs. (3.26)-(3.28) and neglect the ac space charge term. Defining the differential gain as $(1/\mathcal{E}^2)(d\mathcal{E}^2/d\xi)$ and following the procedure closely given in Ref. [42] for the conventional undulator based FEL, we get the following expression for the small-signal gain:

$$G(\eta_0) = 4\mathcal{J}\Big(\frac{1-\cos\eta_0 - \eta_0\sin\eta_0/2}{\eta_0^3}\Big). \tag{3.34}$$

The term in parentheses is the usual gain function and $\eta_0 = (k_0 L/\beta_R^2\gamma_R^3)(\gamma-\gamma_R)$ is the normalised energy detuning at $\xi = 0$. The gain function has a maximum value of 6.75×10^{-2} at $\eta_0 = 2.6$. By substituting the maximum value of gain function and using $\mathcal{J}$ from Eq. (3.25) in the above equation, the expression for the small-signal gain in a single pass operation of CFEL is written as follows:

$$G = 4\times 6.75\times 10^{-2}\times 2\pi\frac{\chi}{I_A}\frac{I}{\Delta y}\frac{k_0 L^3}{\beta_R^3\gamma_R^4}e^{-2\Gamma h}. \tag{3.35}$$

The gain increases linearly with the surface current density, and has cubic dependence on the length of the dielectric slab. It has a negative exponential dependence on the beam height h, and dependencies on dielectric constant ϵ and slab thickness d are given through the parameter χ.

The gain of a CFEL crucially depends upon the diffraction effects in the electromagnetic surface mode. Due to diffraction, the optical beam size increases, resulting in partial overlap of the optical mode with the electron beam, which reduces the gain of the CFEL. One has to choose the electron beam size Δy same as the effective optical beam size in the y-direction for maximum overlap. The effective optical beam size can be estimated by considering the diffraction of electromagnetic fields in y-direction in a similar way as described in Refs. [78, 89]. These calculations are performed in the next chapter, where the effective beam size of the surface mode that needs to be taken in Eq. (3.35) is obtained as $\Delta y = \sqrt{\pi\beta_R\lambda L/4}$. We find $\Delta y =$ 10.6 mm for the parameters listed in Table 3.1. The value of small-signal gain predicted by our calculations is about 56.3 %. This value of gain is low and the system will not able to reach saturation in a single pass. For such case, one has to operate the system in oscillator configuration by using a set of mirrors. The solution of coupled Maxwell-Lorentz equation in the oscillator configuration will be the subject of discussion in Sec. 3.4, where we will study the saturation behaviour of a single slab based CFEL system.

3.3.2 Small-signal high-gain regime

Analysis in the previous sub-section was done for the small-signal, small-gain regime. Another regime of interest is the small-signal, high-gain regime, where we calculate the growth rate in the system. Several authors have presented the calculation of the growth rate in the single slab based CFEL [84, 98, 136]. In this section, we perform the calculation of growth rate in CFEL using collective variables. These variable were introduced for the study of conventional undulator based FELs [86] and later extended for the case of SP-FELs [88]. For the small-signal regime, we assume a perturbative solution of the coupled Maxwell-Lorentz equations. We have neglected the ac space charge effect here. For simplicity, we assume a monoenergetic and unbunched electron beam at the entrance, i.e., $\langle e^{-i\psi_0}\rangle = 0$. We can then write the equilibrium solutions of Eqs. (3.26)-(3.28) as $\mathcal{E} = 0$, $\eta_i = \eta_0$ and $\psi_i = \eta_0\xi + \psi_{i,0}$. The perturbative solutions for these equations are defined as: $\mathcal{E}_p = \mathcal{E}$, $\eta_{i,p} = \eta_0 + \delta\eta_i$ and $\psi_{i,p} = \psi_i + \delta\psi_i$. The collective variables are introduced as:

$$p = \langle \delta\psi e^{-i\psi_0}\rangle, \tag{3.36}$$

$$q = \langle \delta\eta e^{-i\psi_0}\rangle. \tag{3.37}$$

Using above variables, we linearise the set of Eqs. (3.26)-(3.28) and keep the terms only up to the first order. Doing this, we obtain

$$\frac{\partial p}{\partial \xi} = q - i\eta_0 p, \tag{3.38}$$

$$\frac{\partial q}{\partial \xi} = \mathcal{E} - i\eta_0 q, \tag{3.39}$$

$$\frac{\partial \mathcal{E}}{\partial \xi} = i\mathcal{J} p. \tag{3.40}$$

In order to solve the above equations, we assume solution of the type $e^{\nu\xi}$, i.e. $p = p_0 e^{\nu\xi}$, $q = q_0 e^{\nu\xi}$ and $\mathcal{E} = \mathcal{E}_0 e^{\nu\xi}$. With these solutions, Eqs. (3.38)-(3.40) now assume the form:

$$\nu p_0 = q_0 - i\eta_0 p_0, \quad \nu q_0 = \mathcal{E}_0 - i\eta_0 q_0, \quad \nu \mathcal{E}_0 = i\mathcal{J} p_0. \tag{3.41}$$

The above expression can be solved to obtain the following cubic equation:

$$\nu^3 + 2i\eta_0 \nu^2 - \eta_0^2 \nu = i\mathcal{J}. \tag{3.42}$$

The growth rate will be maximum for $\eta_0 = 0$. Solving the above equation for the positive value of real ν and substituting $\mathcal{J}$ from Eq. (3.25), we obtain the maximum growth rate as:

$$\mu = \frac{\sqrt{3}}{2L}\left(2\pi \frac{\chi}{\Delta y}\frac{I}{I_A}\frac{k_0 L^3}{\beta_R^3 \gamma_R^4} e^{-2\Gamma h}\right)^{1/3}. \tag{3.43}$$

The growth rate depends on cube root of the beam current density. This form of growth rate is already familiar in the hydrodynamic approach [84, 98, 136]. Note that we have used a flat electron beam in our calculations. The growth rate for a thick beam having thickness Δx in the x direction has been calculated by Li *et al.* [136] using the hydrodynamic approach. If we take limit $\Delta x \rightarrow 0$ in the formula given in Ref. [136], we recover Eq. (3.43).

Using the parameters listed in Table 1, we find the value of growth rate parameter as 8 m^{-1}. The growth rate calculated by Andrew and Brau [98] for these parameters, using the three dimensional analysis is about 10 m^{-1}, which is in agreement with our calculations. The value of the growth rate parameter reported in the Dartmouth experiment is 250 to 450 m^{-1} [66]. The value of growth rate parameter obtained from two different analyses are approximately same, but not in agreement with the results of Dartmouth experiment. It is likely that a larger growth rate was measured in Dartmouth experiment due to coherent spontaneous emission.

3.4 Numerical simulations

Next, we discuss the numerical solution of the coupled Maxwell-Lorentz equations, in order to understand the saturation behaviour of the CFEL system. For this purpose, we have written a computer code based on the leapfrog method, which is widely used to compute oscillatory solutions of differential equations [137, 138]. This is a second order method like the second-order Runge-Kutta method, but takes less time and less memory compared to the latter [138]. In the leapfrog scheme, we require the initial value of variables on the left side in Eqs. (3.26)-(3.29) at ξ, and the value of terms on the right side in Eqs. (3.26)-(3.29) at $\xi + \Delta\xi/2$, to find the value of variables at $\xi + \Delta\xi$ using the mid-point method. In the first step, i.e., from $\xi = 0$ to $\xi = \Delta\xi$, we solve Eqs. (3.26)-(3.28) by taking the initial value of variables at $\xi = 0$ in the Euler method to find the value of variables at $\Delta\xi/2$. These value are then used to find the value of terms on the right side in Eqs. (3.26)-(3.29) at $\Delta\xi/2$ and to finally estimate the value of variables at $\Delta\xi$. Next, the values of variables at $\Delta\xi/2$ are set as initial conditions, and value of variables at $\Delta\xi$ are used in the right hand side of Eqs. (3.26)-(3.29) to find the solution of Eqs. (3.26)-(3.29) at $3\Delta\xi/2$. This scheme is repeated step by step, and we ensure that the energy conservation [Eq. (3.32)] is satisfied in each step of integration.

For the initial conditions, the input electron beam is considered to be monoenergetic with $\eta = 2.6$ for maximum gain, and the initial dimensionless electric field is set to be very small, i.e., $\mathcal{E} = 0.001$. In order to evaluate the first term on the right side of Eq. (3.26), we need to perform an averaging over the electrons distributed over one wavelength of the evanescent wave. Hence, in the simulation, we need to take the number of electrons same as the number

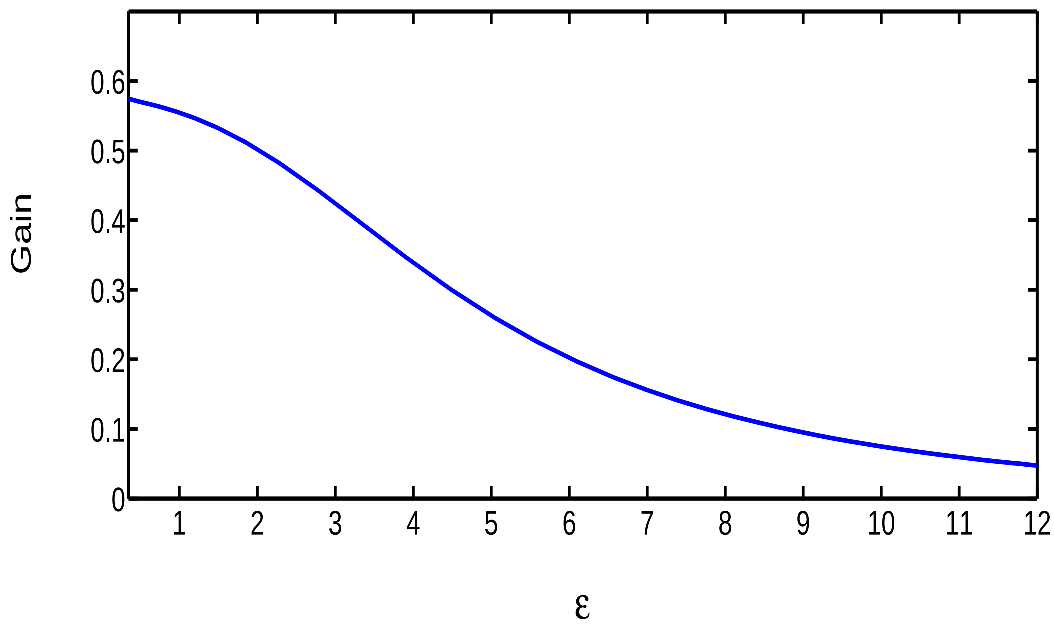

FIGURE 3.3: Plot of gain as a function of dimensionless input electric field in a CFEL.

of electrons distributed over one spatial wavelength of the evanescent wave i.e., $N_{\lambda_z} = I\lambda_z/ev_R$. We obtain $N_{\lambda_z} \simeq 2^{16}$ for our system. The numerical solution for the trajectories of 2^{16} particles will require a large computer memory and will be a time consuming task. Instead of taking the actual number of particles, we consider macroparticles [42] in our simulations, where each macroparticle carries a charge larger than the charge on actual particle, but the same charge to mass ratio. In this way, we have taken 2^{13} particles, which carry the same charge as carried by the actual electron bunch, and can be easily handled in the numerical simulations. To initialize the electron beam in the phase space, we have used the quiet start scheme [139]. In this scheme, electrons are assumed to have uniform distribution in the phase space. The phase of nth electron is set to be $2\pi n/N_{\lambda_z}$, which ensures that $\langle e^{-i\psi}\rangle = 0$ at $\xi = 0$. The total length of the system is divided into a number of small steps having step size $\Delta\xi = 0.01$.

We now discuss the results of our numerical simulations. The parameters used in the calculations are listed in Table 3.1. Figure 3.3 shows the gain as a function of dimensionless input electric field. We obtain a small-signal gain of about 57%, which is consistent with our analytical calculations. For the chosen parameters, CFEL is a low gain system and has to be operated in the oscillator configuration, as discussed in Sec. 3.1. For this purpose, a set of

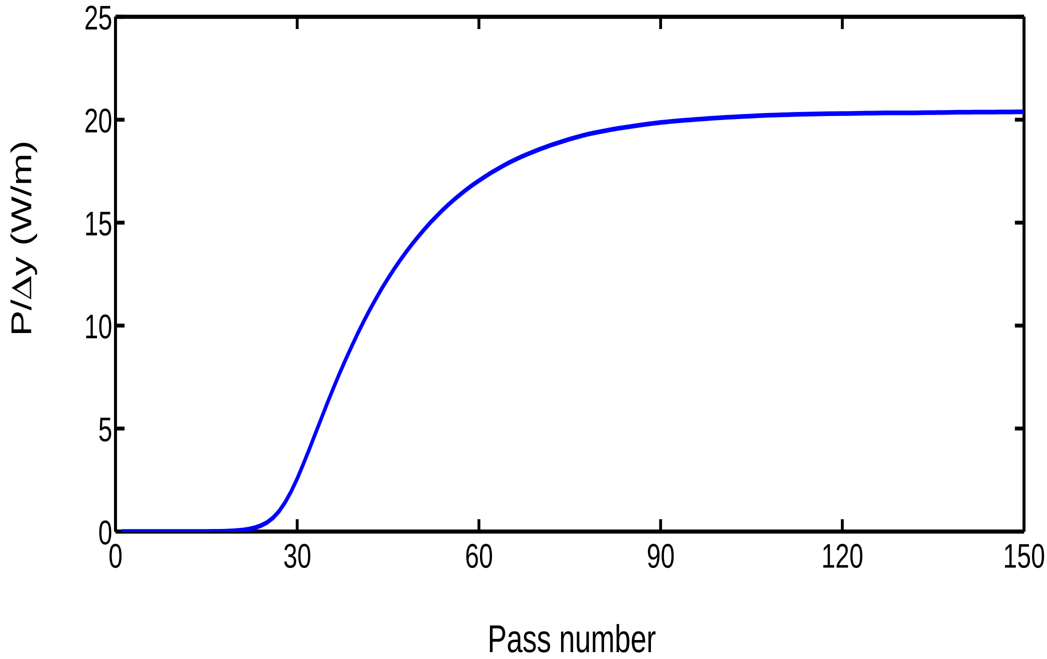

FIGURE 3.4: Plot of output power per unit beam width in the surface mode as a function of number of passes in a CFEL oscillator.

mirrors is used to provide an external feedback. One mirror at the upstream end is assumed to have 100% reflectivity for the field amplitude, while the second mirror at the downstream end is assumed to have an amplitude reflectivity of 98%. A fraction of the intra-cavity power can be outcoupled through the mirror at the downstream end, and the output THz radiation can be guided via suitable optical arrangements to a nearby experimental station. In this configuration, the recirculation of THz pulse is simulated by numerically copying the electromagnetic field, which is reflected from the second mirror at the downstream end. The electromagnetic field then propagates to the upstream mirror (which is 100% reflective), and becomes input field for the next pass. This input field interacts with the incoming electron beam as it propagates down the interaction region. The coupled Maxwell-Lorentz equations have been solved under the above mentioned conditions for an oscillator configuration to obtain the power in the surface mode.

We examine the non-linear behaviour of the system by performing numerical simulation, as discussed above. Figure 3.4 shows the growth in power of the surface mode with the number of passes. The power builds up slowly in this low-gain system, and saturates at 20.4 W/m. The input power per unit width of the electron beam is about 2.8 kW/m. This gives us efficiency of about 0.7% at saturation. As discussed by Walsh and Murphy [81], the upper bound of the efficiency for power conversion in a CFEL can be written as:

$$\eta_{eff} = \frac{\beta_R^3 \gamma_R^3}{(\gamma_R - 1)} \frac{\lambda}{L}. \tag{3.44}$$

We get an upper bound of 1.4 % for the efficiency of the considered CFEL. This is in good agreement with the results of numerical simulations as the analytic expression is only a rough estimate for the maximum value of efficiency.

We also examined the evolution of the phase space distribution of the electrons along the interaction region. Figure 3.5(a) shows the amplitude of bunching parameter $|\langle e^{-i\psi} \rangle|$ along the distance after the saturation of output power. We observed that the electrons are nicely bunched at the exit of the interaction region, where the amplitude of bunching parameter is about 0.7. Similar mechanism is observed in Fig. 3.5(b), where we have plotted the phase space distribution of electrons at the entrance and at the exit of the interaction region. We clearly see in Fig. 3.5(b) that the electrons are randomly distributed at the entrance, and become bunched at the end due to the interaction with the co-propagating surface mode. Also, due to over-bunching of the electron beam as seen in Fig. 3.5(a), there will be a double-peaked distribution of the electron phase. This will generate higher harmonics in the electromagnetic field. The interaction of the higher-order modes with the electron beam is however feeble since the phase velocity of the higher-order modes is not matched with the electron beam velocity.

3.5 Discussions and conclusion

In this chapter, we have established a novel approach for the analysis of a single slab based CFEL driven by a flat electron beam. The calculations have been performed by analyzing the reflectivity of the system for the incident evanescent wave generated by a flat electron beam

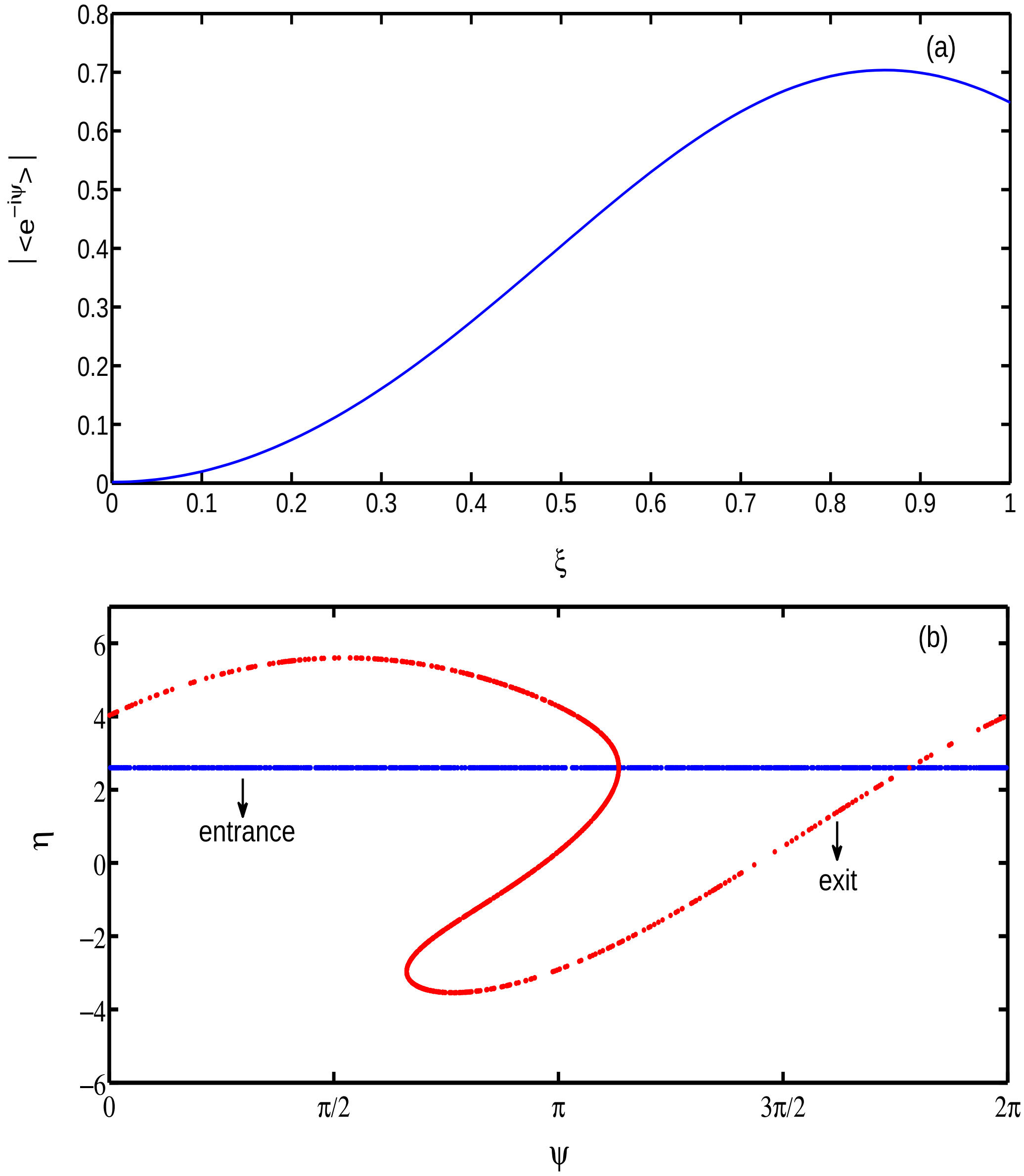

FIGURE 3.5: (a) Plot of growth of the bunching parameter along the interaction length at saturation of the power in the surface mode. (b) The phase space of electron beam at the entrance and at the exit of interaction region at saturation.

propagating very close to the dielectric surface. As discussed in the previous chapter, the amplitude reflectivity shows a singularity at a certain frequency for a particular phase velocity of the surface mode, meaning that the system supports a surface mode at this frequency. In this chapter, we have studied the interaction of this surface mode with a co-propagating electron beam by performing a Laurent series expansion of reflectivity around the singularity condition, as a function of growth rate parameter μ. The reflectivity has been expressed in terms of parameter χ and χ_1, where parameter χ is related to the growth of the surface mode and the parameter

χ_1 is related to the ac space charge field. Using this parametrization, we set up the coupled Maxwell-Lorentz equations for the system. In the small-signal, small-gain regime, we find an analytical expression for the small-signal gain, which is given by Eq. (3.35). We would like to mention here that the expression for gain obtained from our analysis, and the expression derived by Walsh *et al*. in the Ref. [82] give comparable results in the relativistic regime. In Ref. [82], the gain analysis has been done for the relativistic regime, while our analysis is applicable to both relativistic as well as non-relativistic regimes. In the small-signal, high-gain regime, we have solved the coupled Maxwell-Lorentz equations to find an analytical expression for the growth rate. Our results for the growth rate are in agreement with the hydrodynamic approach. To study the non-linear regime, we have written a computer code based on the leapfrog scheme.

We have considered the parameters used in the Dartmouth experiment [66] to perform calculations. The output power reported in the Dartmouth experiment [66] was of the order of picowatt. To get an appreciable output power, authors in Ref. [66] suggested the use of the flat electron beam to drive the CFEL. We performed the analysis with flat electron beam and obtained an output power of around 216 mW with an efficiency of about 0.7% at saturation in the oscillator configuration. Outcoupling of THz radiation can be done by putting a hole in the outcoupling mirror and the radiation power can be directed to useful experiments. Note that these calculations have been performed by ignoring the effect of attenuation in the surface mode due to the dielectric and Ohmic losses. These effects will be discussed in the next chapter.

It is important to note here that while calculating the output power, we have assumed that a fraction of the total intra-cavity power can be outcoupled through the outcoupling mirror. Total intra-cavity power is the sum of the power in the radiative mode inside the dielectric slab, and the power in the evanescent mode in the vacuum region. Although the radiation inside the dielectric may undergo total internal reflection at the ends, the power in the evanescent mode in the vacuum region can be outcoupled through a hole in the mirror, where it will get converted to useful radiative mode. Here, the hole can also be used to extract the electron beam. Although the detailed analysis of outcoupling will be an involved one, we have assumed that with a suitable design of outcoupling system, a small fraction (4 % in our case) of the intra-cavity power can be outcoupled through the downstream mirror. In order to model this situation in a simple manner, we have assumed that the downstream mirror is semi-transparent with 98 % reflectivity in the field amplitude. The upstream mirror in our analysis is assumed to be transparent to the electron beam. In practice, the electron beam is injected by putting a hole in the upstream mirror, and it is not 100 % reflective, as assumed in our calculations. Also, due to the presence of hole in the mirrors, field inside the cavity will contain higher order modes, which are not considered in our model. These are some of the approximations used in our analysis to model the oscillator configuration.

Our overall analysis is built up on the earlier analysis of SP-FEL [88], where the parameters χ and χ_1 are obtained numerically from the Laurent expansion of reflectivity of the reflection grating system around the singularity. The expression for power in the surface mode was obtained in terms of the χ parameter using the energy conservation principle in a way discussed in Sec. 3.3. As discussed in Chapter 2, it is not possible to derive a simple expression for power in the surface mode by integrating the Poynting vector in the SP-FEL since a reflection grating is a complex electromagnetic system and has infinite number of space harmonics. Thus, the power calculation in terms of χ parameter could not be cross checked with the expression derived by integration of Poynting vector in Ref. [88]. On the other hand, for the case of a CFEL, it has been possible to derive an analytical expression for the power by integrating the Poynting vector as discussed in Chapter 2 since a dielectric placed on the conducting surface is a much simpler system compared to a reflection grating. We have thus been able to check the analytical expression of power calculated in terms of χ parameter with that of that using the Poynting vector, and confirmed that the formulation in terms of the χ parameter is correct.

To conclude, we have presented an analysis for the working of a single slab based CFEL by studying the singularity in the reflectivity of the dielectric slab. We have set up the single particle based coupled Maxwell-Lorentz equations, taking into account the evanescent nature of surface mode and also the ac space charge field. For the conventional undulator based FELs [85] and for the SP-FELs [88], this approach has already been very successful, and by extending this approach to the CFELs, we have stepped forward towards having a unified theory for all FELs.

Chapter 4

Diffraction and attenuation effects in Čerenkov and Smith-Purcell FELs

In Chapter 2, we presented a detailed two-dimensional (2D) analysis of the surface mode supported in a single slab configuration of the CFELs. The surface mode exponentially decays in the direction perpendicular to the dielectric surface, i.e., the x-direction, and propagates in the z-direction, which is the direction of the propagation of the electron beam. Under the 2D approximation, the surface mode was assumed to have a translational invariance along the horizontal direction, i.e., the y-direction, and it was therefore non-localized in the (y, z) plane. Using the results of 2D surface mode analysis from Chapter 2, we developed a 2D non-linear analysis to study the beam-wave interaction in a single slab based CFEL driven by a flat electron beam in Chapter 3. The electron beam in this analysis was assumed to have an infinite width along the horizontal direction and a vanishing thickness in the vertical direction. Analytical expressions for the small-signal gain and growth rate of CFEL were derived for this case. Although an arbitrary width Δy was chosen for the electron beam, the model presented in Chapter 3 essentially describes the interaction of a surface current and a surface wave having infinite extent along the y-direction. In a realistic situation, however, the electron beam size as well as the radiation beam size will be finite along the y-direction. Size of the radiation beam will increase due to diffraction. This will affect the overlap of the radiation beam with the electron beam, resulting in reduction of the small-signal gain, as well as the saturated power obtained in the device. For an effective beam-wave interaction, one has to ensure that the electron beam envelope remains inside the radiation beam envelope over the entire interaction region. A realistic estimate of the radiation beam size requires the inclusion of diffraction effects and a detailed three-dimensional (3D) analysis of the surface mode.

One way to invoke 3D effects is to solve the electromagnetic Helmholtz wave equation by considering the diffraction in the surface mode. Andrew and Brau [98] used this technique to study the effect of diffraction on the growth rate in a single slab based CFEL. Growth rate was found to be decreasing on the accounts of the 3D effects as compared to the 2D analysis. The analysis in Ref. [98] is however performed for uniform electron beam having infinite vertical size, and hence, is not very useful to obtain the electron beam parameters in the vertical direction, which are critical to improve the performance of the system.

We have followed a different approach to consider the diffraction effects, where a 3D surface mode is constructed by combining plane waves propagating along different directions in the (y, z) plane with suitable weight factor. The surface mode constructed in this way is localized in the horizontal direction and represents a realistic situation. The technique of localization of electromagnetic modes by using superposition of plane waves is a standard technique in laser optics [110, 140, 141]. Kim and Kumar [78, 90] used this approach to study the diffraction effects in SP-FELs, and worked out the requirements on the electron beam parameters for a THz SP-FEL [78, 89]. They observed that a SP-FEL system can produce copious amount of THz radiation if a specially designed electron beam with a flat transverse profile that allows the beam to travel very close to the grating surface, is used to drive the system. They also pointed out that these criteria were not met in the earlier experimental studies of SP-FELs [69]. As a consequence, the observed output power in these experiments has been low. Observation of low output power has also been mentioned in experimental studies on single slab based CFELs at ENEA Frascati Centre [63, 64] and at the Dartmouth college[65, 66]. In this chapter, we have examined the conditions under which performance of the CFELs can be improved. For this purpose, we have extended the work of Kim and Kumar [78, 90] on SP-FELs to CFELs, and determined the requirements on the electron beam parameters, i.e., beam size, beam emittance, and beam current for the successful operation of a THz CFEL.

Another important effect that can deteriorate the system performance is the attenuation of the surface mode due to the losses present in the system. In a CFEL, the amplitude of the surface mode attenuates as it propagates inside a lossy dielectric slab supported over a metallic structure having finite conductivity. It is well known to the microwave community that the effect of attenuation increases with the frequency of the guided surface modes in dielectric-metal hybrid structures [122]. Despite this, the existing model on THz CFELs have always neglected such deleterious effect by assuming it to be insignificant. In our analysis, we have found that the dielectric and Ohmic losses can even prevent a CFEL from lasing, especially in the low-gain regime. For a low gain CFEL oscillator system, the small-signal gain has a cubic dependence on the length L [142]. Hence, one would like to increase the interaction length to obtain a higher gain [142]. However, at higher interaction length, attenuation effects increase as the power in the surface mode decays by a factor of $e^{-4\alpha L}$ for a round trip, where α is the field attenuation coefficient. Thus one needs to optimize the system length by considering the attenuation effects due to the dielectric and Ohmic losses present in the system. The calculations for the attenuation coefficient due to the dielectric losses and Ohmic losses were presented in Chapter 2 for a single slab based CFEL. In this chapter, we have used these results to perform a detailed optimization study for a real world THz CFEL.

Considering the effects of attenuation and diffraction, we have established 3D coupled Maxwell-Lorentz equations for the CFELs. Following an approach similar to the approach discussed for CFELs, we have set up the 3D coupled Maxwell-Lorentz equations for the SP-FELs too. Although for the case of SP-FELs, the diffraction and attenuation effects have been studied in detail in Refs. [78, 89, 90, 93], a detailed derivation for the 3D coupled Maxwell-Lorentz equations was not presented, which is provided in this chapter. While discussing the 3D analysis of the CFELs and SP-FELs, we have highlighted important differences between the CFELs and SP-FELs in terms of diffraction effects, and explained the fundamental reason for these differences.

This chapter is organized as follows. In Sec. 4.1.1, we have discussed the effect of attenuation due to the dielectric losses and Ohmic losses on the performance of a single slab based CFEL. We determine the properties of the surface mode, including the effect of diffraction in Sec. 4.1.2. Next, in Sec. 4.1.3, we set up the 3D coupled Maxwell-Lorentz equations for a CFEL system. Considering the effect of diffraction, the requirements on the quality of electron beam for the successful operation of such devices become very stringent, which is discussed in Sec. 4.2 for the case of a CFEL. We also discuss the techniques to relax these stringent requirements, and also the methods for production of electron beam of required quality in the same section. In Sec. 4.3, we perform an optimization study of a THz CFEL to show that with achievable beam quality, it should be possible to generate copious amount of THz radiation in this device, even after including the 3D effects and the effects due to attenuation. Next, in Sec. 4.4.1, we describe essential features of the 3D surface mode analysis in SP-FELs [78, 89] and set up the 3D coupled Maxwell-Lorentz equations for the SP-FEL system. Here, we also highlight the differences in the analyses of a SP-FEL and a CFEL. Finally, we discuss the results and conclude our analysis in Sec. 4.5.

4.1 Attenuation and diffraction effects in Čerenkov FELs

4.1.1 Attenuation effects

In this section, we will consider the effect of attenuation of the surface mode on the performance of a single slab based CFEL. The field attenuation coefficient α is the sum of the dielectric attenuation coefficient α^d and the Ohmic attenuation coefficient α^c, which can be obtained by adding the results of Eqs. (2.29) and (2.31), as discussed in Chapter 2. We find the following expression for the total attenuation coefficient of the surface mode in a CFEL:

$$\alpha = \frac{\gamma_R k_0 Z_0 \tan\delta(2-\epsilon\beta_R^2) + \beta_R \epsilon^2 k_0 (1+a^2)(2R_s + \beta_R k_0 Z_0 d \tan\delta)}{2Z_0[\gamma_R(1+\epsilon^2 a^2) + \epsilon k_0 d(1+a^2)]}, \tag{4.1}$$

where $\tan\delta$ represents tangent loss of the dielectric medium, $R_s = \sqrt{\mu_0\omega/2\sigma_{cond}}$ is surface resistance of the metal, μ_0 is the permeability of the free-space and σ_{cond} represents conductivity of the metal.

In a CFEL based on a positive refractive index dielectric, the surface mode will have a positive group velocity v_g and will be amplified as it co-propagates with the electron beam in the positive z-direction [98]. The longitudinal component of the electric field of a 2D non-localized surface mode supported in a CFEL is given by

$$E_z(x, z, t) = Ee^{i(k_0 z-\omega t)}e^{-\Gamma x}, \tag{4.2}$$

where E is the amplitude of the field at the location of the electron beam i.e., $x = 0$, k_0 is the propagation wavenumber in the z-direction, and Γ is the attenuation constant due to evanescent nature in the x-direction. The evolution of the amplitude E of the surface mode is mathematically described by Eq. (3.26), which after including the attenuation of the surface mode can be written as:

$$\frac{\partial E}{\partial z} + \frac{1}{\beta_g c}\frac{\partial E}{\partial t} = \frac{-Z_0\chi}{2\beta_R\gamma_R}\frac{dI}{dy}e^{-2\Gamma h}\langle e^{-i\psi}\rangle - \alpha E, \tag{4.3}$$

Here, the subscript R is meant for the resonant particle having velocity same as the phase velocity of the surface mode, $\psi = k_0 z - \omega t$ is the electron phase, and the second term on the right hand side represents attenuation of the surface mode due to losses present in the dielectric and metallic structures. It should to be noted that in the oscillator configuration, the electromagnetic field will be attenuated as it propagates from the beginning to the end of the dielectric slab, and also during its backward propagation from the end point to the beginning of the dielectric slab. This results in a decay in the power of the surface mode by a factor of $e^{-4\alpha L}$ during a round trip. The input field for the next pass is $e^{-\alpha L}$ times the field in the previous pass, which is reflected from the mirror placed at the end point. The dynamical field equation given by Eq. (4.3) together with the Lorentz equations of motion given by Eqs. (3.18) and (3.19) need to be solved under the above mentioned conditions to obtain the saturated power in the non-linear regime.

In the linear regime, the coupled Maxwell-Lorentz equations were solved without taking the effect of attenuation in Chapter 3 and an analytical expression was obtained for the small-signal gain, which is given by Eq. (3.35). Taking into account the effect of attenuation, there will be a single trip loss given by $(1 - e^{-2\alpha L})$ in addition to the gain described by Eq. (3.35). Note that in these calculations, we have assumed the losses to be small, i.e., $2\alpha L \ll 1$. Taking the effect of attenuation, the growth rate of a CFEL system can be written as $\mu - \alpha$, where μ is given by Eq. (3.43). For an optimum performance of the system, one has to maximize the net gain and the net growth rate of the system. The gain and the growth rate will also reduce due to diffraction. This is because of the partial overlap of the diffracting radiation beam and the co-propagating electron beam. To estimate the size of the diffracting radiation beam, we need to perform a full 3D analysis of the surface mode, which is presented in the following section.

4.1.2 Diffraction effects

Now, we consider the effect of diffraction of the surface mode in the y-direction and construct the 3D localized surface mode supported in a single slab based CFEL system. As shown in Fig. 4.1, the dielectric slab is an open structure in the y-direction. Hence, the electromagnetic surface mode supported in this configuration is expected to behave like a freely propagating radiation beam and will undergo diffraction in the (y, z) plane. The diffracting electromagnetic surface mode can be constructed by combining plane waves propagating at different angles in the (y, z) plane, with suitable weight function $A(k_y)$ in k_y as

$$E_z(x, y, z, t) = \frac{1}{\sqrt{2\pi}} \int dk_y A(k_y) e^{i(k_z z - \omega t)} e^{ik_y y} e^{-\Gamma' x}. \tag{4.4}$$

Here, E_z is the longitudinal electric field, Γ' is the attenuation constant due to evanescent nature in the x-direction, when the wave is propagating in the (y, z) plane with wavenumbers k_y and

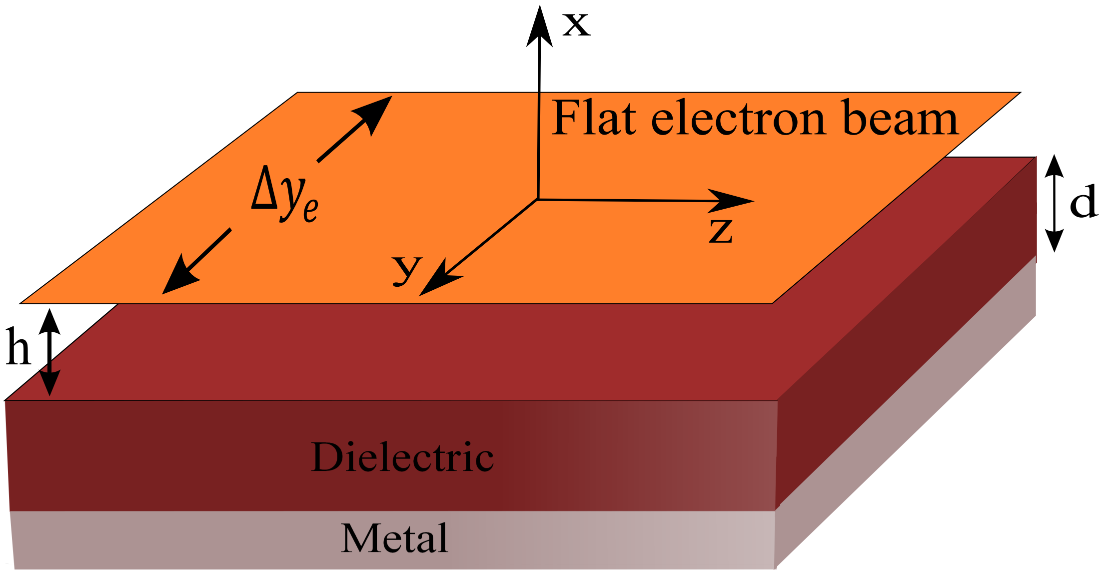

FIGURE 4.1: Schematic of a 3D configuration of CFEL driven by a flat electron beam.

k_z in the y-direction and the z-direction respectively. The surface mode constructed in this way will have a variation along the y-direction and will represent the generalized case of surface mode given by Eq. (4.2). We now invoke the paraxial wave approximation, i.e., $k_y \ll k_z$. Considering this, the electromagnetic surface mode given by Eq. (4.4) is mainly propagating in the z-direction and undergoes diffraction in the y-direction.

In the CFEL based on an uniform and isotropic dielectric medium, the optical properties of the surface mode will remain invariant under any arbitrary rotation of the propagating wave vector in the (y, z) plane. In this situation, the 2D dispersion relation of the surface mode propagating along the z-axis can be easily generalized to the case where the surface mode is propagating along any arbitrary direction in the (y, z) plane. For a given frequency ω, if the phase velocity of the surface mode propagating along the z-axis is v, we obtain the following relation between ω, k_y and k_z for a surface wave propagating in the (y, z) plane:

$$\omega = v\sqrt{k_y^2 + k_z^2}. \tag{4.5}$$

The wavenumber in the longitudinal direction can be written as $k_z = k_0 + \Delta k$, where $k_0 = \omega/v$. By using the paraxial approximation ($k_y \ll k_z$), we obtained the following expression for k_z:

$$k_z = k_0\left(1 - \frac{k_y^2}{2k_0^2}\right). \tag{4.6}$$

Note that due to the property of isotropy in the (y, z) plane, $\Gamma' = \Gamma$. We can substitute Eq. (4.6) for k_z and $\Gamma' = \Gamma$ in Eq. (4.4) to obtain the localized surface mode in a CFEL as

$$E_z(x, y, z, t) = \frac{e^{-\Gamma x} e^{i(k_z z - \omega t)}}{\sqrt{2\pi}} \int \underbrace{A(k_y) e^{-ik_y^2 z/2k_0}} e^{ik_y y} dk_y. \tag{4.7}$$

Above expression for the longitudinal field appears as a Fourier transform in k_y of the underbraced term. If we choose $A(k_y) = e^{-k_y^2/2\sigma_{k_y}^2}$, the integration in Eq. (4.7) is Fourier transform of a Gaussian function. Gaussian functions belong to the distinct family of functions which are self-Fourier functions [143]. Hence, the resultant of integration in Eq. (4.7) is also a Gaussian function, and we obtain the intensity for the localized Gaussian mode at $x = 0$ as:

$$\text{Intensity} : E_z \times E_z^* \propto e^{-\frac{y^2}{2} \frac{2\sigma_{k_y}^2}{1+\sigma_{k_y}^4 z^2/k_0^2}}. \tag{4.8}$$

We want to emphasize that this approach can easily be generalized for higher order modes by taking Gauss-Hermite functions for $A(k_y)$, which are also self-Fourier functions and will give higher order Gauss-Hermite modes.

Next, we analyze the transverse properties of the localized surface mode. Using Eq. (4.8), we obtain an expression for the variation of rms optical beam size σ_y with z as

$$\sigma_y^2(z) = \sigma_y^2(0)\left(1 + \frac{z^2}{Z_R^2}\right), \tag{4.9}$$

Here, $\sigma_y(0)$ is the rms optical beam waist at $z = 0$ and Z_R is the Rayleigh range, which is obtained as:

$$Z_R = \frac{4\pi\sigma_y^2(0)}{\beta_R\lambda}. \tag{4.10}$$

Another quantity of interest is the product of rms beam waist size and rms angular divergence σ_θ, which is given by

$$\sigma_y(0) \times \sigma_\theta = \frac{\beta_R\lambda}{4\pi}. \tag{4.11}$$

Note that above expressions are similar to the standard expressions for the case of Gaussian mode propagating in free-space except that λ is replaced with $\beta_R\lambda$. It is well known in optics that for a Gaussian mode propagating in a uniform, isotropic medium, λ gets replaced with λ/n in the above formulas, where n is the refractive index of the medium. Using $n = c/v_p$, where $v_p = \beta_R c$ is the phase velocity of light in the medium, λ/n is same as $\beta_R\lambda$. This is thus similar to our results obtained for a surface mode supported by a uniform, isotropic dielectric slab in a CFEL.

The present analysis for the localized surface mode will be used in Sec 4.2 to estimate the required parameters of the electron beam for efficient working of the CFEL.

4.1.3 3D Maxwell-Lorentz equations

Next, we will extend our 2D analysis of the beam-wave interaction in a CFEL for the 3D case by setting up the 3D Maxwell-Lorentz equations. For this purpose, we will perform the analysis of the 3D localized surface mode given by Eq. (4.4) in terms of its Fourier components, which are evolving due to their interaction with the corresponding Fourier components of the current density vector of a co-propagating electron beam. We start with the generalized expression for the sinusoidal component of the beam current density: $\mathcal{J} = J(x,y)e^{i(k_0 z-\omega t)}\langle e^{-i\psi}\rangle$+c.c., where $J(x,y)$ is the dc current density, $\langle e^{-i\psi}\rangle$ indicates bunching of the electron beam due to interaction with the surface mode and c.c. represents the complex conjugate of quantity written on the right hand side. We can express the beam current density into its Fourier components as:

$$\mathcal{J} = \frac{e^{i(k_z z-\omega t)}}{\sqrt{2\pi}} \int \underbrace{\widetilde{J}(x,k_y) e^{ik_y^2 z/2k_0} \langle e^{-i\psi} \rangle}\, e^{-ik_y^2 z/2k_0} e^{ik_y y} dk_y + \text{c.c.}. \tag{4.12}$$

Note that we have cast the integral in a form such that the Fourier component of the electromagnetic field can be understood to be evolving with the Fourier component of the electron beam current density. For further calculations, we consider a flat electron beam for which $J(x,y) = j(y)\delta(x)$ and its Fourier transform is written as $\widetilde{J}(x,k_y) = \widetilde{j}(k_y)\delta(x)$. The longitudinal component of the electromagnetic field that evolves due to interaction with this current density is given by:

$$E_z(x,y,z,t) = \frac{e^{-\Gamma x} e^{i(k_z z-\omega t)}}{\sqrt{2\pi}} \int \underbrace{A(k_y,z,t)}\, e^{-ik_y^2 z/2k_0} e^{ik_y y} dk_y + \text{c.c.}. \tag{4.13}$$

The amplitude $A(k_y,z,t)$ of the surface mode will evolve due to interaction with the co-propagating electron beam and we have assumed it to be a slowly varying function of z and t. The beam-wave interaction mechanism in a CFEL system, which describes the evolution of the 2D surface mode and the dynamics of the electron beam in the presence of this surface mode, has been discussed in detail in Chapter 3. Now, by following the same approach and realizing that the underbraced term in Eq. (4.13), which is the amplitude of the Fourier component of the electromagnetic field, is evolving due to interaction with the amplitude of the corresponding Fourier component of the current density denoted by the underbraced terms in Eq. (4.12), we obtain the following time dependent differential equation for the evolution of $A(k_y,z,t)$:

$$\frac{\partial A}{\partial z} + \frac{1}{\beta_g c}\frac{\partial A}{\partial t} = \frac{-Z_0 \chi}{2\beta_R \gamma_R} \widetilde{j}(k_y) e^{ik_y^2 z/2k_0} e^{-2\Gamma h} \langle e^{-i\psi} \rangle - \alpha A. \tag{4.14}$$

By taking Fourier transform with respect to k_y in above equation and using the fact that $Ae^{-ik_y^2 z/2k_0}$ is the Fourier transform of the longitudinal surface field E, we obtain the following dynamical equation for the 3D surface mode:

$$\frac{\partial E}{\partial z} - \frac{i}{2k_0}\frac{\partial^2 E}{\partial y^2} + \frac{1}{\beta_g c}\frac{\partial E}{\partial t} = \frac{-Z_0\chi}{2\beta_R\gamma_R}\frac{dI}{dy}e^{-2\Gamma h}\langle e^{-i\psi}\rangle - \alpha E. \tag{4.15}$$

Here, E is the amplitude of the longitudinal field E_z and dI/dy is the linear current density of the flat beam. Note that while deriving the above equation, we have assumed dI/dy to be constant, although it is a function of x and y. The second term on the left hand side of above equation represents diffraction of the surface mode and allows us to study the transverse profile of the optical beam. In an approximate way, the effect of partial overlap between the electron beam and optical mode can be considered in the numerical solutions of 2D Maxwell-Lorentz equations by writing the linear current density dI/dy as $I/\Delta y$, where Δy is the electron beam width, and is replaced with the effective optical beam width Δy_e. The effective optical mode width Δy_e here has to be chosen by suitably matching the optical beam size given by Eq. (4.9) and the corresponding electron beam size. To find the electron beam size in the horizontal direction, we need to give a detailed description of the transverse profile of the electron beam, which is discussed in the following section.

4.2 Electron beam requirements and its production for the Čerenkov FELs

In this section, based on the analysis of the surface mode presented in Sec. 4.1.2, we will work out the electron beam requirements for successful operation of a CFEL. To perform these calculations, we will closely follow the approach given in Refs. [78, 89], where the requirements on the electron beam parameters have been determined for the successful operation of a SP-FEL system. Before discussing the transverse profile of the electron beam, we will first review some of the properties of the electron beam in phase space. The electron beam distribution in the four dimensional phase space (x, φ, y, ϕ) is assumed to be Kapchinskij-Vladimirskij (KV) distribution [144], where x and y are the vertical and horizontal coordinates respectively, and

φ and ϕ represents vertical and horizontal angles, respectively. The electron beam distribution is assumed to have half-widths $(\Delta x, \Delta\varphi, \Delta y, \Delta\phi)$ at the middle of the dielectric slab and the half widths are two times the rms values $(\sigma_x, \sigma_\varphi, \sigma_y, \sigma_\phi)$. Thus, $\Delta x = 2\sigma_x$, $\Delta\varphi = 2\sigma_\varphi$, $\Delta y = 2\sigma_y$ and $\Delta\phi = 2\sigma_\phi$. The geometric rms emittance in the y-direction is therefore given by $\boldsymbol{\varepsilon}_y^0 = (1/4)\Delta y \Delta\phi$. The Courant-Snyder envelope β_y, also known as the beta function in the y-direction, is defined as $\beta_y = \sigma_y^2/\boldsymbol{\varepsilon}_y^0$. Similar quantities are defined with the subscript x in the x-direction.

Let us first look for the requirements on the electron beam in the y-direction. The product of rms beam size $\sigma_y(o)$ and divergence σ_θ for the surface mode supported in the CFEL is given by $\beta_R\lambda/4\pi$. Now to ensure that electron beam envelope is within the envelope of optical beam, the rms unnormalized emittance is required to be less than this product. Applying this for the case of the CFEL, we get

$$\boldsymbol{\varepsilon}_y \leq \frac{\beta_R^2\gamma_R\lambda}{4\pi}, \tag{4.16}$$

where $\boldsymbol{\varepsilon}_y = \beta_R\gamma_R\boldsymbol{\varepsilon}_y^0$ is the normalized beam emittance in the y-direction. Next, the half width Δy of the electron beam, which is taken the same as the half width $2\sigma_y$ of the optical beam, is chosen by requiring that the Rayleigh range Z_R is equal to the interaction length L. This choice of Z_R ensures that the variation in the rms optical beam size over the interaction length is within 10%, as can be seen by putting $z = L/2$ ($z = 0$ corresponds to middle of the dielectric slab and $z = \pm L/2$ corresponds to the end points), and $Z_R = L$ in Eq.(4.9). Now, by using Eq. (4.10), we find $\sigma_y = \sqrt{\beta_R\lambda Z_R/4\pi}$ and by inserting it in the above-mentioned condition, we obtain

$$\Delta y = \sqrt{\frac{\beta_R\lambda L}{\pi}}. \tag{4.17}$$

Let us now discuss the required electron beam parameters in the x-direction. In the view of the exponential factor $e^{-2\Gamma h}$ in Eq. (3.35), where $\Gamma = 2\pi/\beta_R\gamma_R\lambda$, it is desirable that the height h of the electrons should satisfy $h \leq 1/2\Gamma$ for sufficient beam-wave interaction. Assuming that the electron beam is propagating over the dielectric slab such that its centroid is at height h and its lower edge just touches the dielectric surface, we can take the half-width Δx of the electron beam same as $h = 1/2\Gamma$, and obtain

$$\Delta x = \frac{\beta_R \gamma_R \lambda}{4\pi}. \tag{4.18}$$

This implies that rms electron beam size $\sigma_x = \Delta x/2 = \beta_R \gamma_R \lambda/8\pi$ at the middle of the dielectric slab. The rms beam size in the x-direction at the end of the dielectrics slab is given by $\sqrt{\varepsilon_x^0 \beta_x [1 + (L/2\beta_x)^2]}$ [78]. In order to ensure that the variation in σ_x over the interaction length $\lesssim 10\%$, we require $\beta_x \geq L$. Using these two conditions and the relation that $\varepsilon_x^0 = \sigma_x^2/\beta_x$, we obtain

$$\varepsilon_x \leq \frac{\beta_R^3 \gamma_R^3 \lambda^2}{64\pi^2 L}, \tag{4.19}$$

where $\varepsilon_x = \beta_R \gamma_R \varepsilon_x^0$ is the normalized beam emittance in the x-direction. The condition on the normalized beam emittance ε_x comes out to be very stringent. As discussed in detail in the next section, a flat electron beam with transverse emittance ratio, $\varepsilon_y/\varepsilon_x \simeq 1000$ is required for the operation of a practical THz CFEL. This value is roughly 10 times higher than the value achieved in a recent experiment [145, 146].

The stringent requirement on the emittance of a flat electron beam can be relaxed by introducing an external focusing by either using a wiggler field [147, 148] or by using a solenoid field [149–151]. Details of the two schemes are described in Ref. [89] for the case of a SP-FEL. Both the schemes are applicable for the case of the CFEL also. In the next two subsections, we will discuss these two schemes for a CFEL system.

4.2.1 Focusing of a flat electron beam by using a wiggler field

A flat electron beam can be focused in both the vertical and horizontal planes by using a wiggler field, as discussed and demonstrated by Booske *et al.* [152]. A flat electron beam for this

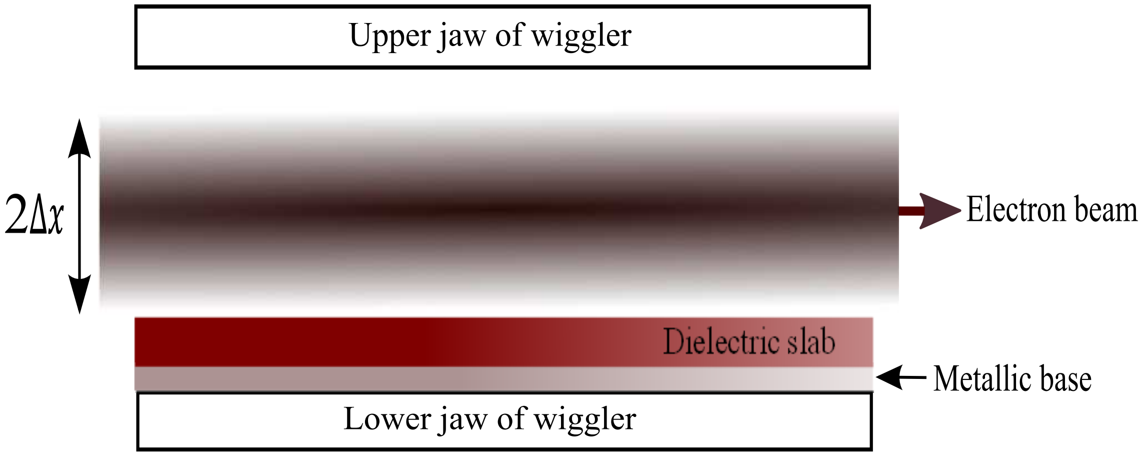

FIGURE 4.2: Schematic of external focusing in a Čerenkov FEL using a wiggler.

scheme can be generated by a novel phase space technique [78, 153], in which a round electron beam is first produced from a cathode placed in an axial magnetic field, and then the angular momentum of the beam is removed by using a set of quadrupoles. This gives a flat electron beam with transverse emittance ratio [78]:

$$\frac{\varepsilon_y}{\varepsilon_x} = \left(\frac{eB}{mc}\frac{r_t^2}{4\varepsilon_I}\right)^2, \tag{4.20}$$

where B represents the magnetic field at the cathode, r_t is the radius of the thermionic cathode, and $\varepsilon_I = \sqrt{\varepsilon_x \varepsilon_y}$ is the initial beam emittance of the round beam. The radius r_t is related to the initial emittance as $r_t = 2\varepsilon_I / \sqrt{k_B T / mc^2}$ [78], where k_B is Boltzmann's constant and T is the absolute temperature of the thermionic cathode. The magnetic field required to produce an electron beam with the desired transverse emittance ratio is evaluated by using Eq. (4.20) as $B = k_B T / e\varepsilon_x c$. Note that B is independent of ε_y. The current density J_t at the cathode for a given beam current I is $J_t = I/\pi r_t^2$ [78].

In Fig. 4.2, we have shown the schematic for focussing of the above mentioned flat beam in a CFEL by using a wiggler with a parabolic pole shape. In the presence of a wiggler magnetic field, the electron beam will be focused in both x- and y-directions. We need to find an electron beam matched to the focusing forces such that the beam size remains minimum and nearly uniform along the wiggler length. By neglecting the space charge effect in the envelope equation, the matched rms beam sizes in the x- and y-directions are obtained as [89]:

$$\sigma_{x,y} = 2^{1/4}\sqrt{\frac{\varepsilon_{x,y}}{a_u k_{x,y}}}. \tag{4.21}$$

Here, $a_u = eB_u/k_u mc$, B_u represents the peak value of the magnetic field in the x-direction, along the z-axis, $k_u = 2\pi/\lambda_u$, λ_u is the wiggler period, and k_x and k_y represent spatial frequency of the wiggler field in the x- and the y-direction respectively. We require $k_u^2 = k_x^2 + k_y^2$ to satisfy the Maxwell equations. In Eq. (4.21), we choose $\sigma_y = 1/2\Delta y$ and $\sigma_x = 1/2\Delta x$, where Δy and Δx are given by Eqs. (4.17) and (4.18) respectively, and find the appropriate value of a_u, k_x and k_y for a given values of emittances $(\varepsilon_x, \varepsilon_y)$, such that the beam sizes are matched inside a wiggler and thus maintain a constant size throughout the wiggler. For a typical set of parameters of a CFEL, the focusing requirement in the vertical direction is very strong as compared to the horizontal direction. We can therefore choose $k_y = 0$ and $k_x = k_u$. It is clear from Eq. (4.21) that for a matched beam size, one can tolerate a larger vertical emittance by choosing a higher value of the peak wiggler magnetic field B_u. This helps us to relax the stringent requirement given by Eq. (4.19). Note that in case of external focusing in the vertical direction, we do not need to satisfy Eq. (4.19).

4.2.2 Focusing of a flat electron beam by using a solenoid field

In the second scheme, a solenoid magnetic field is used to focus a low energy flat electron beam. The required flat beam is generated by using an elliptically shaped, planar thermionic cathode with major axis $\Delta y_c = \Delta y$ and minor axis $\Delta x_c = \Delta x$. The normalized thermal emittances for the thermionic cathode are given by $(\varepsilon_x, \varepsilon_y) = 0.5(\Delta x_c, \Delta y_c)\sqrt{k_B T/mc^2}$, and current density at cathode, corresponding to current I, is given by $J_c = I/\pi\Delta x_c\Delta y_c$ [78]. For generating a flat beam, the vertical dimension of the cathode is very small compared to the horizontal dimension, and such a cathode is called a line cathode. The line cathode together with the dielectric slab is immersed inside the solenoid such that the electron beam is generated in the uniform field region of the solenoid. On the contrary, if line cathode is placed outside the solenoid in the field-free region then the flat electron beam generated from such line cathode starts rotating as it enters into the solenoid field. To avoid the rotation of flat beam as it propagates over the dielectric slab, both the line cathode and the dielectric slab are placed inside the solenoid. The solenoid field strength required to focus a flat beam can be evaluated with the condition that the Larmor radius should be much smaller than the vertical rms beam size σ_x [89], which gives us the following expression for the required axial magnetic field $B(0)$ near the cathode [89]:

$$B(0) \gg \frac{mc\boldsymbol{\varepsilon}_x}{e\sigma_x^2}. \tag{4.22}$$

The nonuniformity in the longitudinal on-axis magnetic field gives rise to a rotation θ to the flat beam, which is given by [89]

$$\theta(z) = \frac{z\omega_L}{3\beta_R c}\frac{\Delta B(z)}{B(0)}, \tag{4.23}$$

where $\Delta B(z) = B(z) - B(0)$ and ω_L is the Larmor frequency. Here, it is assumed that the cathode is placed at the centre of the solenoid ($z = 0$), where the field is maximum, and the variation of the quantities in the radial direction is assumed to be very slow. We have to ensure that the electron beam does not rotate significantly such that the flat beam nature is preserved.

Clearly, both the external focusing techniques allow us to tolerate larger emittance of the electron beam. A large emittance of the electron beam, however, gives rise to a spread in the trajectory angle θ_t, and therefore in the longitudinal velocity given by

$$\frac{\Delta\beta_R}{\beta_R} = 1 - \cos\theta_t. \tag{4.24}$$

Using $(1 - \cos\theta_t) \simeq \theta_t^2/2$ and $\theta_t^2 = \boldsymbol{\varepsilon}_x^2/\beta_R^2\gamma_R^2\sigma_x^2$ in the above equation, we obtain

$$\frac{\Delta\beta_R}{\beta_R} \sim \frac{\boldsymbol{\varepsilon}_x^2}{2\beta_R^2\gamma_R^2\sigma_x^2}. \tag{4.25}$$

Focusing in the y-direction will also give similar contribution to the velocity spread. The effect of the longitudinal velocity spread is equivalent to an effective energy spread. The deleterious effect of energy spread become prominent as we increase the interaction length to achieve a higher gain. The maximum energy spread that can be tolerated in a CFEL corresponds to the phase mismatch of π between the electrons and the co-propagating surface mode at the exit of the interaction region, or equivalently $\Delta\beta_R L/\beta_R = \beta_R\lambda/2$. This condition gives us the maximum value of emittance which can be tolerated by the system as:

$$\varepsilon_x < \sigma_x \sqrt{\frac{\beta_R^3\gamma_R^2\lambda}{L}}. \tag{4.26}$$

With the external focussing, we can increase the length L of the dielectric slab to obtain a higher gain. However, increase in L value will restrict the maximum emittance that can be tolerated, as indicated by Eq. (4.26). We need to choose an optimum value of L for which the deleterious effects due to the energy spread are significantly less.

Finally, we summarize the procedure for optimization of the focusing strength and the emittance as follows: we first choose the vertical beam size from Eq. (4.18) for the given parameters of a CFEL, and then we choose the maximum focussing strength by using Eq. (4.21) (in the case of wiggler focusing) or using Eq. (4.22) (in the case of solenoid focusing) to attain the maximum tolerance on the vertical emittance, keeping in mind that the constraint is given by Eq. (4.26).

4.3 Optimization study of a THz Čerenkov FEL

In this section, we will perform an optimization study of a THz CFEL in accordance with the analysis given in the earlier sections. For an example case of a practical CFEL, we take the parameters of the Dartmouth experiment [66] discussed earlier in Chapters 2 and 3, where a CFEL device was tested with an operating frequency of 0.1 THz by using an electron beam having 1 mA beam-current and 30 keV (β_R = 0.33) beam-energy. Two different materials, GaAs (ϵ = 13.1) [120] and sapphire (ϵ varying from 9.6 to 10.0) [119] were used for the dielectric slab having slab thickness 350 μm, and a silver polished copper metal was used to support the dielectric slabs. Among the above-mentioned dielectric materials, we have considered GaAs in our calculations for the reasons discussed earlier in Chapter 2. GaAs has a tangent loss $\tan\delta = 2 \times 10^{-4}$ at room temperature, i.e., at 300 K. For these parameters, we find $\lambda = 2.7$ mm (operating frequency = 0.1 THz), $\beta_g = 0.23$ and $\chi = 181$ per m. The conductivity of silver metal at 300 K is given by $6.3 \times 10^7/\Omega$-m [154], for which the Ohmic attenuation coefficient, α^c = 2.5 m^{-1}, as calculated by using Eq. (2.31). The dielectric attenuation coefficient is calculated by using Eq. (2.29) as $\alpha^d = 0.9$ m^{-1} at 300 K. Note that the dielectric losses are less compared to the Ohmic losses. In the context of 3D analysis, the linear current density dI/dy, which is needed to evaluate the gain and the growth rate of the system by using Eqs. (3.34) and (3.43) respectively, can be interpreted as the peak value at the middle of the electron beam distribution. We obtain the following expression for the linear current density [78]

$$\frac{dI}{dy} = \frac{I}{\pi\Delta y/2}, \tag{4.27}$$

for the KV distribution discussed in Sec. 4.3. The effective electron beam width in the y-direction is thus taken as π times the rms optical beam waist size $\sigma_y(0)$. We denote the effective electron beam width in the y-direction as Δy_e, which we have evaluated by using Eq. (4.17) as $\Delta y_e = \sqrt{\pi\beta_R\lambda L/4}$. The centroid of the electron beam is taken at height $h = \Delta x = \beta_R\gamma_R\lambda/4\pi$. The length of the dielectric slab was taken around 1 cm in the Dartmouth experiment. Note that in the previous chapter a larger interaction length (15 cm) was considered to achieve a reasonable gain, i.e., 56%. However, If we include the effect due to attenuation, we find a round trip loss $(1 - e^{-4\alpha L})$ of around 87% for this length, which is higher than the gain and the system is unable to lase in these conditions. By taking the system length, i.e., $L = 1$ cm, we find the small signal gain of around 0.04%, which is also too low to overcome the losses present in the system as the round trip loss is around 13.0%. To get an appreciable gain, we take $L = 5$ cm and increase the electron beam current from 1 mA to 35 mA. With the increased length, power loss due to attenuation also increases. To reduce the attenuation, we kept the silver metal and the dielectric slab at low temperature i.e., at 77 K, which is boiling point of liquid nitrogen. At

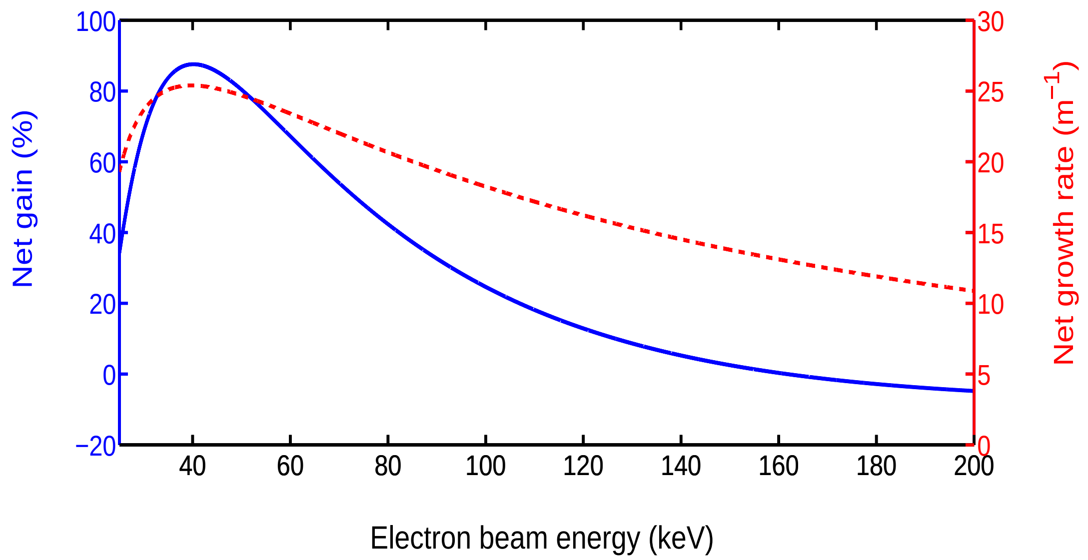

FIGURE 4.3: Plot of net gain and net growth rate as a function of electron beam energy for the parameters discussed in the text.

77 K, the tangent loss of GaAs is 2×10^{-5} and the conductivity of silver is about $3.3 \times 10^8/\Omega$-m [154]. Now to find the optimum value of electron beam energy and dielectric thickness, we have kept the operating wavelength fixed, i.e., λ = 2.7 mm, and plotted the net gain and net growth rate as a function of beam energy and dielectric thickness respectively [155]. Note that we have to vary both the electron beam energy and the dielectric thickness simultaneously such that they satisfy dispersion relation to give λ = 2.7 mm. The plots of net gain and net growth rate as a function of electron beam energy are shown in Fig. 4.3. We obtain an optimum value of electron beam energy as 40 keV for which the net gain comes out to be 88% and net growth rate is obtained as 25.4 m^{-1}. Figure 4.4 shows plots of net gain and net growth rate as a function of dielectric slab thickness. The optimum value of slab thickness is obtained as 265 μm. For the 40 keV beam energy and 265 μm of slab thickness, the attenuation coefficient is calculated as 1.73 m^{-1} at 77 K, which gives us a round trip loss of 29.3% over the 5 cm length.

The proposed system is a low-gain device, and has to be operated in the oscillator configuration. The Maxwell-Lorentz equations have been solved numerically to obtain the power in the surface mode supported in this configuration by using the leapfrog scheme [138] discussed in Chapter 3. The power builds up slowly and saturates at 3.6 W, as shown by the solid curve in Fig 4.5. The input electron beam power is 1.4 kW for the considered beam kinetic energy of 40

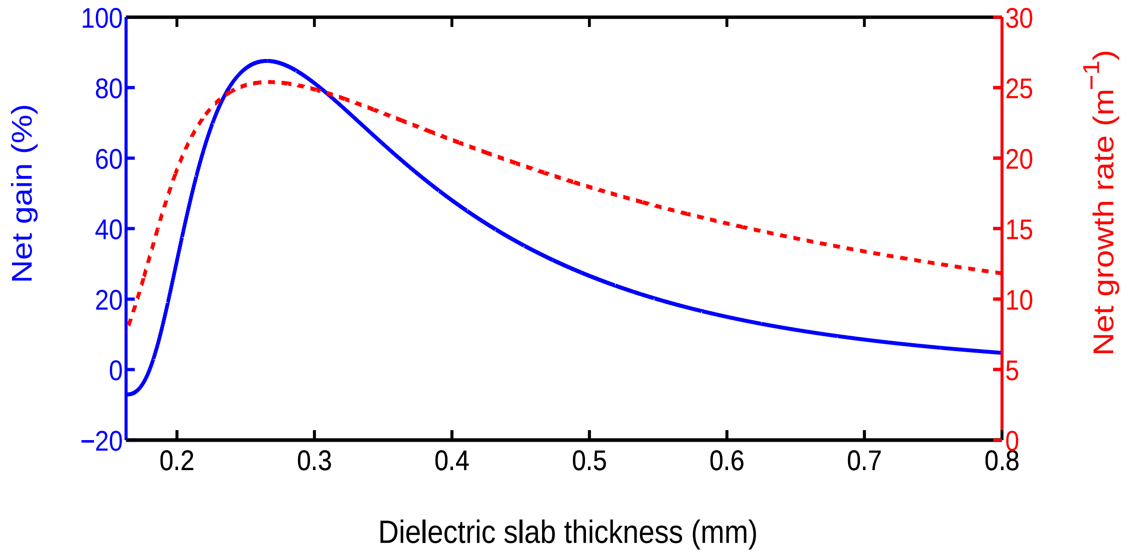

FIGURE 4.4: Plot of net gain and net growth rate as a function of dielectric thickness.

keV ($\beta_R = 0.374$, $\gamma_R = 1.078$), and beam current of 35 mA. For these parameters, we find the efficiency of the optimized CFEL as 0.26%. The analytic estimate for the upper bound of the efficiency η_{eff} is given by Eq. (3.44) in Chapter 3, which represents the fraction of electron beam energy which appears in the form of outcoupled power plus the heat dissipated in the system. In the oscillator configuration, the outcoupled power is given by $P_{in}(1-R_m^2)$, where P_{in} is the mean intra-cavity power and $R_m = 0.98$ is the reflection coefficient of the outcoupling mirror. Taking the effect of attenuation, there will be a round trip loss of power given by $P_{in}(1-e^{-4\alpha L})$. Considering these effects, efficiency of the system is obtained as $\eta_{eff} = P_{in}((1-R_m^2)+(1-e^{-4\alpha L}))/P_b$. We define η_{sim} as the efficiency observed in the simulation, which is also the actual efficiency representing the fraction of electron beam power that appears in the form of outcoupled power, i.e., $\eta_{sim} = P_{in}((1-R_m^2))/P_b$. This gives us $\eta_{sim} = [(1-R_m^2)/((1-R_m^2)+(1-e^{-4\alpha L}))]\eta_{eff}$. Thus, the upper bound for η_{sim} is obtained by multiplying a factor of $(1-R_m^2)/((1-R_m^2)+(1-e^{-4\alpha L}))$ to Eq. (3.22) as

$$\eta_{sim}^{upper\ bound} = \frac{\beta_R^3\gamma_R^3\lambda(1-R_m^2)}{L(\gamma_R-1)[(1-R_m^2)+(1-e^{-4\alpha L})]}. \tag{4.28}$$

For the prescribed parameters, we obtain an upper bound $\eta_{sim}^{upper\ bound}$ as 0.54%, which is in agreement with our numerical results. Figure 4.5 also shows the output power (dashed curve) of a CFEL, where Ohmic and dielectric losses are assumed to be zero. In this case, the CFEL

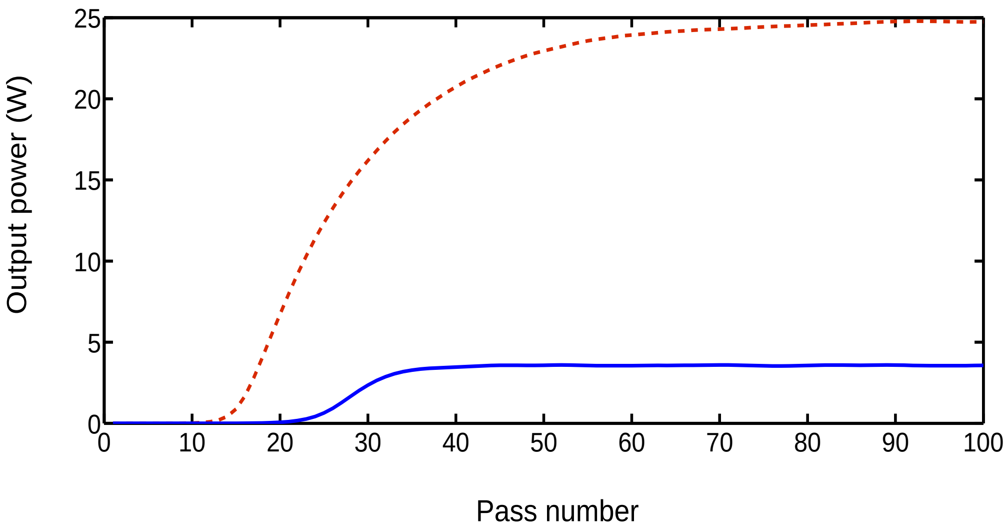

FIGURE 4.5: Plot of output power as a function of pass number for the optimized parameters of a Čerenkov FEL discussed in the text. The dashed curve represents the case, where Ohmic losses are assumed to be zero, and solid curve shows the output power with finite Ohmic losses in the system at 77 K temperature. The linear current density (dI/dy) of the electron beam is taken as 5.6 A/m.

system gives 24.75 W output power on saturation with an efficiency of 1.77%, which is less than the analytically estimated value for the upper bound of 4%. Note that the presence of dielectric losses and Ohmic losses on the metallic surface severely affects the output power and efficiency of a CFEL system, and one has to optimize the system for minimum losses.

The requirements on electron beam sizes are evaluated by using Eqs. (4.17) and (4.18), as Δy = 4.0 mm in the y-direction and Δx = 87 μm in the x-direction respectively. By using Eq. (4.19), we find that an electron beam with normalized vertical emittance $\varepsilon_x \leq 1.5\times10^{-8}$ m-rad is needed in the absence of any external focussing, which is a very stringent requirement. In the horizontal direction, the condition on beam emittance is quite relaxed as an electron beam with $\varepsilon_y \leq 3.3\times10^{-5}$ m-rad is required, which is calculated from Eq. (4.16). If we take $\varepsilon_y = 1.65\times10^{-5}$ m-rad, which is 2 times less than the maximum allowed value, then a flat electron beam with transverse emittance ratio $\varepsilon_y/\varepsilon_x = 1000$ is required for the operation of the CFEL. In the Dartmouth experiment [66], these conditions have been clearly violated, where a round electron beam having large vertical emittance was used to drive the Čerenkov FEL.

To relax the stringent requirement on the electron beam emittance, external focusing can be provided by using a wiggler field as described in Sec. 4.2.1. Here, we will take an explicit example to perform the calculations for the analytical results discussed in Sec. 4.2.1. We assume a round electron beam with initial normalized emittance $\varepsilon_I = 1 \times 10^{-6}$ m-rad, which is easily achievable. A flat electron beam can be produced by using round to flat beam transformation as discussed earlier, and under this transformation $\varepsilon_I = \sqrt{\varepsilon_x \varepsilon_y}$. We choose the ratio of horizontal and vertical emittances as $100 : 1$, i.e., $\varepsilon_y = 10^{-5}$ m-rad and $\varepsilon_x = 10^{-7}$ m-rad. Taking the cathode temperature 1300 K, this scheme requires an axial magnetic field $B = 71.87$ Gauss at the position of the cathode, which can be generated by using either a permanent magnet or an electromagnet [78]. The current density at the cathode, which is required to produce an electron beam of desired emittances as discussed above, is obtained by using the prescription given in Sec.4.2.2 as $J_T = 0.12$ A/cm^2 at $T = 1300$ K. This value of current density (current density upto 10 A/cm^2) can be easily achieved in thermionic cathodes e.g., oxide, dispenser and M-type cathodes [156, 157], which can be operated for tens of thousands of hours at around 1300 K. Next, we discuss the requirements of the wiggler parameters to focus the flat beam described above. For a matched beam size $\sigma_x = 43.5$ μm and vertical emittance $\varepsilon_x = 10^{-7}$ m-rad, we require $B_u = 1.3$ kG. This value of magnetic field can be obtained by using an array of regular pure permanent magnets in a Halbach configuration, which gives a peak field strength of $1.43 B_{rem} \exp(-\pi g_u/\lambda_u)$ [158], where B_{rem} is the remnant field of the magnetic material and g_u is the gap between the jaws of the wiggler. We have considered NdFeB as the magnetic material for which $B_{rem} = 1.1$ T [158]. We have considered two example cases for the wiggler gap, i.e., $g_u = 1$ mm and $g_u = 2$ mm, such that the beam transport is feasible. For $g_u = 1$ mm, we need a mini-wiggler with 1.25 mm period and for $g_u = 2$ mm, we need a wiggler period of 2.50 mm to obtain the required magnetic field of 1.3 kG. This type of mm or sub mm period wiggler can be fabricated by using laser micromachining of bulk permanent magnets as discussed in Ref. [159]. We would like to mention that when an electron beam is focused by a spatially modulated magnetic field as discussed above, it can cause a parametric instability of the beam envelope oscillations due to the mismatch of the beam parameters and the focusing field [160, 161]. These oscillations, if amplified enough, could cause emittance growth and lead to an unstable electron beam [160, 161]. In this case, the envelope equation for the flat beam evolving in the presence of wiggler magnetic field can be used to obtain the following stability condition: $(e\lambda_u B_u/2\sqrt{2}\pi mc\beta_R\gamma_R)^2 < 0.5$ [162]. This condition is known as the Mathieu stability condition of wiggler focusing [162]. We have checked that for the proposed wiggler field and wiggler period, the condition for the Mathieu stability of the wiggler focusing is satisfied. It has also been checked that the criterion for the maximum tolerance on beam emittance as given by Eq. (4.26) is easily met for the above discussed case.

Next, we discuss another possibility to relax the stringent requirement on the vertical beam emittance, where we can use a line cathode immersed in a solenoid field to produce a flat electron beam. This method has been discussed in detail in Sec. 4.2.2. To produce a flat electron beam with beam half widths $\Delta x = 87$ μm and $\Delta y = 4.0$ mm, we need a line cathode with $\Delta x_c = 87$ μm, and $\Delta y_c = 4.0$ mm. At $T = 1300$ K, we obtain $\boldsymbol{\varepsilon}_x = 2.2 \times 10^{-8}$ m-rad and $\boldsymbol{\varepsilon}_y = 9.7 \times 10^{-7}$ m-rad using equation $(\boldsymbol{\varepsilon}_x, \boldsymbol{\varepsilon}_y) = 0.5(\Delta x_c, \Delta y_c)\sqrt{k_B T/mc^2}$. These values for $(\boldsymbol{\varepsilon}_x, \boldsymbol{\varepsilon}_y)$ are quite acceptable. For a beam current of 35 mA, the current density at the line cathode is obtained as $J_c = 3.2$ A/cm^2. By using Eq. (4.22), we find that the solenoid magnetic field $B(0)$ is required to be greater than 0.25 kG to focus such a flat electron beam. We choose $B(0) =$ 1.0 kG. The Larmor radius is obtained as 10.3 μm for these parameters, which is significantly smaller than the rms beam size $\sigma_x = 43.5$ μm. To keep the flat beam rotation less than 10 mrad over a length $L = 5$ cm, we require the field uniformity $\Delta B/B$ to be better than 0.4%, as calculated by using Eq. (4.23).

4.4 Attenuation and diffraction effects in Smith-Purcell FELs

The essential features of the analysis of surface mode supported in a SP-FEL system have been worked out earlier in Refs. [78, 88–93, 163] and are summarized in Sec. 2.4. Here, we further elaborate these results to highlight interesting differences in the analyses of CFEL and SP-FEL systems. We first review some important results of the 2D analysis of the beam-wave interaction in SP-FELs [88], which is similar to the 2D analysis of the CFELs presented in

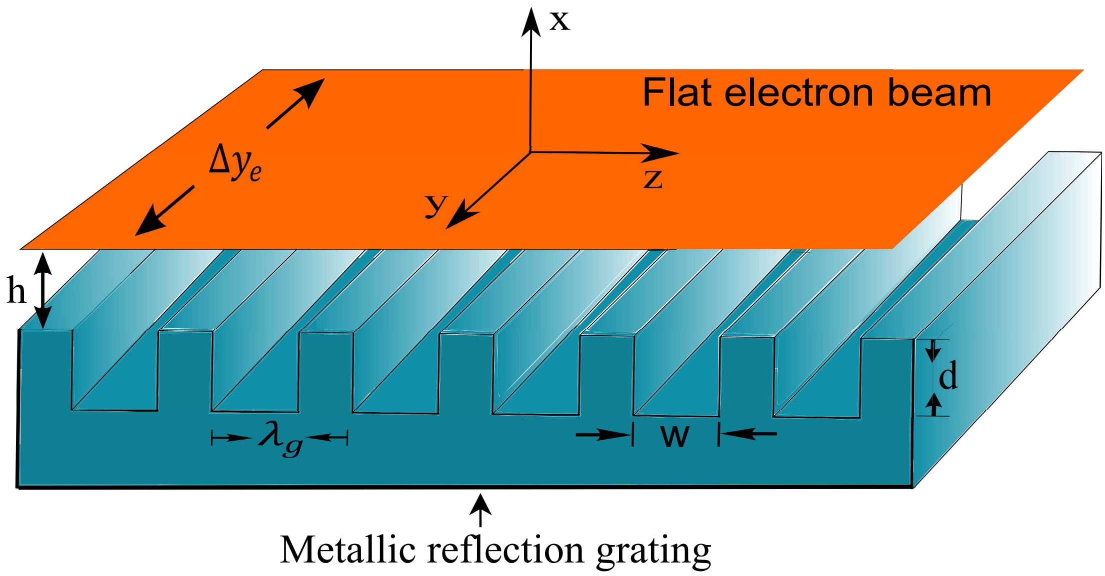

FIGURE 4.6: Schematic of a 3D SP-FEL, using a flat electron beam.

Chapter 3. Then, we extend the results obtained in the earlier analysis of SP-FELs presented in Refs. [78, 88–90] to set up the 3D Maxwell-Lorentz equations for the system.

A schematic of a SP-FEL system is shown in Fig. 4.6, where a flat electron beam skims over the surface of a metallic reflection grating having length L, period λ_g, groove depth d and groove width w. A metallic grating supports an electromagnetic field, which is a combination of Floquet space harmonics since the grating is a periodic structure. Under the 2D approximation, the longitudinal component of electric field can be written as:

$$E_z(x,z,t) = \sum_n E_n e^{i[(k_z+nk_g)z-\omega t]} e^{-\Gamma_n x}, \tag{4.29}$$

where k_z is the propagation wavenumber in the z-direction for the $n = 0$ term , $k = \omega/c$, $k_g = 2\pi/\lambda_g$ and $\Gamma_n = \sqrt{(k_z + nk_g)^2 - k^2}$. The zeroth-order field component has a similar structure as given by Eq. (4.2) [88] and shows the strongest interaction with the electron beam since it is the only component that has phase velocity equal to the electron beam velocity [88]. Higher space harmonics will have a feeble interaction since the phase velocity is not matched with the beam velocity. However, one needs to include higher space harmonics in order to satisfy the boundary condition and to find the dispersion relation of the surface mode as discussed in Ref. [88]. Similar to the case of the CFEL described in the previous chapter, the electron beam interacts with the co-propagating surface mode and the dynamical equation for the evolution of the amplitude of surface mode is given by [78, 88]

$$\frac{\partial E}{\partial z} - \frac{1}{\beta_g c}\frac{\partial E}{\partial t} = \frac{Z_0\chi}{2\beta_R\gamma_R}\frac{dI}{dy}e^{-2\Gamma h}\langle e^{-i\psi}\rangle + \alpha E. \tag{4.30}$$

Here, E is the amplitude of the zeroth-order longitudinal field. The calculation of χ for a SP-FEL requires numerical evaluation of R as a function of growth rate for a given value of (ω, k_0) of the surface mode, and details regarding the procedure for this calculation are described in Ref. [88]. Evaluation of the attenuation coefficient α requires calculation of the heat dissipation at the metallic surfaces for the given surface mode, which has been discussed for the case of the SP-FEL in Ref. [99]. Note the difference in sign of terms containing β_g, χ and α in above equation as compared to Eq. (4.3) for the CFEL. This is due to the fact that the SP-FEL has negative group velocity for the surface mode, as described in Ref. [88], whereas the group velocity is positive in case of the CFEL system. The negative group velocity for the SP-FEL makes it a BWO and oscillations build up when the linear current density dI/dy exceeds a threshold value dI_s/dy [78, 88]:

$$\frac{dI}{dy} > \frac{dI_s}{dy} = \mathcal{J}(\eta_s)\frac{I_A\beta_R^4\gamma_R^4}{2\pi\chi k L^3}e^{2\Gamma h}. \tag{4.31}$$

Here, $\mathcal{J}(\eta_s)$ represents a dimensionless start current as a function of the loss parameter $\eta_s = \alpha L$. The calculations of $\mathcal{J}(\eta_s)$ are given in Ref. [164].

After having briefly discussed the 2D analysis, we next discuss the localized surface mode and set up the 3D coupled Maxwell-Lorentz equations for the SP-FEL system.

4.4.1 Localized surface mode and 3D Maxwell-Lorentz equations

In order to construct the localized surface mode, we need to combine the plane waves propagating at different angles in the (y, z) plane with a suitable weight factor. In order to perform this calculation, we need to know the 3D dispersion relation of the metallic grating, i.e., the dependence of ω on k_z, for different values of k_y. The 3D dispersion relation for a rectangular metallic grating is obtained by Kumar and Kim [90] by deriving the condition for singularity in R. A remarkable observation in their analysis is that if we replace ω by $\sqrt{\omega^2 - c^2k_y^2}$ in the expression for the reflectivity for the case $k_y = 0$; we obtain the reflectivity for the 3D case, where a finite value of k_y is considered [90, 163]. This is because here we have electromagnetic field present only in one medium, i.e., the space above the surface of the reflection grating (including the grooves of the grating), which is in vacuum. Due to this feature, the expression for reflectivity has terms like $(\omega^2 - c^2k_z^2)$ in the 2D case, which can be simply replaced with $(\omega^2 - c^2k_y^2 - c^2k_z^2)$ for the 3D case. This amounts to replacing ω in the 2D case by $\sqrt{\omega^2 - c^2k_y^2}$, to determine the dispersion relation for the 3D case with finite k_y.

It is important here to note the difference between the dispersion relation of the SP-FEL and the CFEL systems. A careful observation of the 2D dispersion relation of a CFEL: $\sqrt{\epsilon\omega^2/c^2 - k_0^2}\times \tan(d\sqrt{\epsilon\omega^2/c^2 - k_0^2}) = \epsilon\sqrt{k_0^2 - \omega^2/c^2}$ indicates that the simple "replacement rule" as in the case of the SP-FEL system i.e., replacing ω in 2D dispersion relation with $\sqrt{\omega^2 - c^2k_y^2}$ will not give us the 3D dispersion relation. This is because here, the electromagnetic field in a CFEL is present in vacuum as well as in the dielectric medium, unlike in the SP-FEL case; therefore terms like $(\omega^2 - c^2k_o^2)$ as well as $(\omega^2 - c^2k_o^2/\epsilon)$ appear in the 2D dispersion relation. In the case of the CFEL, the "isotropic nature" of the dielectric slab in (y, z) plane facilitates us to analyze the diffraction in the surface mode as described in Sec. 4.1.2. The grating structure used in the SP-FEL system has grooves along the surface in the transverse direction and lacks isotropic behaviour in the (y, z) plane. Due to this difference, the optical properties of the surface mode in the SP-FEL system are different as compared to the CFEL system, as elaborated in the following paragraph.

We now discuss the construction of localized surface mode in the SP-FEL. Due to the replacement rule: $\omega_{3D}(k_y) = \sqrt{\omega_{2D}^2 + (ck_y)^2}$, we write the longitudinal wavenumber k_z as

$$k_z = k_0 + \left.\frac{\partial k}{\partial \omega}\right|_{k_y=0} \Delta\omega, \tag{4.32}$$

where $\Delta\omega = \omega_{2D} - \omega_{3D}$ and the term $\partial k/\partial\omega$ at $k_y = 0$ is identified as $(-1/\beta_g c)$. Using these results along with the paraxial approximation in Eq. (4.32), we obtain

$$k_z = k_0\left(1 + \frac{k_y^2}{2\beta_R\beta_g k_0^2}\right). \tag{4.33}$$

Here, we note the difference between above equation and corresponding equation [Eq. (4.6)] for the case of the CFEL. On the account of 3D effects, the magnitude of change in the longitudinal wavenumber ($|k_z - k_0|$) is given by $\beta_R\lambda k_y^2/4\pi$ for the CFEL and $\lambda k_y^2/4\pi\beta_g$ for the SP-FEL case respectively. It can be seen that in this term, $\beta_R\lambda$ in case of the CFEL is replaced with λ/β_g for the case of the SP-FEL.

Next, by satisfying the wave equation for the electromagnetic field, we obtain the expression for Γ' as:

$$\Gamma' = \Gamma\left(1 + \frac{k_y^2(1 + \beta_R\beta_g)}{2\beta_R\beta_g\Gamma^2}\right). \tag{4.34}$$

By following an approach similar to the one described in Sec. 4.1.2, the analysis for the localized surface mode supported by the grating structure is performed. The Rayleigh range for the optical surface mode is obtained as [78]:

$$Z_R = \frac{4\pi\beta_g\sigma_y^2(0)}{\lambda}, \tag{4.35}$$

where $\sigma_y(0)$ is the rms beam size at the waist. Under paraxial approximation, the product of rms beam waist size and rms divergence is given by [78]

$$\sigma_y(0) \times \sigma_\theta = \frac{\lambda}{4\pi\beta_g}. \tag{4.36}$$

Note that Eqs. (4.35) and (4.36) have dependence on the group velocity, while equivalent quantities in the CFEL system [Eqs. (4.10) and (4.11)] have dependence on the phase velocity of the surface mode. In these expressions, the term $\beta_R\lambda$ in the case of the CFEL is replaced with λ/β_g in the case of the SP-FEL, as expected. We emphasize that this difference arises due to a fundamental difference in the way the dispersion relation for the two systems gets modified for the 3D case, which we have explained. Due to this nature, it can be seen that the diffraction effects are more prominent in case of the SP-FEL as compared to the CFEL. The length L of the grating in case of SP-FEL has to be kept small to maintain sufficient interaction of the surface mode with the co-propagating electron beam.

Next, the expression for k_z and Γ' can be used in Eq. (4.4) to set up the three-dimensional electromagnetic surface mode for the SP-FEL. By following the procedure described in Sec. 4.1.3, the following time dependent 3D differential equation for the evolution of the surface mode in a SP-FEL is obtained [90]:

$$\frac{\partial E}{\partial z} + \frac{i}{2\beta_R\beta_g k_0}\frac{\partial^2 E}{\partial y^2} - \frac{1}{\beta_g c}\frac{\partial E}{\partial t} = \frac{Z_0\chi}{2\beta_R\gamma_R}\frac{dI}{dy}e^{-2\Gamma h}\langle e^{-i\psi}\rangle + \alpha E. \tag{4.37}$$

Note the difference in the second term of above equation as compared to the corresponding term in Eq. (4.15) for the CFEL. Here, a factor $\beta_R\beta_g$ appears, which shows large diffraction in the surface mode in an SP-FEL as compared to the CFEL. We would like to emphasize that although the diffraction term in the above equation has the same form as in the case of undulator based FEL [42], the free-space wavelength λ appearing in this term for the undulator based FEL is replaced with $\beta_R\lambda$ in the CFEL and λ/β_g in the SP-FEL, and this is an important finding of our analysis.

4.5 Discussions and conclusion

In this chapter, we have presented a three-dimensional analysis of the surface mode in Čerenkov and Smith-Purcell FELs. Expressions have been derived for the electromagnetic field in a localized surface mode by suitably combining the plane wave solutions of Maxwell equations, propagating at different angles in the (y, z) plane. A crucial input for this calculation was to have the information about the change in k_z, after we include the $\exp(ik_y y)$-type dependence in the electromagnetic field, keeping the value of ω fixed. For the case of the CFEL, this was simplified due to "isotropic nature" of the system in the (y,z) plane, and in the case of the SP-FEL, this was simplified due to the "replacement rule" for the evaluation of reflectivity of the incident evanescent wave. Interestingly, the "isotropic nature" is not applicable for the SP-FEL case and the "replacement rule" is not applicable for the CFEL case.

A three-dimensional analysis of the surface mode allows us to include the effect of diffraction, which plays an important role in the performance of the CFEL and the SP-FEL systems. We have explained in the chapter that for an isotropic system, as in the case of the CFEL, the free-space wavelength λ in the diffraction term in the wave equation gets replaced with $\beta_R\lambda$. On the other hand if the system is not isotropic, but the electromagnetic field is present only in vacuum, as in the case of the SP-FEL, λ gets replaced with λ/β_g. Due to this difference, diffraction effects are observed to be prominent in the SP-FELs as compared to the CFELs. To incorporate the 3D effects in the analytical formulas for the gain and the growth rate of the CFEL system discussed in Chapter 3, we have taken the electron beam size to be same as the effective optical beam size, which has been evaluated by taking the 3D variations in the surface mode.

We also included the effect of the dielectric losses and losses due to finite conductivity of the metal, which play an important role when we increase the interaction length in order to increase the gain in a CFEL. Although all earlier analyses on the single slab CFELs have ignored this effect, it is important to take such realistic effects into account in a practical device, as is the case in any device using guided waves at high frequency. It is interesting to point out that even in the case of SP-FELs, the effect of attenuation was neglected in earlier studies, and its importance was realized in later studies [99, 164]. In order to reduce the loss due to finite conductivity of metal in a CFEL, we have proposed that the metallic base can be kept at low temperature, i.e., 77 K. We have optimized the parameters for a CFEL designed to operate at 0.1 THz and have shown that using a 40 keV electron beam with a current of 35 mA, an optimized CFEL oscillator can deliver an output power of 3.6 W at saturation with an efficiency of 0.26%.

Our overall approach to study CFELs is built on the earlier analyses given for SP-FELs in

Refs. [78, 89]. Like the SP-FEL [89], the requirements on the vertical beam emittance in a CFEL come out to be stringent and we have discussed two ways to relax the stringent requirements. In the first scheme, a wiggler magnetic field is used to focus a flat electron beam, which is produced by a novel phase-space technique discussed in Ref. [78]. This scheme requires a peak wiggler field of about 1.3 kG to focus a flat electron beam having transverse emittance ratio $\varepsilon_y/\varepsilon_x = 100$. Such a DC electron beam can be produced by employing a round to flat beam transformation to the initially round electron beam produced using a thermionic cathode such as LaB_6 as described in Ref. [78]. This technique of round to flat beam transformation has been demonstrated experimentally at Fermi National Accelerator Laboratory to generate an electron beam directly from a photoinjector with transverse emittance ratio of 100 [145]. In the second scheme, we used a solenoid field to focus a flat electron beam, which is produced by a line shaped tungsten cathode placed at the centre of a solenoid. The solenoid field is taken as 1 kG with field uniformity $\Delta B/B$ required to be better than 0.4% over a length of 5 cm. We would like to mention that although both the external focusing schemes may add to the complexity of the system, these are implementable and are needed to satisfy the stringent requirements for optimum performance of the system.

It is important to mention here that there could be problems with the transmission of a flat beam by using a uniform solenoid magnetic field at higher beam currents as discussed earlier in Refs. [152, 165], where it is pointed out that due to $E_s \times B(0)$ drift, where E_s is the electric field from space charge, the flat beam gets a vertical kick in the opposite direction at its two edges, which results in the edge curling phenomenon. Beyond a certain threshold, this leads to instabilities like diocotron and/or filamentation instabilities [152], which can disrupt the flat nature of the electron beam resulting in significant interception of the beam. An analytic estimate for the threshold length L_D, after which the diocotron instability grows exponentially can be given by $L_D(\text{cm}) \simeq 800\beta_R^2\gamma_R^3 B(0)(\text{kG})/J_c$ (A/cm^2) [152]. It can be seen that for a given beam energy and focussing field strength, the diocotron instability is suppressed at low beam current densities J_c or equivalently at reduced effective space charge. The considered electron beam in our analysis is not space charge dominated as the space charge term in the envelope equation is small compared to the emittance term, i.e., $I\Delta x^3/4\beta_R\gamma_R I_A \boldsymbol{\varepsilon}_x^2(\Delta x + \Delta y) < 1$ [144] for the x-direction. We have evaluated the left-hand side in this inequality and obtained its value as 0.86. The condition in the y-direction is less restrictive for our case. For the beam current density of 3.2 A/cm^2 and axial magnetic field of 1.0 kG, we find the lower bound estimate for L_D as 44.1 cm. The proposed length of CFEL system (5 cm) is about 9 times less than the threshold growth length, hence, the diocotron instability due to $E_s \times B(0)$ effect is not of concern in our system.

It is also important to mention here that for the thermionic cathode, we have taken only the thermal emittance into consideration. In reality, the beam emittance could be larger than this [166]. We have checked that with suitable change in the parameters, our schemes would still work. For the case of wiggler focusing, this would requires us to choose a smaller cathode size and hence, the beam current density at cathode would increase and also the magnetic field required at cathode for the flat beam production would increase. We have checked that even if the total emittance is twice the thermal emittance, the required current density and magnetic field required at cathode are increased by 4 times, and these values are still easily achievable. For the case of solenoid focussing, if we take the total emittance as twice the thermal emittance, the required minimum solenoid focussing field $B(0)$ increases by a factor of two and therefore becomes 0.50 kG. In our calculation, we have considered a solenoid focussing field of 1 kG, which is still higher than 0.50 kG.

To summarize, we have performed a 3D analysis of the surface mode and set up 3D Maxwell-Lorentz equations for a CFEL and a SP-FEL system. Based on these results, we have made some interesting comparison between the analyses of these systems. We have optimized the parameters of a Čerenkov FEL by including the 3D effects and attenuation due to dielectric and Ohmic losses, and found that the device can produce copious THz radiation even after including these effects. Our analysis can be used for the detailed optimization of both the CFEL and the SP-FEL systems.

Chapter 5

Novel configurations of slab-type Čerenkov FELs

In Chapter 3, we discussed the dynamics of a single slab based CFEL driven by a flat electron beam, and it was noted that the small-signal gain of the system is proportional to the effective surface current density $K = I/\Delta y_e$, where I is the electron beam current and Δy_e is the effective mode width in the y-direction. Over an interaction length L, the minimum possible value of Δy_e is constrained by the diffraction effects. In the previous chapter, we included the diffraction effects and found that $\Delta y_e = \sqrt{\pi\beta_p\lambda L/4}$ [167], where $\beta_p = v_p/c$, v_p is the phase velocity of the surface mode, c is the speed of light, and λ is the free-space wavelength. For a low-gain CFEL system, the small-signal gain has a cubic dependence on the length L as shown in Ref. [142], and therefore one tends to increase L to increase the value of gain. However, as L is increased to get a reasonable value of gain, the value of Δy_e increases, which reduces the gain. The question therefore arises whether the effective mode width Δy_e can be made independent of L and be reduced below the limiting value described above. It turns out that this can be achieved with the help of waveguiding of the surface mode, as is done in conventional undulator based FELs [97] and in cylindrical [54–59, 75, 168, 169] or rectangular [62, 170, 171] geometry of CFELs. This helps in increasing the gain, and thus achieving a reasonable value of gain in a shorter interaction length.

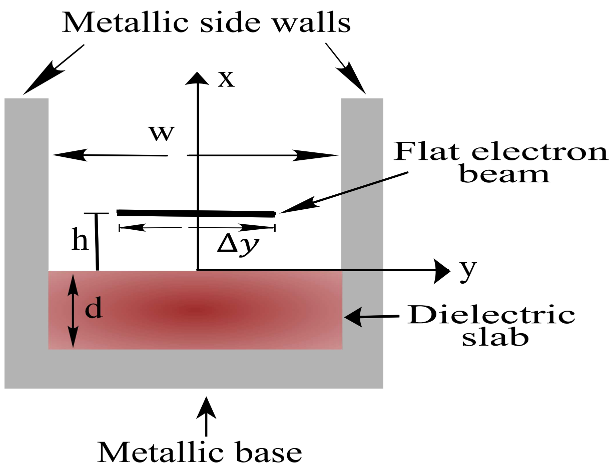

FIGURE 5.1: Schematic of a single slab based Čerenkov FEL with metallic side walls.

The simplest way to achieve waveguiding in single slab based CFELs is to put a pair of metallic sidewalls along the sides of dielectric slab in the y-direction, as shown in Fig. 5.1. This is a novel configuration of single slab based CFEL, which is open from the top in the x-direction and has metallic sidewalls along the y-direction. Due to the presence of metallic side walls, the surface mode is guided in the y-direction, and maintains a constant width over any arbitrary interaction length. A smaller value of mode width results in a good overlap between the electron beam and a copropagating guided surface mode, and consequently the gain of CFEL can be increased. This is the primary advantage of the waveguiding. The second advantage is that the requirement on vertical emittance of the electron beam is relaxed with the help of side walls, which can be understood as follows. The surface mode supported in single slab based CFELs is evanescent in the direction perpendicular to the dielectric surface with a scale height $h = \beta_p\gamma_p\lambda/4\pi$ [80], where $\gamma_p = 1/\sqrt{1-\beta_p^2}$. To maintain a good overlap with the radiation beam, the electron beam should maintain its vertical beam size around this value over the entire interaction length. As discussed in Refs. [64, 80], one of the challenges in a CFEL is to maintain a very small vertical beam size over the entire interaction length. Waveguiding reduces the required interaction length and therefore we need to maintain a small vertical beam size now over a *smaller* interaction length, which relaxes the requirement on the vertical beam emittance. The third advantage of the sidewall configuration is that it helps in reducing the losses due to attenuation of surface mode, which is caused by the Ohmic and dielectric losses. For a low gain CFEL oscillator system, the small-signal gain has a cubic dependence on L, whereas the attenuation results in exponential decay of power by $e^{-4\alpha L}$ for a round trip. Here, α is the field attenuation coefficient. In order to reduce the degradation in net gain due to attenuation, it is therefore desired to reduce the interaction length. With the help of waveguiding, we can choose a shorter interaction length, and still obtain higher gain such that the device can produce powerful electromagnetic radiation.

We would like to mention that waveguiding in CFELs has been discussed earlier for the cylindrical [54–59, 75, 168, 169] and single slab based rectangular [62, 170, 171] configurations. As discussed in detail in Chapter 1, both the cylindrical and the rectangular waveguide geometries of CFELs are closed structures and may have problems in the power handling capacity at high frequency operation. This is because in a cylindrical CFEL driven by a low energy electron beam, the supported electromagnetic field decays quickly as we move towards the axis of the waveguide. In such a situation, we require a hollow electron beam having a radius nearly equal to the radius of the waveguide to have an effective beam-wave interaction. For operation at higher frequencies, the transverse dimension of cylindrical waveguide is required to be small [59], and we therefore need to use a hollow electron beam of very small radius. This reduces the cross sectional area of the beam, thereby increasing the space charge effects, which may inhibit high power operation of the device. Also, in order to ensure that the beam remains close to the dielectric surface as it propagates, the hollow cylindrical beam is required to have very stringent transverse emittance in the radial direction, which may be difficult to achieve. These problems are overcome in the planar configuration i.e., a CFEL in single or double slab configuration [66, 80–82, 98, 136, 142], or a CFEL in rectangular waveguide geometry [170, 171]. In the planar configuration, a flat electron beam can be used, which remains close to the dielectric surface but has relatively larger size in the horizontal direction. Hence, the cross sectional area of the beam can be larger such that the space charge effect is relatively reduced and the stringent emittance is required to be maintained only in the vertical direction. In a rectangular waveguide geometry of a CFEL, the field decays in the vertical direction as we move away from the dielectric surface. Although the surface mode is already confined close to the dielectric surface, the top surface of the rectangular waveguide helps in further confining

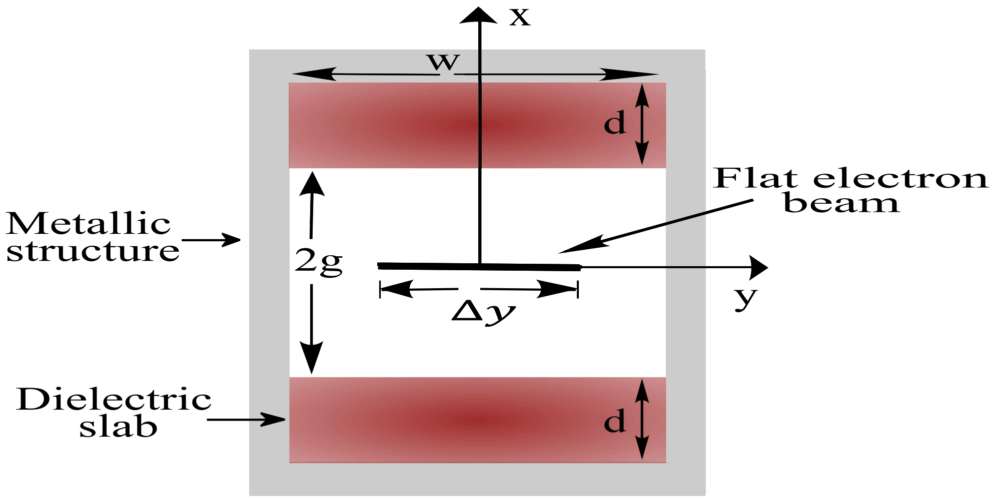

FIGURE 5.2: Schematic of a rectangular configuration of a double slab based CFEL system.

the electromagnetic surface mode if the vertical dimension of the waveguide is small. This however may result in attenuation of the wave due to the additional heat dissipation on the top surface. One option is to remove the top surface such that the structure is *open*, and thus use only two side walls to confine the surface mode in the horizontal direction as shown in Fig. 5.1. In this chapter, we present a detailed analysis of this configuration in both linear as well as non-linear regimes. As discussed earlier, a waveguided configuration has lots of advantages, i.e., in reducing the loss due to diffraction and attenuation effects, and in relaxing the stringent criteria on the electron beam emittance. Hence, it is a novel configuration of a CFEL. We therefore investigate the performance of this system in more realistic conditions, i.e., by considering the effect due to finite beam-size, finite energy-spread and finite beam-emittance, and also the attenuation of the surface mode at room temperature conditions. We have also extended our analysis based on the coupled Maxwell-Lorentz equations for a double slab based rectangular CFEL system, as shown in Fig. 5.2. An open configuration of double slab based CFEL, i.e., without any sidewall, has been studied extensively in the literature [101, 102, 128, 172]. Here, we will investigate the effect of waveguiding in the double slab based rectangular CFEL and compare its performance with the open configuration of a double slab based CFEL and a single slab based sidewall CFEL.

In the next section, we derive the dispersion relation of the surface mode supported by a single slab based CFEL having metallic side walls. The coupled Maxwell-Lorentz equations are set up for a sidewall CFEL driven by a flat electron beam in Sec. 5.1.2. In Sec. 5.1.3 we extend our analysis based on the coupled Maxwell-Lorentz equations for the finite-thickness electron beam. The numerical solutions of the coupled Maxwell-Lorentz equations are obtained in Sec. 5.1.4 for the case of single slab based sidewall CFEL. In Sec. 5.2, we establish the Maxwell-Lorentz approach for the double slab based rectangular CFEL, and compare the results with those obtained for a single slab based sidewall CFEL. Finally, we present some discussions and conclude our analysis in Sec. 5.3.

5.1 Single-slab based Čerenkov FEL with metallic side walls

5.1.1 Formula for the resonant wavelength

The sidewall configuration of a single slab based CFEL is shown in Fig. 5.1, where the dielectric slab supported by a conducting surface is surrounded with metallic side walls having spacing w along the y-direction. The dielectric slab has thickness d, length L and relative dielectric permittivity ϵ. The electromagnetic surface mode supported by this geometry can be obtained by combining the plane wave solutions of an open structure, i.e., the structure without any side wall, in a suitable manner such that it satisfies the boundary conditions. Field components of the lowest order TM surface mode, which satisfy the Maxwell equations with the given boundary conditions, are discussed in detail in Appendix A. The expression for longitudinal electric field E_z^I is given by

$$\begin{aligned} E_z^I &= E_0 e^{-\Gamma(x-h)} e^{i(k_z z-\omega t)} \cos(k_y y) + \text{c.c.}, \\ &= \frac{E_0}{2}[e^{i(k_z z+k_y y-\omega t)} + e^{i(k_z z-k_y y-\omega t)}]e^{-\Gamma(x-h)} + \text{c.c.}. \end{aligned} \tag{5.1}$$

Here, $2E_o$ is defined as the peak amplitude of E_z^I at the location of the electron beam at $x = h$, $k_z = 2\pi/\beta\lambda$ is the propagation wavenumber in the z-direction, $\beta = v/c$, $\omega = 2\pi c/\lambda$, λ is the free space wavelength, $\Gamma = \sqrt{k_y^2 + k_z^2 - \omega^2/c^2}$, $k_y = \pi/w$, and c.c. denotes complex conjugate

TABLE 5.1: Parameters of a sidewall CFEL used in the calculation

Electron energy	40.0 keV
Electron-beam height (h)	90.0 μm
Electron-beam current (I)	35 mA
Dielectric constant (ϵ)	13.1
Length of slab (L)	5 cm
Dielectric thickness (d)	265 μm
Side walls separation (w)	4.2 mm
Operating frequency	0.11 THz

of written right hand side. The phase velocity of the surface mode here is taken as equal to the electron velocity v. As seen in the above equation, the guided surface mode is a combination of two plane evanescent waves travelling in different directions in the (y, z) plane, each having frequency ω and wave vector $k_0 = \sqrt{k_y^2 + k_z^2}$. Each of these two plane evanescent waves is a solution of the wave equation for a CFEL without side walls, and should therefore satisfy the corresponding dispersion relation $k_0 = \tan^{-1}(1/a_p)/b_p$ for that case [81, 84, 142]. Here, $a_p = (\gamma_p/\epsilon)\sqrt{\epsilon\beta_p^2 - 1}$, $b_p = d\sqrt{\epsilon\beta_p^2 - 1}$, and $\beta_p = \omega/ck_0$. It should be emphasize here that the representation of the surface mode as a combination of two plane evanescent waves as given by Eq. (5.1) is possible only when the dielectric slab is an isotropic structure in that plane. For this case, the optical properties of the system will remain invariant under any arbitrary rotation in the (y, z) plane. Now, using $k_0 = \tan^{-1}(1/a_p)/b_p$, $k_y = \pi/w$ and $k_z = 2\pi/\beta\lambda$ in the expression $k_0 = \sqrt{k_y^2 + k_z^2}$, and solving for the operating wavelength λ, we obtain

$$\lambda = \frac{2\pi}{\beta\sqrt{[\tan^{-1}(1/a_p)/b_p]^2 - [\pi/w]^2}}. \tag{5.2}$$

From the above equation, it is clear that for a finite sidewall spacing w, we obtain a higher value of operating wavelength λ as compared to that obtained in a CFEL without any side wall since the denominator term gets reduced for finite w. Now, to achieve the same λ, we can increase β for the case of a sidewall CFEL. Hence, in sidewall CFEL, we require an electron beam with higher energy to achieve the same operating wavelength as compared to the case of a

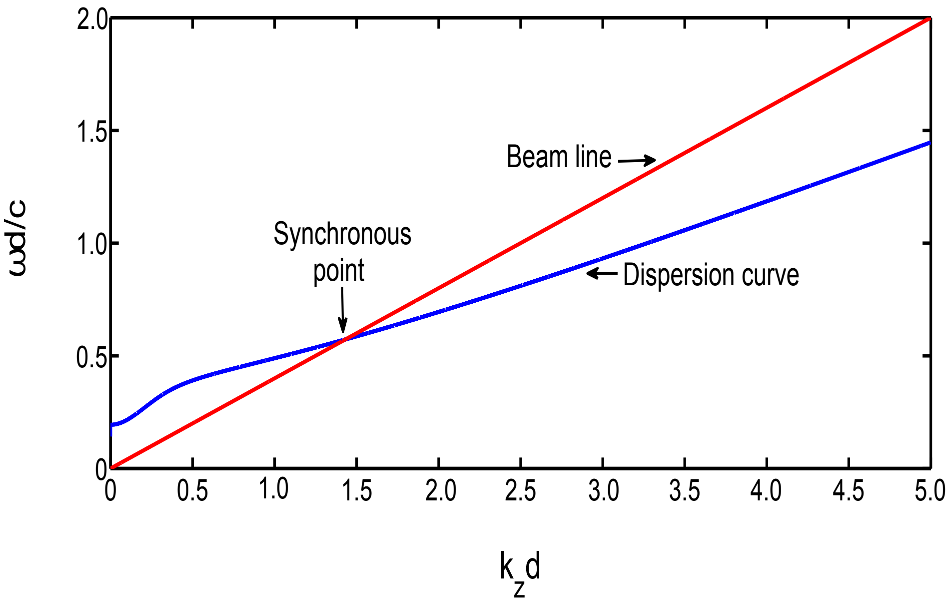

FIGURE 5.3: Plot of the dispersion curve of the electromagnetic surface mode (in the empty structure, i.e., without the electron beam), and the beam line for the electron beam. The parameters used in this calculation are listed in Table 5.1. The resonant frequency of the CFEL system is obtained at the intersection, which we obtain as 0.11 THz.

CFEL without any side wall, provided that all other parameters are same. The dispersion curve for the CFEL with side walls is shown in Fig. 5.3. The parameters used in our calculations are summarized in Table 5.1. For the dielectric slab, we choose GaAs having $\epsilon = 13.1$ [66]. We have taken side wall spacing $w = (2/3)\sqrt{\pi\beta_p\lambda L/4}$, which gives an enhancement in small-signal gain up to a factor of three as compared to the case of a CFEL without any side wall, as discussed in detail in the next section. The resonant frequency is obtained as 0.11 THz for these parameters.

5.1.2 Maxwell-Lorentz equations and small-signal gain for a sidewall Čerenkov FEL driven by a flat beam

We now derive the coupled Maxwell-Lorentz equations to study the interaction of a guided surface mode with a co-propagating electron beam in a sidewall CFEL. For this, we have closely followed an approach given by Levush *et al.* [133], which is very successful to study the beam-wave interaction in BWOs. In this model [133], we first set up the electromagnetic fields by solving Maxwell equations in the empty configuration, i.e., without the electron beam, and then solve the Maxwell equations in the presence of the electron beam with the assumption that the amplitude of the fields vary slowly due to the interaction with the electron beam. This approach is mathematically simple as it only requires the solution of the Maxwell field equations as compared to the approach discussed in Chapters 3 and 4, where one has to perform the residue analysis of reflectivity in terms of the parameters χ and χ_1. The calculations of χ and χ_1 may get involved in a complex electromagnetic system. However, once calculated, the parameter χ_1 gives us the space charge field in the system, which is not calculated in the approach given by Levush *et al.* [133]. We would like to mention here that both these approaches give similar results as shown in Ref. [88], and therefore can be used interchangeably to study the beam-wave interaction.

For simplicity, we will first perform the analysis for a flat electron beam having vanishing thickness in the x-direction and width Δy in the y-direction. The flat electron beam here is assumed to be propagating with velocity v along the z-direction at a height h above the dielectric surface. In the presented model, an ensemble of electrons interacts with a co-propagating surface mode, and we have assumed that the amplitude of the surface mode is a slowly varying function of z and t due to interaction with the co-propagating electron beam. Now, the electromagnetic surface field described in the earlier section can be written in a more general form as

$$\boldsymbol{E^T} = [A(z,t)\boldsymbol{E_p}(x,y,k_y) + \boldsymbol{E_{sc}}]e^{i(k_z z-\omega t)} + \text{c.c.}, \tag{5.3}$$

$$\boldsymbol{B^T} = [A(z,t)\boldsymbol{B_p}(x,y,k_y) + \boldsymbol{B_{sc}}]e^{i(k_z z-\omega t)} + \text{c.c.}, \tag{5.4}$$

where $A(z,t)$ is the amplitude of the fundamental mode and the symbols $\boldsymbol{E_p}$ and $\boldsymbol{B_p}$ represent the field distributions for the fundamental mode in the empty structure, i.e., in the absence of an electron beam. Here, $\boldsymbol{E_{sc}}$ and $\boldsymbol{B_{sc}}$ denote the small first-order ac space charge fields. The total electromagnetic fields $\boldsymbol{E^T}$ and $\boldsymbol{B^T}$ in Eqs. (5.3) and (5.4) will satisfy Maxwell equations with the beam current density $\boldsymbol{J}$ to give:

$$\frac{1}{c^2}\frac{\partial A}{\partial t}\boldsymbol{E_p} - \frac{i\omega}{c^2}\boldsymbol{E_{sc}} = \nabla\times\boldsymbol{B_{sc}} + ik_z\hat{z}\times\boldsymbol{B_{sc}} + \frac{\partial A}{\partial z}\hat{z}\times\boldsymbol{B_p} - \mu_0\boldsymbol{J}e^{-i(k_z z-\omega t)}, \tag{5.5}$$

$$-\frac{\partial A}{\partial t}\boldsymbol{B_p} + i\omega\boldsymbol{B_{sc}} = \nabla\times\boldsymbol{E_{sc}} + ik_z\hat{z}\times\boldsymbol{E_{sc}} + \frac{\partial A}{\partial z}\hat{z}\times\boldsymbol{E_p}, \tag{5.6}$$

where μ_0 is the permeability of free space. By taking the dot product of Eq. (5.5) with $\boldsymbol{E_p^*}$ and Eq. (5.6) with $\boldsymbol{B_p^*}$, and subtracting the resultants respectively, we obtain

$$\begin{aligned}\left[\frac{|\boldsymbol{E_p}|^2}{c^2} + |\boldsymbol{B_p}|^2\right]\frac{\partial A}{\partial t} + \hat{z}.[\boldsymbol{E_p^*}\times\boldsymbol{B_p} + \boldsymbol{E_p}\times\boldsymbol{B_p^*}]\frac{\partial A}{\partial z} &= -\mu_0\boldsymbol{J}.\boldsymbol{E_p^*}e^{-i(k_z z-\omega t)} \\ &+ \nabla.[\boldsymbol{B_{sc}}\times\boldsymbol{E_p^*} - \boldsymbol{E_{sc}}\times\boldsymbol{B_p^*}].\end{aligned} \tag{5.7}$$

Note that while deriving the above equation, we have used the fact that the complex conjugate fields $\boldsymbol{E_p^*}$ and $\boldsymbol{B_p^*}$ satisfy the Maxwell wave equation in the empty structure (i.e., without the electron beam). We performed integration on both sides of Eq. (5.7) over a volume having $x \in [-d, \infty]$, $y \in [-w/2, w/2]$ and $z \in [z - \lambda_z/2, z + \lambda_z/2]$. In doing this, we assume that $A(z,t)$ varies slowly in the longitudinal direction, and can therefore be taken out of the integral. Further, the tangential components of $\boldsymbol{E_p}$ vanish at the metallic surfaces located at $x = -d$, and at $y = \pm w/2$. The same condition will also be satisfied by the tangential components of $\boldsymbol{E_{sc}}$ in the presence of the electron beam. The electromagnetic fields are evanescent in the x-direction, and vanish at $x = \infty$. Due to these conditions, the last term on the right hand side of Eq. (5.7) will vanish upon integration, and we obtain

$$\frac{\partial A}{\partial t} + v_g\frac{\partial A}{\partial z} = \frac{-|A|^2}{w\lambda_z\mathcal{U}}\int_{z-\lambda_z/2}^{z+\lambda_z/2}\int_{-w/2}^{w/2}\int_{-d}^{\infty}\boldsymbol{J}.\boldsymbol{E_p^*}e^{-i(k_z z-\omega t)}dxdydz, \tag{5.8}$$

where v_g is the group velocity of the surface mode given by $P/w\mathcal{U}$ for the CFEL [121, 142], P is total power contained in the surface mode, and $\mathcal{U}$ is the electromagnetic energy stored in the fields per unit mode width w per unit length in the z-direction. The current density of the flat beam propagating at a height h from the dielectric surface is given by $\boldsymbol{J} = e\sum_i \delta(x - h)\delta(y - y_i)\delta[z - z_i(t)]v\hat{z}$, where e is the magnitude of the electron's charge and y_i and z_i are the coordinates of the ith particle in the y and z-direction respectively at time t. The z component of the field $\boldsymbol{E_p}$, which interacts with the electron beam is given by $E_0\cos(k_y y)e^{-\Gamma(x-h)}\hat{z}$, and the term AE_o is represented by E in further calculations. Substituting $\boldsymbol{E_p^*}$ and $\boldsymbol{J}$ in Eq. (5.8) and performing the integral, we obtain the following dynamical equation for E:

$$\frac{\partial E}{\partial z} + \frac{1}{v_g}\frac{\partial E}{\partial t} = -\frac{I|E|^2}{v_g w \mathcal{U}}\langle\cos(k_y y)e^{-i\psi}\rangle. \tag{5.9}$$

Here, $I = evN_{\lambda_z}/\lambda_z$ is the electron beam current, N_{λ_z} is the number of electrons distributed over one spatial wavelength of the evanescent wave, i.e., λ_z, $\psi = k_z z - \omega t$ is the phase of the electron, and $\langle\cdots\rangle$ represents the averaging over the total number of electrons distributed over λ_z and over the beam width Δy in the y-direction. The term $\langle\cos(k_y y)e^{-i\psi}\rangle$ represents a weighted bunching factor, which arises due to interaction of the electron beam with the co-propagating surface mode. Taking the effect of attenuation, the generalized time dependent differential equation for the E can be written as

$$\frac{\partial E}{\partial z} + \frac{1}{v_g}\frac{\partial E}{\partial t} = -\frac{I|E|^2}{v_g w \mathcal{U}}\langle\cos(k_y y)e^{-i\psi}\rangle - \alpha E. \tag{5.10}$$

Here, α is the field attenuation coefficient, which can be calculated by using Eqs. (A.15) and (A.16).

Now, we discuss the longitudinal dynamics of the electron beam. We neglect the transverse motion of the electrons, and write the equations for the evolution of energy and phase of ith electron respectively as:

$$\frac{\partial \gamma_i}{\partial z} + \frac{1}{v}\frac{\partial \gamma_i}{\partial t} = \frac{eE}{mc^2}\cos(k_y y)e^{i\psi_i} + \text{c.c.}, \tag{5.11}$$

$$\frac{\partial \psi_i}{\partial z} + \frac{1}{v}\frac{\partial \psi_i}{\partial t} = \frac{\omega}{c\beta_R^3\gamma_R^3}(\gamma_i - \gamma_R). \tag{5.12}$$

Here, the subscript i represents the ith particle, subscript R represents the resonant particle having velocity same as the velocity of the surface mode, $\beta_R = v_R/c$, $\gamma_R = 1/\sqrt{1-\beta_R^2}$ is the relativistic Lorentz factor, and m is the rest mass of the electron. For the parameters of a CFEL discussed earlier, the ac space charge field does not have any significant effect on the dynamics of the electron beam [142], and we have therefore neglected it in our calculations. Equations (5.10-5.12) can be expressed in a more elegant form by defining the following dimensionless variables [88, 142]:

$$\xi = z/L, \tag{5.13}$$

$$\tau = \left(t - \frac{z}{v_R}\right)\left(\frac{1}{v_g} - \frac{1}{v_R}\right)^{-1}\frac{1}{L}, \tag{5.14}$$

$$\eta_i = \frac{k_z L}{\beta_R^2\gamma_R^3}(\gamma_i - \gamma_R), \tag{5.15}$$

$$\mathcal{E} = \frac{4\pi k_z L^2}{I_A Z_0 \beta_R^2 \gamma_R^3} E, \tag{5.16}$$

$$\mathcal{J} = \frac{4\pi k_z L^3}{Z_0\beta_R^2\gamma_R^3}\frac{I}{I_A}\frac{|E|^2}{v_g w \mathcal{U}}. \tag{5.17}$$

The definition and physical significance of the above mentioned dimensionless variables has already been discussed in the paragraph following Eq. (3.25) in Chapter 3. With these dimensionless variables, the set of Eqs. (5.10-5.12) assumes the following form:

$$\frac{\partial \mathcal{E}}{\partial \xi} + \frac{\partial \mathcal{E}}{\partial \tau} = -\mathcal{J}\langle \cos(k_y y)e^{-i\psi}\rangle - \alpha L\mathcal{E}, \tag{5.18}$$

$$\frac{\partial \eta_i}{\partial \xi} = \mathcal{E}\cos(k_y y)e^{i\psi_i} + \text{c.c.}, \tag{5.19}$$

$$\frac{\partial \psi_i}{\partial \xi} = \eta_i. \tag{5.20}$$

In the limit of a narrow electron beam i.e., $\Delta y \ll w$, and in the small-signal small-gain regime, we can find an approximate analytical solution of the above equations by following a procedure given in Ref. [42]. Neglecting the attenuation effect, and taking the initial detuning parameter

$\eta = 2.6$ to maximize the gain [42], we obtain the expression for the small-signal gain in a single pass operation of the sidewall CFEL as:

$$G = 6.75 \times 10^{-2} \frac{16\pi k_z L^3}{Z_0 \beta_R^2 \gamma_R^3} \frac{I}{I_A} \frac{|E|^2}{v_g w \mathcal{U}} \left(\frac{\sin(k_y \Delta y/2)}{k_y \Delta y/2} \right)^2. \tag{5.21}$$

The expression for $\mathcal{U}/|E|^2$ is given by Eq. (A.12) through which it can be seen that the gain has $e^{-2\Gamma h}$ dependence on the height h of the flat electron beam. Note that, as we move away from the limit $\Delta y \ll w$, the value of gain obtained by numerically solving the Eqs. (5.18-5.20) may no longer be in a good agreement with that obtained using Eq. (5.21). We observe that the above equation is similar to Eq. (3.35) for the gain of a CFEL without any side wall as discussed in Chapter 3, with some notable differences. First, the parameter w appearing in the denominator of the above equation appears as $\Delta y_e = \sqrt{\pi \beta_p \lambda L/4}$ in the corresponding equation [Eq. (3.35)] for the case of a CFEL without any side wall. Here, w is independent of L because of waveguiding, and can be made much smaller compared to Δy_e. Next, by comparing the expression for $\mathcal{U}/|E|^2$ given by Eq. (A.12) with the corresponding equation [Eq. (2.24)] for the case of a CFEL without any side wall, we observe that the value of $\mathcal{U}/|E|^2$ is reduced nearly by a factor of 2 due to the presence of side walls. Thus the effective mode width for the case of a sidewall CFEL can be taken as $w/2$. Also, one can enhance the gain of a sidewall CFEL by n times as compared to the open configuration of a CFEL by choosing the sidewall spacing as $2/n$ times the value of the minimum surface mode width that can be achieved in the absence of waveguiding. However, one cannot take an arbitrary small value of w as it would require an electron beam with very a fine horizontal emittance and also increases the space charge effects. Considering this, we choose $w = (2/3)\Delta y_e = (2/3)\sqrt{\pi \beta_p \lambda L/4}$ such that the gain in a sidewall CFEL can be enhanced by a factor of 3. Finally, we observe that there is a term containing the square of a sinc function on the right hand side of Eq. (5.21). This term is maximum if $\Delta y \to 0$, which means that if all the electrons are at $y = 0$, they experience the peak of the electric field amplitude, and the gain is maximum. Taking the effect of attenuation, there will be a single pass loss $(1 - e^{-2\alpha L})$ in addition to the gain given by Eq. (5.21).

5.1.3 Maxwell-Lorentz equations and small-signal gain for a sidewall Čerenkov FEL driven by a finite-thickness beam

Analysis in the previous section was performed for a CFEL driven by an electron beam having vanishing thickness in the x-direction. In this section, we will generalize our results by explicitly taking into account the finite-thickness of the electron beam in the x-direction. We assume that the thick electron beam can be described as a combination of N_l layers, where the lth layer is at a height $h_l = (2l-1)\Delta x/2N_l$ with current I_l, and thickness $\Delta x_l = \Delta x/N_l$, corresponding to $x \in [(l-1)\Delta x/N_l, l\Delta x/N_l]$. The dimensionless current $\mathcal{J}_l$ for the lth layer is defined as:

$$\mathcal{J}_l = \frac{4\pi k_z L^3}{Z_0\beta_R^2\gamma_R^3}\frac{I_l}{I_A}\frac{|E|^2}{v_g w\mathcal{U}}. \tag{5.22}$$

The electromagnetic surface mode interacts with current in all layers, and the dynamical field equation for the surface mode can be written as:

$$\frac{\partial\mathcal{E}}{\partial\xi} + \frac{\partial\mathcal{E}}{\partial\tau} = -\sum_{l=1}^{l=N_l}\mathcal{J}_l e^{-\Gamma h_l}\langle\cos(k_y y)e^{-i\psi}\rangle_l - \alpha L\mathcal{E}, \tag{5.23}$$

where $\langle\cdots\rangle_l$ indicates averaging over all the electrons present in the lth layer. The Lorentz equations for the energy and phase of ith electron in lth layer are given by:

$$\frac{\partial\eta_i^l}{\partial\xi} = \mathcal{E}\cos(k_y y)e^{i\psi_i}e^{-\Gamma h_l} + \text{c.c.}, \tag{5.24}$$

$$\frac{\partial\psi_i^l}{\partial\xi} = \eta_i^l. \tag{5.25}$$

To find an analytical expression for gain in this case, we proceed as follows. Gain of a CFEL driven by the flat electron beam propagating at height h varies as $e^{-2\Gamma h}$, as discussed earlier. The finite-thickness electron beam with $\Delta x = 2h$, and its centroid at $x = h$ can be equivalently represented by a set of infinite number of flat layers located between $x = 0$, and $x = 2h$, and the gain for the finite-thickness case can be obtained by averaging over all the layers between $x = 0$ and $x = 2h$. This gives us a factor of $(1/2h)\int_0^{2h} e^{-2\Gamma x}dx = (1-e^{-4\Gamma h})/4\Gamma h$. This factor, together with the term $e^{2\Gamma h}$, has to be multiplied in the formula for gain given by Eq. (5.21) to account for the effect of finite beam thickness. We therefore obtain the formula for the small-signal gain as:

$$G = 6.75 \times 10^{-2} \frac{16\pi k_z L^3}{Z_0 \beta_R^2 \gamma_R^3} \frac{I}{I_A} \frac{|E|^2}{v_g w \mathcal{U}} \frac{e^{2\Gamma h}(1 - e^{-4\Gamma h})}{4\Gamma h} \left(\frac{\sin(k_y \Delta y/2)}{k_y \Delta y/2} \right)^2. \tag{5.26}$$

Note that in our analysis, the electron beam is assumed to be uniformly distributed in the region above the dielectric surface in the x-direction. One can also simulate an arbitrary profile of the electron beam by taking different surface current density in different layers.

5.1.4 Numerical simulations

To study the saturation behaviour of the system, we now solve the coupled Maxwell-Lorentz equations numerically by using the leapfrog method [138] as described in Chapter 3. First, we seek a steady state solution of Eqs. (5.18-5.20) for the flat beam case. The input electron beam is taken as a monoenergetic DC beam with η = 2.6, and the initial dimensionless electric field is set to be very small i.e., $\mathcal{E}$=0.001. To save the computation time and memory, we have taken 2^{17} macroparticles, which are significantly less than the number of electrons distributed over one wavelength of the evanescent wave, i.e., $N_{\lambda_z} = I\lambda_z/ev_R = 10^{21}$. In order to simulate a flat electron beam, we have put all the electrons in one layer located at a height h. Further, to model the width Δy of the electron beam, this layer consists of 2^5 arrays, which are equally distributed along the y-direction in the range $(-\Delta y/2, \Delta y/2)$. Each array consists of 2^{12} electrons propagating along the z-direction, and all electrons in one array will see the same magnitude of the electric field depending upon the array position along the y-direction. The energy and phase of electrons evolve in accordance with Eqs. (5.19) and (5.20) respectively. In each array, the electron beam is initialised in the phase space by using the quiet start scheme [139].

The main parameters used in the simulations have been listed in Table 5.1. In the CFEL

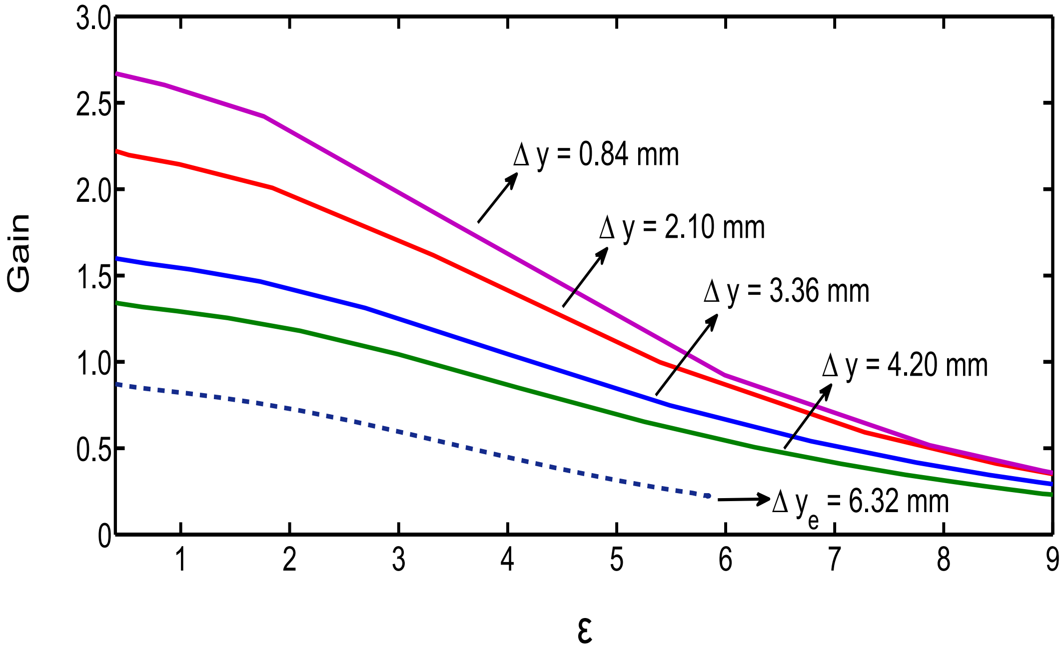

FIGURE 5.4: Plot of net gain as a function of dimensionless input electric field in a single slab based sidewall CFEL driven by a monoenergetic flat electron beam. Dashed curve shows gain plot for a single slab based CFEL without any side wall, and solid curves represent the case of single slab based sidewall CFEL having sidewall spacing w=4.2 mm.

system, the gain has $e^{-2\Gamma h}$ dependence on the height h of the flat beam, and therefore it is desirable that $h \leq 1/2\Gamma$ to have a sufficient beam-wave interaction. Here $\Gamma = 2\pi/\beta_R\gamma_R\lambda$. Using this criteria, we take $h = 1/2\Gamma = 90.0\ \mu$m in our calculations. For the metallic structure, we choose silver metal, which is maintained at 77 K to reduce the ohmic loss. At this temperature, the conductivity of silver is given by $3.3 \times 10^8/\Omega$-m [154], and the Ohmic attenuation coefficient is calculated by using Eq. (A.16) in Appendix A as 1.62 m^{-1}. The value of tangent loss ($\tan\delta$) for GaAs dielectric at 77 K is 2×10^{-5} [120], and by using this value in Eq. (A.15) in Appendix A, we obtain the dielectric attenuation coefficient as 0.11 m^{-1}. The single pass loss $(1 - e^{-2\alpha L})$ due to attenuation in the system is calculated as 15.8%. The sidewall spacing w is taken as $w = (2/3)\sqrt{\pi\beta_p\lambda L/4} = 4.2$ mm. In Fig. 5.4, gain has been plotted as a function of input field for different values of electron beam width assuming an initially mono-energetic and flat electron beam. The dashed curve shows gain of a CFEL without any side wall, and solid curves represent gain of a side wall CFEL for different values of electron beam width Δy. The values of small-signal gain obtained from numerical simulations are in good agreement

TABLE 5.2: Comparison of analytical and simulation results for the net small-signal gain of a single slab based CFEL, assuming different values of electron beam width. Here, $\Delta x = 0$, and $w = 4.2$ mm.

Electron beam width	Analytically calculated gain	Simulation results for gain
6.3 mm(without side walls)	88%	87%
4.2 mm	103%	134%
3.4 mm	152%	160%
2.1 mm	222%	223%
0.84 mm	267%	267%

with the analytical results obtained using Eq. (5.21), and these results have been summarized in Table 5.2. It is observed that in the case of the sidewall configuration of a CFEL, we can obtain an enhancement in gain up to a factor of 3 as compared to the gain of a CFEL without any side wall. For the sidewall configuration of a CFEL, gain is enhanced when we decrease the electron beam width. It can be noted that as we decrease Δy, the agreement between the gain obtained using numerical simulations, and the gain calculated using Eq. (5.21) becomes better. For further simulations discussed in this section, we take the electron beam size in the y-direction as $\Delta y = w/2 = 2.1$ mm.

Next, we take into account the effect of finite beam-thickness in the vertical direction in simulations by following the prescription given in Sec. 5.1.3. We first consider an electron beam of thickness $\Delta x = 2h = 180\ \mu$m with its centroid located at $x = h$. The gap g' between the lower edge of the electron beam and the dielectric surface is taken as zero. The finite-thickness of the electron beam is represented by N_l number of layers distributed along the vertical direction. In our simulations, we have taken $N_l = 4$. We have solved coupled Maxwell-Lorentz equations [Eqs. (5.23-5.25)] for this case, and plotted the results for the gain as a function of dimensionless input field, as shown in Fig. 5.5. The small-signal gain is obtained as 261% for the thick beam case having zero beam-dielectric gap g', which is about 17% higher compared to the case of a flat beam. This is because for a thick electron beam, the enhancement in the gain due to some electrons coming closer to the dielectric surface is significant due to $e^{-2\Gamma h}$ dependence of the gain. This effect has been included in Eq. (5.26) to obtain a modified

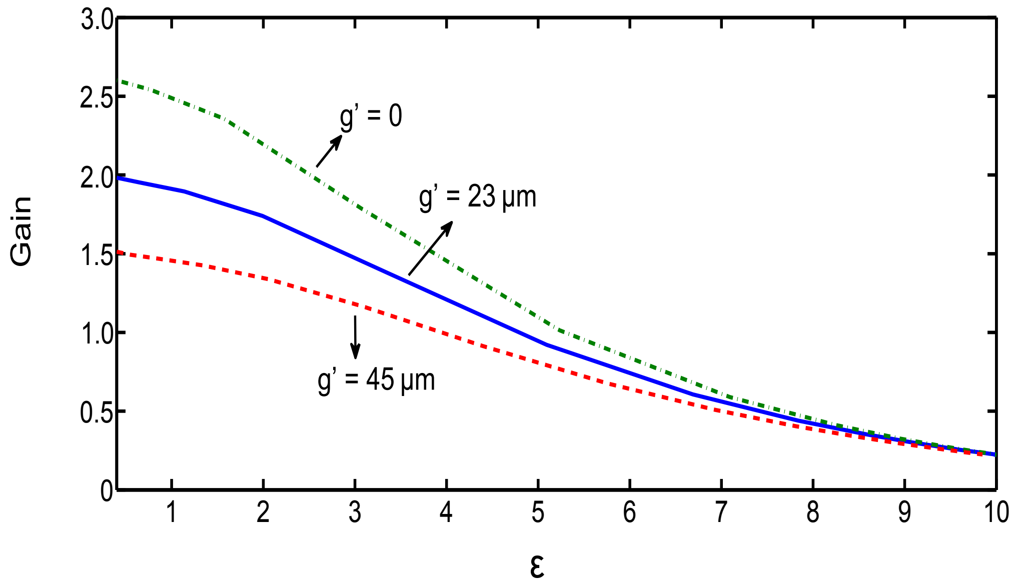

FIGURE 5.5: Plot of net gain as a function of dimensionless input electric field for different values of gap g' between the lower edge of the thick electron beam, and the dielectric surface in a single slab based sidewall CFEL. The electron beam is monoenergetic with Δx=180 μm, and Δy = 2.1 mm.

formula for the gain for the case of finite thickness beam. The numerical results described above are in agreement with this modified formula. We have also varied the gap g' between the lower edge of the electron beam and the dielectric surface. The CFEL gain for $g' = 23$ μm and 45 μm are shown in Fig. 5.5. The vertical thickness of the electron beam is taken as 180 μm. For $g' = 23$ μm, we obtain a small-signal gain of 198%, which is 24% less as compared to the $g' = 0$ case. As expected, the gain decreases exponentially with an increase in the gap g'. We would like to mention that we have also performed the numerical simulations for a thick beam by taking $N_l = 2, 8$ and 12, and observed that for $N_l \geq 4$, the simulation results converge. Most importantly, the converged result for the gain is in good agreement with the gain calculated using Eq. (5.26). For further simulations discussed in this section, we have considered $g' = 23$ μm, and taken $N_l = 4$ to represent the electron beam with a vertical thickness of 180 μm.

We now consider the effect of energy spread in the electron beam. For this, we assume a uniform distribution of electron energy around the mean value. We have considered three cases corresponding to relative rms energy spread of 0.5%, 1.0%, and 1.5%, which correspond to

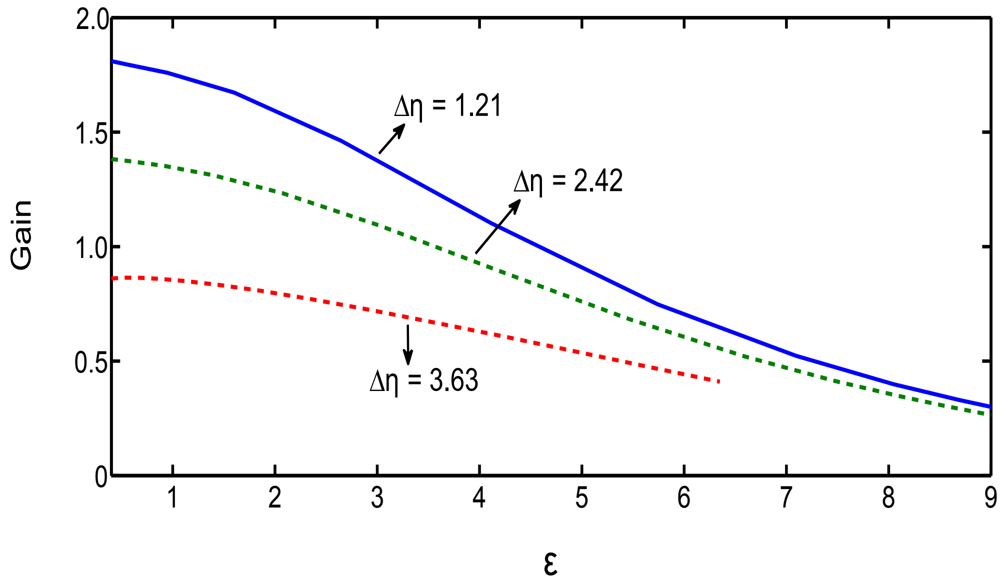

FIGURE 5.6: Plot of net gain as a function of dimensionless input electric field in a single slab based sidewall CFEL driven by a thick electron beam having finite energy spread.

half width in $\Delta\eta$ of 1.21, 2.42, and 3.63 respectively. Note that $\Delta\eta = k_z L \Delta\gamma/\beta_R^2\gamma_R^3$. As shown in Fig. 5.6, we obtain a small-signal gain of 178% for an electron beam having 0.5 % relative rms energy spread. This value of gain is 10% less than the gain for the case of a monoenergetic electron beam. We find that as the energy spread increases, the small-signal gain of the system decreases. For further simulations discussed in the section, we have considered 0.5 % relative rms energy spread. We would like to mention that as in conventional FELs, the effect of transverse emittance can be considered in terms of equivalent energy spread [42]. The equivalent rms energy spread corresponding to a normalized emittance $\boldsymbol{\varepsilon_n}$ is given by $\gamma_R mc^2 \boldsymbol{\varepsilon}_{\boldsymbol{n}}^2/2\sigma_e^2$, where σ_e is the rms beam size. Since the emittance of the electron beam considered in our analysis is very small, the equivalent relative rms energy spread is less than 0.1%, and therefore not significant. However, it is important to note that we need a very low emittance such that a small beam size can be maintained over the interaction length. This condition is particularly important for the vertical direction since we need to maintain a very small beam size in the vertical direction. Larger value of vertical emittance will lead to larger beam size in the vertical direction, resulting in an increase in the height of the beam centroid above the dielectric surface. This will deteriorate the value of gain, and will lead to a $e^{-4\Gamma\sqrt{\varepsilon_x L/\beta_R\gamma_R}}$ type dependence of gain on the normalized rms vertical emittance $\boldsymbol{\varepsilon}_x$ [142].

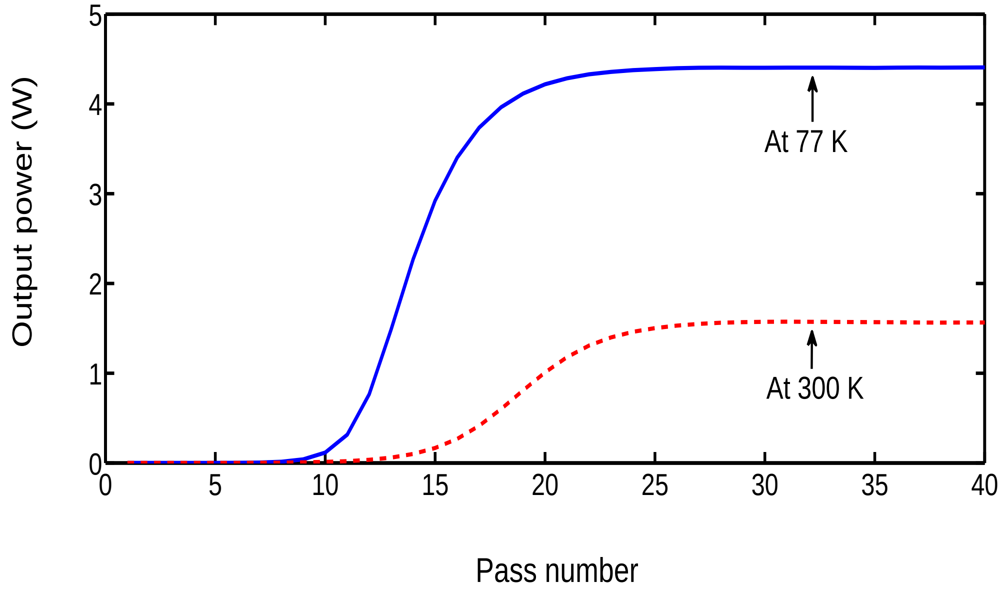

FIGURE 5.7: Plot of output power as a function of pass number for a single slab based sidewall CFEL oscillator, and for a single slab based CFEL oscillator without any side wall. The solid curves represent the case where the dielectric, and the metallic structure are kept at 77 K, whereas the dashed curve shows output power for the case having dielectric, and metallic structure at 300 K.

The sidewall CFEL discussed here is a low gain system, and the device has to be operated in an oscillator configuration to achieve saturation. Using the detailed scheme discussed in the previous chapter, we therefore model the CFEL in an oscillator configuration and solved the coupled Maxwell-Lorentz equations to obtain the power in the surface mode. The solid curve in Fig. 5.7 shows output power as a function of pass number for a sidewall CFEL oscillator, where the temperature of the metallic and the dielectric structure is taken as 77 K. The sidewall CFEL oscillator saturates to give an output power of 4.4 W. For 35 mA current and 40 keV energy, the input electron beam power is given by $P_b = 1.4$ kW. For these parameters, we obtain an efficiency of 0.3% for the sidewall CFEL oscillator, which is in agreement with the theoretically estimated upper bound value of 0.55% as calculated by using Eq. (4.28).

In Fig. 5.7, we have also plotted the output power (dashed curve) of a sidewall CFEL oscillator with its dielectric and metallic structure kept at room temperature (300 K). At 300 K, the conductivity of silver is $6.3 \times 10^7/\Omega$-m [154], and the tangent loss for GaAs is 2×10^{-4} [120]. The total attenuation coefficient is calculated as $\alpha = 4.75$ m^{-1} at 300 K, which results in a round trip loss (in power) of 62%. The system is above the threshold at 300 K, and saturates at an output power of 1.6 W as shown by the dashed curve in Fig. 5.7. The efficiency of the CFEL system is 0.1 % at room temperature, which is around 67% less than the efficiency of the CFEL system at 77 K. This is because the attenuation of the surface mode increases at room temperature, and reduces the output power of the CFEL system.

Next, we would like to discuss that for the case of a waveguided CFEL, we can take a shorter interaction length to improve the performance of the system. As mentioned earlier, by taking a smaller beam size Δy, one can achieve a higher value of gain. However, the condition on the electron beam horizontal emittance becomes stringent at smaller beam size. In order to maintain a given value of electron beam size Δy over the interaction length L, we require that the normalized rms beam emittance should satisfy $\boldsymbol{\varepsilon_y} \leq \beta_R\gamma_R\Delta y^2/16L$ [78]. Similar condition can be written with subscript x in the x-direction. For $L = 5$ cm, we have taken $\Delta y = w/2 = 2.1$ mm, and $\Delta x = 180\ \mu$m, which requires a flat beam with fine beam emittances $\boldsymbol{\varepsilon_y} \leq 2.2 \times 10^{-6}$ m-rad and $\boldsymbol{\varepsilon_x} \leq 1.5 \times 10^{-8}$ m-rad. Hence, to drive the CFEL system, we require an asymmetric electron beam with transverse emittance ratio $\boldsymbol{\varepsilon_y}/\boldsymbol{\varepsilon_x} \sim 150$. The stringent requirements on the beam emittances can be relaxed by taking a smaller interaction length L. The additional advantage is that we can achieve a higher efficiency at small L, as is clear from Eq. (4.28). It is to be noted that with a decrease in L, the gain will decrease. Hence, one has to take an optimum value of L such that the system can overcome the losses. This criterion can be easily achieved in the sidewall CFEL, which has improved gain as compared to a CFEL without side walls. We take $L = 3.5$ cm for a sidewall CFEL for which the net small-signal gain is 85%. We require an electron beam with relaxed transverse emittance ratio of 100 for this case. In Fig. 5.8, the solid curve shows the output power of a sidewall CFEL oscillator with $L = 3.5$ cm. As expected, a CFEL oscillator at shorter interaction length saturates at a higher power of about 7.3 W and has an increased efficiency of 0.52 %. Analysis in the linear as well as in the non-linear regimes shows that guiding of the surface mode in a CFEL is helpful in improving the performance of the system.

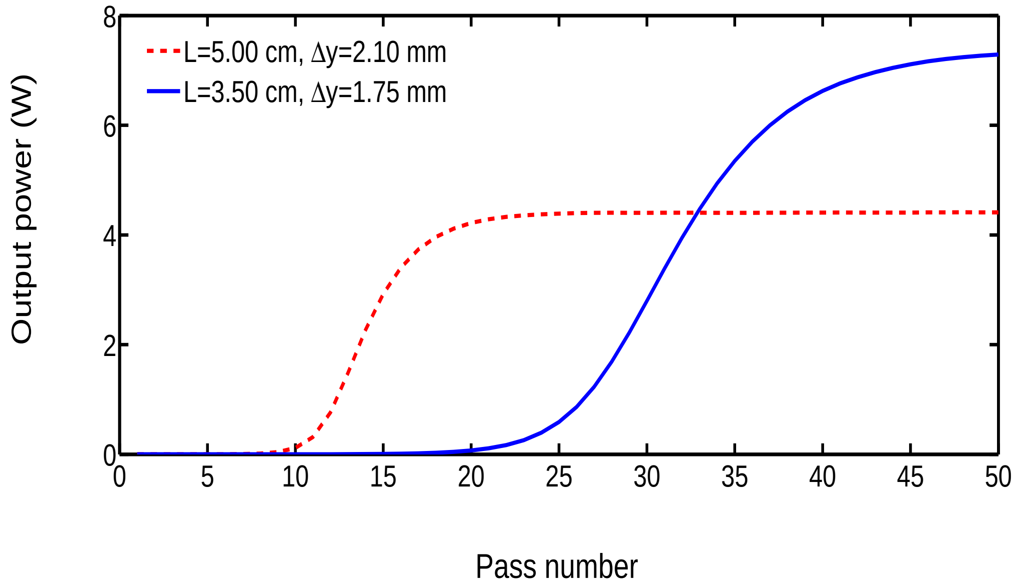

FIGURE 5.8: Plot of output power as a function of pass number in single slab based sidewall CFEL oscillator with its metallic, and dielectric structure kept at 77 K. The dashed and solid curves represent the power of a side wall CFEL with L = 5 cm, and L = 3.5 cm respectively.

5.2 Double-slab based Čerenkov FEL in rectangular waveguide configuration

After studying the effect of waveguiding in a single slab based CFEL, we now analyze the effect of waveguiding in a rectangular waveguide configuration of a double slab based CFEL, which is shown in Fig. 5.2. As compared to the single slab based sidewall CFEL [173], this configuration has an extra dielectric slab supported by the top conducting surface. A relatively simple form of this configuration, i.e., an open configuration (without any side wall) of double slab based CFEL was proposed by Garate *et al*. [128, 174] to generate mm wave in 1980's. Since then, several experimental studies have been performed for the open configuration of a double slab based CFEL at the Dartmouth College, USA [174], ENEA Frascati Centre, Italy [174], and at Osaka Sangyo University and Kansai University in Japan [67]. We have proposed that the metallic side walls can be implemented in an open configuration of a double slab based CFEL, which will be helpful in improving the performance of the above mentioned experiments. We also perform a comparative analysis between the performance of a single slab based sidewall CFEL and a double slab based rectangular CFEL. It is important to mention here that a comparative study of the spontaneous emission spectrum in the open configuration of single and double slab based CFELs was presented by Ciocci *et al.* in Refs. [80, 175]. They suggested that a double slab based CFEL can give an enhanced performance as compared to the single slab based geometry. These analyses were however carried out by neglecting the effect of attenuation due to dielectric losses and Ohmic losses. In this section, we will investigate the performance of a double slab based rectangular CFEL by including the effect of attenuation.

In the following subsection, we will set up the coupled Maxwell-Lorentz equations and obtain small-signal gain for a double slab based rectangular CFEL. The coupled Maxwell-Lorentz equations are solved numerically to obtain the saturation power of the surface mode, and results have been compared with the results of a similar single slab CFEL system.

5.2.1 Theoretical analysis and results

The geometry of a rectangular configuration of a double slab based CFEL with the coordinate system used in our analysis is shown in Fig. 5.2. A rectangular metallic waveguide with inner width w and inner height $2(g + d)$ supports dielectric slabs of thickness d on the top as well as on the bottom surface. Hence the structure is symmetric along both the x- and y-directions. For simplicity, we have assumed a flat electron beam having a vanishing thickness in the x-direction, and width Δy in the y-direction. We will not consider the effect of finite beam thickness here, which, however can be included by following the analysis discussed earlier in Sec. 5.1. The flat electron beam is propagating with a velocity v along the z-direction at a location $x = 0$, and at a distance g from the dielectric surface. As discussed earlier in Sec. 5.1, the expression for electromagnetic surface mode supported by a sidewall configuration of CFEL based on an isotropic dielectric can be obtained by combining the plane wave solutions of an open structure, i.e., without any side wall, in a suitable manner such that it satisfies the boundary conditions. Field components of the lowest order TM surface mode, which satisfy the Maxwell equations with the given boundary conditions, are discussed in detail in Appendix B for the case of a double slab based rectangular CFEL. We find the following expression for the longitudinal electric field E_z^I:

$$E_z^I \quad = \quad E_0 \cosh(px)\cos(k_y y)e^{i(k_z z-\omega t)} + \text{c.c.}, \tag{5.27}$$

Here, $2E_o$ is defined as the peak amplitude of E_z^I at the location of the electron beam at $x = 0$, $k_z = 2\pi/\beta\lambda$ is the propagation wavenumber in the z-direction, $p = \sqrt{k_y^2 + k_z^2 - \omega^2/c^2}$, and $k_y = \pi/w$. For the isotropic dielectric slab, the electromagnetic surface mode given in Eq. (5.27) can be represented as a combination of two plane waves travelling in different directions in the (y, z) plane, each having frequency ω and wave vector $k_0 = \sqrt{k_y^2 + k_z^2}$. The wave vector k_0 here is a solution of the dispersion relation $a_p \tan(k_0 b_p)\tanh(k_0 g/\gamma_p) = 1$ [128] for the open configuration of a double slab based CFEL [81, 84, 142]. Here, $a_p = (\gamma_p/\epsilon)\sqrt{\epsilon\beta_p^2 - 1}$, $b_p = d\sqrt{\epsilon\beta_p^2 - 1}$, $\beta_p = \omega/ck_0$, and $\gamma_p = 1/\sqrt{1-\beta_p^2}$. This dispersion relation can be solved numerically to obtain the resonant wavelength ($\lambda_p = 2\pi/\beta_p k_0$) of the open configuration of a double slab CFEL. Using this information and the property that the dielectric slabs are isotropic structures in the (y, z) plane, we obtain the resonant wavelength of a rectangular configuration of double slab based CFEL as

$$\lambda = \frac{2\pi}{\beta\sqrt{[2\pi/\beta_p\lambda_p]^2 - [\pi/w]^2}}. \tag{5.28}$$

Above equation has been solved for the parameters listed in Table 5.3. These parameters are similar to the one considered for the single slab based sidewall CFEL, except that the gap $2g$ between the two dielectric slabs is here taken as 180 μm, which is same as the vertical size of the electron beam. We obtain the resonant frequency of 0.12 THz for these parameters.

Next, we extend our approach based on the coupled Maxwell-Lorentz equations to study the beam-wave interaction in a double slab based rectangular CFEL. For this, we have followed the approach discussed earlier in Sec. 5.1.2, and obtain the following dynamical equation for the longitudinal field:

$$\frac{\partial E}{\partial z} + \frac{1}{v_g}\frac{\partial E}{\partial t} = -\frac{I|E|^2}{P}\langle\cos(k_y y)e^{-i\psi}\rangle - \alpha E. \tag{5.29}$$

Note that we have assumed the longitudinal field E to be a slowly varying function of z and t while deriving the above equation, and have substituted $wv_g\mathcal{U} = P$. The expression for $P/|E|^2$ for a double slab based rectangular CFEL is given by Eq. (B.20) in Appendix B. Here, α is the field attenuation coefficient, which can be obtained by using Eqs. (B.22) and (B.23) given in Appendix B for the case of the double slab based rectangular CFEL. The electron beam will evolve under the influence of the dynamical field given by Eq. (5.29). The equations for the evolution of energy and phase of the ith electron can be written in a way similar to the Eqs. (5.19) and (5.20). In the small-signal small-gain regime and in the limit of a narrow electron beam i.e., $\Delta y \ll w$, we find an approximate analytical solution of the coupled Maxwell-Lorentz equations by following a procedure described earlier in the chapter. By neglecting the attenuation effects, we obtain the expression for the maximum small-signal gain in a single pass operation of the double slab rectangular based CFEL as:

$$G = 6.75 \times 10^{-2} \frac{16\pi k_z L^3}{Z_0 \beta_R^2 \gamma_R^3} \frac{I}{I_A} \frac{|E|^2}{P} \left(\frac{\sin(k_y \Delta y/2)}{k_y \Delta y/2} \right)^2. \tag{5.30}$$

Note that the form of the above equation is similar to the form of corresponding Eq. (5.21) for the case of a single slab based sidewall CFEL. Here, we have to use Eq. (B.20) given in Appendix B for the case of a double slab based rectangular CFEL, to evaluate the term P/E^2. As discussed earlier, we chose the sidwall spacing as $2/3$ times the minimum surface mode width.

Next, we would like to compare the performance of the following two waveguided configurations of the CFELs- (i) single slab based sidewall CFEL discussed in Sec. 5.1, and (ii) double slab based rectangular CFEL discussed in this section. For this purpose, we perform analytical calculations by taking a monoenergetic flat electron beam having a width $\Delta y = w/2$ in both the cases. The metallic structure and the dielectric medium are maintained at 77 K. For the parameters listed in Table 5.3 and taking $\Delta y = w/2 = 2.1$ mm, we find the small-signal gain using Eq. (5.30) as 286%. Taking the effect of attenuation, we obtain a single pass loss of about 31%, which reduces the small-signal gain of the double slab based rectangular CFEL to 255%. This value is 15% higher than the net gain of 222% in the single slab based sidewall CFEL

TABLE 5.3: Parameters of double slab based rectangular CFEL used in the calculation

Electron-beam energy	40.0 keV
Electron-beam current (I)	35 mA
Dielectric constant (ϵ)	13.1
Length of dielectric slabs (L)	5 cm
Dielectric slab thickness (d)	265 μm
Vacuum-gap between slabs ($2g$)	180 μm
Waveguide width (w)	4.2 mm
Operating frequency	0.12 THz

with similar parameters. The improvement in the net gain in the double slab based rectangular CFEL is due to the confinement of the surface mode in the vertical direction due to the presence of an extra dielectric slab on the top conducting surface as compared to the single slab based sidewall CFEL, which is open in the vertical direction. Our results indicate that a double slab rectangular CFEL has better performance as compared to the single slab based sidewall CFEL in the single pass operation. However, to reach the saturation, both these devices have to be operated in the oscillator configuration. In the oscillator configuration, there will be an additional attenuation of the surface mode during its backward propagation from the end point to the beginning of the dielectric slab. The attenuation effects during the round trip are prominent in a double slab based rectangular CFEL that has 31% loss during the backward propagation of the electromagnetic field, which is twice the corresponding value of 15% in a single slab based CFEL, for the considered parameters. Due to the presence of higher losses, the output power and efficiency of a double slab based rectangular CFEL is expected to reduce significantly in the oscillator configuration as compared to the single slab based sidewall CFEL. To investigate this, we have solved the coupled Maxwell-Lorentz equations numerically for the double slab based rectangular CFEL by using the leapfrog scheme, and compared the results with the case of a single slab based sidewall CFEL. As shown by the solid curve in Fig. 5.9, the double slab based rectangular CFEL saturates to give an output power of about 2.8 W at a saturation efficiency of 0.2%, which are about 42% less than that of a single slab based sidewall CFEL, as represented by dashed curve.

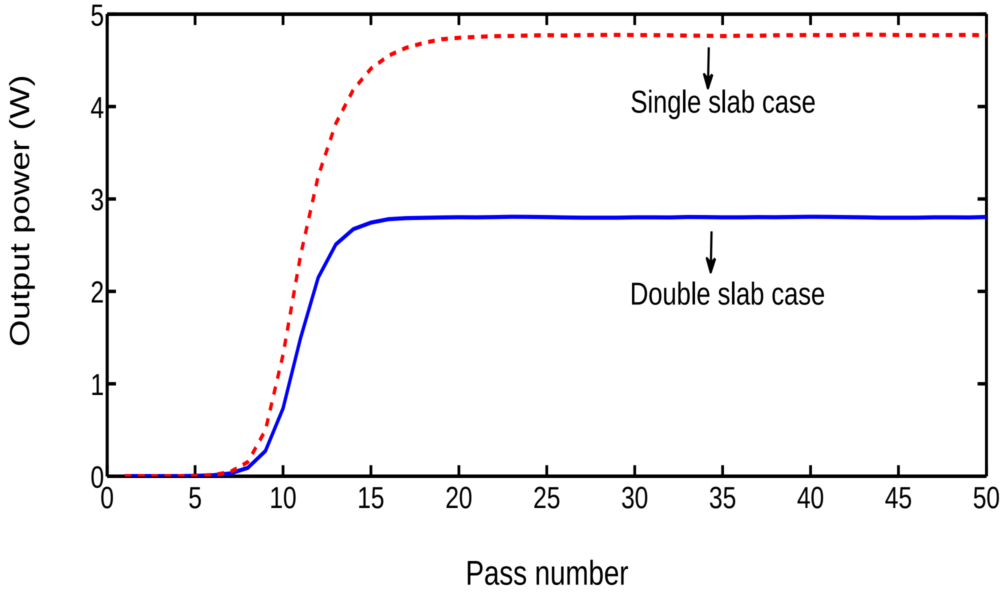

FIGURE 5.9: Plot of power as a function of pass number in the waveguided configuration of slab-type CFELs. For the parameters discussed in the text, the solid curve shows power of a double slab based rectangular CFEL and the dashed curve shows power of a single slab based sidewall CFEL.

5.3 Discussions and conclusion

In this chapter, we have studied the effect of waveguiding in the single slab as well in the double slab configurations of CFELs by setting up the coupled Maxwell-Lorentz equations. The waveguiding provided by the metallic side walls is very useful to enhance the performance of a CFEL at longer wavelengths, where diffraction effects are prominent and cause a reduction of gain. Due to waveguiding, we can reduce the mode width below the minimum possible value that can be achieved in the absence of waveguiding. Hence, we can achieve higher gain as well as higher saturation power as compared to the CFEL system without any waveguiding. We also observed that the stringent requirements on electron beam emittances also get relaxed in the waveguided CFELs as compared to the corresponding open configurations. Hence, our analysis can be very useful in improving the performance of ongoing experiments on the single slab and double slab based CFELs by implementing waveguiding in them.

It is interesting to point out here that the electromagnetic surface mode supported in the proposed waveguided configuration has a $\cos(k_y y)$ variation along the y-direction, where k_y =

π/w for the fundamental mode, and has maximum amplitude at the middle of the dielectric, i.e., $(y = 0)$. For a very narrow electron beam, most of the electrons are at $y = 0$ and will experience the peak of the electric field amplitude resulting in an effective exchange of energy. This gain peaking effect is observed to become more pronounced as we decrease the transverse width Δy of the electron beam in the single as well as in the double slab based waveguided CFELs. Higher order modes corresponding to $k_y = (2n + 1)\pi/w$ will not have a good overlap with the electron beam in these configurations, and will not be able to exchange energy with the electron beam in an effective manner. We have therefore not considered these modes in our analysis.

Based on the results obtained in this chapter, we have compared the performance of a single slab based sidewall CFEL and a double slab based rectangular CFEL. We find that a marginally higher single pass gain can be achieved in a double slab based rectangular CFEL as compared to a single slab based sidewall CFEL, because of the vertical confinement of the surface mode in the presence of an extra dielectric slab supported by the top conducting surface. However, dielectric and Ohmic losses also increase by a factor of 2 in the double based rectangular CFEL, which reduces the net gain in the round trip in an oscillator configuration, and this system becomes less efficient than a single slab based sidewall CFEL. We would like to mention that the performance of a double slab based rectangular CFEL can be further optimized by independently changing the slab thickness and the relative dielectric permittivity of the top and the bottom dielectric slabs, which we have not considered in this chapter. An independent variation of system parameters of the top and the bottom dielectric slabs will make this configuration an asymmetric one. An open configuration of a double slab based asymmetric CFEL has been studied by Sharma and Mishra in Ref. [102]. Our analysis for the waveguided CFELs can be extended for this configuration too, which may be taken up in the future.

To explore the viability of a compact single slab based sidewall CFEL in more realistic conditions, we have included several realistic effects, i.e., finite beam size, finite beam emittance, and finite energy spread. We find that a single slab based sidewall CFEL with length $L = 3.5$ cm and spacing between the side walls as 3.5 mm, can be operated at 0.11 THz by using a 40.0 keV, 35 mA electron beam to give output power of 7.3 W with an efficiency of 0.5 % at saturation.

The relative rms energy spread is taken as 0.5 % for a 180 μm thick electron beam. It is to be noted that we have not considered the fluctuations in the dielectric slab properties (relative permittivity, slab uniformity), which can reduce the gain as well as the saturated power [176, 177]. We can however estimate the tolerable fluctuations of liner thickness and relative permittivity along the length of the dielectric. For a given beam energy, if we vary the liner thickness d, or relative permittivity ϵ, the resonant wavelength will change along the length. Like in the case of conventional FEL, this will result in a spread in the detuning parameter η, and therefore gain will decrease. In order to ensure that the gain does not deteriorate significantly, it is required that the spread in η is much less than 2π. Using this criterion, we have estimated that the tolerable fluctuation in liner thickness and relative permittivity are around 10 μm and 5% respectively for the above mentioned CFEL parameters.

To conclude, we have performed a detailed analysis of the single and double slab based CFEL systems with metallic side walls by setting up coupled Maxwell-Lorentz equations. CFELs with metallic side walls are shown to have a gain significantly higher than the CFELs without side walls. In contrary to the results obtained for the single pass operation, we observed that a single slab based sidewall CFEL has an enhanced performance compared to the double slab based rectangular CFEL in the oscillator configurations.

Chapter 6

Terahertz undulator radiation using a high-power industrial linac

In the previous chapters, we have theoretically investigated the planar configuration of CFELs and SP-FELs for the generation of coherent THz radiation, taking the deleterious effect of diffraction and attenuation into account. These devices support surface modes, which are confined very close to the dielectric or grating surface in the vertical direction. The electron beam therefore needs to have a very small vertical size such that it can propagate very close to the dielectric or grating surface and can interact efficiently with the surface mode. Maintaining a small vertical size over the full interaction length requires a very small vertical emittance. In the horizontal direction, requirement on the beam emittance depends upon the diffraction effects and is observed to be less stringent. Hence, one requires a specially designed flat electron beam having very small vertical emittance and large horizontal emittance to generate THz radiation from a CFEL and a SP-FEL, which are yet to be demonstrated [78]. Another device, which converts the kinetic energy of electrons into coherent electromagnetic radiation is an undulator based FEL system, where a *relativistic* electron beam is passed through an undulator immersed in a quasi-optical resonator. THz radiation is produced in the undulator based FEL due to interaction of the electron beam with the on-axis, static transverse magnetic field, varying sinusoidally along the undulator axis, in the presence of an electromagnetic field building up in the resonator cavity [43]. Note that in contrast to a CFEL and an SP-FEL, where the electron beam interacts with the surface mode confined in the close vicinity of the dielectric or the grating surface, the electron beam here couples, via the static magnetic field of undulator, with a freely propagating electromagnetic mode. This implies that the electron beam size and therefore the electron beam emittance can be relatively relaxed in an undulator based FEL compared to a CFEL or an SP-FEL. However, the gain of an undulator based FEL depends strongly on the electron beam size and energy spread, and a very high peak beam current is required to achieve a reasonable gain [42]. The electron beam needs to have a very short pulse duration ($\sim$ picoseconds) to achieve such a high peak beam current. Typically, a low average power electron beam with very fine energy spread and emittance is used to generate powerful THz radiation in an undulator based FEL system through coherent stimulated emission. The infrastructure needed to meet these requirements is quite complex, which makes these devices impractical for table top THz experiments.

Recently, there has been a lot of interest in making high average power (up to 100 kW) industrial electron linear accelerators (linac) for various industrial applications such as polymer reforming, materials irradiation, and for pasteurization of food products [107–109]. A high energy ($\sim$ 10 MeV) electron beam is favourable for the irradiation processes due to its high penetration depth. A beam energy higher than 10 MeV is not allowed for food irradiation applications due to radiation safety issues. The quality of the electron beam from a typical industrial linac may not be very good for the operation of a free-electron laser, but when such a high average power electron beam passes through an undulator, it can emit copious amount of THz radiation even through spontaneous emission. This radiation can fulfil the requirements of many scientific applications, such as imaging of biological samples, inspection of packages and analyzing chemical composition of materials [19, 178, 179]. After the spontaneous emission of THz radiation in an undulator, the spent electron beam can *still* be used for the irradiation application, which gives us two fold advantage. An experimental observation of THz radiation from undulator through spontaneous emission by using a 2 mA, 7.5 MeV electron beam has been reported recently in Ref. [180]. In this chapter, we have performed analytical as well as

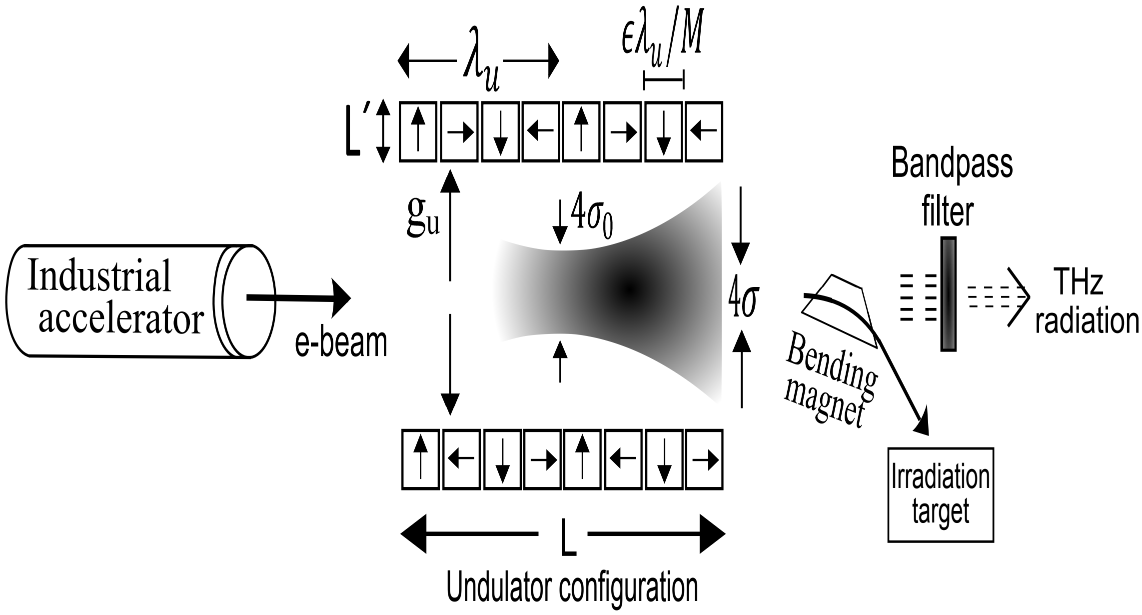

FIGURE 6.1: Schematic of a device based on a high average power industrial linac and an optimized undulator, to produce THz radiation along with the intended irradiation applications.

numerical calculations to estimate the power of emitted spontaneous radiation when an electron beam emerging from a high average power industrial linac dedicated for irradiation applications is passed through an undulator with optimized parameters.

In the next section, we discuss the theoretical analysis of the undulator radiation and present the calculations of magnetic field of a pure permanent magnet (PPM) based undulator. By taking an example case of parameters of a high average power industrial electron linac, we perform a detailed optimization of the parameters of the undulator to obtain useful THz radiation in Sec. 6.2. In Sec. 6.3, we present results of numerical simulations by using a computer code GINGER [181]. Finally, we conclude with a discussion of results in Sec. 6.4.

6.1 Theoretical analysis

A schematic of a THz device based on a high average power industrial linac and an undulator is shown in Fig. 6.1. A high energy electron beam emerging from a powerful industrial linac is allowed to pass through an undulator, before being directed on the target to be irradiated. It will generate a useful THz radiation in the undulator through spontaneous emission. The proposed system is a single pass system, i.e., without any optical resonator. Hence, we will perform an analysis for the calculation of power radiated through spontaneous emission in the single pass operation. The undulator is assumed to consist of N_u number of periods having a period length λ_u. A detailed analysis for the motion of electron beam in the undulator is already available in the literature [42, 110, 111, 113, 182, 183], and we can write the expression for the energy radiated per unit frequency width dω per unit solid angle dΩ by a system of N electrons in a bunch, along the direction of unit vector $\boldsymbol{n}$ as [182]:

$$\frac{d^2\mathcal{I}}{d\omega d\Omega} = [N + (N^2 - N)f(\omega)]\frac{e^2\omega^2}{16\pi^3\epsilon_0 c^3}\left|\int_{-\infty}^{\infty} \boldsymbol{n}\times(\boldsymbol{n}\times\boldsymbol{v})e^{i(\omega t - k_R \boldsymbol{n}.\boldsymbol{r})}dt\right|^2. \tag{6.1}$$

Here, $\omega = ck_R$ is the angular frequency of the emitted radiation, k_R is the wavenumber of light, c is the speed of light, e is the electronic charge, ϵ_0 is permittivity of free space, $\boldsymbol{r}$ and $\boldsymbol{v}$ represent the instantaneous position and velocity respectively of the electron bunch centre that evolves due to interaction with the undulator field, $f(\omega) = |\int e^{i\omega r/c}S(\boldsymbol{r})d^3r|^2$ is a form factor, which describes coherence of the emitted light, and $S(\boldsymbol{r})$ is a continuous normalized density distribution function of the electron bunch such that the factor $NS(\boldsymbol{r})d^3r$ gives the probability of finding an electron in the region d^3r around $\boldsymbol{r}$. The total power radiated by an electron beam passing through an undulator will depend upon the bunch length of the electron beam. If the electron bunch length is significantly greater than the wavelength of light, then the form factor $f(\omega) = 0$ represents the incoherent limit and the emitted power will be N times the result from a single electron [182]. This is known as incoherent spontaneous emission or simply spontaneous emission (SE). For the electron bunch length shorter than the wavelength of light; form factor $f(\omega) = 1$ represents the coherent limit and the power radiated by the electron beam will be N^2 times the result of a single electron [182]. This is known as coherent spontaneous emission (CSE). Thus, a pre-bunched electron beam with bunch length smaller than the wavelength of light can generate high power, coherent THz radiation, when passed through an undulator[184, 185]. This scheme has been used in a Compact Advanced Terahertz Source (CATS) at ENEA, Italy to generate THz radiation [186]. However, this approach requires an electron beam with low energy spread, and an additional RF cavity to produce a pre-bunched electron beam. Moreover, the performance of the system is critically dependent on the shape of the electron bunch [38–40, 187]. In the scheme proposed in this chapter, we are considering the situation where the electron beam bunch length is significantly greater than the wavelength of light, which is the case of spontaneous emission. The finite energy spread of the electron beam also affects the radiation emitted when the electron beam passes through the undulator. In the case of lasing in an FEL, the gain resulting due to stimulated emission is very sensitive to the electron energy and therefore, one requires a high quality electron beam with low energy spread to maintain the resonance condition of the system [188, 189]. In the proposed system, the electron beam emerging from the industrial linac has high relative energy spread (around 10%) and large pulse duration (~ 0.5 ms). When this electron beam passes through an undulator, the output radiation will be generated only through spontaneous emission, unlike in the case of FELs where it is through stimulated emission. It is to be noted that if the energy spread of the electron beam is large, the intensity spectrum in the case of spontaneous emission of radiation will be broad, keeping the total output power nearly the same [190]. The relative frequency width $\delta\omega/\omega$ due to the energy spread is $2\delta\gamma/\gamma$, where γ is the energy of the electron beam in units of its rest mass energy.

It may be in order to explain here some of the important features of the undulator radiation spectrum. The characteristics of the undulator radiation spectrum can be analyzed by studying the motion of electron [110, 111, 191]. In the presence of undulator magnetic field, the electron undergoes a periodic transverse deflection with maximum angular excursion given by K/γ, where $K = eB_0/k_u mc$ is the deflection parameter or peak value of the undulator parameter, B_0 represents peak on-axis undulator magnetic field, $k_u = 2\pi/\lambda_u$, and m is the rest mass of the electron. Due to this periodic deflection, the average longitudinal velocity of the electron gets reduced to $c\sqrt{1 - 1/\gamma^{*2}}$ [191], following the law of energy conservation. Here, $\gamma^* = \gamma/\sqrt{1 + K^2/2}$. Over and above this average value, the longitudinal velocity will have an oscillatory component too. In a frame of reference moving with the electron's average longitudinal velocity, the electron executes a simple harmonic motion in the transverse direction, and acts like an oscillating dipole. It will have a doughnut-like angular distribution of the radiated

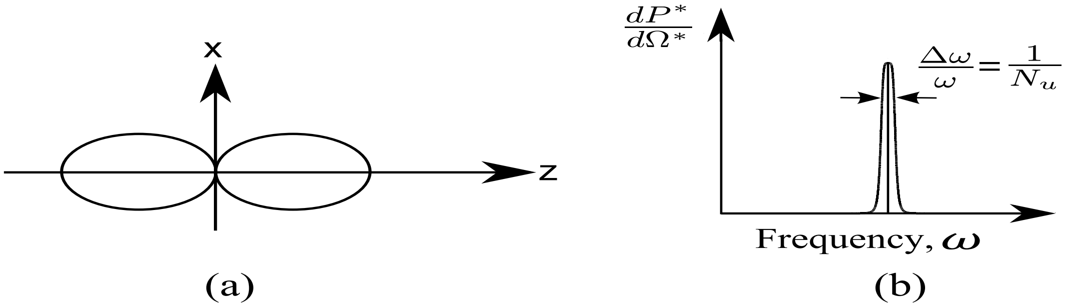

FIGURE 6.2: (a) Schematic representation of the radiation pattern of an oscillating electron in the frame of reference moving with electron's average velocity in an undulator. (b) The radiation spectrum in this frame is narrow with a spectral band width $1/N_u$.

power as shown in Fig. 6.2(a)[191]. In this reference frame, an electron will emit radiation with a narrow relative spectral bandwidth of the order of $1/N_u$, as shown in Fig. 6.2(b). For the case when N_u is very large, i.e., $N_u \to \infty$, the emitted radiation spectrum from the relativistic electron ($v \simeq c$) will be like a delta function at wavelength $\lambda^* = \lambda_u/\gamma^*$, which is contracted by a factor γ^* from the undulator period. Note that in this reference frame, the electron radiates at the same frequency in all directions. Now, upon the transformation to the laboratory frame, the radiated power gets confined into a half angle $\theta \simeq 1/2\gamma^*$ around the direction of motion as shown in Fig. 6.3(a). The radiation spectrum undergoes a Doppler shift to a higher frequency, and more importantly, this spectrum gets broadened due *angle dependent* Doppler effects. The Doppler shifted wavelength in the laboratory frame is given by

$$\lambda_R^\theta = \frac{\lambda_u}{2\gamma^{*2}}\left(1 + \gamma^{*2}\theta^2\right), \tag{6.2}$$

where θ is the observation angle measured form the direction of motion. Note that the second term is responsible for the angle dependent broadening in the radiation spectrum. A schematic illustration for the undulator radiation spectrum in the laboratory frame of reference has been shown in Fig. 6.3(b). It can be seen that the natural spectral width ($\sim 1/N_u$) of the undulator radiation spectrum in the electron's reference frame gets broadened considerably upon the transformation into the laboratory frame due to the off-axis Doppler effects. A practical choice of interest is to select the near-axis radiation, as shown in Fig. 6.3(c), which is quasi-monochromatic

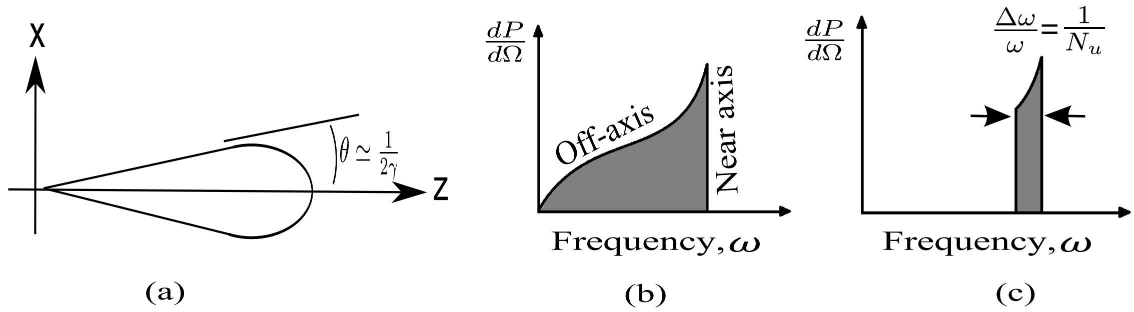

FIGURE 6.3: (a) Schematic representation of the radiation pattern of a relativistic electron in the laboratory frame during its motion inside an undulator. In this case the radiation gets confined in a cone having semi angle $1/2\gamma$. (b) The radiation spectrum seen in the laboratory frame in an undulator. The wavelength gets shorter and the radiation spectrum gets broader due to the angle dependent Doppler effects. (c) The selection of near axis radiation having natural bandwidth $\Delta\omega/\omega = 1/N_u$ in the laboratory frame, where N_u is the number of undulator periods.

in nature with a narrow spectral bandwaidth, and is useful for the spectroscopy and imaging related applications. Since the undulator radiation has a natural spectral width of $1/N_u$, it is more useful to select the radiation having the natural spectral bandwidth $\Delta\lambda/\lambda \simeq 1/N_u$, by using a monochromator in the path of the radiation on the axis. This radiation is contained in a very narrow cone, known as the *central radiation cone* having half angle θ_{cen} around the beam-axis. The half angle θ_{cen} can be estimated by requiring that the additional spectral width of the radiation emitted within the central cone due to angle dependent Doppler effect is equal to the natural width, i.e., $1/N_u$. This gives us the following expression for θ_{cen}:

$$\theta_{cen} = \frac{1}{\gamma^* \sqrt{N_u}}. \tag{6.3}$$

Note the appearance of N_u in the above equation. Typically N_u is large, which means that the central radiation cone is confined into a very small angle around the beam axis. The electromagnetic radiation is quasi-monochromatic around the beam axis, with on-axis central wavelength given by:

$$\lambda_R = \frac{\lambda_u}{2\gamma^2}\left(1 + \frac{K^2}{2}\right). \tag{6.4}$$

Th electromagnetic radiation inside the central radiation cone can be selected by using a narrow bandpass filter in the path of the output radiation as shown in Fig. 6.1. For the case of spontaneous emission by N electrons in a beam having beam current I, the average power in the central radiation cone for an arbitrary K is given by [110]:

$$P_{cen} = \frac{\pi e\gamma^2 I}{\epsilon_0\lambda_u}\frac{f(K)K^2}{(1+K^2/2)^2}, \tag{6.5}$$

where $f(K) = [J_0(x) - J_1(x)]^2$, J_0 and J_1 are zeroth and first order Bessel function of first kind respectively, and $x = K^2/(4+2K^2)$. Note that the power emitted in the central radiation cone goes as square of the beam energy for a relativistic electron beam. Therefore higher energy beams are preferred for the generation of radiation through spontaneous emission. Note that the above mentioned power in the central radiation cone is far less than the total power radiated in all harmonics, integrated over all wavelengths, and angles, which is given by $P_T = \pi e\gamma^2 I N_u K^2/3\epsilon_0\lambda_u$ [110, 111].

Another important property of electromagnetic radiation is the spectral brightness, which is defined as the photon flux per unit area and per unit solid angle at the source within a relative bandwidth of 0.1%. This quantity is conserved in a perfect optical system, and is very important for the imaging related applications. A higher brightness is desired to obtain high-resolution images. In the case of undulator radiation spectrum, as we move away from the beam axis, the brightness of radiation decreases [111], which makes the off-axis radiation less useful for experiments. On the axis, however, the brightness of radiation is high due to a very narrow spectral bandwidth. The expression for the on-axis spectral brightness of undulator radiation is given by [110, 111]

$$\mathcal{B}_{(\Delta\omega/\omega)} = \frac{7.25\times 10^6 \times \gamma^2 I(\mathrm{A}) N_u^2 K^2 f(K)}{\sigma_T^2(\mathrm{mm}^2)(1+\sigma_e'^2/\theta_{cen}^2)(1+K^2/2)^2}\frac{\mathrm{photons/s}}{\mathrm{mm^2 mrad^2}\ (0.1\%\ \mathrm{BW})}, \tag{6.6}$$

where I is in amperes, $\sigma_T = \sqrt{\sigma_e^2+\sigma_0^2}$ is the rms source size of the undulator radiation in millimeters, σ_e is the rms electron beam size, σ_0 is the rms beam waist of radiation, and σ_e' is the rms beam divergence. Note that above formula is valid for a monoenergetic electron beam having very small divergence, i.e., $\sigma_e^{'} \ll \theta_{cen}$. For the case $\sigma_e^{'} \simeq \theta_{cen}$, Eq. (6.6) overestimates the brightness by a factor of 2, and we need to use numerical simulations for more accurate estimate of the spectral brightness [111].

The emitted radiation while propagating along the direction of the electron beam, can be out-coupled by putting a window at the end of the interaction region, and can be used for experiments. The radiation beam will undergo diffraction in the transverse direction. A rigorous analysis for the representation of the undulator radiation with diffraction effects has been recently given by Lindberg and Kim [183]. In the central radiation cone, which is the region of our interest in this chapter, authors in Ref. [183] have shown that the electron beam generates a freely diffracting Gaussian radiation beam having rms beam waist size $\sigma_0 = \sqrt{\lambda_R L}/2\pi$, and rms beam divergence $\sigma_0' = (1/2)\sqrt{\lambda_R/L}$ [183], where L is the length of the undulator. In this analysis, the beam waist is assumed to be formed at the centre of the undulator. As we move away from the centre of the undulator, the beam size increases due to diffraction, which is described here in terms of Rayleigh range $Z_R = L/\pi$ [183]. The rms beam size σ at the exit of the undulator is given by $\sigma = \sigma_0\sqrt{1 + (L/2Z_R)^2}$. Note that this calculation assumes an electron beam of negligible size and divergence. Taking a finite size and divergence for the electron beam, the formulae for the rms beam size at the waist and the rms beam divergence get modified as $\sigma_T = \sqrt{\lambda_R L/4\pi^2 + \sigma_e^2}$, and $\sigma_T' = \sqrt{\lambda_R/4L + \sigma_e'^2}$ respectively [110]. We would like to mention that the effect of finite electron beam size and divergence is not very significant if the unnormalized rms electron beam emittance ε_{un}, which can be understood as product of rms electron beam waist size and divergence, is much less than $\lambda_R/4\pi$, which is the product of rms optical beam waist size and divergence [110]. In terms of normalized rms beam emittance ε_n, this criterion can be expressed as $\varepsilon_n \ll \beta\gamma\lambda_R/4\pi$, where β is the speed of electron in units of speed of light.

In order to ensure that the radiation beam does not hit the vacuum chamber of the undulator, the undulator gap g_u should be chosen sufficiently greater than the total beam diameter at the undulator exit, i.e., four times the rms beam size σ. Here, one has to keep in mind that increase in g_u value will diminish the on-axis undulator magnetic field since it is proportional to

$\exp(-k_u g_u/2)$ [42]. One needs to optimize the magnetic field strength together with the undulator length such that the beam diameter at the undulator exit remains sufficiently less than the undulator gap g_u. The expression for the peak undulator field B_0 for the Halbach configuration of a pure permanent magnet (PPM) based undulator is given by [42]:

$$B_0 = 2B_{rem}e^{-k_u g_u/2}(1 - e^{-k_u L'})\frac{\sin(\epsilon\pi/M)}{\pi/M}. \tag{6.7}$$

Here, B_{rem} is the remnant field of the PPM, and has value 1.1 T for NdFeB magnets [158], M is the number of magnets required to complete one period, L' represents the height of the magnet, and width of the magnet is $\epsilon\lambda_u/M$. The schematic of the Halbach configuration of the undulator is shown in Fig. 6.1. In the most common configuration, $M = 4$, $\epsilon = 1$ and $L' = \lambda_u/4$. Using these values in Eq. (6.7), we obtain the peak magnetic field in an undulator as [42]:

$$B_0 = 1.57 \times \exp\left(-\frac{\pi g_u}{\lambda_u}\right). \tag{6.8}$$

The expression for the peak value of undulator parameter K is given by:

$$K = 1.48 \times \lambda_u(\mathrm{cm}) \times \exp\left(-\frac{\pi g_u}{\lambda_u}\right). \tag{6.9}$$

The analysis which we have presented in this section for the spontaneous emission of THz radiation in an undulator will be helpful in obtaining the parameters of a practical device, as described in the following section.

6.2 An example case

To perform the calculations, we now take an example case of a high average power industrial linac, and optimize the parameters of undulator in accordance with the analysis described in the previous section. The considered parameters in our calculations are listed in Table 6.1, which are close to the parameters of the ILU-14 linac operating in Budker Institute of Nuclear Physics,

TABLE 6.1: Linac parameters used in our calculations. These parameters are taken from "ILU-14 industrial electron linear accelerator with a modular structure" by A. A. Bryazgin *et al.*, 2011, Instruments and Experimental Techniques, **54**, pp. 295-311. Copyright © Pleiades Publishing, Ltd., 2011.

Electron beam energy	10 MeV
Beam peak current	480 mA
Beam pulse duration	420 μs
Repetition rate	50 Hz
Average beam current (I)	10 mA
Average beam power	100 kW
Relative rms energy spread ($\delta\gamma/\gamma$)	7%
Electron beam diameter ($4\sigma_e$)	2.4 mm
Normalized beam emittance (ε_n)	30 mm-mrad

Russia [109, 192]. This device is a pulsed linac having the electron beam energy in the range 7.5 to 10 MeV, average beam current of 10 mA, and average power up to 100 kW. The relative rms energy spread $\delta\gamma/\gamma$ for this system is around 7% [109, 192].

For a given energy spread of the electron beam from linac, we choose the number of undulator periods $N_u \simeq \gamma/\delta\gamma$. Based upon this argument, we have chosen $N_u = 15$ in our calculations. A longer undulator will generate brighter radiation according to Eq. (6.6). However, as discussed, Eq. (6.6) is valid for monoenergetic beam. For a beam with finite energy spread, the brightness will reduce since finite energy spread will lead to additional width in radiation spectrum. If we take $\delta\gamma/\gamma > 1/N_u$, the brightness and the spectral width of the emitted radiation will be limited by the energy spread of the electron beam. Also, if we take a longer undulator, the radiation beam size at the exit of the undulator will increase and the radiation beam may strike the edge of the vacuum pipe of the undulator. We have taken the undulator period λ_u as 50 mm and the undulator parameter K from 0.6 to 2.1. These values of the K parameter can be achieved by choosing the undulator gap g_u between 40 to 20 mm for an undulator made up of pure permanent magnets, as can be seen using Eq. (6.9).

In Fig. 6.4, we have shown the variation of the output power in the central cone, and the radiation wavelength, as a function of undulator parameter K for a 10 MeV electron beam. The parameters used in the calculations have been listed in Table 6.1 and Table 6.2. The radiation

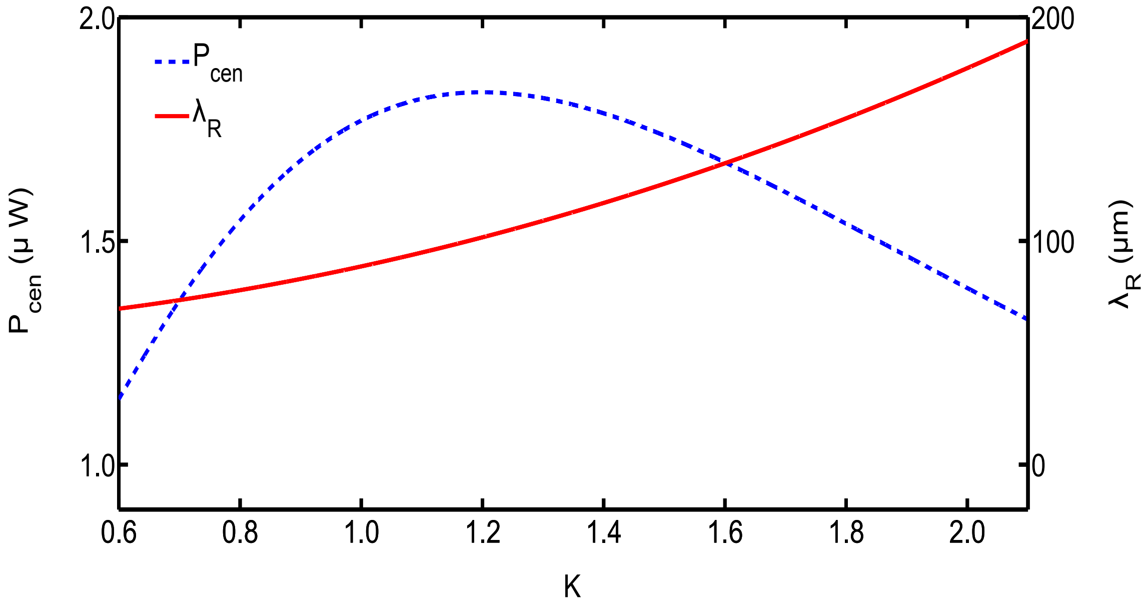

FIGURE 6.4: Plot of output power (dashed) in central cone and operating wavelength (solid) as a function of undulator parameter K for E = 10 MeV, I = 10 mA, N_u = 15, and λ_u=50 mm.

wavelength increases with K value, and the output power shows a maxima near $K = 1.2$. The maximum output power in the central radiation cone is obtained as 1.8 μW at 3 THz frequency. The selection of a narrow spectrum around the central wavelength can be made by using a THz bandpass filter in the path of the output radiation. The bandpass filters fabricated from gold-mesh frequency-selective surfaces are commercially available, and have transmission of about 80% at 3 THz frequency [193]. The filtered radiation will thus have a continuous average power of 1.5 μW, and can be transported into a nearby experimental station via suitable optical arrangements. We would like to mention that an average power of around tens of nW can be achieved in conventional THz sources such as parametric oscillators and photoconductive

TABLE 6.2: Parameters of the undulator used in our calculation.

Undulator period (λ_u)	50 mm
No. of periods (N_u)	15
Undulator gap (g_u)	20 - 40 mm
Undulator parameter (K)	2.1 - 0.6
Peak magnetic field (B_0)	0.45 - 0.13 T
Radiation wavelength (λ_R)	190 - 70 μm

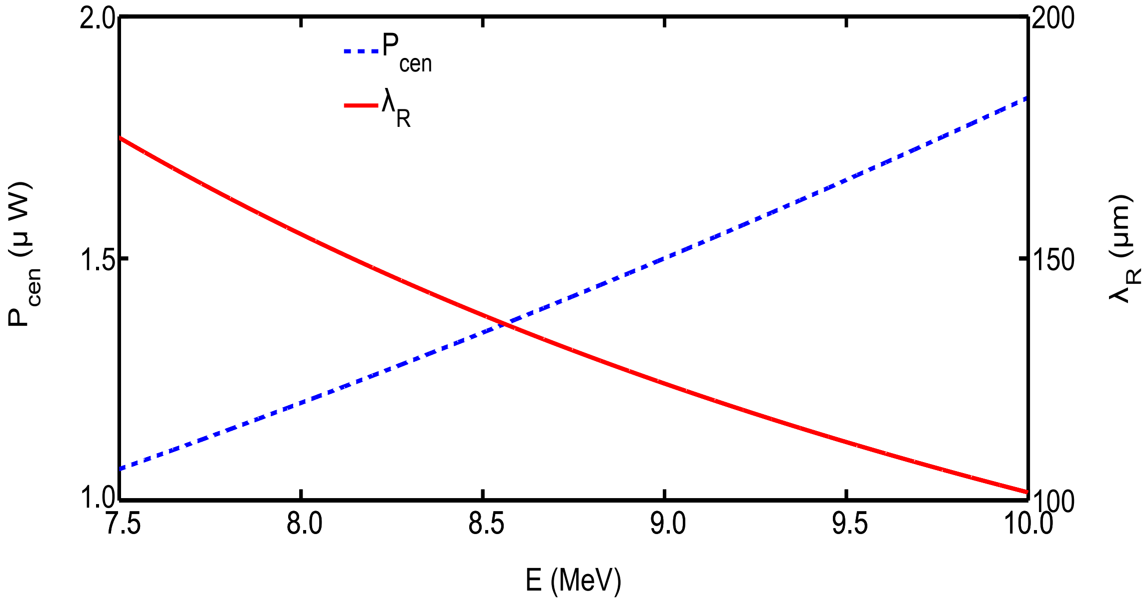

FIGURE 6.5: Plot of output power (dashed) in central cone and operating wavelength (solid) as a function of electron beam energy for I = 10 mA, K = 1.2, λ_u = 50 mm, and N_u = 15.

antennas [194]. However, all these sources are not continuously tunable. Further, the relative bandwidth of the output radiation at central wavelength in the proposed system is around 14%, which is nearly three times less than the relative bandwidth of output radiation in the conventional sources described above [194].

For a fixed undulator period, the wavelength of the output radiation in the proposed system can be tuned by either changing the electron beam energy or by changing the undulator gap. In our example case, we take the energy range from 7.5 MeV to 10 MeV, and the undulator gap g_u can be changed from 20 mm to 40 mm under normal tuning range. As shown in Fig. 6.4, the radiation wavelength can be tuned from 70 μm to 190 μm by varying K from 0.6 to 2.1 for a 10 MeV electron beam. For E = 10 MeV and K = 2.1, the rms radiation beam waist size σ_T is calculated as 2 mm by taking into account the finite electron beam size as mentioned in the previous section. The radiation beam diameter at the exit of undulator is obtained as 15.3 mm. It is thus ensured that the maximum value of optical beam size is sufficiently smaller than the minimum value of the undulator gap. Further increment in K value will make the optical beam size comparable or larger than the minimum undulator gap. The radiation wavelength can also be tuned by changing the electron beam energy. In Fig. 6.5, we have shown such an example.

Here, we have considered $K = 1.2$ to keep the output power around the maximum value and varied the electron beam energy in range 7.5 MeV to 10 MeV. By using these parameters, we can get output radiation ranging from 1.6 THz to 4.3 THz with average power of the order of 1 μW.

An approximate value of spectral brightness $\mathcal{B}_{\Delta\omega/\omega}$ of the emitted radiation for K=1.2 and E=10 MeV is estimated by using Eq. (6.6) as 9×10^8 photons/s/mm^2/ mrad^2 (0.1% BW), which can also be written as $\mathcal{B}_{\Delta\omega/\omega} = 0.6\times10^{-6}$ W/mm^2/sr (0.1% of BW). The spectral brightness of output radiation in the proposed system is comparable to the brightness of coherent synchrotron radiation at the meterology light source [195], and higher than the conventional thermal sources.

We would now like to mention some applications that can be performed by using a continuously tunable radiation in the frequency range from 1.6 THz to 4.3 THz, having an average power of the order of μW. As discussed in the literature [4, 5], THz radiation is easily passed through the paper based envelopes and is partially passed through the plastics and ceramics [5]. This has great utility in performing the multispectral THz imaging to identify substances without opening the envelopes containing sensitive materials [179]. THz radiation with average power of the order μW is useful in non-destructive probing of sensitive biological materials and fragile electronic parts [2, 10, 12], where low average power (form tens of $\sim$ nW up to 1 μW) is required [8]. At the present time, most of the commercially available conventional THz sources produce tens or hundreds of nW average power [194], which is commonly used in the imaging and spectroscopy applications [2, 4, 10, 12]. The proposed THz source with average power of the order of μW and very high brightness will be helpful in obtaining the high-resolution images in the spectroscopy and imaging related applications [19].

In our calculations, a moderate value of normalized electron beam emittance is considered, i.e., $\varepsilon_n = 30$ mm-mrad, which can be easily achieved in a typical 10 MeV electron linac [196]. Note that the effect of finite electron beam size and divergence is not be significant as long as the normalized rms electron beam emittance is much less than $\beta\gamma\lambda_R/4\pi$, which is 310 mm-mrad for $\lambda_R = 190\ \mu$m, and 115 mm-mrad for $\lambda_R = 70\ \mu$m. We have also found that the space charge effects are negligible for the chosen parameters of the electron beam as the space-charge term turns out to be much smaller then the emittance term in the beam envelope equation. This condition can be expressed as [144]:

$$\frac{\sigma_e^2}{2\beta\gamma\varepsilon_n^2}\frac{I_p}{I_A} < 1, \tag{6.10}$$

where $I_p = 4.8$ A is the peak current of micropulse. The value of the left-hand side of the above equation is obtained as 0.003, for which the inequality is satisfied.

6.3 Numerical simulations

We have also performed numerical simulations using the computer code GINGER [181] to study the power growth and power spectrum of the spontaneous emission in the optimized undulator. GINGER is a multi-dimensional [full 3D for particles and 2D $(r - z)$ for radiation], time dependent computer code, which is primarily developed to simulate FELs in various configurations. In addition, it can also simulate the process of spontaneous emission discussed in this chapter. It solves KMR [197] undulator-period-averaged equations in slowly varying envelope approximation. Spontaneous emission evolves from the shot noise, which is modelled in GINGER by appropriately giving a controlled amount of randomness in initial longitudinal phases of particles [198].

Here, we describe the simulation results for one particular case, i.e., beam energy of 10 MeV and $K = 1.2$, which has been discussed in the previous section. The rest of the parameters of the electron beam and the undulator are same as described earlier in the text. The simulation code GINGER has taken a Gaussian profile for the electron beam with the transverse beam sizes given in Table 6.1. Figure 6.6 shows the evolution of the radiated power along the length of the undulator. It is seen that ~3 μW of average power is radiated at the undulator exit, which is higher than the value of 1.8 μW obtained using the analytic formula for the power radiated in the central cone. This is because the computer code GINGER integrates the power over a bandwidth,

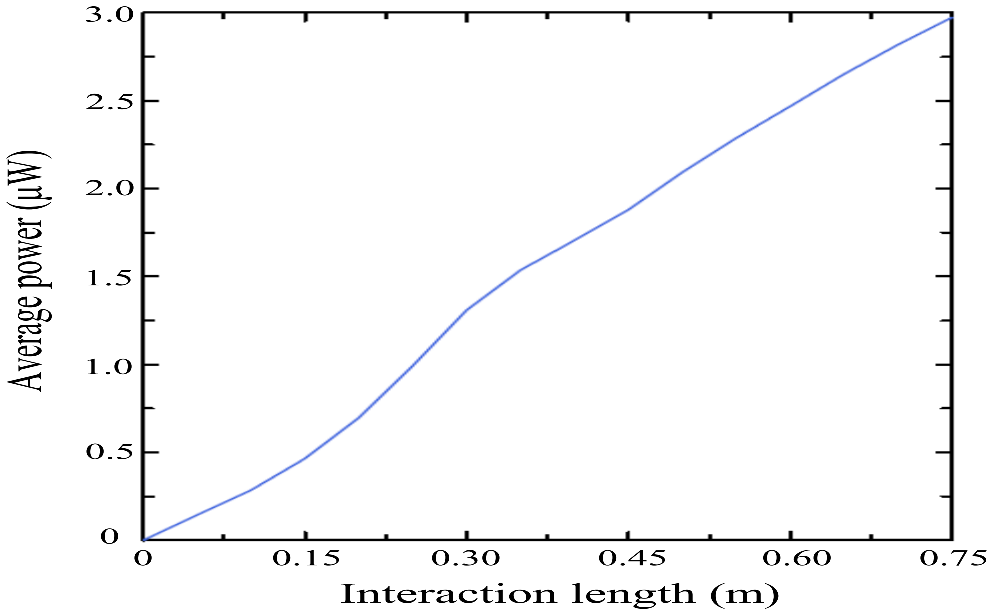

FIGURE 6.6: Plot of radiated power as a function of interaction length for the spontaneous emission in an undulator having $K = 1.2$, $N_u = 15$, and λ_u=50 mm. For the input electron beam, energy E is taken as 10 MeV, and average current I is considered as 10 mA.

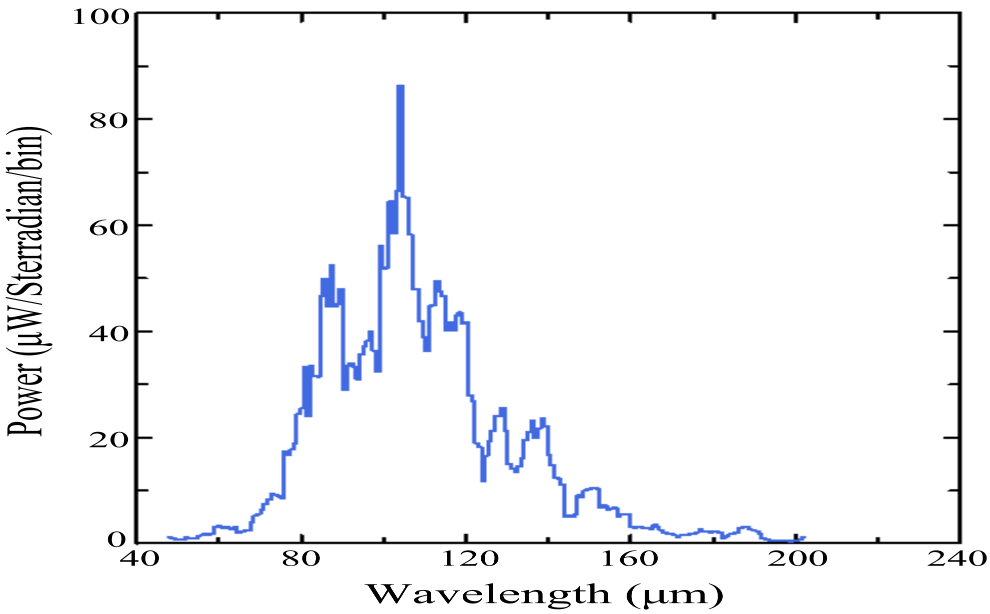

FIGURE 6.7: Plot of power spectrum in spontaneous emission of radiation at the exit of a 75 cm long undulator having $K = 1.2$, $N_u = 15$, and $\lambda_u = 50$ mm. The input electron beam energy E is taken as 10 MeV, and input electron beam current I is considered as 10 mA.

which is larger than the bandwidth of the radiation emitted in the central radiation cone [199], as seen in Fig. 6.7. The full spectrum of radiation emitted in the central radiation cone should have wavelength in the range $100 \pm 14\mu$m, whereas the radiation spectrum calculated using GINGER has wavelength even outside this range. The simulation result thus reasonably agrees

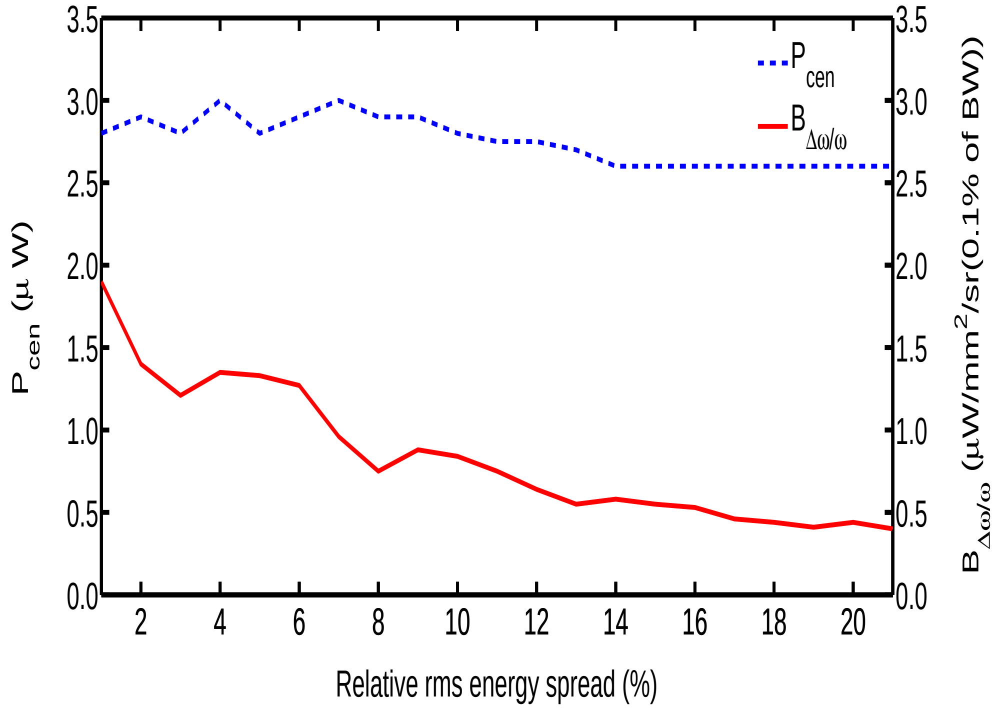

FIGURE 6.8: Plot of output power (dashed) and spectral brightness (solid) as a function of relative rms beam energy spread for ε_n = 30 mm-mrad, I = 10 mA, and K = 1.2. Calculations are performed using the code GINGER.

with the results of the analytical calculations.

We have also performed numerical simulations to study the effect of energy spread and emittance of the electron beam on the power and brightness of undulator radiation. Figure 6.8 shows the effect of variation of energy spread, when the beam emittance is kept constant at 30 mm-mrad. As expected, there is only a nominal reduction in the radiated power with energy spread, whereas the brightness decreases significantly with energy spread. This is because as the energy spread increases, there are more particles with reduced energy, resulting in slightly reduced emission of spontaneous emission. The bandwidth of emitted radiation however increases significantly with energy spread as discussed in Sec. 6.2, which results in significant reduction of brightness. We have then studied the effect of variation in beam emittance as shown in Fig. 6.9. Here, as the beam emittance increases, the electron beam size increases because of which more number of particles become off axis and radiate with less efficiency. Also, as the emittance increases, the radiated power decreases because the average longitudinal speed of particles decreases due to increase in the off-axis component of velocity. This also leads to a

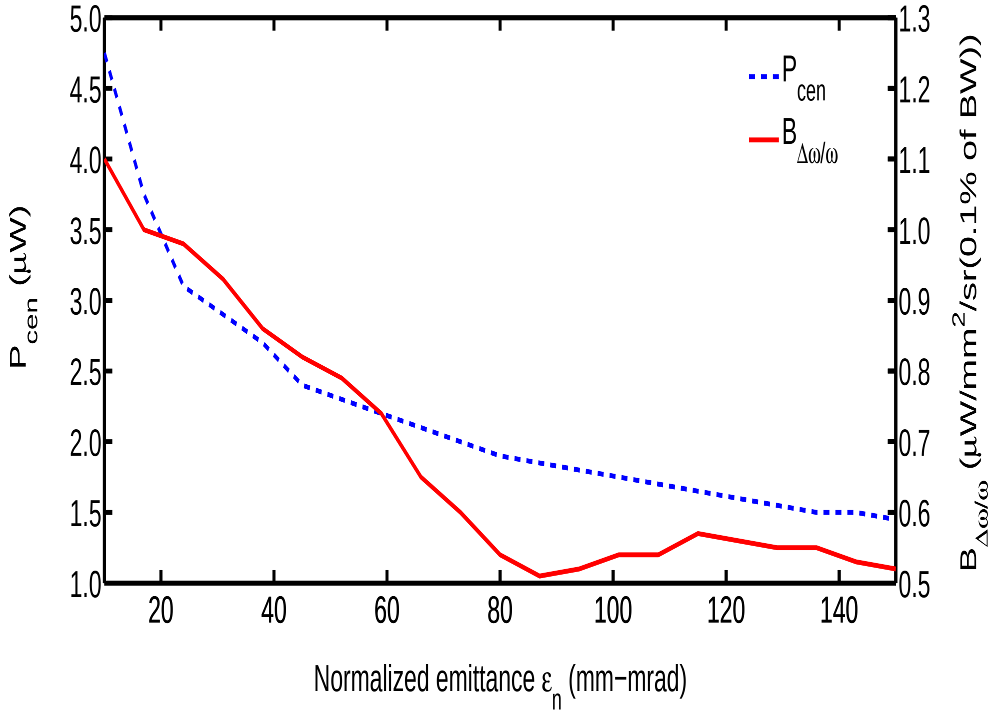

FIGURE 6.9: Output power (dashed) and spectral brightness (solid) as a function of normalized beam emittance for the undulator parameters $K = 1.2$. The beam current is here assumed to be 10 mA and the relative rms energy spread of the electron beam is taken as 7%. Calculations are performed using the code GINGER.

spread in the frequency of radiation emitted by different electrons. As can be understood from the formula for the source size described in Sec. 6.2, the source size increases with emittance. Due to the broadening of the radiation spectrum and increase in the source size, the brightness decreases with emittance, as seen in Fig. 6.9. We would like to mention that we have verified in the simulation that the power and brightness are here directly proportional to the beam current, which is expected from Eqs. (6.5) and (6.6).

Based on the results of numerical simulation studies presented in this section, we find that the proposed system will be able to generate $\sim 1\ \mu$W of terahertz power with a brightness 10^9 photons/s/mm^2/ mrad^2 (0.1% BW), including the effect of finite emittance and energy spread of the electron beam.

6.4 Discussions and conclusion

In this chapter, we have discussed a proposal to enhance the utilization of a high average power industrial electron linac by using an undulator to generate terahertz radiation, in addition to the intended irradiation application. In an FEL, the average power of the electron beam is typically low, which is usually of the order of few tens or hundreds of Watts. Such an electron beam typically generates THz radiation of sub-nW power through spontaneous emission, which gets enhanced to the order of few tens or hundreds of mW through the process of stimulated emission. To have a strong interaction between the electron beam and the optical beam in an FEL system such that it generates stimulated radiation, the electron beam envelope has to be well inside the optical beam envelope throughout the interaction length, and its average electron beam radius over the length of the undulator needs to be minimum. This requires that the parameters related to the profile of the electron beam are suitably matched at the entrance of the undulator. Also, for the operation in the FEL oscillator configuration, we need to use an achromat to bend the electron beam and match it with axis of the undulator immersed in the quasi-optical resonator. All this is achieved by having a suitable beam transport line between the linac and the undulator. In addition, as discussed, very high quality electron beam with low energy spread, low emittance and high peak current is needed for the generation of stimulated emission in an FEL. These requirements are not there, when we use a high average power electron beam for the generation of THz radiation through the process of spontaneous emission, as discussed in the chapter. This makes the proposed device simpler.

We would like to mention that as the electron beam propagates down the undulator, an additional energy spread will be induced due to the quantum fluctuations of the spontaneous undulator radiation [200]. For parameters considered in our example case, we have calculated the relative energy spread induced by the undulator as 0.015% by following an analysis given in Ref. [200]. This value of induced energy spread is quite low as compared to the considered initial relative energy spread of 7.0%. Hence, the spent electron beam after emitting the THz radiation can still be used for the irradiation applications.

To conclude, we have presented an analysis of a device, which is based on the arrangement of a powerful industrial linac and an undulator, to produce useful THz radiation, along with the intended irradiation applications. For the analysis of undulator radiation, we followed a recent approach given in Ref. [183]. By taking an example case of the high average power industrial linac, we have optimized the parameters of an undulator which can be used to produce copious THz radiation. We observed that an undulator with moderate parameters such as length 0.75 m, period 50 mm and K from 0.6 to 2.1, can be used with 7.5 to 10 MeV, 100 kW linac to produce a continuous tunable THz radiation (1.6 THz to 4.3 THz) with an output power in the central cone of the order of μW and spectral brightness of the order of 10^9 photons/s/mm^2/ mrad^2 (0.1% BW). We have also verified these calculations by performing the numerical simulations using a computer code GINGER [181]. Thus, the utilization of a high power electron linac can be enhanced with the help of a short undulator, which . The device can simultaneously be used for terahertz generation, as well as irradiation applications. The output radiation can be tuned by changing the undulator gap or by changing the electron beam energy. Tunable continuous THz radiation generated using such a device will be very useful in the imaging and spectroscopy related applications [19, 179].

Chapter 7

Conclusions and outlook

In this thesis, we have performed theoretical studies on electron beam based compact devices, which utilize either the phenomena of Čerenkov radiation or Smith-Purcell radiation or undulator radiation to generate copious THz electromagnetic waves for various possible applications. Currently, undulator based conventional FELs are used to generate coherent electromagnetic radiation starting from the THz up to X-ray wavelengths. Successful operation of such FELs, however, requires a relativistic electron beam with stringent parameters such as a small energy spread and emittance, and a high peak current. Generation of such high quality electron beams requires large and expensive infrastructure, and the radiological hazard associated with such electron beams requires an elaborated radiation shielding for its mitigation. It is therefore imperative to look for alternate innovative schemes wherever possible. Although undulator based FELs are inevitable for the production of high power radiation at X-ray wavelengths, it is possible to use low energy electron beam based FELs utilizing Čerenkov radiation or Smith-Purcell radiation as an alternative to undulator based FELs for the generation of high power radiation at THz wavelengths. Use of a low energy electron beam here leads to two important advantages - (1) it requires only a nominal radiation shielding, and (2) the device becomes compact. The research work presented in this thesis is mainly focused towards the theoretical understanding of such compact sources of THz radiation, namely the Čerenkov FEL and the Smith-Purcell FEL. Amongst different configurations of these sources, the single slab based

CFELs and single grating based SP-FELs in the open configuration are observed to be more feasible for *high-frequency* and *high-power* operation. Our aim in this thesis has been to understand the challenges involved in the successful operation of CFELs and SP-FELs in this configuration and suggest ways to overcome these challenges such that it become feasible to generate a copious amount of tunable THz radiation using low energy electron beams, even after including the realistic effects.

In order to study a single slab based CFEL system, we have established a single particle approach based on coupled Maxwell-Lorentz equations, in analogy with the undulator based FELs. Due to the evanescent nature of the electromagnetic field, taking a flat electron beam having vertical size very small compared to the horizontal size leads to a better performance. We have therefore set up the coupled Maxwell-Lorentz equations for the single slab based CFEL driven by a flat electron beam. In order to do this, we have followed an approach developed by Kumar and Kim [88] for setting up the coupled Maxwell-Lorentz equations for SP-FELs, where they analyzed the singularity in the reflectivity of an evanescent wave incident on the grating surface. This singularity arises when the frequency and wavenumber of the wave satisfy the dispersion relation. The Laurent series expansion of reflectivity around this singularity here gives two important parameters- χ and χ_1 related to the growth rate and the ac space charge term respectively. Following a similar approach, we could derive analytical expressions for χ and χ_1 for the case of a single slab based CFEL. Note that for the SP-FEL, the analytical calculations for χ and χ_1 were not possible, and therefore these parameters were obtained numerically. We then set up the Maxwell-Lorentz equations for a CFEL in terms of χ and χ_1 parameters. By analytically solving these equations in the small-signal regime, we have obtained expressions for the gain and the growth rate of the system. We have probed the non-linear behavior of this system by numerically solving the Maxwell-Lorentz equations using a self-written computer code, and calculated the saturated power to obtain the efficiency of the system. It is possible to include the effect of finite beam thickness and finite energy spread in our analysis. To perform the calculations, we have considered the parameters of the Dartmouth experiment [66]. The observed output power in the Dartmouth experiment was very low compared to the theoretical results. The observation of low output power has also been reported in the experimental studies on the SP-FEL system at Dartmouth College [69] and Vanderbit University [71] in USA, and at CEA/Cesta [72] in France.

With an objective to explain the poor performance of the past experiments on CFELs and SP-FELs, we performed a full 3D analysis for these devices by including the realistic effects of diffraction and attenuation. For a CFEL, we derived the attenuation coefficient due to Ohmic and dielectric losses. We showed that these effects are significant, and it may be required to operate the system at lower temperature, i.e. at 77 K. In order to study the effect of diffraction, we have set up localized surface modes supported by a dielectric slab placed on the conducting surface and calculated its important properties. By analyzing the surface mode in terms of its Fourier components which interact with the corresponding Fourier components of the current density vector, we could set up the 3D Maxwell-Lorentz equations for a single slab based CFEL. We use the same approach to derive 3D Maxwell-Lorentz equations for a SP-FEL, which are applicable in low as well as high gain regime. We found that there is a difference in the way diffraction is manifested in the CFEL system and in the SP-FEL system. We observed that the free-space wavelength λ is replaced by $\beta\lambda$ in CFELs and by λ/β_g in SP-FELs, and have provided an interesting explanation for this difference. In a low gain FEL, the gain is maximum when the radiation beam size averaged over the interaction length is minimum. We found the value of this minimum possible radiation beam size in the horizontal direction for the CFEL case using the expressions derived for the localized surface mode. We showed that for the gain calculation, this minimum possible radiation beam size should be taken as the effective horizontal size of the flat electron beam. In the vertical direction, the electron beam size was taken same as the decay length of the evanescent wave. Having derived the electron beam sizes in the vertical and horizontal directions, the required beam emittances in both these directions were evaluated such that these values of beam sizes are maintained over the entire interaction length. It is observed that a flat electron beam with vertical to horizontal emittance ratio of about 1000 is required for a typical THz CFEL, which is very difficult to achieve experimentally [146]. To relax the stringent requirements on the vertical beam emittance, we have discussed techniques of external focusing of a flat beam by using wiggler and solenoid magnetic fields, and also proposed several ways to achieve the required beam quality. These schemes are similar to the ones proposed for THz SP-FELs [78, 89].

Taking the effects of attenuation and diffraction into account, we have developed a technique to optimize the value of electron beam energy and dielectric slab thickness for the given values of operating wavelength and dielectric constant in a single slab based CFEL. We found that for an operating frequency of 0.1 THz and taking the dielectric material as GaAs (ϵ = 13.1), the most optimum electron beam energy is 40 keV and dielectric thickness is 265 μm. The electron beam current was taken as 35 mA and the dielectric slab and the metallic base were maintained at 77 K during this optimization study. For these parameters, a CFEL having 5 cm long dielectric slab can deliver an average output power of about 3.6 W with 0.26% efficiency.

In order to circumvent the deleterious effect of diffraction, we have explored the use of waveguiding in improving the performance of CFELs, while keeping in mind that waveguiding leads to an additional attenuation. We have used the Maxwell-Lorentz approach to analyze two such novel configurations- single-slab based sidewall CFEL and double-slab based rectangular CFEL. A detailed analysis of the surface mode is performed and a formula for the small-signal gain is derived for both these configurations. This was followed by analyzing the non-linear behaviour by numerically solving the Maxwell-Lorentz equations. It has been explicitly shown in our analysis that the small-signal gain and saturation power in a single slab based CFEL having metallic side walls are larger compared to the configuration without the side walls but with similar system parameters. Our results reveal that a waveguided CFEL can be operated with a shorter interaction length to achieve higher efficiency, and also to relax the stringent requirements on the vertical beam emittance as compared to the CFEL system without any waveguiding. It has also been observed that in the single pass operation, the gain as well as the loss increases in a double-slab based rectangular CFEL as compared to a single slab based sidewall CFEL, and there is increase of 15% in net gain for a particular set of parameters discussed in thesis. Now for the oscillator configuration, in a round trip, the loss needs to be considered twice. Thus the marginal gain that is achieved during a single pass is offset by the loss in a double slab based rectangular CFEL, and this configuration becomes less efficient than the single slab based sidewall CFEL.

Finally, we have explored the possibility of generating THz radiation by utilizing a high average power (100 kW) electron beam emerging from an industrial electron linac. The basic idea here was that such a high power industrial linac may not give good quality electron beam for lasing in an FEL, but when such a beam is passed through an undulator with suitably optimized parameters, it could generate useful THz radiation through spontaneous emission. We showed that for a 10 MeV, 100 kW electron linac having 7% beam energy spread, we can put a 75 cm long undulator with a period length of 50 mm in between the linac exit and the irradiation target to generate THz radiation having an average power of around 1 μW and brightness around 10^9 photons/s/mm^2/ mrad^2 (0.1% BW). The output radiation can be tuned from 1.6 to 4.3 THz by changing the undulator parameter K from 0.6 to 2.1 and the electron beam energy from 7.5 MeV to 10 MeV. Thus, the utility of an industrial linac can be enhanced with a moderate investment in terms of putting a small undulator as an additional component.

In summary, we have performed a rigorous analysis to understand the working mechanism of CFELs in planar geometry by setting up the coupled Maxwell-Lorentz equations. We have used analytical as well as numerical technique to solve these equations, and included realistic effects such as diffraction, attenuation, finite beam-size, and finite energy spread in our calculations. We have also pointed out the importance of a good quality electron beam for the successful operation of this system and proposed different methods for production of the required beam quality. While setting up the 3D Maxwell-Lorentz equations, important differences between CFELs and SP-FELs have been understood, which has implication on their performances. Two novel configurations of CFELs - Sidewall CFEL in single slab geometry and rectangular CFEL in double slab geometry have been studied, which show enhanced performance. In addition, we have performed an optimization study to explore the possibility of generating THz radiation through spontaneous emission in an undulator, when a high average power electron beam emerging from an industrial linac is allow to pass through the undulator.

Outlook and future perspective

In the past two decades, the field of THz science has evolved significantly due to rapid development of coherent THz sources. During these years, there has been emphasis on the development of compact and tunable sources of high power coherent THz radiation, which are useful for tabletop experiments. Our work on electron beam based compact THz sources in this thesis contributes to this development.

Our approach based on the single particle coupled Maxwell-Lorentz equations, which includes the 3D effects and attenuation effects, is useful to understand the working of real world CFEL and SP-FEL systems. The 3D coupled Maxwell-Lorentz equations derived for the case of the CFEL and the SP-FEL are observed to have a form which is similar to the corresponding equations for the case of undulator based FELs. Hence, the numerical techniques that are applied for solution of such equations in a typical 3D FEL code such as GENESIS [201] can be extended for the 3D simulation of CFELs and SP-FELs.

We have followed two different approaches to set up the coupled Maxwell-Lorentz equations for the CFELs: (1) by analyzing the reflectivity of the system in terms of χ and χ_1 parameters, and (2) an approach discussed by Levush *et al*. [133] for the case of a BWO. In Ref. [88], it has been shown that both these approaches give similar results for the SP-FELs having no side walls. We have checked that even in the presence of side walls, the χ and χ_1 parameters can be derived and an analysis can be performed in terms of these parameters, and it gives the same results as described in this thesis for the case of sidewall CFELs. The same will be applicable to SP-FELs [88, 202], and the approach based on Maxwell-Lorentz equations can certainly be extended to the case of sidewall SP-FELs. The analytical formulas for χ and χ_1 can also be used for the case of negative index material based CFELs. In that case the CFEL system will work like a BWO [136], and can be studied by following an approach given in Refs. [78, 88] for Smith-Purcell BWOs.

To drive the CFEL and the SP-FEL systems, we have used a DC electron beam and hence neglected the time-dependent effects while solving the coupled Maxwell-Lorentz equations in our analysis. Both these systems can also be operated by using a bunched electron beam produced by an rf accelerator [64, 203], and the time dependent effects i.e., slippage effects become prominent for very short electron pulses and at long wavelengths, as discussed in Ref. [121]. These effects can be included in the approach based on the coupled Maxwell-Lorentz equations discussed here. In the pulsed operation mode of CFELs and SP-FELs, we can increase the output THz radiation power, which can be very useful in the dynamical study of molecular systems.

In this thesis, we have considered an operating frequency of about 0.1 THz for the CFELs in order to perform an optimization study around the parameters considered in the existing experiments [66]. For high frequency operation, the vertical decay length ($\beta\gamma\lambda/2\pi$) of the surface mode decreases and one has to use an electron beam having very small vertical size and vertical emittance for effective beam-wave interaction. Another option is to use a relativistic electron beam. Our detailed optimization study is also applicable for this case.

For the dielectric slab in the CFEL system, we have chosen an isotropic material. Sapphire crystals, which have also been used in CFEL projects [65], are anisotropic. It may be involved but interesting and useful to develop a detailed theory of a CFEL based on anisotropic dielectric.

As discussed in the thesis, the power that grows in the surface mode in CFELs and SP-FELs due to its interaction with an electron beam, is in the form of near field and non-radiative electromagnetic radiation. In order to make it useful for experiments, it is important to outcouple this electromagnetic energy in the form of freely propagating radiation. This requires a detailed analysis of the outcoupling effects, which could be taken up as future work.

Based on the results obtained in this thesis, it is interesting to compare some of the features of the CFEL and the SP-FEL system that can be helpful in the development of a practical THz source. First, it is observed that the diffraction effects are prominent in the SP-FEL as compared to the CFEL. Therefore, in the case of SP-FEL, the grating length has to be kept small to reduce the diffraction loss and to maintain the sufficient interaction of the surface mode with the co-propagating electron beam. Second, the attenuation due to the finite conductivity of the metal is more in the case of the SP-FEL compared to the CFEL. This is because the SP-FEL has more metallic surface area for a unit length as compared to the CFEL. The attenuation effect increases with the operating frequency [99, 167]. Hence, at higher frequency, it will be preferable to use the structure which has less attenuation. From this point of view, it will be preferable to opt for CFEL for *high-frequency* operation, and SP-FEL for *low-frequency* operation. Third, we have more number of variables to tune the radiation properties in a SP-FEL as compared to a CFEL. This is because the basic system parameters of CFEL are d and ϵ, where ϵ is fixed for a particular dielectric material. We are thus effectively left with only one variable in the single slab based CFEL. On the other hand, in the SP-FEL, the system variables are: grating period, groove depth, and groove width [88, 204]. Although the efficiencies of both these systems are similar, varying from fraction of a percent to few percent, it is possible to obtain slightly higher efficiency for the SP-FEL since there are more number of system parameters that can be optimized.

For the undulator based THz source driven by a high power industrial linac that we have discussed in the thesis, we have taken the vacuum chamber diameter such that the THz beam does not get cut by hitting the vacuum chamber. This puts a constraint on the undulator gap and corresponding K parameter. In order to operate at higher values of K parameter, it may be useful to explore the concept of waveguiding in this system, which is similar to the theory of waveguided CFELs discussed in the thesis.

Appendix A

Surface mode analysis in a single-slab based sidewall Čerenkov FEL

In this appendix, we present a detailed analysis of the surface mode supported by an empty configuration (without the electron beam) of a single slab based sidewall CFEL. This system is shown in Fig. A.1, where a dielectric slab with thickness d, length L, and relative dielectric permittivity ϵ is placed on a metallic surface. Along the y-direction, the dielectric slab is surrounded with metallic side walls, which are placed at $y = \pm w/2$. We assign the region above the dielectric slab as region I, and dielectric medium as region II. The dielectric slab is assumed to be an isotropic structure in the (y, z) plane. The optical properties of the system will therefore remain invariant under any arbitrary rotation in the (y, z) plane. Hence, the electromagnetic surface mode supported by this geometry can be obtained by combining the plane wave solutions of an open structure [142], i.e., the structure without any side wall, in a suitable manner such that it satisfies the boundary conditions. The detailed analysis of the surface mode supported by a CFEL without any sidewall has been presented in Chapter 2. By using the property of isotropy in this way, we combine two plane evanescent waves each having frequency ω and wave vector $k_0 = \sqrt{k_y^2 + k^2}$, travelling in different directions in the (y, z) plane to obtain the following field components of the surface mode in region I:

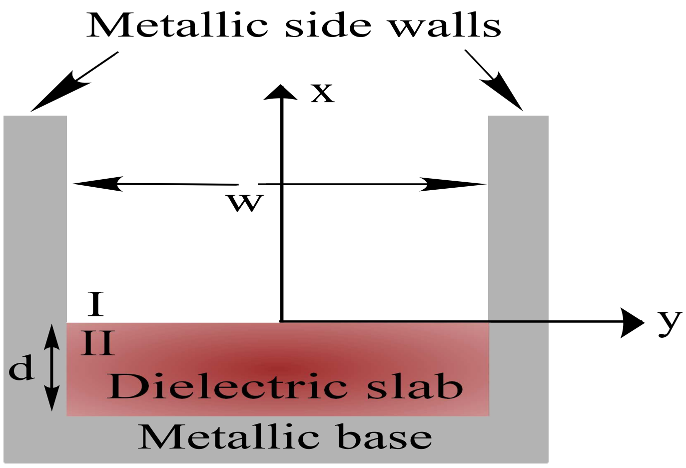

FIGURE A.1: Schematic of a single slab based CFEL having metallic side walls. The electron beam is not shown here.

$$H_y^I = (k_z H/k_0)\cos(k_y y)^{i(k_z z-\omega t)} e^{-\Gamma(x-h)} + \text{c.c.}, \tag{A.1}$$

$$H_z^I = (-ik_y H/k_0)\sin(k_y y) e^{i(k_z z-\omega t)} e^{-\Gamma(x-h)} + \text{c.c.}, \tag{A.2}$$

$$E_x^I = (k_0 H/\epsilon_0 \omega)\cos(k_y y) e^{i(k_z z-\omega t)} e^{-\Gamma(x-h)} + \text{c.c.}, \tag{A.3}$$

$$E_y^I = (k_y \Gamma H/\epsilon_0 \omega k_0)\sin(k_y y) e^{i(k_z z-\omega t)} e^{-\Gamma(x-h)} + \text{c.c.}, \tag{A.4}$$

$$E_z^I = (-ik_z \Gamma H/\epsilon_0 \omega k_0)\cos(k_y y) e^{i(k_z z-\omega t)} e^{-\Gamma(x-h)} + \text{c.c.}, \tag{A.5}$$

and $H_x^I = 0$. Here, $k_z = 2\pi/\beta\lambda$ is the propagation wavenumber in the z-direction, $\beta = v/c$, $\omega = 2\pi c/\lambda$, λ is the free space wavelength, $\Gamma = \sqrt{k_y^2 + k_z^2 - \omega^2/c^2}$, $k_y = \pi/w$, and c.c. denotes complex conjugate. Inside region II, the components of electromagnetic field are obtained as:

$$H_y^{II} = \frac{\epsilon k_z \Gamma H}{k_1 k_0} \frac{\cos[k_1(x+d)]}{\sin(k_1 d)} \cos(k_y y) e^{\Gamma h} e^{i(k_z z-\omega t)} + \text{c.c.}, \tag{A.6}$$

$$H_z^{II} = \frac{-i\epsilon k_y \Gamma H}{k_1 k_0} \frac{\cos[k_1(x+d)]}{\sin(k_1 d)} \sin(k_y y) e^{\Gamma h} e^{i(k_z z - \omega t)} + \text{c.c.}, \tag{A.7}$$

$$E_x^{II} = \frac{k_0 \Gamma H}{\epsilon_0 \omega k_1} \frac{\cos[k_1(x+d)]}{\sin(k_1 d)} \cos(k_y y) e^{\Gamma h} e^{i(k_z z - \omega t)} + \text{c.c.}, \tag{A.8}$$

$$E_y^{II} = \frac{k_y \Gamma H}{\epsilon_0 \omega k_0} \frac{\sin[k_1(x+d)]}{\sin(k_1 d)} \sin(k_y y) e^{\Gamma h} e^{i(k_z z - \omega t)} + \text{c.c.}, \tag{A.9}$$

$$E_z^{II} = \frac{-ik_z \Gamma H}{\epsilon_0 \omega k_0} \frac{\sin[k_1(x+d)]}{\sin(k_1 d)} \cos(k_y y) e^{\Gamma h} e^{i(k_z z - \omega t)} + \text{c.c.}. \tag{A.10}$$

Here, $H_x^{II} = 0$ and $k_1 = \sqrt{\epsilon\omega^2/c^2 - k_y^2 - k_z^2}$.

The power flow in the surface mode can be evaluated by integrating the Poynting vector over $x \in [-d, \infty]$, and over $y \in [-w/2, w/2]$. The total power in the surface mode is sum of power flow in the vacuum and inside the dielectric medium, which we obtain as

$$P = \frac{w\beta_p \gamma_p^3}{2k_z Z_0} \left[1 + \frac{1}{\epsilon^2 a_p^2} + \frac{k_0 d(1 + a_p^2)}{\epsilon \gamma_p a_p^2}\right] |E|^2 e^{2\Gamma h}. \tag{A.11}$$

Here, $\beta_p = \omega/ck_0$ is the phase velocity of the surface mode in units of c, $\gamma_p = 1/\sqrt{1-\beta_p^2}$, $a_p = (\gamma_p/\epsilon)\sqrt{\epsilon\beta_p^2 - 1}$, and $Z_0 = 1/\epsilon_0 c$ is the characteristic impedance of the free space. Note that the above equation has been expressed in term of half amplitude E of the peak field at the location of electron beam by using Eq. (A.5). It should be noted that the total power in the sidewall CFEL is $k_z/2k_0$ times the power contained in the surface mode supported in the CFEL without any side wall [142], which is given by Eq. (2.21). This is obvious as the electromagnetic field in the sidewall CFEL is propagating at an angle, whose cosine gives the factor k_z/k_0 with respect to the z-direction. The factor 1/2 accounts for the variation of electromagnetic field along the y-direction. The energy stored in the electromagnetic fields is obtained by integrating the energy density over the volume of the dielectric, and over the volume of the vacuum region. The expression for the time-averaged energy stored per unit mode width w per unit length in the z-direction is obtained as:

$$\frac{\mathcal{U}}{|E|^2} = \frac{k_o\gamma_p^3}{2ck_z^2 Z_0}\Big[1 + \frac{1}{\epsilon^2 a_p^2} + \frac{k_0 d\beta_p^2(1+a_p^2)}{\gamma_p a_p^2}\Big]e^{2\Gamma h}. \tag{A.12}$$

The energy velocity of the electromagnetic fields is given by $P/w\mathcal{U}$. Using Eqs. (A.11) and (A.12), we obtain the group velocity of the surface mode supported in the sidewall CFEL as:

$$v_g = \frac{\beta_p c k_z}{k_0}\frac{[\beta_p^2\gamma_p^3(\epsilon-1) + k_0 d\epsilon(1+a_p^2)]}{[\beta_p^2\gamma_p^3(\epsilon-1) + k_0 d\epsilon^2\beta_p^2(1+a_p^2)]}\ . \tag{A.13}$$

In the sidewall CFEL, the group velocity of the surface mode is k_z/k_0 times the group velocity of the CFEL without any side wall [142].

Next, by following the approach given in chapter 2, we evaluate the attenuation coefficient of the surface mode, which is given by [122]

$$\alpha^{d,c} = \frac{P_l^{d,c}}{2P}, \tag{A.14}$$

where P_l represents the power loss per unit length along the z-direction, and the subscripts d and c are used to represent the dielectric medium and the metallic conductor respectively. Inside the dielectric medium, losses are described in the terms of complex relative permittivity $\tilde{\epsilon} = \epsilon - i\epsilon'$ with tangent loss defined as $\tan\delta = \epsilon'/\epsilon$ [123]. The power loss per unit length inside the dielectric material is given by $P_l^d = \epsilon_0\epsilon\omega\tan\delta\int_{-d}^{0}\int_{-w/2}^{w/2}(|E_x^{II}|^2+|E_y^{II}|^2+|E_z^{II}|^2)dxdy$. By using Eqs. (A.8-A.10), we first evaluate P_l^d, and then by using Eq. (A.14), we obtain the attenuation coefficient α^d as:

$$\alpha^d = \frac{k_0^2\tan\delta}{2k_z}\frac{[\gamma_p(2-\epsilon\beta_p^2) + \epsilon^2\beta_p^2 k_0 d(1+a_p^2)]}{[\gamma_p(1+\epsilon^2 a_p^2) + \epsilon k_0 d(1+a_p^2)]}. \tag{A.15}$$

In the metallic structure with finite conductivity σ_{cond}, dissipation of power occurs due to the Ohmic losses. At the location $x = -d$, the power loss per unit length along the surface of metal is given by:$(R_s/2)\int_{-w/2}^{w/2}|H_y^{II}|^2dy$ [113], where $R_s = \sqrt{\mu_0\omega/2\sigma_{cond}}$ is the surface resistance of metal. At the location of side walls, i.e., at $y = \pm w/2$, we can write the power loss per unit length as $(R_s/2)(\int_{-d}^{0}|H_z^{II}|^2dx + \int_0^\infty |H_z^I|^2dx)$ [113]. Note that the limit of integration over x has been extended up to infinity, which is due to the fact that the electromagnetic field is decaying in the x-direction, and has a negligible value at the top of the side walls. The total power dissipated along the metallic surface P_l^c is sum of power dissipated at the metallic surface located at $x = -d$, and the power dissipated at the side walls located at $y = \pm w/2$. By performing the required algebra for P_l^c and by using the expression (A.14), we obtain the ohmic attenuation coefficient as:

$$\alpha^c = \frac{2\beta_p R_s k_y^2}{\gamma_p w k_z \Gamma Z_0}\frac{[1 + (w\Gamma k_z^2/2a_p^2k_y^2)(1 + a_p^2) + (\epsilon^2\Gamma^3/k_1^3)(a_p + k_1 d(1 + a_p^2))]}{[1 + (1/\epsilon^2 a_p^2) + (k_0 d/\epsilon\gamma_p a_p^2)(1 + a_p^2)]}. \tag{A.16}$$

Total attenuation coefficient α of the surface mode can be written as $\alpha = \alpha^d + \alpha^c$, which gives us attenuation due to both the Ohmic losses and the dielectric losses.

Appendix B

Surface mode analysis in a double-slab based rectangular Čerenkov FEL

In this appendix, we describe the electromagnetic fields supported by the empty configuration (without the electron beam) of a double slab based rectangular CFEL. By using the Poynting vector approach, we calculate power in the surface mode. These results are then explored to find the attenuation coefficient by following an approach [113, 122] discussed earlier in Chapter 2 and Appendix A. The schematic of the transverse cross section of a double slab based rectangular CFEL is shown in Fig. B.1, where a rectangular metallic waveguide with inner height $2g$ and inner width w supports dielectric slab on the top as well as on the bottom surface. The configuration is symmetric in both the x- and the y-direction. Both the dielectric slabs have thickness d and dielectric constant ϵ. We assign the vacuum region inside the waveguide as region I, dielectric medium in region between $x = d$ to $x = g + d$ as region II, and the lower dielectric slab with vertical dimension $-(g + d) < x < -g$ as region III. The electromagnetic surface mode in this configuration can be obtained by following an approach discussed in Appendix A, where it is shown that for an isotropic system in the (y, z) plane, the surface modes in the waveguided geometry can be constructed by taking the superposition of plane wave solutions of the electromagnetic field supported in an open configuration, i.e., the configuration without any side wall along the y-direction. The solution of electromagnetic fields in the open

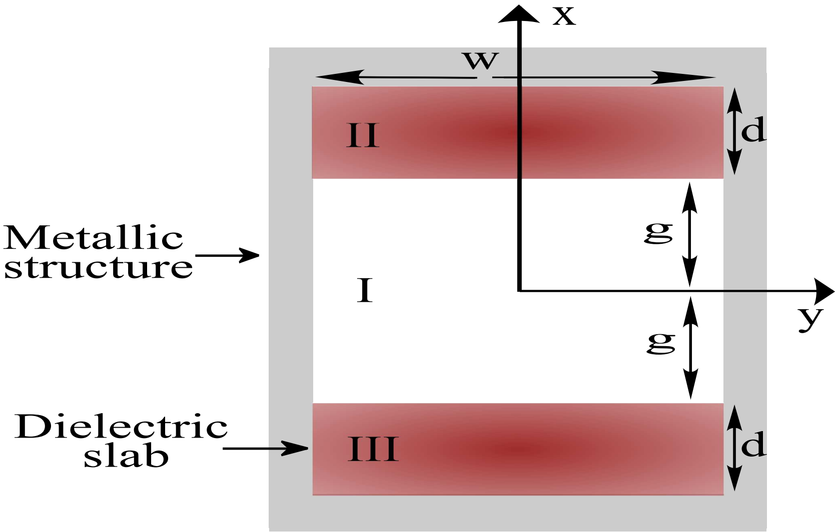

FIGURE B.1: Schematic of a double slab based rectangular CFEL system. The electron beam is not shown here.

configuration of a double slab CFEL has been discussed earlier in the literature [101, 128, 175]. We use results given in Refs. [101, 128, 175] and the property of isotropy of the dielectric slabs in the (y, z) plane to obtain the following components of electromagnetic fields in region I of the double slab based rectangular CFEL

$$E_z^I = \frac{k_z A}{k_0} \cosh(px)\cos(k_y y)e^{i(k_z z-\omega t)} + \text{c.c.}, \tag{B.1}$$

$$E_y^I = \frac{ik_y A}{k_0} \cosh(px)\sin(k_y y)e^{i(k_z z-\omega t)} + \text{c.c.}, \tag{B.2}$$

$$E_x^I = \frac{-ik_0 A}{p} \sinh(px)\cos(k_y y)e^{i(k_z z-\omega t)} + \text{c.c.}, \tag{B.3}$$

$$H_y^I = \frac{-i\epsilon_0 \omega k_z A}{pk_0} \sinh(px)\cos(k_y y)e^{i(k_z z-\omega t)} + \text{c.c.}, \tag{B.4}$$

$$H_z^I = \frac{-\epsilon_0 \omega k_y A}{pk_0} \sinh(px)\sin(k_y y)e^{i(k_z z-\omega t)} + \text{c.c.}, \tag{B.5}$$

and $H_x^I = 0$. Here, $k_z A/k_0$ is half peak amplitude of the longitudinal electric field at $x = 0$, and is represented by E in our analysis, $k_z = 2\pi/\beta\lambda$ is the propagation wavenumber in the z-direction, $\beta = v/c$, $\omega = 2\pi c/\lambda$, λ is the free space wavelength, $k_y = \pi/w$, $k_0 = \sqrt{k_y^2 + k_z^2} = 2\pi/\beta_p\lambda$, $p = \sqrt{k_y^2 + k_z^2 - \omega^2/c^2}$, and c.c. denotes complex conjugate. Inside region II, the components of electromagnetic field are given by

$$E_z^{II} = \frac{k_z C}{k_0}[\sin(qx) - \tan[q(g+d)]\cos(qx)]\cos(k_y y)e^{i(k_z z - \omega t)} + \text{c.c.}, \tag{B.6}$$

$$E_y^{II} = \frac{ik_y C}{k_0}[\sin(qx) - \tan[q(g+d)]\cos(qx)]\sin(k_y y)e^{i(k_z z - \omega t)} + \text{c.c.}, \tag{B.7}$$

$$E_x^{II} = \frac{ik_0 C}{q}[\cos(qx) + \tan[q(g+d)]\sin(qx)]\cos(k_y y)e^{i(k_z z - \omega t)} + \text{c.c.}, \tag{B.8}$$

$$H_y^{II} = \frac{i\epsilon_0\epsilon\omega k_z C}{qk_o}[\cos(qx) + \tan[q(g+d)]\sin(qx)]\cos(k_y y)e^{i(k_z z - \omega t)} + \text{c.c.}, \tag{B.9}$$

$$H_z^{II} = \frac{\epsilon_0\epsilon\omega k_y C}{qk_o}[\cos(qx) + \tan[q(g+d)]\sin(qx)]\sin(k_y y)e^{i(k_z z - \omega t)} + \text{c.c.}, \tag{B.10}$$

and $H_x^{II} = 0$. Here, $q = \sqrt{\epsilon\omega^2/c^2 - k_y^2 - k_z^2}$. As the system is symmetric in the vertical direction, we replace x to $-x$ in the above equations to obtain the following equations for the electromagnetic fields in region III:

$$E_z^{III} = \frac{-k_z C}{k_0}[\sin(qx) + \tan[q(g+d)]\cos(qx)]\cos(k_y y)e^{i(k_z z - \omega t)} + \text{c.c.}, \tag{B.11}$$

$$E_y^{III} = \frac{-ik_y C}{k_0}[\sin(qx) + \tan[q(g+d)]\cos(qx)]\sin(k_y y)e^{i(k_z z - \omega t)} + \text{c.c.}, \tag{B.12}$$

$$E_x^{III} = \frac{ik_0 C}{q}[\cos(qx) - \tan[q(g+d)]\sin(qx)]\cos(k_y y)e^{i(k_z z-\omega t)} + \text{c.c.}, \tag{B.13}$$

$$H_y^{III} = \frac{i\epsilon_0\epsilon\omega k_z C}{qk_o}[\cos(qx) - \tan[q(g+d)]\sin(qx)]\cos(k_y y)e^{i(k_z z-\omega t)} + \text{c.c.}, \tag{B.14}$$

$$H_z^{III} = \frac{\epsilon_0\epsilon\omega k_y C}{qk_o}[\cos(qx) - \tan[q(g+d)]\sin(qx)]\sin(k_y y)e^{i(k_z z-\omega t)} + \text{c.c.}, \tag{B.15}$$

and $H_x^{III} = 0$. Here, $C = (D_1 k_0/k_z)E$ and D_1 is given by the following expression:

$$D_1 = \frac{\cosh(pg)}{\sin(qg) - \cos(qg)\tan[q(g+d)]}. \tag{B.16}$$

The total power flow in the surface mode is sum of power flow in the dielectric and vacuum regions. In vacuum region, i.e., region I, the time-averaged power flow is given by $P^v = (1/2)\int_{-w/2}^{w/2}\int_{-g}^{g}(\boldsymbol{E^I} \times \boldsymbol{H^{I*}})dxdy$, which we have calculated as:

$$P^v = \frac{\epsilon_0\omega w k_o^2|E|^2}{2k_z p^3}[\sinh(2pg) - 2pg]. \tag{B.17}$$

In region II, the time-averaged power flow is given by $p^{II} = (1/2)\int_{-w/2}^{w/2}\int_{g}^{g+d}(\boldsymbol{E^{II}} \times \boldsymbol{H^{II*}})dxdy$. A similar contribution will be from the bottom dielectric, namely region III. After performing the required algebra, we obtain the time-averaged power flow in both the dielectric slabs as:

$$P^d = \frac{\epsilon_0\epsilon\omega w k_o^2 D_2 D_1^2|E|^2}{k_z q^3}, \tag{B.18}$$

where D_2 is given by the following expression

$$D_2 = qd + \sin(qd)\cos[q(2g+d)] + \tan^2[q(g+d)](qd - \sin(qd)\cos[q(2g+d)]) \\ +2\tan[q(g+d)]\sin(qd)\sin[q(2g+d)]. \tag{B.19}$$

The total time-averaged power is obtained by taking sum of Eqs. (B.17) and (B.18), which we write as:

$$\frac{P}{|E|^2} = \frac{\epsilon_0 \omega w k_o^2}{2k_z p^3 q^3}[q^3(\sinh(2pg) - 2pg) + 2\epsilon D_2 D_1^2 p^3], \tag{B.20}$$

where the coefficients D_1 and D_2 are given by Eqs. (B.16) and (B.19) respectively.

Now, we find the attenuation coefficient of the surface mode due to the presence of dielectric and Ohmic losses. The attenuation coefficient is defined as:

$$\alpha^{c,d} = \frac{P_l^{c,d}}{2P}. \tag{B.21}$$

As discussed in Chapter 1 and Appendix A, the Ohmic losses occur due to the finite conductivity σ_{cond} of the metallic structure. By assuming that the dissipation occurs in a very small region near the metallic surface, the Ohmic losses occur at the metallic sidewalls located at $y = \pm w/2$ and at the bottom and top conducting surfaces located at $x = -(g+d)$ and $x = (g+d)$ respectively. We can write the total power loss per unit length at locations $x = \pm(g+d)$ as $(R_s/2)\int_{-w/2}^{w/2}(|H_y^{II}|^2 + H_y^{III}|^2)dy$ [113], where $R_s = \sqrt{\mu_0\omega/2\sigma_{cond}}$. At the location of metallic sidewalls, i.e., $y = \pm w/2$, we can write the power loss per unit length as $(R_s/2)(\int_{-(g+d)}^{g}|H_z^{III}|^2 dx + \int_{-g}^{g}|H_z^{I}|^2 dx + \int_{g}^{g+d}|H_z^{II}|^2 dx)$ [113]. The total power dissipated per unit length P_l^c is calculated in this way, and by using Eq. (B.20), we find the Ohmic attenuation coefficient as

$$\alpha^c = \frac{2R_s\epsilon_0\omega}{wk_z k_0^2}\frac{[k_y^2 q^3(\sinh(2pg) - 2pg) + 2\epsilon^2 k_y^2 p^3 D_2 D_1^2 + wq\epsilon^2 k_z^2 p^3 D_1^2 \cos^2[q(g+d)](1+\tan^2[q(g+d)])^2]}{[q^3(\sinh(2pg) - 2pg) + 2\epsilon D_2 D_1^2 p^3]}. \tag{B.22}$$

Inside the dielectric medium, losses are described in the terms of tangent loss, i.e., $\tan\delta = \epsilon'/\epsilon$, where ϵ and ϵ' are real and complex part of the dielectric permittivity $\tilde{\epsilon} = \epsilon - i\epsilon'$ respectively. The power loss per unit length inside the dielectric material is given by $P_l^d = \epsilon_0\epsilon\omega\tan\delta(\int_{-(g+d)}^{-g}\int_{-w/2}^{w/2}(|E_x^{III}|^2 + |E_y^{III}|^2 + |E_z^{III}|^2)dxdy + \int_{g}^{g+d}\int_{-w/2}^{w/2}(|E_x^{II}|^2 + |E_y^{II}|^2 + |E_z^{II}|^2)dxdy)$. By using the set of Eqs. (B.6-B.8) and (B.11-B.13), we first evaluate P_l^d, and then by using

Eq. (B.20), we obtain the dielectric attenuation coefficient α^d as:

$$\alpha^d = \frac{2\epsilon p^3 \tan\delta D_1^2[k_0^2 D_2 + q^2 D_3]}{k_z[q^3(\sinh(2pg) - 2pg) + 2\epsilon D_2 D_1^2 p^3]}, \tag{B.23}$$

where the coefficient D_3 is given by the following expression

$$D_3 = qd - \sin(qd)\cos[q(2g+d)] + \tan^2[q(g+d)](qd - \sin(qd)\cos[q(2g+d)]) \\ -2\tan[q(g+d)]\sin(qd)\sin[q(2g+d)]. \tag{B.24}$$

The sum of the Ohmic losses and the dielectric losses gives the total losses present in the system, which we have represented by the total attenuation coefficient: $\alpha = \alpha^c + \alpha^d$, and can be obtained by adding Eqs. (B.22) and (B.23).

Bibliography

[1] E. J. Nichols and J. D. Tear, Astrophys. J. **61**, 17 (1925).

[2] P. H. Siegel, IEEE Trans. Microwave Theory Tech. **50**, 910 (2002).

[3] G. P. Gallerano and S. Biedron, in *Proceedings of FEL Conference* (JACoW, Trieste, Italy, 2004), pp. 216–221.

[4] M. Tonouchi, Nature Photonics **1**, 97 (2007).

[5] R. A. Lewis, *Terahertz Physics* (Cambridge University Press, New York, USA, 2013).

[6] B. Zhu, Y. Chen, K. Deng, W. Hu, and Z. S. Yao, in *Proceedings of Progress In Electromagnetics Research Symposium (Beijing, China)* (2009), pp. 1166–1170.

[7] A. Barychev, A. Belitskaya, H. Van der Linden, and W. Jellema, *Method and system for inspection of composite assemblies using terahertz radiation* (2015), US Patent App. 13/962,210.

[8] A. R. Orlando and G. P. Gallerano, J. Infrared and Mili. Terahz Waves **30**, 1308 (2009).

[9] L. V. Titova, A. K. Ayesheshim, A. Golubov, D. Fogen, R. Rodriguez-Juarez, F. A. Hegmann, and O. Kovalchuk, Biomed. Opt. Express **4**, 559 (2013).

[10] P. H. Siegel, IEEE Trans. Microwave Theory Tech. **52**, 2438 (2004).

[11] B. M. Fischer, M. Hoffmann, H. Helm, R. Wilk, F. Rutz, T. Kleine-Ostmann, M. Koch, and P. U. Jepsen, Opt. Express **13**, 5205 (2005).

[12] M. S. Sherwin, C. A. Schmuttenmaer, and P. H. Bucksbaum, in *Report of a DOE-NSF-NIH Workshop* (U.S. Department of Energy, 2004).

[13] J. W. Waters, Adv. Space Res. **21**, 1363 (1998).

[14] P. Y. Han and X.-C. Zhang, Meas. Sci. Technol. **12**, 1747 (2001).

[15] P. Jepsen, D. Cooke, and M. Koch, Laser & Photonics Reviews **5**, 124 (2011).

[16] J.-F. Roux, F. Garet, and J.-L. Coutaz, *Principles and Applications of THz Time Domain Spectroscopy* (Springer Netherlands, 2014), pp. 203–231.

[17] Q. Wu, T. D. Hewitt, and X.-C. Zhang, Appl. Phys. Lett. **69**, 1026 (1996).

[18] H.-T. Chen, R. Kersting, and G. C. Cho, Appl. Phys. Lett. **83**, 3009 (2003).

[19] W. L. Chan, J. Deibel, and D. M. Mittleman, Rep. Prog. Phys. **70**, 1325 (2007).

[20] C. A. Schmuttenmaer, Chem. Rev. **104**, 1759 (2004).

[21] A. Pashkin, M. Porer, M. Beyer, K. W. Kim, A. Dubroka, C. Bernhard, X. Yao, Y. Dagan, R. Hackl, A. Erb, et al., Phys. Rev. Lett. **105**, 067001 (2010).

[22] U. Bovensiepen, Physics **3**, 63 (2010).

[23] A. Crocker, H. A. Gebbie, M. F. Kimmitt, and L. E. S. Mathias, Nature **201**, 250 (1964).

[24] L.-H. Xu, R. M. Lees, E. C. C. Vasconcellos, S. C. Zerbetto, L. R. Zink, and K. M. Evenson, IEEE J. Quantum Electron. **32**, 392 (1996).

[25] R. Kohler, A. Tredicucci, F. Beltram, H. E. Beere, E. H. Linfield, A. G. Davies, D. A. Ritchie, R. C. Iotti, and F. Rossi, Nature **417**, 156 (2002).

[26] B. S. Williams, S. Kumar, H. Callebaut, Q. Hu, and J. L. Reno, Appl. Phys. Lett. **83**, 5142 (2003).

[27] E. Normand, I. Howieson, and M. McCulloch, Laser Focus World **43**, 90 (2007).

[28] E. Bründermann, D. Chamberlin, and E. Haller, Infrared Physics & Technology **40**, 141 (1999).

[29] D. H. Auston, K. P. Cheung, J. A. Valdmanis, and D. A. Kleinman, Phys. Rev. Lett. **53**, 1555 (1984).

[30] X. Zhang and D. H. Auston, J. Appl. Phys. **71**, 326 (1992).

[31] G. D. Boyd and A. Ashkin, Phys. Rev. **146**, 187 (1966).

[32] E. R. Brown, K. A. McIntosh, K. B. Nichols, and C. L. Dennis, Appl. Phys. Lett. **66**, 285 (1995).

[33] K. J. Button and J. C. Wiltse, *Infrared and millimeter waves* (Academic Press, University of Michigan, USA, 1979).

[34] M. Abo-Bakr, J. Feikes, K. Holldack, G. Wüstefeld, and H.-W. Hübers, Phys. Rev. Lett. **88**, 254801 (2002).

[35] G. P. Williams, Rev. Sci. Instrum. **73**, 1461 (2002).

[36] P. Kung, H. Lihn, H. Wiedemann, and D. Bocek, Phys. Rev. Lett. **73**, 967 (1994).

[37] A. Gover, F. V. Hartemann, G. P. Le Sage, N. C. Luhmann, R. S. Zhang, and C. Pellegrini, Phys. Rev. Lett. **72**, 1192 (1994).

[38] D. A. Jaroszynski, R. J. Bakker, A. F. G. van der Meer, D. Oepts, and P. W. van Amersfoort, Phys. Rev. Lett. **71**, 3798 (1993).

[39] K. Berryman, E. Crosson, K. Ricci, and T. Smith, Nucl. Instrum. Methods Phys. Res. A **375**, 526 (1996).

[40] S. Kuruma, K. Mima, K. Imasaki, S. Nakai, and C. Yamanaka, Nucl. Instrum. Methods Phys. Res. A **358**, 90 (1995).

[41] W. Barletta, J. Bisognano, J. Corlett, P. Emma, Z. Huang, K.-J. Kim, R. Lindberg, J. Murphy, G. Neil, D. Nguyen, et al., Nucl. Instrum. and Methods in Phys. Res. A **618**, 69 (2010).

[42] C. A. Brau, *Free-electron lasers* (Academic Press, San Diego, 1990).

[43] S. Krishnagopal, V. Kumar, S. Maiti, S. Prabhu, and S. K. Sarkar, Curr. Sci. **87**, 1066 (2004).

[44] G. L. Carr, M. C. Martin, W. R. McKinney, G. R. N. K. Jordan, and G. P. Williams, Nature(London) **420**, 153 (2002).

[45] G. Ramian, Nucl. Instrum. Methods Phys. Res. A **318**, 225 (1992).

[46] J. Blau, K. Cohn, W. B. Colson, and R. Vigil, in *Proceedings of FEL Conference* (New York, USA, 2013), pp. 486–490.

[47] A. Doria, V. Asgekar, D. Esposito, G. Gallerano, E. Giovenale, G. Messina, and C. Ronsivalle, Nucl. Instrum. Methods Phys. Res. A **475**, 296 (2001).

[48] S. G. Biedron, J. W. Lewellen, S. V. Milton, N. Gopalsami, J. F. Schneider, L. Skubal, Y. Li, M. Virgo, G. P. Gallerano, A. Doria, et al., in *Proceedings of the IEEE* (IEEE, 2007), vol. 95, pp. 1666–1678.

[49] A. V. Smirnov, R. Agustsson, W. J. Berg, S. Boucher, J. Dooling, T. Campese, Y. Chen, L. Erwin, B. Jacobson, J. Hartzell, et al., Phys. Rev. ST Accel. Beams **18**, 090703 (2015).

[50] V. Ginzburg, Dokl. Akad. Nauk SSSR **56**, 253 (1947).

[51] M. Danos, S. Geschwind, H. Lashinsky, and A. V. Trier, Phys. Rev. **92**, 828 (1953).

[52] M. Danos, J. Appl. Phys. **26**, 2 (1955).

[53] G. T. di Francia, Nuovo Cimento **16**, 61 (1960).

[54] V. K. Tripathi, J. Appl. Phys. **56**, 1953 (1984).

[55] J. E. Walsh, T. C. Marshall, and S. P. Schlesinger, Phys. Fluids **20**, 709 (1977).

[56] K. Felch, K. Busby, R. Layman, D. Kapilow, and J. E. Walsh, Appl. Phys. Lett. **38**, 601 (1981).

[57] S. V. Laven, J. Branscum, J. Golub, R. Layman, and J. Walsh, Appl. Phys. Lett. **41**, 408 (1982).

[58] E. P. Garate, S. Moustaizis, J. M. Buzzi, C. Rouille, H. Lamain, J. Walsh, and B. Johnson, Appl. Phys. Lett. **48**, 1326 (1986).

[59] I. de la Fuente, Ph.D. thesis, Laser Physics and Non-Linear Optics Group, University of Twente (2007).

[60] E. P. Garate, J. Walsh, C. Shaughnessy, B. Johnson, and S. Moustaizis, Nucl. Instrum. Methods Phys. Res. A **259**, 125 (1987).

[61] Q. Wang, S. Yu, P. Xun, S. L. K. Hu, Y. Chen, and P. Wang, Appl. Phys. Lett. **59**, 2378 (1991).

[62] Q. Wang, K. Zhao, C. Chen, K. Hu, Y. Chen, and P. Wang, Nucl. Instrum. Methods Phys. Res. A **349**, 299 (1994).

[63] F. Ciocci, G. Dattoli, A. Angelis, A. Dipace, A. Doria, E. Fiorentino, G. P. Gallerano, T. Letardi, A. Marino, A. Renieri, et al., Nucl. Instrum. Methods Phys. Res. A **259**, 128 (1987).

[64] F. Ciocci, A. Doria, G. P. Gallerano, I. Giabbai, M. F. Kimmitt, G. Messina, A. Renieri, and J. E. Walsh, Phys. Rev. Lett. **66**, 699 (1991).

[65] E. E. Fisch and J. E. Walsh, Appl. Phys. Lett. **60**, 1298 (1992).

[66] I. J. Owens and J. H. Brownell, J. Appl. Phys. **97**, 104915 (2005).

[67] M. R. Asakawa, K. Nakao, M. Kusaba, and Y. Tsunawaki, in *Proceedings of the FEL Conference* (JACoW, Berlin, 2006), pp. 364–367.

[68] N. Miyabe, A. Ikeda, M. R. Asakawa, M. Kusaba, and Y. Tsunawaki, in *Proceedings of the 29th Free Electron Laser Conference, Novosibirsk, Russia* (BINP, Novosibirsk, 2007), pp. 406–408.

[69] J. Urata, M. Goldstein, M. F. Kimmitt, A. Naumov, C. Platt, and J. E. Walsh, Phys. Rev. Lett. **80**, 516 (1998).

[70] M. Mross, T. Lowell, R. Durant, and M. Kimmitt, J. Biol. Phys. **29**, 295 (2003).

[71] J. Gardelle, L. Courtois, P. Modin, and J. T. Donohue, Phys. Rev. ST Accel. Beams **12**, 110701 (2009).

[72] H. L. Andrews, C. A. Brau, J. D. Jarvis, C. F. Guertin, A. O'Donnell, B. Durant, T. H. Lowell, and M. R. Mross, Phys. Rev. ST Accel. Beams **12**, 080703 (2009).

[73] H. P. Bluem, R. H. Jackson, J. D. Jarvis, A. M. M. Todd, J. Gardelle, P. Modin, and J. T. Donohue, IEEE Trans. Plasma Sci. **43**, 3176 (2015).

[74] P. A. Čerenkov, Phys. Rev. **52**, 378 (1937).

[75] J. Wieland, J. Couperus, P. J. M. van der Slot, and W. J. Witteman, Nucl. Instrum. Methods Phys. Res. A **429**, 17 (1999).

[76] S. J. Smith and E. M. Purcell, Phys. Rev. **92**, 1069 (1953).

[77] O. H. Kapp, Y. e Sun, K.-J. Kim, and A. V. Crewe, Rev. Sci. Instrum. **75**, 4732 (2004).

[78] K.-J. Kim and V. Kumar, Phys. Rev. ST Accel. Beams **10**, 080702 (2007).

[79] H. P. Freund and T. M. Abu-Elfadl, IEEE Trans. Plasma Sci. **32**, 1015 (2004).

[80] F. Ciocci, G. Dattoli, A. Doria, G. Schettini, A. Torre, and J. E. Walsh, Nuovo Cimento **10D**, 1 (1988).

[81] J. E. Walsh and J. B. Murphy, IEEE J. Quantum Electron. **18**, 1259 (1982).

[82] J. Walsh, B. Johnson, G. Dattoli, and A. Renieri, Phys. Rev. Lett. **53**, 779 (1984).

[83] H. Fares, Phys. Plasmas **19**, 053109 (2012).

[84] I. J. Owens and J. H. Brownell, Phys. Rev. E **67**, 036611 (2003).

[85] W. B. Colson, Phys. Lett. **59A**, 187 (1976).

[86] R. Bonifacio, C. Pellegrini, and L. M. Narducci, Opt. Commun. **50**, 373 (1984).

[87] P. Sprangle and C. M. Tang, Appl. Phys. Lett. **39**, 677 (1981).

[88] V. Kumar and K.-J. Kim, Phys. Rev. E **73**, 026501 (2006).

[89] V. Kumar and K.-J. Kim, Phys. Rev. ST Accel. Beams **12**, 070703 (2009).

[90] V. Kumar and K.-J. Kim, in *Proceedings of the 29th Free Electron Laser Conference, Novosibirsk, Russia* (BINP, Novosibirsk, 2007), pp. 38–41.

[91] L. Schachter and A. Ron, Phys. Rev. A **40**, 876 (1989).

[92] K.-J. Kim and S.-B. Song, Nucl. Instrum. Methods Phys. Res. A **475**, 158 (2001).

[93] H. L. Andrews and C. A. Brau, Phys. Rev. ST Accel. Beams **7**, 070701 (2004).

[94] B. W. Gore, V. B. Asgekar, and A. Sen, Phys. Scripta. **53**, 62 (1996).

[95] V. B. Asgekar and G. Dattoli, Opt. Commun. **206**, 373 (2002).

[96] V. B. Asgekar and G. Dattoli, Opt. Commun. **255**, 309 (2005).

[97] Y. U. Jeong, S. Miginsky, B. Gudkov, K. Lee, J. Mun, G. I. Shim, S. Bae, H. W. Kim, K.-H. Jang, S. Park, et al., IEEE Trans. Nucl. Sci. **99**, 1 (2015).

[98] H. L. Andrews and C. A. Brau, J. Appl. Phys. **101**, 104904 (2007).

[99] H. L. Andrews, C. H. Boulware, C. A. Brau, and J. D. Jarvis, Phys. Rev. ST Accel. Beams **8**, 050703 (2005).

[100] J. D. Jarvis, H. L. Andrews, and C. A. Brau, Phys. Rev. ST Accel. Beams **13**, 020701 (2010).

[101] D. Li, G. Huo, K. Imasaki, and M.Asakawa, Nucl. Instrum. Methods Phys. Res. A **606**, 689 (2009).

[102] G. Sharma and G. Mishra, Nucl. Instrum. Methods Phys. Res. A **685**, 35 (2012).

[103] R. Prazeres, Phys. Rev. Accel. Beams **19**, 060703 (2016).

[104] D. Li, K. Imasaki, X. Gao, Z. Yang, and G.-S. Park, Appl. Phys. Lett. **91**, 221506 (2007).

[105] H. L. Andrews, J. D. Jarvis, and C. A. Brau, J. Appl. Phys. **105**, 024904 (2009).

[106] J. T. Donohue and J. Gardelle, Phys. Rev. ST Accel. Beams **14**, 060709 (2011).

[107] M. Kumar, N. Chaudhury, D. Bhattacharjee, V. Yadav, S. R. Ghodke, R. Baranwal, J. Mondal, R. R. Tiwary, S. Chandan, A. R. Tillu, et al., Indian J. Pure Appl. Phys. **50**, 802 (2012).

[108] S. H. Kim, H. R. Yang, Y. G. Son, S. D. Jang, S. J. Park, M. Cho, W. Namkung, and J. S. Oh, in *Proceedings of LINAC Conference* (JACoW, 2008), pp. 548–550.

[109] A. A. Bryazgin, V. I. Bezuglov, E. N. Kokin, M. V. Korobeinikov, G. I. Kuznetsov, I. G. Makarov, G. N. Ostreiko, A. D. Panfilov, V. M. Radchenko, G. V. Serdobintsev, et al., Instruments and experiments techniques **54**, 295 (2011).

[110] K.-J. Kim, in *Proceedings of Physics of Particle Accelerators Conference, AIP Conference Proceedings No. 184 (Fermilab, Cornell University, New York)* (1989), pp. 565–632.

[111] D. Atwood, *Soft X-rays and extreme ultraviolet radiation* (Cambridge University Press, New York, 1999).

[112] D. M. Pozar, *Microwave engineering* (John Wiley & Sons, Inc., New York, 1998).

[113] J. D. Jackson, *Classical Electrodynamics* (John Wiley, Singapore, 1999).

[114] D. J. Griffith, *Introduction to electrodynamics* (Prentice Hall of India, New Delhi, 2002).

[115] V. Kumar and K.-J. Kim, in *Proceedings of the 21st Particle Accelerator Conference, Knoxville, TN* (IEEE, Piscataway, NJ, 2005), pp. 1616–1618.

[116] A. M. Cook, R. Tikhoplav, S. Y. Tochitsky, G. Travish, O. B. Williams, and J. B. Rosenzweig, Phys. Rev. Lett. **103**, 095003 (2009).

[117] D. Mihalcea, P. Piot, and P. Stoltz, Phys. Rev. ST Accel. Beams **15**, 081304 (2012).

[118] R. J. England, R. J. Noble, K. Bane, D. H. Dowell, C.-K. Ng, J. E. Spencer, S. Tantawi, Z. Wu, R. L. Byer, E. Peralta, et al., Rev. Mod. Phys. **86**, 1337 (2014).

[119] E. V. Loewenstein, D. R. Smith, and R. L. Morgan, Appl. Opt. **12**, 398 (1973).

[120] J. Krupka, D. Mouneyrac, J. G. Hartnett, and M. E. Tobar, IEEE Trans. Microwave Theory Tech. **56**, 1201 (2008).

[121] J. S. Choi, K.-J. Kim, and M. Xie, Nucl. Instrum. Methods Phys. Res. A **331**, 587 (1993).

[122] S. Y. Liao, *Microwave Devices and Circuits* (Dorling Kindersley, India, 2011).

[123] R. A. Waldron, *Theory of Guided Electromagnetic Waves* (Van Nostrand Reinhold Inc., U.S., 1970).

[124] Lord Rayleigh(J. W. Strutt), Proc. R. Soc. London, Ser. A **79**, 399 (1907).

[125] M. Neviere, *Electromagnetic Theory of Gratings* (Springer-Verlag,Berlin, 1980).

[126] P. M. V. den berg, J. Opt. Soc. Am. A **63**, 1588 (1973).

[127] P. M. V. den berg and T. H. Tan, J. Opt. Soc. Am. A **64**, 235 (1974).

[128] E. P. Garate, C. H. Shaughnessy, and J. Walsh, IEEE J. Quantum Electron. **23**, 1627 (1987).

[129] H. Fares and M. Yamada, Phys. Plasmas **18**, 093106 (2011).

[130] G. Dattoli, A. Renieri, and A. Torre, *Lectrures on the Free Electron Laser Theory and related Topics* (World Scientific, Singapore, 1993).

[131] V. Kumar, Ph.D. thesis, School of Physics, Devi Ahilya Vishwavidyalaya, Indore, India (2000).

[132] Y. Seo., E. H. Choi, and G. S. Cho, J. Phys. D: Appl. Phys. **33**, 654 (2000).

[133] B. Levush, T. M. Antonsen, A. Bromborsky, W. R. Lou, and Y. Carmel, IEEE Trans. Plasma Sci. **20**, 263 (1992).

[134] S. J. Cooke, A. A. Mondelli, B. Levush, T. M. Antonsen, D. P. Chernin, T. H. McClure, D. R. Whaley, and M. Basten, IEEE Trans. Plasma Sci. **28**, 841 (2000).

[135] R. J. Pierce, *Travelling wave tubes* (D.Van Nostrand Company Inc.; First edition, 1950).

[136] D. Li, Y. Wang, M. Hangyo, Y. Wei, Z. Yang, and S. Miyamoto, Appl. Phys. Lett. **104**, 194102 (2014).

[137] R. P. Feynman, *The Feynman Lectures on Physics: volume I* (Pearson Publication, New Delhi, 2002).

[138] R. S. Palais and R. A. Palais, *Differential Equations, Mechanic, and Computation* (American Mathematical Society, USA, 2009).

[139] C. Penman and B. McNeil, Opt. Commun. **90**, 82 (1992).

[140] A. E. Siegman, *Lasers* (University Science books Mil Valley, California, 1986).

[141] F. Pampaloni and J. Enderlein (2004), arXiv:physics/0410021.

[142] Y. Kalkal and V. Kumar, Phys. Rev. ST Accel. Beams **18**, 030707 (2015).

[143] T. P. Horikis and M. S. McCallum, J. Opt. Soc. Am. A **23**, 829 (2006).

[144] A. Chao, *Physics of Collective Beam Instabilities in High Energy Accelerators* (John Wiley & Sons, Inc., New York, 1993).

[145] P. Piot, Y.-E. Sun, and K.-J. Kim, Phys. Rev. ST Accel. Beams **9**, 031001 (2006).

[146] J. Zhu, P. Piot, D. Mihalcea, and C. R. Prokop, Phys. Rev. ST Accel. Beams **17**, 084401 (2014).

[147] E. Scharlemann, J. Appl. Phys. **58**, 2154 (1985).

[148] J. H. Booske, W. W. Destler, Z. Segalov, D. J. Radack, E. T. Rosenbury, J. Rodgers, T. M. Antonsen, V. L. Granatstein, and I. D. Mayergoyz, J. Appl. Phys. **64**, 6 (1988).

[149] D. Li, Z. Yang, K. Imasaki, and G.-S. Park, Phys. Rev. ST Accel. Beams **9**, 040701 (2006).

[150] J. T. Donohue and J. Gardelle, Phys. Rev. ST Accel. Beams **9**, 060701 (2006).

[151] L. Schächter, Journal of Applied Physics **67**, 3582 (1990).

[152] J. H. Booske, B. D. McVey, and T. M. Antonsen, J. Appl. Phys. **73**, 4140 (1993).

[153] R. Brinkmann, Y. Derbenev, and K. Flöttmann, Phys. Rev. ST Accel. Beams **4**, 053501 (2001).

[154] D. B. Tanner and D. C. Larson, Phys. Rev. **166**, 652 (1968).

[155] Y. Kalkal and V. Kumar, in *DAE-BRNS National Laser Symposium (NLS-24)* (Department of atomic energy, India, 2015), p. 1.26.

[156] R. Forman and D. H. Smith, IEEE Trans. Electron Devices **26**, 1567 (1979).

[157] A. Taran, D. Voronovich, S. Plankovskyy, V. Paderno, and V. Filipov, IEEE Trans. Electron Devices **56**, 812 (2009).

[158] J. A. Clarke, *The Science and Technology of Undulators and Wigglers* (Oxford University Press, New York, USA, 2004).

[159] B. Peterson, O. Oniku, W. Patterson, D. L. Roy, A. Garraud, F. Herrault, N. Dempsey, D. Arnold, and M. Allen, Physics Procedia **52**, 36 (2014).

[160] C. Ekdahl, IEEE Trans. Plasma Sci. **43**, 4123 (2015).

[161] C. Ekdahl (2015), arXiv:1503.06824v1.

[162] B. E. Carlsten, L. M. Earley, F. L. Krawczyk, S. J. Russell, J. M. Potter, P. Ferguson, and S. Humphries, Phys. Rev. ST Accel. Beams **8**, 062001 (2005).

[163] J. T. Donohue and J. Gardelle, Phys. Rev. ST Accel. Beams **14**, 060709 (2011).

[164] V. Kumar and K.-J. Kim, in *Proceedings of FEL Conference* (JACoW, Berlin, 2006), pp. 67–70.

[165] K. T. Nguyen, J. A. Pasour, T. M. Antonsen, P. B. Larsen, J. J. Petillo, and B. Levush, IEEE Trans. Electron Devices **56**, 744 (2009).

[166] K. Togawa, T. Shintake, H. Baba, T. Inagaki, K. Onoe, T. Tanaka, and H. Matsumoto, in *Proceedings of LINAC Conference* (JACoW, Lübeck, 2004), pp. 261–265.

[167] Y. Kalkal and V. Kumar, Phys. Rev. Accel. Beams **19**, 060702 (2016).

[168] H. P. Freund and A. K. Ganguly, Phys. Fluids B **2**, 2506 (1990).

[169] G. Kheiri and M. Esmaeilzadeh, Phys. Plasmas **20**, 123107 (2013).

[170] D. Zhao and Y. Ding, Phys. Plasmas **19**, 024508 (2012).

[171] Z. Ding and D. Yao-Gen, Chin. Phys. B **21**, 094102 (2012).

[172] D. Li, G. Huo, K. Imasaki, M.Asakawa, and Y. Tsunawaki, Infrared Phys. Techn. **53**, 204 (2010).

[173] Y. Kalkal and V. Kumar, Nucl. Instrum. Methods Phys. Res. A **827**, 85 (2016).

[174] B. Johnson and J. Walsh, Nucl. Instrum. Methods Phys. Res. A **237**, 239 (1985).

[175] F. Ciocci, G. Dattoli, A. Doria, G. P. Gallerano, G. Schettini, and A. Torre, Phys. Rev. A **36**, 207 (1987).

[176] I. de la Fuente, P. J. M. van der Slot, and K.-J. Boller, Phys. Rev. ST Accel. Beams **10**, 020702 (2007).

[177] I. de la Fuente, P. J. M. van der Slot, and K.-J. Boller, J. Appl. Phys. **100**, 053108 (2006).

[178] P. Dean, A. Valavanis, J. Keeley, K. Bertling, Y. L. Lim, R. Alhathlool, A. D. Burnett, L. H. Li, S. P. Khanna, D. Indjin, et al., J. Phys. D: Appl. Phys. **47**, 374008 (2014).

[179] Y. Watanabe, K. Kawase, T. Ikari, H. Ito, Y. Ishikawa, and H. Minamide, Appl. Phys. Lett. **83**, 800 (2003).

[180] L. Gabrielyan, Y. Garibyan, Y. R. Nazaryan, K. B. Oganesyan, M. Oganesyan, M. L. Petrosyan, N. S. Ananikyan, M. V. Fedorov, I. Artemiev, D. N. Klochkov, et al., in *Proceedings of WIRMS, AIP Conference Proceedings No. 1214 (Alberta, Canada)* (2010), pp. 39–41.

[181] W. Fawley, Tech. Rep. LBNL-49625-Version-2.0k, Lawrence Berkley National Laboratory (2012).

[182] C. J. Hirschmugl, M. Sagurton, and G. P. Williams, Phys. Rev. A **44**, 1316 (1991).

[183] R. R. Lindberg and K.-J. Kim, Phys. Rev. ST. Accel. Beams **18**, 090702 (2015).

[184] J. Schmerge, J. Lewellen, Y. Huang, J. Feinstein, and R. Pantell, IEEE J. Quantum Electron. **31**, 1166 (1995).

[185] LIN Xu-ling and Zhang Jian-bing and LU Yu and LUO Feng and LU Shan-liang and YU Tie-min and DAI Zhi-min, Chin. Phys. Lett. **27**, 044101 (2010).

[186] A. Doria, G. P. Gallerano, E. Giovenale, G. Messina, and I. Spassovsky, Phys. Rev. Lett. **93**, 264801 (2004).

[187] S. Kuruma, K. Mima, M. Goto, and C. Yamanaka, **407**, 50 (1998).

[188] T. I. Smith, J. M. J. Madey, L. R. Elias, and D. A. G. Deacon, J. Appl. Phys. **50**, 4580 (1979).

[189] Z. Huang, Y. Ding, and C. B. Schroeder, Phys. Rev. Lett. **109**, 204801 (2012).

[190] M. Gehlot and G. Mishra, Opt. Commun. **283**, 1445 (2010).

[191] A. Hofmann, Nucl. Instrum. Methods Phys. Res. A **152**, 17 (1978).

[192] V. Bezuglov, A. Bryazgin, K. Chernov, B. Faktorovich, V. Gorbunov, E. Kokin, M. Korobeynikov, A. Lukin, I. Makarov, S. Maximov, et al., in *Proceedings of LINAC Conference, Geneva, Switzerland* (JACoW, 2014), pp. 409–412.

[193] URL https://www.thorlabs.com/thorproduct.cfm?partnumber=FB19M100.

[194] E. R. Muller, The industrial Physicist (American Institute of Physics) **9**, 27 (2003).

[195] R. Muller, A. Hoehl, R. Klein, G. Ulm, M. Abo-Bakr, K. Bürkmann-Gehrlein, J. Feikes, M. Hartrott, J. S. Lee, J. Rahn, et al., in *Proceedings of EPAC08, (Genova, Italy)* (2008), pp. 2058–2060.

[196] J.-P. Labrie, in *Proceedings of the Linear Accelerator Conference, (Williamsburg, Virginia, USA)* (1988), pp. 611–613.

[197] N. M. Kroll, P. L. Morton, and M. R. Rosenbluth, IEEE J. Quantum Electron. **17**, 1436 (1981).

[198] W. Fawley, Phys. Rev. ST Accel. Beams **5**, 070701 (2002).

[199] B. Fawly, (private communication).

[200] J. Rossbach, E. L. Saldin, E. A. Schneidmiller, and M. V. Yurkov, Nucl. Instrum. Methods Phys. Res. A **393**, 152 (1997).

[201] S. Reiche, Nucl. Instrum. Methods Phys. Res. A **429**, 243 (1999).

[202] V. Kumar and K.-J. Kim, in *Proceedings of FEL Conference* (JACoW, Stanford, 2005), pp. 274–277.

[203] F. Ciocci, G. Dattoli, A. Angelis, A. Dipace, A. Doria, G. P. Gallerano, A. Renieri, E. Sabia, A. Torre, M. F. Kimmitt, et al., Nucl. Instrum. Methods Phys. Res. A **296**, 79 (1990).

[204] B. Hafizi, P. Sprangle, and P. Serafim, Phys. Rev. A **45**, 8846 (1992).